

DOTTORATO DI RICERCA IN FISICA

CICLO XX

Settore scientifico disciplinare di afferenza: FIS/02

**DEVELOPMENT OF A
PHYSICAL-TEMPLATE SEARCH FOR
GRAVITATIONAL WAVES FROM
SPINNING COMPACT-OBJECT BINARIES
WITH LIGO**

Presentata da: **Diego Fazi**

Coordinatore dottorato:
Chiar.mo Prof. Fabio Ortolani

Relatore:
Chiar.mo Prof. Giovanni Venturi

Co-relatori:
Prof. Yanbei Chen
Dr. Michele Vallisneri

Esame finale anno 2009

Acknowledgements

During my wonderful years at both the University of Bologna and the California Institute of Technology and as a member of the LSC I have had the chance to work and interact with many great scientists but, most of all, with great people.

I would like to give credit to several people who contributed to this work, directly and indirectly: thanks to my advisor Prof. Giovanni Venturi for giving me the possibility of conducting part of my research at the California Institute of Technology and for supporting me over the past four years; thanks to my co-advisors Prof. Yanbei Chen and Dr. Michele Vallisneri for their guidance and for having allowed me to complete my research work at Caltech; thanks to Prof. Duncan Brown for patiently introducing me to LIGO data analysis, for supervising the first part of my research and for his contribution to the writing of the PTF code; thanks to Prof. Alan Weinstein for his many helpful advices, for his encouragement and for his continued interest in this research work; thanks also for hiring me as a postdoc and hence giving continuity to my research.

Thanks to Roberto Casadio and Gianluigi Alberghi for the work on gravitational collapse together and for being co-authors of my first paper.

Thanks to Riccardo DeSalvo for having made my visit to Caltech possible and for his assistance in times of trouble.

Thanks to Albert Lazzarini for assisting me with many bureaucratic issues and for providing funds necessary to pursue my research through LIGO.

Thanks to LIGO lab and Prof. Yanbei Chen (TAPIR) for funding me and enabling me to attend many conferences.

Thanks to LisaH Goggin for her constant presence behind the divider and for sharing many important moments of our work and social life.

Thanks to Drew Keppel for sharing hotel rooms with me at the LSC meetings, for many interesting discussions and for patiently answering my many questions about the pipeline.

Thanks to my office mates Pinkesh Patel, Kari Hodge and Becky Tucker for sharing the LIGO experience as graduate students.

Thanks to Chad Hanna for his many helpful advices and for the discussions about the chi-square veto.

Thanks to Kipp Cannon for sharing his expertise in coding and related issues.
Thanks to Chris Van Den Broeck and Andrew Lundgren for attending the SBBH telecons and for many interesting discussions and suggestions.

Thanks to Lucia Santamaria for the interesting discussions about science and life and for good times at the LSC meetings.

Thanks to all the members of the CBC group and of the LSC for help, guidance and inspiration: in particular thanks to Patrick Brady, Gabriela Gonzalez, Stephen Fairhurst, Gareth Jones, Craig Robinson, Anand Segunpta, Thomas Cokelaer, Alex Dietz, Nick Fotopolous, Romain Gouaty, Jeff Kissel, Jessica Clayton, Vicky Kalogera, Eirini Messaritaki, Bangalore Sathyaprakash, Ruslan Vaulin, Peter Shawhan, Patrick Sutton, Parameswaran Ajith, Shourov Chatterji and John Whelan.

Thanks to Stuart Anderson, Phil Ehrens, Dan Kozac and Paul Armor for always being available when I had to fight with m9.

Thanks to the Italian community at Caltech, UCLA and LA in general (including "adopted" italians) for making me feel less homesick during these years: thanks to Michael Amori for all the lunches and dinners I-cook-you-pay style and soccer games; thanks to Guido Maretto for many manly discussions and for inviting me over, lending his shower and hosting me several times; thanks to Michela Biancolella and Francesca Lombardi for their patience and for the bathrobe; thanks to Ariadne Soledad Milligan (Chole) for becoming such a close and dear friend in such a short time; thanks to Luca Giacchino and Juliana Mancilla, Martina Carbone and Laurent Matheviet, Riccardo Schmidt and Zaynah Rahman, Fabio Michelucci, Elisa Franco, Arianna di Cintio for all the lunches, dinners, coffee breaks, parties and trips together; thanks to Paolo Focardi and Marta Valier for being the closest thing to relatives in a foreign country; thanks to Gangi Sacco for his friendship, for many guitar improvisations together and for sharing Yoga practice; thanks to Erika D'Ambrosio for all the times she invited me over and for being my biggest fan at shows; thanks to Massimo Rosi for the jam sessions at Caltech; thanks to Misha Gorshteyn and Cinzia Marongiu, Ciro Donalek and Simona Cianciulli, Domenico Pacifici and Claudia Leotta, Dado Marcora, Stefano Profumo and Tesla Jeltema, Paola Sgobbo, Stefano di Cairano, Luca Caneparo, Stefano Campagnola, Monica (Sonica) Varvella, John Miller, Silvia Ameglio, Veronica De Sanctis, Alberto Villa and Chiara Antonazzi, Manuel Lombardini for many lunches at Caltech and/or parties and/or good times together. Thanks to Daniela Maniezzo and Alessandro Sorrentino for the parties together and for lending us their surfboards; thanks to Sara Berretta for her friendship, for running on the beach and going to the movies together, thanks to Susy (Pow-Pow) Tran for the spring rolls; thanks to Juri Agresti and Chiara Vanni, Francesca Salsi, Ilaria Taurasi, Maria Paola Clarizia, Maria Principe, Marco Tarallo and Enrico Sibilio for the beautiful summer/fall 2005; thanks to Livia Cerullo and Antonella Iuorio for good times in the summer

of 2006.

Thanks to Kelle Cruz for carpooling in her brand-new hybrid and for not throwing her CDs!

Thanks to my band mates for all the great times together and for all the kick-ass shows we played. Thanks to Vitalogy: Jason Jennings, Ziad Afana, Eddie Lucero and Lupe Carranza, Dave Miller and thanks to Aramae: Rick (Rickstar) Fowler and Courtney Isbel, Chris (Kurusu) Biolchino (originally Biolchini from Sestola) and Christopher Schnack.

Thanks to the UCLA and co. friends for great times on the beach, dinners and parties: Sergio Abarca, Alvaro de la Camara, Slodoban (Jovca) Jovicic, Verica Savic, Sarah Kapnik; thanks to Louise (Aloisia) Nuijens for being such a good friend, for still being so European and for many chatty dinners together!

Thanks to the friends who shared part of their graduate school experience with me and to those who found the time for a beer or a pizza together when I came back home; thanks to Deborah (zia Deb) Prezzi, Davide Barbieri, Olivia Bernardi, Marco Baldi, Emilio Monti and Tonia Ouzounova, Diego Bombardelli and the horses, Marcello Bindi, Danilo Cinti, Lisa (Ganascina) Bartoli, Nicoletta Mauri, Silvia (Guancia) Romagnoli, Lisa (Maga) Ferrini, Sofia and Federico Fazi, Karin Pedron, Filippo Bianco and Carla Angelini; thanks to Elisabetta (Baghino) Cesarini for the LVC conferences together and for visiting me in California.

Thanks to those few friends who have always been there despite of the long distance that separated us: thanks to Marco (G.. you know what) Rossi for his tears when I left Italy, for being one of the few guys to tell me "ti voglio bene" and for always finding the time to see me when I came back; thanks to Francesco (Cecio) Cecinato for his continued friendship, for sharing our live's events and for always being in tune with me; thanks to Luca (Bobo) Ferroni and Eleonora Latini (Winnie Pooh) for their close and dear friendship, for having chosen me as best man for their wedding and for the beautiful vacation together in the summer of 2008; thanks to Pietro for knowing what friendship means and for visiting me in summer 2008; thanks to Gianluca (Mello) Rimei for being the oldest friend I have and still being there; thanks to Lucio (Bucio) Cristino for always finding a way to meet me when I came back and for his true friendship.

Thanks to everybody who surfed the waves and rode the dunes with me.

Thanks to Dino Barbiera and Heather Frascchetti and everybody I played soccer with...it's been fun!

Thanks to my family for the constant love and support; thanks to Mum and Dad, Chiara and Paolo, beautiful Maddalena and Lucia for being the strongest point of reference in my life since I was born.

Finally thanks to Laura for her unconditional love and patience; we would not have made it through these tough years if you hadn't been so loving, caring and present.

Anyone I forgot...sorry!

Disclaimer

This thesis contains some results concerning the playground data from the LIGO S5 run. These results do not reflect the opinion of the LIGO Scientific Collaboration and have not been reviewed by the Collaboration.

Contents

Notations and conventions	xiii
Introduction	1
1 Gravitational Waves: the theory	5
1.1 The Generation of Gravitational Waves	5
1.2 Sources of Gravitational Waves	8
1.2.1 Periodic Sources: Spinning Neutron stars	8
1.2.2 Unmodeled Bursts	8
1.2.3 Stochastic Background	9
1.2.4 Compact Binaries	9
1.2.5 Ringdowns	10
1.3 Coalescing Binaries	10
1.3.1 The Post-Newtonian equations of motion	11
1.3.2 End Point of Evolution	14
1.3.3 Single-Spin Binaries	15
1.3.4 The Radiative Gravitational Field of a Spinning Binary	16
1.3.5 The Precessing Convention	17
2 The Detection of Gravitational Waves	19
2.1 Effects of Gravitational Waves on Test Masses	19
2.2 The LIGO Detectors	21
2.2.1 Data Sets	23
2.2.2 The S5 Data Set	24
2.3 The Inspirational Pipeline	25
2.4 Matched Filtering	27
2.4.1 Introduction	27
2.4.2 Wiener Optimal Filtering	28
2.4.3 Detection Statistic	29
2.4.4 Inner Product	30
2.4.5 The Stationary-Phase Approximation	31

2.5	Template Bank	31
2.5.1	Intrinsic and Extrinsic Parameters	32
2.5.2	Parameter Space Metric	32
2.5.3	Template Placement	34
2.6	The χ^2 Veto	36
2.7	Searching for Gravitational Waves from Spinning Binaries	38
2.7.1	Detector Strain	38
2.7.2	Non-Spinning Templates	41
2.7.3	Phenomenological Spinning Templates - BCV	43
2.7.4	Physical Spinning Templates	44
3	The Physical Template Family of Spinning Waveforms - PTF	47
3.1	Symmetric Trace-Free Expansion of the GW-Induced Strain	47
3.2	SNR Statistic	52
3.2.1	Unconstrained Detection Statistic	56
3.2.2	Normalization and False-Alarm Statistic	60
3.2.3	A Posteriori SNR Statistics	65
3.2.4	Digital Matched Filtering	66
3.3	χ^2 Veto	67
3.3.1	Numerical Implementation	69
3.4	Detection Pipeline	70
3.4.1	Integration of the Equations of Motion	71
3.4.2	Template Implementation	78
3.4.3	Template Bank Generation	81
3.4.4	Coincidence Stage	87
4	Results	90
4.1	Testing the Filtering Code	90
4.1.1	Gaussian Noise	90
4.1.2	Gaussian Noise with Injected Software Signals	94
4.2	Bank Simulations	97
4.3	First Inspiral Stage	105
4.3.1	H1 Results	108
4.3.2	H2 Results	112
4.3.3	L1 Results	116
4.3.4	Follow-up of Nearby Missed Injections	120
4.4	The Coincidence Stage	125
4.5	χ^2 Veto	127
	Conclusions	134
	Future Prospects	135

CONTENTS

Bibliography

137

Notations and Conventions

Units of Measure

In all the formulae that appear in this work we will use units for which both the speed of light c and the gravitational constant G are set to unity, $c = G = 1$, except where explicitly stated.

The unit of measure for astrophysical masses is M_{\odot} and it indicates the mass of the sun.

Notations

Throughout this thesis we will adopt the following notations:

- \Re and \Im indicate respectively the real and imaginary parts of a complex quantity.
- A tilde indicates the Fourier transform of a function $\tilde{x}(f) \equiv \mathcal{F}[x(t)]$
- We will use both latin $i, j, k...$ and greek $\alpha, \beta, \gamma...$ letters as tensor indices, with the convention that latin indices run from 1 to 3 while greek indices run from 0 to 3.
- We will use repeated raised and lowered indices to denote contraction; when the contraction indices are latin the implicit metric is always Euclidian, so covariant and contravariant components are equal. For example we have

$$a_{ij}b^{ij} \equiv \sum_i \sum_j a_{ij}b^{ij} = \sum_i \sum_j a_{ij}b_{ij} \quad (1)$$

Conventions

- We define the continuous forward and inverse Fourier transforms of a time-domain function $x(t)$ and its frequency-domain counterpart as

$$\begin{aligned}\tilde{x}(f) &= \int_{-\infty}^{\infty} x(t) e^{-2\pi i f t} dt \\ x(t) &= \int_{-\infty}^{\infty} \tilde{x}(f) e^{2\pi i f t} df\end{aligned}\tag{2}$$

- We will denote the statistical average of a variable x with probability density $p(x)$ with an overbar, i.e.

$$\bar{x} = \int_{-\infty}^{+\infty} x p(x) dx\tag{3}$$

- We define the Minkowski metric to be $\eta_{\mu\nu} = \text{diag}(-1, 1, 1, 1)$

Introduction

One of the most interesting predictions of General Relativity is the emission of energy in the form of gravitational radiation by accelerated masses in non-axisymmetric motion; at large distance from the source the radiative gravitational field can be modeled as a wave-like perturbation of the flat space-time background that travels at the speed of light c . Massive astrophysical objects in the distant universe characterized by a time dependent stress-energy tensor with a non null quadrupolar distribution are typical sources of gravitational radiation; the non-stationary gravitational field they generate can propagate almost unchanged through the Universe, however, by the time the waves reach the earth, their strength is so weak that the detection problem is extremely challenging. As a matter of fact, no direct observation has ever been made and some people even doubt the very existence of gravitational waves (GWs).

The strongest indirect evidence of the existence of GWs comes from the Hulse-Taylor binary pulsar (PSR B1913+16) discovered in 1974 [34]; this system is composed of two neutron stars, each of mass $\sim 1.4M_{\odot}$, with average separation of $\sim 10^9$ m and orbital velocity of $\sim 10^5$ m/s. The period of the orbit is ~ 7.75 Hr and the binary is at a distance from the earth of ~ 6 Kpc. Hulse and Taylor observed that orbital period of the binary is slowly decreasing as the system loses orbital energy and the rate of energy loss shows perfect agreement (within 0.3%) with what General Relativity predicts if all the energy was to be emitted as gravitational radiation.

Gravitational waves are perturbations of space-time that cause distances between freely falling particles to change in time so, in principle, a simple measurement should allow to detect them; if the distance between two particles is $d = L$ in flat space-time, when a gravitational wave is present the distance will oscillate in time $d(t) = L + \Delta L(t)$, with a typical maximum displacement ΔL which is proportional to the strength of the gravitational wave $h \sim \Delta L/L$. However, if we consider a typical source candidate of gravitational waves such as a neutron star binary with component masses $1.4M_{\odot}$ and orbital separation of 10^5 m at a distance of 1 Mpc and estimate the strength of the gravitational waves by the time they reach the earth, we obtain an extremely small value $h \sim 10^{-19}$; as a term of com-

parison, this corresponds to measuring displacements of baseline lengths $L \sim 1$ Km of the order of one tenth of the typical size of an atomic nucleus.

Today, with the advent of laser-interferometric detectors, it is possible to achieve unprecedented sensitivities and design experiments aimed to test the ultimate prediction of General Relativity. As a matter of fact a worldwide network of interferometric gravitational-wave detectors has been constructed and a great amount of data have already been taken and is currently being analyzed. Among these detectors is the Laser Interferometer Gravitational-Wave Observatory (LIGO).

Among the most promising sources of gravitational waves that lie in the frequency band of ground-based interferometric detectors including LIGO are low-mass compact-object binaries which radiate energy in the form of GWs throughout the three phases of the coalescence: inspiral, merger and ringdown. While the dynamics of low-mass non-spinning binaries is very well understood and gravitational waves are modeled with great accuracy, generic binary systems are expected to carry spin; in particular binaries consisting of two black holes (BH-BH) or a black hole in combination with a neutron star (BH-NS) might have at least one significantly spinning component. As a matter of fact, while observations of visible pulsar binaries suggest that NSs of interest for current GW detectors carry negligible spin $S_{NS}/m_{NS}^2 \sim 10^{-3}$ [30, 31, 32], very little is known about the statistical distribution of BH spin magnitudes in binaries: the spins could very well be large, with a significant impact on both binary dynamics and gravitational waveforms [5, 8, 6].

Furthermore, population-synthesis studies [7] suggest that in BH-NS binaries there is a significant possibility for the BH spin to be substantially misaligned with the orbital angular momentum of the binary; early investigations [9, 11] showed that when this is the case and the BH spin magnitude is large, the evolution of the GW phase and amplitude during the adiabatic inspiral is significantly affected by spin-induced modulations.

The dominant technique used in data analysis to detect GWs emitted by binary systems in the distant universe is called matched filtering [13] and it consists in comparing the output of the interferometer with theoretical model waveforms (templates) which can be obtained solving the Post Newtonian (PN) approximation to Einstein field equations for the source; these templates are described by a certain number of parameters related to the source configuration and the orientation of the detector with respect to the source.

The parameters a template depends on can be divided in intrinsic and extrinsic; extrinsic parameters can be disentangled from the dynamical variables of the system and they can generally be searched over analytically or numerically; conversely, intrinsic parameters influence the shape of the waveform in such a way that fast maximization is not possible. Therefore a large number of templates, each cor-

responding to a different set of intrinsic parameters, is created to construct a template bank, in such a way that any signal is matched by at least one template in the bank with a given minimal-match. For non-spinning binaries this kind of search can be performed easily as the number of intrinsic parameters that need to be searched over (the dimensionality of the template bank) is in practice only two, i.e. the two component masses. The dynamical evolution of spinning systems is complicated by spin-orbit and spin-spin interactions which cause precession of the orbital plane and therefore modulations in the phase and amplitude of the gravitational waves emitted; templates are in fact described by a large number of parameters (up to 17) so that, in general, template banks with higher dimensions are needed and matched filtering might require excessive computational costs.

To circumvent this problem, approximated phenomenological waveforms have been introduced which are described by a smaller number of non-physical phenomenological parameters; these templates can significantly speed up the matched filtering process but they tend to match a much higher number of non-physical signals, drastically increasing the false-alarm rate (the rate of events caused by noise artifacts in the output of the detector).

If we restrict our attention to GWs emitted by asymmetric binaries with only one significant spin carried by the more massive object (typically the BH in BH-NS binaries), then the dynamics of the system greatly simplifies as spin-spin coupling interactions disappear and the spin of the massive object is conserved. Furthermore, adopting a convenient reference frame, local parameters intrinsic to the binary, such as masses and spins, can be separated from directional parameters, allowing a semi-analytic maximization over all the angles and leaving a reduced parameter space to search over with matched filtering. These kinds of templates are called *physical* as they are described only in terms of the physical parameters of the source and its direction and orientation with respect to the detector.

In this thesis we present the development of the theoretical techniques and the implementation of all the numerical algorithms necessary to analyze LIGO data using a new family of Physical Templates for gravitational waves emitted by low-mass asymmetric compact-object binaries with only one significantly spinning component. All the code has been written in C language and integrated in the LIGO Algorithm Library (LAL) as part of the Compact Coalescence Group (CBC) inspiral search pipeline.

This is the outline of the thesis:

- In chapter 1 we review the theory underlying the generation of gravitational waves, including the multipole expansion of the radiative gravitational field and the Post Newtonian expansion of Einstein equations for the dynamics of binary systems of spinning compact objects. We also review other types of gravitational wave sources.

- In chapter 2 we present the problem of gravitational-wave detection using laser interferometric gravitational-wave detectors and we describe the Laser Interferometer Gravitational Wave Observatory (LIGO). We then review the matched filtering techniques used in data analysis to search for known signals hidden in noise and we describe the detection pipeline adopted by the LIGO Compact Binary Coalescence (CBC) data analysis group. We end the chapter introducing the main families of template waveforms used to search for gravitational waves emitted by spinning binaries.
- In chapter 3 we describe the implementation of a new Physical Template Family (PTF) aimed to model gravitational waves emitted by compact-object binaries with only one significantly spinning component. We first present the theoretical framework that is behind the data analysis strategy and we then describe the numerical implementation of the code in the LIGO Algorithm Library (LAL) and its integration in the CBC group detection pipeline. We discuss specific numerical issues and their solutions.
- In chapter 4 we present results from tests and simulations performed at the different stages of the pipeline using the PTF template waveforms. We run parallel simulations using the current most developed LIGO search strategy that deploys non-spinning low-mass templates and we compare results.
- Conclusions: the final chapter summarizes and concludes this thesis with a discussion of future prospects for searches for gravitational waves from compact binaries with spinning components.

Chapter 1

Gravitational Waves: the theory

1.1 The Generation of Gravitational Waves

Let us consider an isolated nearly-Newtonian *slow-motion* source of size $\sim R$ with time-dependent stress-energy tensor $T^{\mu\nu}(t)$ which emits gravitational waves with characteristic reduced wavelength $\lambda/2\pi \gg R$. Gravitational waves emitted by this distribution of matter/energy can be described in linearized theory, where the weak gravitational field generated at large distance from the source (in the radiation zone) is represented as a perturbation of the flat metric in vacuum [1, 61]

$$g_{\mu\nu} = \eta_{\mu\nu} + h_{\mu\nu} \quad (1.1)$$

with $|h_{\mu\nu}| \ll 1$.

In linearized theory $\eta_{\mu\nu}$ is used to raise and lower indices of $h_{\mu\nu}$ and we find that, up to terms linear in the perturbation $h_{\mu\nu}$, the contravariant component of the metric are given by

$$g^{\mu\nu} = \eta^{\mu\nu} - h^{\mu\nu} \quad (1.2)$$

while the determinant of the metric is

$$g = (1 + h)\eta \quad (1.3)$$

where $h = \eta^{\mu\nu} h_{\mu\nu} = h^\mu{}_\mu$. For our purposes, it is useful to introduce the *trace-reversed metric perturbation*

$$\bar{h}_{\mu\nu} \equiv h_{\mu\nu} - \frac{1}{2}\eta_{\mu\nu} h \quad (1.4)$$

If we use the gauge freedom to impose the *Lorentz gauge*

$$\bar{h}^{\mu\alpha}{}_{,\alpha} = 0 \quad (1.5)$$

Einstein's field equations in vacuum for $\bar{h}_{\mu\nu}$ read

$$\square \bar{h}_{\mu\nu} = 0 \quad (1.6)$$

where \square is the flat-space scalar wave operator $-\partial_t^2 + \nabla^2$. We note that (1.5) does not completely fix the gauge, but we have a further gauge freedom we will use later. A general outgoing-wave solution to this equation in the center of mass frame at distance R from the source can be expressed as a multipole series in the form [14]

$$\bar{h}_{\mu\nu} = \begin{cases} \bar{h}_{00} = \frac{4M}{R} + \sum_{l=2}^{\infty} (-1)^l \frac{4}{l!} \left[\frac{1}{R} \mathcal{I}_{A_l}(t-R) \right]_{,A_l} \\ \bar{h}_{0j} = -\frac{2\varepsilon_{j pq} S_p n_q}{R^2} + \sum_{l=2}^{\infty} (-1)^l \frac{4}{l!} \left[\frac{1}{R} \dot{\mathcal{I}}_{j A_{l-1}}(t-R) \right]_{,A_{l-1}} \\ \quad - \sum_{l=2}^{\infty} (-1)^l \frac{4l}{(l+1)!} \left[\frac{1}{R} \varepsilon_{j pq} \mathcal{S}_{p A_{l-1}}(t-R) \right]_{,q A_{l-1}} \\ \bar{h}_{jk} = \sum_{l=2}^{\infty} (-1)^l \frac{4}{l!} \left[\frac{1}{R} \ddot{\mathcal{I}}_{jk A_{l-2}}(t-R) \right]_{,A_{l-2}} \\ \quad - \sum_{l=2}^{\infty} (-1)^l \frac{8l}{(l+1)!} \left[\frac{1}{r} \varepsilon_{pq(j} \dot{\mathcal{S}}_{k)p A_{l-2}}(t-R) \right]_{,q A_{l-2}} \end{cases} \quad (1.7)$$

where $n_j = x^j/R$ is the radial unit vector, \mathcal{I}_{A_l} and \mathcal{S}_{A_l} are symmetric trace-free (STF) tensors and represent respectively the *mass* and the *current* l -pole moments of the radiation field. We introduced the notation $A_l \equiv a_1 \dots a_l$ to indicate a sequence of l indices on a tensor and the dot denotes derivative with respect to time. M is a constant and represents the total mass of the source while S_j is the (constant) total angular momentum of the source.

At the leading order the solution is given just by the mass-quadrupole terms ($l=2$) and reduces to

$$\bar{h}_{\mu\nu} \simeq \begin{cases} \bar{h}_{00} = \frac{4M}{R} + 2 \left[\frac{\mathcal{I}_{jk}(t-R)}{R} \right]_{,jk} \\ \bar{h}_{0j} = -\frac{2\varepsilon_{j pq} S_p n_q}{R^2} + 2 \left[\frac{\dot{\mathcal{I}}_{jk}(t-R)}{R} \right]_{,k} \\ \bar{h}_{jk} = 2 \frac{\ddot{\mathcal{I}}_{jk}(t-R)}{R} \end{cases} \quad (1.8)$$

We can then use the residual gauge freedom and put ourselves in the *transverse-*

1. Gravitational Waves: the theory

traceless (TT) gauge, which can be obtained by requiring

$$\begin{cases} \bar{h}_{\mu 0} &= 0 \\ \bar{h}_{kj,j} &= 0 \\ \bar{h}_{kk} &= 0 \end{cases} \quad (1.9)$$

From the first constraint (1.9) we see that only the spatial components of $\bar{h}_{\mu\nu}^{TT}$ are non-zero, therefore the gravitational-wave field is given by the TT part of the third of (1.8), which yields the *quadrupole formula*

$$h_{jk}^{TT} = \bar{h}_{jk}^{TT} = 2 \frac{\ddot{\mathcal{I}}_{jk}^{TT}(t-R)}{R} \quad (1.10)$$

where the first equality comes from the fact that h_{jk} and \bar{h}_{jk} differ only by trace so they have the same TT part. The last two constraints (1.9) imply that only two components of h_{jk}^{TT} are independent and they are transverse to the direction of propagation of the wave; we define these components to be the two transverse *polarizations of the gravitational wave* h_+ and h_\times .

If we introduce the *projection operator* $P_{lm} = \delta_{lm} - n_l n_m$, we have

$$\mathcal{I}_{jk}^{TT} = P_{jl} \mathcal{I}_{lm} P_{mk} - \frac{1}{2} P_{jk} (P_{lm} \mathcal{I}_{ml}) \quad (1.11)$$

For nearly-Newtonian slow-motion sources the mass l^{th} moment which characterizes the radiation field is equal to the STF part of the l^{th} moment of the effective mass distribution of the source [14]

$$\mathcal{I}_{jk}(t) = \left[\int T_{00}(t, \mathbf{x}) x^j x^k d^3x \right]^{STF} \quad (1.12)$$

If we now consider a binary with total mass $M \equiv m_1 + m_2$, reduced mass $\mu \equiv m_1 m_2 / M$, orbital separation r and define

$$\mathcal{Q}_{jk} = \frac{r}{\mu M} \frac{d^2 \mathcal{I}_{jk}(t-R)}{dt^2} \quad (1.13)$$

we can write (1.10) as

$$h_{jk}^{TT} = \frac{2\mu}{R} \left(\frac{M}{r} \right) [\mathcal{Q}_{jk}]^{TT} \quad (1.14)$$

1.2 Sources of Gravitational Waves

There are many potential sources of gravitational radiation, each of which has its own signature and poses its own detection challenges. In the case of ground-based detectors, due to the effects of seismic noise, they are confined to search for sources with frequencies greater than about 10 Hz. This means that we are restricted to searching for sources which are highly relativistic and not too massive. Future space-based detectors, such as LISA, will be able to search for more massive systems and those in a less relativistic regime. In this Section, we give a brief overview of some of the sources being searched for with the current generation of ground-based detectors [35].

1.2.1 Periodic Sources: Spinning Neutron stars

Slightly deformed, spinning neutron stars will be a source of quasiperiodic gravitational radiation. A particularly interesting class of objects of this type are low-mass X-ray binaries (LMXBs). In these systems, the neutron stars are spun up by accretion from a companion object; however, the systems seem to be locked into a range of spin frequencies of $\sim 300 - 600$ Hz. A plausible mechanism for this locking is that the torque due to accretion is being counteracted by an equal and opposite torque due to gravitational radiation. There are a number of potential mechanisms for the emission of gravitational waves by spinning neutron stars. These include density inhomogeneities, the rotation axis not being aligned with the axis of symmetry of the star, causing it to “wobble”, or instabilities in the star driven by gravitational radiation reaction. The GW signal emitted by such signals will be weak, but due to their continuous nature, it is possible to use long integration times to increase the signal to noise ratio (SNR).

If the cause of gravitational-wave emission is the deviation from axisymmetry, the neutron star will be characterized by an *ellipticity* $\epsilon = (I_{xx} - I_{yy})/I_{zz}$, where I_{jj} represent the moments of inertia about the principal axes. The resulting gravitational wave has a frequency twice the rotational frequency f_{rot} and the expected strain at a distance R is [2]

$$h \sim \frac{4\pi^2 G}{c^4} \frac{I_{zz} f_{rot}^2 \epsilon}{R} = 2 \times 10^{-26} \left(\frac{f_{rot}}{1 \text{ kHz}} \right)^2 \left(\frac{10 \text{ kpc}}{R} \right) \left(\frac{\epsilon}{10^{-6}} \right) \quad (1.15)$$

1.2.2 Unmodeled Bursts

There are many potential sources of gravitational radiation which would be expected to be signals of short duration and be spread over a wide spectral bandwidth. Moreover, the precise form of these signals may presently be poorly un-

derstood, thus making optimal searches using matched filtering impossible. Examples of such sources are mergers of binary compact objects and core collapse supernovae. Searching for such signals typically involves looking for excess power in certain frequency bands at certain times. Various consistency checks are then used, including looking at the cross-correlation between data streams from different detectors and requiring consistency in the relative amplitudes of signals in co-located detectors. While burst searches are less sensitive than matched filtering searches, they have the advantage of not assuming any form for the signal, thus allowing for the prospect of detecting previously unexpected types of signal which may turn out to be present.

1.2.3 Stochastic Background

An omnidirectional source of almost uniform gravitational radiation is expected to arise from the background radiation of the Universe. Such a background could have been created in the early universe and permeate space in a manner analogous to the Cosmic Microwave Background (CMB). Additionally, a background could exist due to unresolved astrophysical sources, such as supernovae with asymmetric core collapse, binary black-hole (BH) mergers, or neutron stars (NS) [36]. Searches for stochastic backgrounds typically involve cross-correlating the data between different detectors. Directional information can be obtained by introducing suitable time delays between the data streams from each detector. When analyzing stochastic backgrounds, it is usual to consider the energy density of the gravitational waves, $\Omega_{gw}(f)$, which is usually measured in units of the critical density to close the universe ρ_c , given by

$$\Omega_{gw} = \frac{1}{\rho_c} f \frac{dE_{gw}}{df} \quad (1.16)$$

Initial detectors should be able to place an upper limit on Ω_{gw} of $\sim 10^{-5}$. The next generation of detectors, such as Advanced LIGO, will be able to measure Ω_{gw} down to $\sim 10^{-9}$. Such a sensitivity will be able to place meaningful constraints on theories of the early universe. However, this limit is orders of magnitude higher than the level predicted by standard inflationary models, so an actual detection would be of profound significance.

1.2.4 Compact Binaries

A major search effort is underway to detect gravitational waves from inspiralling compact binaries, consisting of neutron stars and/or BHs. As the objects orbit each other, they emit gravitational radiation at twice the orbital frequency, causing the system to lose energy. After a period of adiabatic inspiral, the objects will plunge

towards each other and merge to form a single black-hole, which will then radiate gravitational waves as it approaches a stable state. The radiation produced by adiabatic inspiral and the final black-hole's *ringdown* are reasonably well modeled. However, the plunge and merger phase is still poorly understood, despite recent advances in numerical relativity. For a more detailed look at compact binary coalescence, see the next Section.

1.2.5 Ringdowns

When two inspiralling massive objects merge, the plunge can lead to the formation of a black-hole; before the final body settles into an equilibrium state it will radiate gravitational waves in a series of quasi-normal modes. These are well modeled by black-hole perturbation theory and this phase is known as the *ringdown phase*.

Far from the source the ringdown waveform can be written as [3, 4]

$$h_0(t) = \Re \left\{ \frac{\mathcal{A}}{R} e^{-i\omega t} \right\} = \Re \left\{ \frac{\mathcal{A}}{R} e^{-i(2\pi f_0 - i\pi f_0/Q)t} \right\} = \frac{\mathcal{A}}{R} e^{-\frac{\pi f_0}{Q}t} \cos(2\pi f_0 t) \quad (1.17)$$

where \mathcal{A} is the amplitude of the $l = m = 2$ mode, R is the distance from the source and Q is the so called *quality factor* which is related to the rate of energy loss $d\epsilon/dt$ by [3, 4]

$$\frac{2\pi f_0}{Q} = \frac{d\epsilon/dt}{\epsilon} \quad (1.18)$$

1.3 Coalescing Binaries

We study the dynamics and the gravitational-wave emission process of generic spinning binaries and subsequently focus to the case of binaries with only one significantly spinning object.

This second type of binaries can be used to model asymmetric systems composed by a black-hole and a neutron star or by two black-holes with high mass ratio. As a matter of fact, since the maximum spin magnitude a compact star of mass m can carry is given by m^2 for black-holes and by $\sim 0.7 \times m^2$ for neutron stars [21, 22, 23, 24], we see that, in the case of high mass ratio m_1/m_2 , the spin of the less massive star m_2 is, respectively, a factor m_1^2/m_2^2 and $m_1^2/(0.49 \times m_2^2)$ smaller than the spin of the massive component.

Additionally, in the case of BH-NS binaries, the spin of the neutron star is usually negligible regardless of the mass ratio; as a matter of fact, NSs in binaries of interest for current ground-based detectors are old enough to have spun down considerably, even if their initial spin was maximal [21, 23, 24], and dynamical evolution cannot spin them up significantly (even during the final phase of inspiral

when tidal torques become important [25, 26]).

This kind of system can form in different ways, and different population-synthesis models can give different spin distributions for the BH. In particular Kalogera [7] studied systems for which the spinning BH in the binary forms first with its spin aligned with the orbital angular momentum and a subsequent supernova explosion, which gives birth to the companion NS, causes a misalignment; this study shows that 30-80% of the NS-BH binaries that will coalesce within a Hubble time can have a tilt angle larger than 30 degrees. For the case of binaries formed in globular clusters, there is no theoretical argument to suggest any particular spin distribution.

1.3.1 The Post-Newtonian equations of motion

We will study the dynamics of generic low-mass binaries (with component masses $1 - 20M_{\odot}$) of spinning compact objects, restricting our analysis to the adiabatic regime where the inspiral phase can be represented as a sequence of quasicircular orbits; this implies that, by the time the GW signal enters the band of good detector sensitivity, radiation-reaction effects have circularized the orbit and have brought the binary into the adiabatic regime, which is valid until MECO (see Eq. (1.32) below) [16].

At any point along the inspiral, a binary of total mass $M = m_1 + m_2$ and symmetric mass ratio $\eta = m_1 m_2 / M^2$ is completely described by the orbital angular frequency ω , the orbital phase Ψ , the unit vector along the orbital angular momentum $\hat{\mathbf{L}}_N \propto \mathbf{r} \times \mathbf{v}$, and the two spins $\mathbf{S}_1 = \chi_1 m_1^2 \hat{\mathbf{S}}_1$ and $\mathbf{S}_2 = \chi_2 m_2^2 \hat{\mathbf{S}}_2$, where $\hat{\mathbf{S}}_{1,2}$ are unit vectors and $0 < \chi_{1,2} < 1$.

In the adiabatic approach to the evolution of spinning binaries, one builds a sequence of precessing (due to spin effects) and shrinking (due to radiation reaction) circular orbits. The orbital frequency increases as the orbit shrinks. The timescales of the precession and shrinkage are both long compared to the orbital period (this is the adiabatic condition), until the very late stage of binary evolution. These orbits are sometimes also called spherical orbits, since they reside on a sphere with slowly shrinking radius.

The equations of motion of the system are derived from Post-Newtonian expansions of Einstein equations including all the significant terms; we then obtain a system of coupled differential equations which yield the time evolution of the dynamical variables of the system.

The radiation-reaction induced evolution of frequency can be calculated by using the energy-balance equation

$$\dot{\omega} = -\frac{\mathcal{F}}{d\mathcal{E}/d\omega} \quad (1.19)$$

where \mathcal{E} is the orbital-energy function and \mathcal{F} the GW energy-flux (or luminosity)

function. Both have been calculated as functions of the orbital frequency using PN expansion techniques and are determined up to 3.5PN order, with spin effects included up to 2PN order. The resulting evolution equation for ω , obtained by inserting the PN expansions of \mathcal{E} and \mathcal{F} into equation (1.19) and re-expanding in powers of $M\omega$ is given by [17, 16]

$$\begin{aligned}
 \frac{\dot{\omega}}{\omega^2} = & \frac{96}{5} \eta (M\omega)^{5/3} \left\{ 1 - \frac{743 + 924}{336} (M\omega)^{2/3} - \left(\frac{1}{12} \sum_{i=1,2} \left[\chi_i \left(\hat{\mathbf{L}}_N \cdot \hat{\mathbf{S}}_i \right) \right. \right. \right. \\
 & \times \left. \left. \left(113 \frac{m_i^2}{M^2} + 75\eta \right) \right] - 4\pi \right) (M\omega) + \left(\frac{34103}{18144} + \frac{13661}{2016} \eta + \frac{59}{18} \eta^2 \right) (M\omega)^{4/3} \\
 & - \frac{1}{48} \eta \chi_1 \chi_2 \left[247 \left(\hat{\mathbf{S}}_1 \cdot \hat{\mathbf{S}}_2 \right) - 721 \left(\hat{\mathbf{L}}_N \cdot \hat{\mathbf{S}}_1 \right) \left(\hat{\mathbf{L}}_N \cdot \hat{\mathbf{S}}_2 \right) \right] (M\omega)^{4/3} \\
 & - \frac{1}{672} (4159 + 15876\eta) \pi (M\omega)^{5/3} + \left[\left(\frac{16447322263}{139708800} - \frac{1712}{105} \gamma_E + \frac{16}{3} \pi^2 \right) \right. \\
 & + \left. \left(-\frac{273811877}{1088640} + \frac{451}{48} \pi^2 - \frac{88}{3} \hat{\theta} \right) \eta + \frac{541}{896} \eta^2 - \frac{5605}{2592} \eta^3 \right. \\
 & - \left. \frac{856}{105} \log \left[16 (M\omega)^{2/3} \right] \right] (M\omega)^2 \\
 & + \left. \left(-\frac{4415}{4032} + \frac{717350}{12096} \eta + \frac{182990}{3024} \eta^2 \right) \pi (M\omega)^{7/3} \right\} \quad (1.20)
 \end{aligned}$$

where $\gamma_E = 0.577\dots$ is the Euler's constant. We denote by $\hat{\mathbf{L}}_N \propto \mathbf{r} \times \mathbf{v}$ the unit vector along the orbital angular momentum, where \mathbf{r} and \mathbf{v} are the two-body center-of-mass radial separation and relative velocity, respectively. $\hat{\mathbf{L}}_N$ is also the unit normal vector to the orbital plane. The quantity $\hat{\theta}$ is an undetermined regularization parameter that enters the GW flux at 3PN order. Another regularization parameter, ω_s , enters the PN expressions of \mathcal{E} and \mathcal{F} at 3PN order and it has been determined in the ADM gauge [27, 28, 29, 38], but not yet in the harmonic gauge. However, Eq.(1.20) does not depend on ω_s . We do not include the (partial) spin contributions to $\dot{\omega}$ at 2.5PN, 3PN and 3.5PN orders, which arise from known 1.5PN and 2PN spin terms of \mathcal{E} and \mathcal{F} . (To be fully consistent one should know the spin terms of \mathcal{E} and \mathcal{F} at 2.5PN, 3PN and 3.5PN order). We ignore also the quadrupole-monopole interaction [16].

The precession equations for the spins are given by

$$\dot{\mathbf{S}}_1 = \frac{(M\omega)^2}{2M} \left\{ \eta (M\omega)^{-1/3} \left(4 + 3 \frac{m_2}{m_1} \right) \hat{\mathbf{L}}_N + \frac{1}{M^2} \left[\mathbf{S}_2 - 3 \left(\mathbf{S}_2 \cdot \hat{\mathbf{L}}_N \right) \hat{\mathbf{L}}_N \right] \right\} \times \mathbf{S}_1 \quad (1.21)$$

1. Gravitational Waves: the theory

$$\dot{\mathbf{S}}_2 = \frac{(M\omega)^2}{2M} \left\{ \eta (M\omega)^{-1/3} \left(4 + 3 \frac{m_1}{m_2} \right) \hat{\mathbf{L}}_N + \frac{1}{M^2} \left[\mathbf{S}_1 - 3 \left(\mathbf{S}_1 \cdot \hat{\mathbf{L}}_N \right) \hat{\mathbf{L}}_N \right] \right\} \times \mathbf{S}_2 \quad (1.22)$$

where we have replaced $r \equiv \mathbf{r}$ and $|\mathbf{L}_N|$ by their leading order Newtonian expressions in ω

$$r = \left(\frac{M}{\omega^2} \right)^{1/3} \quad (1.23a)$$

$$|\mathbf{L}_N| = \mu r^2 \omega = \eta M^{5/3} \omega^{-1/3} \quad (1.23b)$$

This approximation is appropriate because the next spin-precession term is $\mathcal{O}(\omega^{1/3})$ higher than the leading order, while next terms in the expressions of r and $|\mathbf{L}_N|$ are $\mathcal{O}(\omega^{2/3})$ higher.

The precession of the orbital plane (defined by the normal vector $\hat{\mathbf{L}}_N$) can be computed noting that the total angular momentum \mathbf{J} and its rate of change $\dot{\mathbf{J}}_{RR}$ (due to radiation reaction) depend on ω , $\hat{\mathbf{L}}_N$ and $\mathbf{S}_{1,2}$ as

$$\mathbf{J} = \mathbf{L} + \mathbf{S} = \underbrace{\eta M^2 (M\omega)^{-1/3} \hat{\mathbf{L}}_N [1 + \mathcal{O}(\omega^{2/3})]}_{\mathbf{L}} - 2\eta (M\omega)^{2/3} \mathbf{S}_{\text{eff}} + \mathbf{S} \quad (1.24)$$

$$\dot{\mathbf{J}}_{RR} = -\frac{32}{5} \eta^2 M (M\omega)^{7/3} \hat{\mathbf{L}}_N [1 + \mathcal{O}(\omega^{2/3})] + \mathcal{O}(\omega^{10/3}) \hat{\mathbf{S}}_1 + \mathcal{O}(\omega^{10/3}) \hat{\mathbf{S}}_2 \quad (1.25)$$

where $\mathbf{S} = \mathbf{S}_1 + \mathbf{S}_2$ and the combination

$$\mathbf{S}_{\text{eff}} \equiv \left(1 + \frac{3m_1}{4m_2} \right) \mathbf{S}_1 + \left(1 + \frac{3m_2}{4m_1} \right) \mathbf{S}_2 \quad (1.26)$$

is called *effective spin*. Note that both terms in the \mathbf{L} brace of Eq. (1.24) originate from orbital angular momentum (the second term comes from the spin-orbit coupling). Taking the time derivative of (1.24), we obtain

$$\dot{\mathbf{J}} = \eta M^2 (M\omega)^{-1/3} \dot{\hat{\mathbf{L}}}_N [1 + \mathcal{O}(\omega^{2/3})] - \mathcal{O}(\omega^{2/3}) \dot{\mathbf{S}}_{\text{eff}} + \dot{\mathbf{S}} + \left[\mathcal{O}(\omega^{7/3}) \hat{\mathbf{L}}_N - \mathcal{O}(\omega^{10/3}) \mathbf{S}_{\text{eff}} \right] \quad (1.27)$$

where to get the last term on the right-hand side we have used $\dot{\omega} = \mathcal{O}(\omega^{11/3})$. Comparing Eqs.(1.27) and (1.24), projecting out only the direction perpendicular to $\hat{\mathbf{L}}$, and keeping only the terms up to the leading and next-to-leading orders, we get

$$\begin{aligned} \dot{\hat{\mathbf{L}}}_N = & -\frac{(M\omega)^{1/3}}{\eta M^2} \dot{\mathbf{S}} = \frac{\omega^2}{2M} \left\{ \left[\left(4 + 3 \frac{m_2}{m_1} \right) \mathbf{S}_1 + \left(4 + 3 \frac{m_1}{m_2} \right) \mathbf{S}_2 \right] \times \hat{\mathbf{L}}_N \right. \\ & \left. - \frac{3\omega^{1/3}}{\eta M^{5/3}} \left[\left(\mathbf{S}_2 \cdot \hat{\mathbf{L}}_N \right) \mathbf{S}_1 + \left(\mathbf{S}_1 \cdot \hat{\mathbf{L}}_N \right) \mathbf{S}_2 \right] \times \hat{\mathbf{L}}_N \right\} \end{aligned} \quad (1.28)$$

We now have a set of four coupled equations for the four variables ω , \mathbf{S}_1 , \mathbf{S}_2 and $\hat{\mathbf{L}}_N$. Integrating equation (1.20) for ω we obtain the *accumulated orbital phase* Ψ

$$\Psi \equiv \int_{t_i}^t \omega dt = \int_{\omega_i}^{\omega} \frac{\omega}{\dot{\omega}} d\omega \quad (1.29)$$

which describes the position of the two compact objects along the instantaneous circular orbits of the adiabatic sequence.

1.3.2 End Point of Evolution

The orbital energy of the two-body system at 2PN and 3PN orders, expressed as a function of ω , and assuming the static parameter $\omega_s = 0$ [27, 38], reads [19, 18, 30, 31, 32]

$$\begin{aligned} E_{2\text{PN}}(\omega) = & -\frac{\mu}{2} (M\omega)^{2/3} \left\{ 1 - \frac{(9 + \eta)}{12} (M\omega)^{2/3} + \frac{8}{3} \hat{\mathbf{L}}_N \cdot \mathbf{S}_{\text{eff}}(M\omega) \right. \\ & + \frac{1}{24} (-81 + 57\eta - \eta^2) (M\omega)^{4/3} \\ & \left. + \frac{1}{\eta} \left[\mathbf{S}_1 \cdot \mathbf{S}_2 - 3 (\mathbf{S}_1 \cdot \hat{\mathbf{L}}_N) (\mathbf{S}_2 \cdot \hat{\mathbf{L}}_N) \right] (M\omega)^{4/3} \right\} \end{aligned} \quad (1.30)$$

$$\begin{aligned} E_{3\text{PN}}(\omega) = & E_{2\text{PN}}(\omega) - \frac{\mu}{2} (M\omega)^{2/3} \left\{ \left[-\frac{675}{64} + \left(\frac{34445}{576} - \frac{205}{96} \pi^2 \right) \eta - \frac{155}{96} \eta^2 \right. \right. \\ & \left. \left. - \frac{35}{5184} \eta^3 \right] (M\omega)^2 \right\} \end{aligned} \quad (1.31)$$

In the context of our adiabatic approximation, it is natural to stop the integration of Eqs.(1.30),(1.31) and (1.28) at the point where the energy E_{nPN} reaches a minimum, called the *minimum energy circular orbit* or *MECO*

$$\text{MECO} : \quad \frac{dE_{\text{nPN}}}{d\omega} = 0 \quad (1.32)$$

After this point the adiabatic approximation breaks down and our equations of motion cannot be considered valid anymore. However, if we find that $\dot{\omega} = 0$ (which implies certainly that the adiabatic approximation has become invalid) before the MECO is reached, we stop the evolution there. We will call the instantaneous frequency of GWs at the endpoint of evolution the *ending frequency*, which, up to a correction that arises from precessional effects, is twice the instantaneous orbital frequency defined in this section.

1.3.3 Single-Spin Binaries

For a binary with only one significantly spinning object \mathbf{S}_1 the above equations simplify since all terms containing \mathbf{S}_2 vanish and spin-spin coupling terms disappear. For the time evolution of frequency we obtain

$$\begin{aligned}
 \frac{\dot{\omega}}{\omega^2} = & \frac{96}{5} \eta (M\omega)^{5/3} \left\{ 1 - \frac{743 + 924}{336} (M\omega)^{2/3} - \left(\frac{1}{12} \left[\chi_1 (\hat{\mathbf{L}}_N \cdot \hat{\mathbf{S}}_1) \right. \right. \right. \\
 & \times \left. \left. \left(113 \frac{m_1^2}{M^2} + 75\eta \right) \right] - 4\pi \right) (M\omega) + \left(\frac{34103}{18144} + \frac{13661}{2016} \eta + \frac{59}{18} \eta^2 \right) (M\omega)^{4/3} \\
 & - \frac{1}{672} (4159 + 14532\eta) \pi (M\omega)^{5/3} + \left[\left(\frac{16447322263}{139708800} - \frac{1712}{105} \gamma_E + \frac{16}{3} \pi^2 \right) \right. \\
 & + \left. \left(-\frac{273811877}{1088640} + \frac{451}{48} \pi^2 - \frac{88}{3} \hat{\theta} \right) \eta + \frac{541}{896} \eta^2 - \frac{5605}{2592} \eta^3 \right. \\
 & \left. \left. - \frac{856}{105} \log \left[16 (M\omega)^{2/3} \right] \right] (M\omega)^2 + \left(-\frac{4415}{4032} + \frac{661775}{12096} \eta + \frac{149789}{3024} \eta^2 \right) \pi (M\omega)^{7/3} \right\}
 \end{aligned} \tag{1.33}$$

while for the time evolution of the spin we have

$$\dot{\mathbf{S}}_1 = \frac{\eta}{2M} (M\omega)^{5/3} \left(4 + 3 \frac{m_2}{m_1} \right) \hat{\mathbf{L}}_N \times \mathbf{S}_1 \tag{1.34}$$

The equation for the precession of the orbital plane becomes

$$\dot{\hat{\mathbf{L}}}_N = \frac{\omega^2}{2M} \left(4 + 3 \frac{m_2}{m_1} \right) \mathbf{S}_1 \times \hat{\mathbf{L}}_N \equiv \boldsymbol{\Omega}_L \times \hat{\mathbf{L}}_N \tag{1.35}$$

with

$$\boldsymbol{\Omega}_L \equiv \frac{\omega^2}{2M} \left(4 + 3 \frac{m_2}{m_1} \right) \mathbf{S}_1 \tag{1.36}$$

Equations (1.33), (1.34) and (1.35) describe the adiabatic evolution of the three variables ω , \mathbf{S}_1 and $\hat{\mathbf{L}}_N$; from these it can be easily deduced that the magnitude of the spin, $S_1 = |\mathbf{S}_1| = \chi_1 m_1^2$, and the angle between the spin and the orbital angular momentum, $\kappa_1 \equiv \hat{\mathbf{L}}_N \cdot \hat{\mathbf{S}}_1$, are conserved during the evolution [33].

Equation (1.31) for the orbital energy $\mathcal{E}(\omega)$ at 3PN order now includes spin-

orbit effects up to 1.5PN order and reads

$$\begin{aligned} \mathcal{E}(\omega) = -\frac{\mu}{2} (M\omega)^{2/3} & \left\{ 1 - \frac{(9+\eta)}{12} (M\omega)^{2/3} + \frac{8}{3} \left(1 + \frac{3m_2}{4m_1} \right) \frac{\hat{\mathbf{L}}_N \cdot \mathbf{S}_1}{M2} (M\omega) \right. \\ & - \frac{1}{24} (81 - 57\eta + \eta^2) (M\omega)^{4/3} + \left[-\frac{675}{64} \right. \\ & \left. \left. + \left(\frac{34445}{576} - \frac{205}{96} \pi^2 + \frac{10}{3} \omega_s \right) \eta - \frac{155}{96} \eta^2 - \frac{35}{5184} \eta^3 \right] (M\omega)^2 \right\} \end{aligned} \quad (1.37)$$

where again we assume $\omega_s = 0$.

1.3.4 The Radiative Gravitational Field of a Spinning Binary

The radiative gravitational field generated by binary systems can be expressed by the leading-order mass-quadrupole formula derived in Sec. 1.1 as

$$h^{ij} = \frac{2\mu}{R} \left(\frac{M}{r} \right) \mathcal{Q}^{ij} \quad (1.38)$$

where $M \equiv m_1 + m_2$ is the *total mass*, $\mu \equiv (m_1 m_2)/M$ is the *reduced mass* and R is the distance between the source and the earth. For a binary system in quasicircular motion the STF tensor \mathcal{Q}^{ij} can be written as

$$\mathcal{Q}_c^{ij} = 2[\hat{r}^i \hat{r}^j - \hat{v}^i \hat{v}^j] \quad (1.39)$$

with $\hat{\mathbf{r}}$ and $\hat{\mathbf{v}}$ the unit vectors along respectively the separation vector $\mathbf{r} = r \hat{\mathbf{r}}$ and the relative velocity $\mathbf{v} = \omega r \hat{\mathbf{v}} = \sqrt{M/r} \hat{\mathbf{v}}$ of the binary, in virtue of Eq.(1.23a).

To describe gravitational waves as they are detected by a ground based interferometric detector, we start by defining a fixed *source frame* $\{\mathbf{e}_x^S, \mathbf{e}_y^S, \mathbf{e}_z^S\}$, arbitrarily chosen; we can then introduce a time-dependent reference frame attached to the binary $\mathbf{e}_1(t), \mathbf{e}_2(t), \mathbf{e}_3(t)$, where $\mathbf{e}_{1,2}$ form a basis for the instantaneous orbital plane while \mathbf{e}_3 is aligned along the orbital angular momentum $\mathbf{e}_3(t) \equiv \hat{\mathbf{L}}_N(t)$; the definition of $\mathbf{e}_{1,2}$ is not unique but it can vary depending on the *convention* adopted (see Sec. (1.3.5)).

The unit vectors $\hat{\mathbf{r}}$ and $\hat{\mathbf{v}}$ can then be written as

$$\begin{aligned} \hat{\mathbf{r}}(t) &= \mathbf{e}_1(t) \cos(\Phi(t) + \Phi_0) + \mathbf{e}_2(t) \sin(\Phi(t) + \Phi_0) \\ \hat{\mathbf{v}}(t) &= -\mathbf{e}_1(t) \sin(\Phi(t) + \Phi_0) + \mathbf{e}_2(t) \cos(\Phi(t) + \Phi_0) \end{aligned} \quad (1.40)$$

where Φ is the *orbital phase* and Φ_0 is an arbitrary *initial phase*; the definition of $\Phi(t)$ also depends on the convention adopted for $\mathbf{e}_{1,2}$.

Now, by defining the binary *polarization tensors* \mathbf{e}_+ and \mathbf{e}_\times

$$\begin{aligned}\mathbf{e}_+ &= \mathbf{e}_1 \otimes \mathbf{e}_1 - \mathbf{e}_2 \otimes \mathbf{e}_2 \\ \mathbf{e}_\times &= \mathbf{e}_1 \otimes \mathbf{e}_2 + \mathbf{e}_2 \otimes \mathbf{e}_1\end{aligned}\tag{1.41}$$

the tensor \mathcal{Q}_c^{ij} which appears in the (1.38) can be written as

$$\mathcal{Q}_c^{ij} = -2 \left\{ [\mathbf{e}_+]^{ij} \cos 2(\Phi + \Phi_0) + [\mathbf{e}_\times]^{ij} \sin 2(\Phi + \Phi_0) \right\}\tag{1.42}$$

and we see that $\Phi(t)$ corresponds to half the *gravitational-wave phase*.

Therefore under the hypothesis of quasicircular motion we can write Eq.(1.38) as

$$h^{ij} = \frac{2\mu}{R} \frac{M}{r} \mathcal{Q}_c^{ij} \equiv \frac{2\mu}{R} (M\omega)^{2/3} \mathcal{Q}_c^{ij} \equiv \frac{2\mu}{R} (\pi M f)^{2/3} \mathcal{Q}_c^{ij}\tag{1.43}$$

where we introduced the *gravitational-wave frequency*

$$f \equiv 2 \left(\frac{\omega}{2\pi} \right)\tag{1.44}$$

1.3.5 The Precessing Convention

As said in Sec. 1.3.4 the basis vectors $\mathbf{e}_1(t), \mathbf{e}_2(t)$ that define the orbital plane at every time t can be chosen arbitrarily as long as they are orthogonal to the orbital angular momentum $\hat{\mathbf{L}}_N(t) = \mathbf{e}_3(t)$ (and between themselves). Finn and Chernoff (FC) adopted the convention for which [53]

$$\begin{cases} \mathbf{e}_1 = \frac{\mathbf{e}_z^S \times \hat{\mathbf{L}}_N}{\sin i} \\ \mathbf{e}_2 = \frac{\mathbf{e}_z^S - \hat{\mathbf{L}}_N \cos i}{\sin i} \end{cases}\tag{1.45}$$

where the components of $\hat{\mathbf{L}}_N$ in the source frame are given in terms of the two spherical polar angles (i, α) as $\hat{L}_{Nx} = \sin i \cos \alpha$, $\hat{L}_{Ny} = \sin i \sin \alpha$ and $\hat{L}_{Nz} = \cos i$. With this definition the unit vector \mathbf{e}_1 points in the direction of the ascending node of the orbit on the (x, y) plane and the phase $\Phi(t)$ that appears in Eq.(1.40) is the orbital phase with respect to the ascending node, whose evolution is given by

$$\dot{\Phi}(t) = \dot{\Psi}(t) - \dot{\alpha} \cos [i(t)]\tag{1.46}$$

where Ψ is the *accumulated orbital phase* defined in (1.29). Therefore, while for non-spinning binaries $\dot{\alpha} = 0$ and therefore the accumulated orbital phase corresponds to half the gravitational-wave phase, for spinning binaries these quantities

differ by precessional effects. If however we re-define the basis vectors $\mathbf{e}_1(t), \mathbf{e}_2(t)$ so that they precess alongside the orbital angular momentum $\hat{\mathbf{L}}_N$ [16]

$$\dot{\mathbf{e}}_i = \boldsymbol{\Omega}_e(t) \times \mathbf{e}_i, \quad i = 1, 2 \quad (1.47)$$

with

$$\boldsymbol{\Omega}_e(t) \equiv \boldsymbol{\Omega}_L(t) - \left[\boldsymbol{\Omega}_L(t) \cdot \hat{\mathbf{L}}_N(t) \right] \hat{\mathbf{L}}_N(t) \quad (1.48)$$

and $\boldsymbol{\Omega}_L(t)$ given by (1.36), then we have

$$\frac{d\Phi}{dt} = \omega = \frac{d\Psi}{dt} \quad (1.49)$$

and the gravitational-wave phase corresponds to twice the accumulated orbital phase as in the non-spinning case.

Since the accumulated orbital phase is (almost) non-modulated [16], by adopting the precessing convention, we effectively isolate all the modulational effects due to precession in the evolving polarization tensors $\mathbf{e}_{+, \times}$, while the phase $\Phi \equiv \Psi$ remains non-modulated.

In Sec. 2.7.4 we will see that, using the precessing convention instead of the FC convention, when writing the detector response to a gravitational wave we are able to separate terms that depend on the time-evolution of dynamical variables and on *basic parameters* from terms that depend only on *directional parameters*, which are time-independent. Basic parameters include the two component masses m_1, m_2 the magnitude of the spins S_1, S_2 and the angles that define the orientation of spins with respect to the orbital angular momentum \mathbf{L}_N and with respect to each other. Directional parameters include all the remaining angles that describe the rigid rotation of the binary as a whole in space.

Chapter 2

The Detection of Gravitational Waves

2.1 Effects of Gravitational Waves on Test Masses

The effects of a gravitational wave cannot be seen in isolated point masses, but only by observing the change in separation between pairs of masses. Take as an example a pair of test masses separated by a distance L (as measured in the unperturbed flat spacetime) along the x -axis and a gravitational wave propagating along the z -axis. In the perturbed spacetime the distance between the test masses $d(t)$ is

$$d(t) = \int_0^L [1 + h_{xx}(t, x)]^{1/2} dx \quad (2.1)$$

which, in the long wavelength approximation, can be expressed as

$$d(t) \approx L \left[1 + \frac{1}{2} h_{xx}(t, 0) \right] \quad (2.2)$$

and thus for a change in distance between the two test masses $\delta L(t, 0) = d(t) - L$, the strain produced by the gravitational wave is

$$\frac{\delta L(t, 0)}{L} = \frac{1}{2} h_{xx}(t, 0) \quad (2.3)$$

An illustration of the effects of a gravitational wave is shown in figures 2.1 and 2.2. These show a circular configuration of free test masses in the $z = 0$ plane. From the point of view of an observer in the center of the ring, the gravitational wave manifests itself by stretching and contracting space along orthogonal directions in the plane transverse to the direction of propagation, changing the circular pattern of the test masses to an elliptical configuration. Half a period later the effect is

reversed; those masses which were displaced furthest from the center of the ring are now brought closest and vice versa. The gravitational-wave polarization which causes maximal stretching along the x and y axes is known as the *plus polarization*. Rotating the coordinate axes by 45 in the $z = 0$ plane we can see the effect of the cross polarization. The most general gravitational wave traveling in the z direction is a linear superposition of these two polarizations.

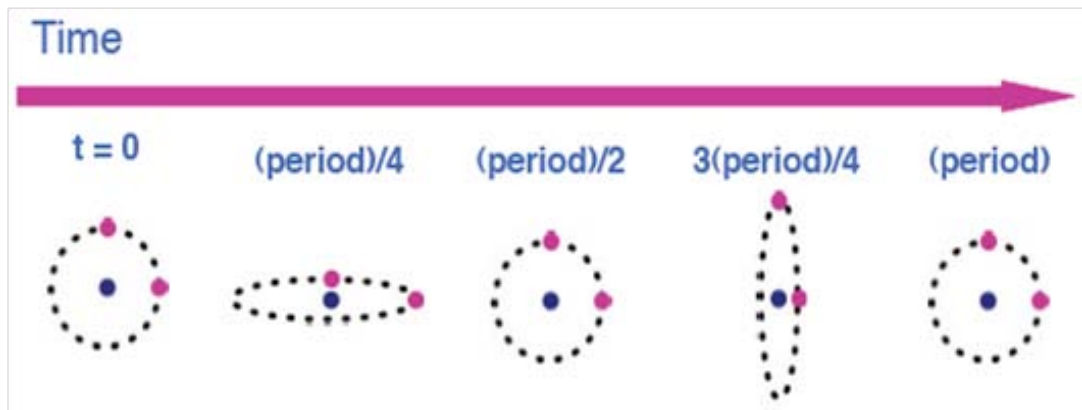


Figure 2.1: Illustration of the effect of a sinusoidal gravitational wave with plus polarization on a ring of test particles when the direction of propagation of the gravitational wave is orthogonal to the plane of the particles.

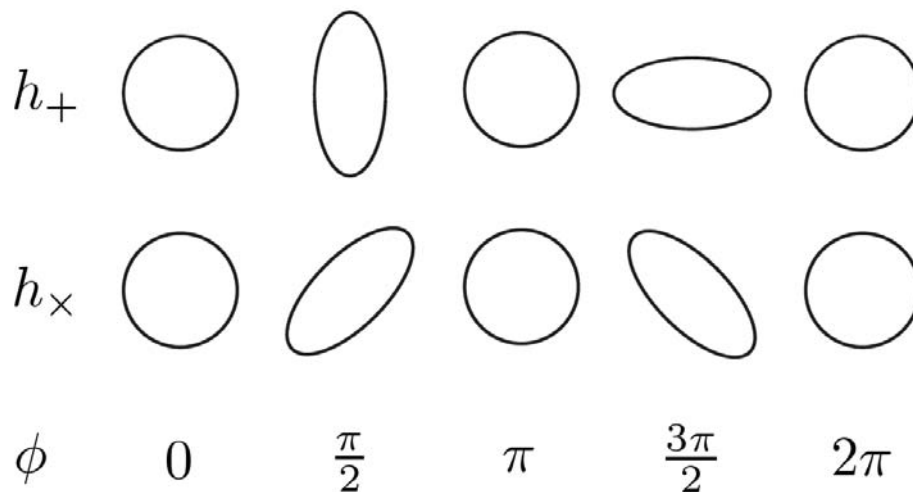


Figure 2.2: The effect of the two polarizations h_+ and h_\times of a sinusoidal gravitational wave propagating through the page on a ring of test particles. As the phase ϕ of the gravitational wave changes through a complete cycle, the rings are distorted.

It is evident from figures 2.1 and 2.2, that the gravitational wave is invariant

under a rotation of π about its direction of propagation, $\theta_{\text{inv}} = \pi$. This is related to the spin S of the massless particle associated with the field, which in the case of gravity is the graviton; from the relation $S = 2\pi/\theta_{\text{inv}}$ it follows that the graviton is a spin-2 particle (the quantum analogue of a classical rank-2 tensor field) [61].

2.2 The LIGO Detectors

In order to detect gravitational-waves from inspiraling binary systems, a gravitational-wave detector must be sensitive to the changes in coordinate distances between free masses as described in figures 2.1 and 2.2. A simple Michelson interferometer can measure the relative change in distance between its two orthogonal arms by recording the light power output at the beam splitter. If the arms are the same length (up to a wavelength of the light), the fields will constructively interfere resulting in a bright output. As the arm's length changes differentially, the change in distance causes the light to interfere destructively, dimming the light, until it is dark. A gravitational-wave propagating orthogonally to the plane of the interferometer will cause the path length of the light to differ in each arm and this will result in a change in the light power output.

The Laser Interferometric Gravitational-wave Observatory (LIGO) is a three detector network of laser-interferometric gravitational-wave detectors located in two observatories in the United States, Hanford, Washington (LHO) and Livingston, Louisiana (LLO). The detectors attempt to measure gravitational-wave strain using a power-recycled Michelson interferometer with Fabry-Perot-cavity arms.

LHO has two detectors called H1 (4 km arm length) and H2 (2 km) while the LLO site has one detector called L1 (4km). In order to measure strain of magnitude $\sim 10^{-21}$ - 10^{-19} , LIGO's optical design must be more complicated than a Michelson interferometer. The key to LIGO's strain sensitivity is its long arm lengths. Fabry-Perot cavities, which employ a set of partially reflective inner mirrors that cause light to circulate multiple times in the cavity, allow the phase difference caused by strain to accumulate as if LIGO's arms were effectively longer. The two end test masses along the x and y arms of the interferometers (ETMX-ETMY) are highly reflecting mirrors, while a 50% reflecting mirror known as a beam splitter (BS) is placed right after the laser, and two additional partially-reflecting mirrors called input test masses (ITMX-ITMY) are placed at the beginning of each beam path; finally a power recycling mirror (PRM) is placed between the laser and the BS, resonantly enhancing the light stored in the interferometer. A diagram of the simplified LIGO optical configuration is given in figure 2.3.

LIGO has successfully completed six science runs since 2002. In figure 2.4 we show the best strain sensitivity curves from each of the five science runs, along with the design sensitivity curve. The plot demonstrates the large increases in sensitivity

achieved between runs to the point where, in S5, the LIGO detectors achieved design sensitivity. The plot also shows that the LIGO detectors are most sensitive to gravitational waves between ~ 40 Hz and 2 kHz.

The noise in the detector is usually measured as the amplitude spectral density, which is the square root of the power spectral density of the detector strain. A complete overview of the noise searches present in the LIGO interferometers can be found in [18]. Here we give a brief overview of the most important sources[8].

- **Seismic noise:** mechanical noise caused by seismic motion of the Earth is an important source of noise, being most dominant at frequencies $f < 40$ Hz. To reduce this noise, it is necessary to isolate the mirrors from the motion of the ground. This is typically done by using mirror suspension systems consisting of coupled pendulums.
- **Thermal noise:** thermal vibrations of the mirrors and suspensions are the dominant source of noise for frequencies in the range $40 \lesssim f \lesssim 200$ Hz. To mitigate the effects of this noise, systems are designed so that their resonant frequencies are far from the measurement frequencies. In addition, materials are chosen so that they have high Q, which means their resonant peaks are very sharp, and there will be minimal leakage into the frequency bands of interest.
- **Shot noise:** this is the dominant source of noise for frequencies $\gtrsim 200$ Hz and it arises because of the quantum nature of light. We know that the actual number of photons collected by the photodetector per unit time is a Poisson process, therefore the error will improve as $\sqrt{\bar{N}}$, where \bar{N} is the average number of photons per unit time. It can be calculated that, to be able to detect changes in phase for a gravitational wave with a frequency of $f \sim 100$ Hz, the laser intensity would need to be ~ 102 W, which is currently beyond the capability of any continuous laser. To get around this limitation, it is necessary to introduce a power recycling mirror into the interferometer design (see Fig. 2.3). This reflects wasted light back into the interferometer, and allows power to build up in the cavity. Using such a design, it is possible to obtain the desired sensitivity using the 10W lasers typically used in the first generation interferometric detectors.
- **Other quantum effects:** although shot noise can be reduced by increasing the laser power, this in turn will increase the size of the fluctuations of the laser intensity, and therefore will increase the fluctuations of the light pressure on the mirrors. At high powers, these fluctuations will become a limiting factor of the noise, known as the quantum limit. For future interferometers, investigations are underway into ways to beat this quantum limit, including signal recycling, and the use of squeezed light.

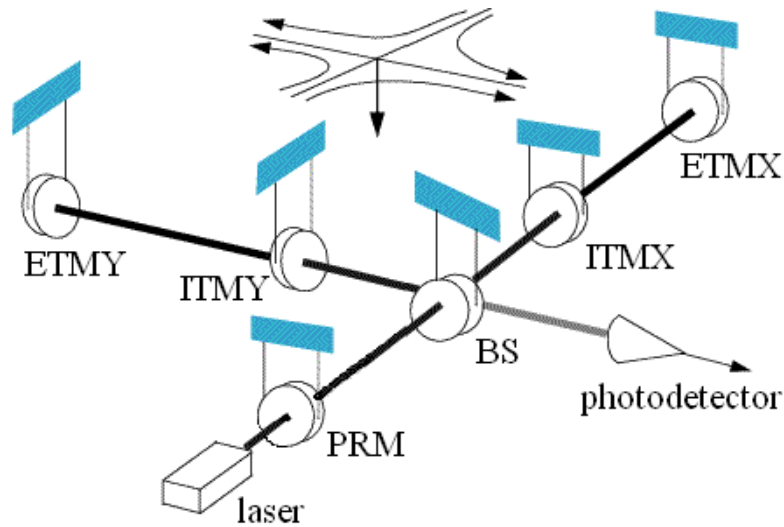


Figure 2.3: Simplified optical layout of LIGO. LIGO is a power recycled laser Michelson interferometer with Fabry-Perot cavity arms. A gravitational-wave propagating perpendicularly to the plane of the interferometer will change the distances between the mirrors asymmetrically in the two arms, as illustrated in figures 2.1 and 2.2. The light circulating in the cavity of one arm accumulates a phase difference with the other arm which changes the power observed at the detector port. Picture courtesy of LIGO lab.

2.2.1 Data Sets

LIGO data are divided into analysis segments. This is done by breaking up the data into stretches of 2048s in duration. To perform the analysis, these stretches are then broken up into 15 overlapping segments of 256s duration. To avoid issues with corruption of data, the first and last 64s in a segment are not used for trigger generation. To ensure this doesn't lead to data ignored in the analysis, the 2048s stretches are selected to overlap by 128s in contiguous data. At the start and end of a science segment, to avoid any transients which might arise, we ignore the first and last 8s of data respectively. Note that this means that science segments of less than 2064s will not be analyzed.

For initial investigations and tuning purposes, data from a fraction of the total time, the *playground* data is used. The playground data consists of approximately 10% of the total data and is chosen by selecting 600 seconds of data every 6370 seconds.

For the analysis of playground data triggers are only kept for 600s stretches of data; however, for the calculation of the power spectral density, 2048s stretches are still used. Once we have the data segments, we generate the template banks

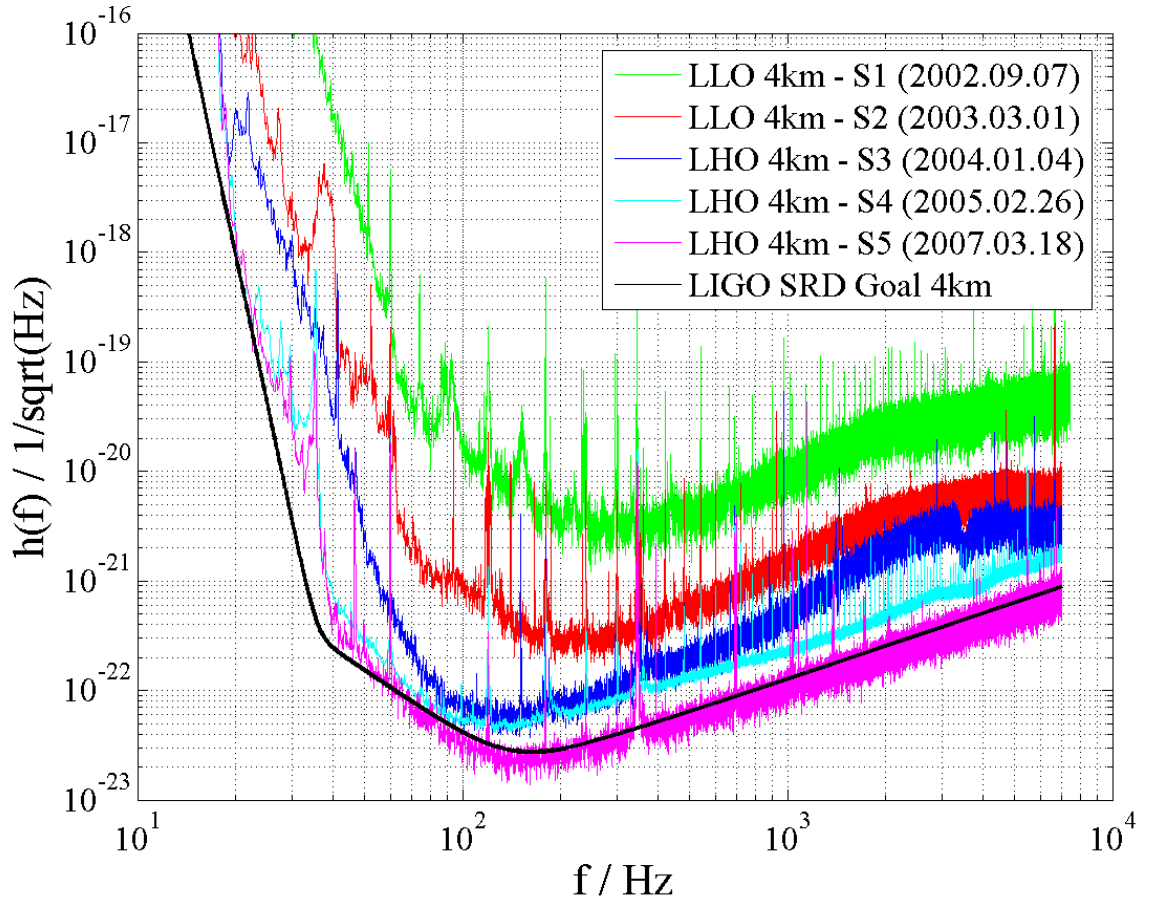


Figure 2.4: Best LIGO strain sensitivity curves for the science runs S1 to S5. The LIGO design sensitivity curve is shown in black.

which will be used in the search. Template banks are generated for each detector and for each 2048s data stretch, to take into account fluctuations of the detector power spectral densities.

2.2.2 The S5 Data Set

The S5 run commenced on 4th November 2005 with only the H1 and H2 detectors running. They were joined in the run by the L1 detector on 14th November 2005. The first calendar year searches analyze data from the start of the run up to the anniversary of L1 joining the run (i.e. up to 14th November 2006). For data to be analyzed, it is required that at least two instruments have data suitable for

analysis for that time. To avoid any bias which may be introduced via the tuning process, any final upper limits will be calculated using only non-playground data. In searching for potential detection candidates, all data will be analyzed.

A list of times for which the instruments have poor data quality has been produced. These times are grouped into different categories, depending on the cause of the poor data quality. Depending on the category the times belong to, the data for that particular instrument will either not be analyzed, or any triggers produced will be vetoed post-generation. In certain circumstances, it is possible that a signal arriving during the vetoed times could nonetheless be detected and validated; however, these vetoed times will be ignored in computing final upper limits. In addition to these, there is a further set of data quality flags which are not significant enough to veto any triggers produced, but may prove useful in following up candidate events.

2.3 The Inspiral Pipeline

Searching for inspiral compact binary sources in gravitational wave data is a challenging task. For the current generation of ground-based detectors, the signals from even strong sources will be buried within the detector noise. To locate the signals, it is therefore necessary to filter the data and utilise various techniques for removing spurious events caused by noise. This process is very computationally intensive. Accordingly, for a search to be carried out in a feasible amount of time, it is necessary to design search pipelines which run across several nodes on large computing clusters. The design of the inspiral pipeline currently used in the flagship LIGO searches consists of a number of stages, as illustrated in Fig. 2.5.

The various stages of the pipeline perform the following tasks:

- **Generate a template bank for each chunk of data:** The bank generated depends upon the choice of mass range, the requested minimal match and the noise power spectrum for that chunk.
- **Match filter the data using the inspiral code:** This takes the templates produced in the previous stage and matched filters them against the data stream. Any time that the signal to noise ratio exceeds a specified threshold, we record a trigger. This stage is the most computationally intensive part of the pipeline.
- **Search for coincident triggers between different detectors:** The triggers generated by the previous stage are read in and triggers from different detectors are compared by their parameters. If the parameters agree to within a certain tolerance, the event is deemed coincident.

- **Trigbank:** Coincident events are processed to create template banks for the following stage. This ensures that only relevant areas of the parameter space are re-filtered using the computationally costly vetoes.
- **Matched filtering with vetoes applied:** The coincident triggers are then returned to the inspiral code to be re-filtered, including the various signal-based vetoes, specifically the chi-squared and r-squared vetoes. This stage is potentially computationally expensive.
- **Repeated coincidence**
- **Coherent stage:** The triggers which survive the second coincident stage are then analysed using a coherent matched filter. Those triggers which survive this stage are considered candidate events and are followed up using various methods.

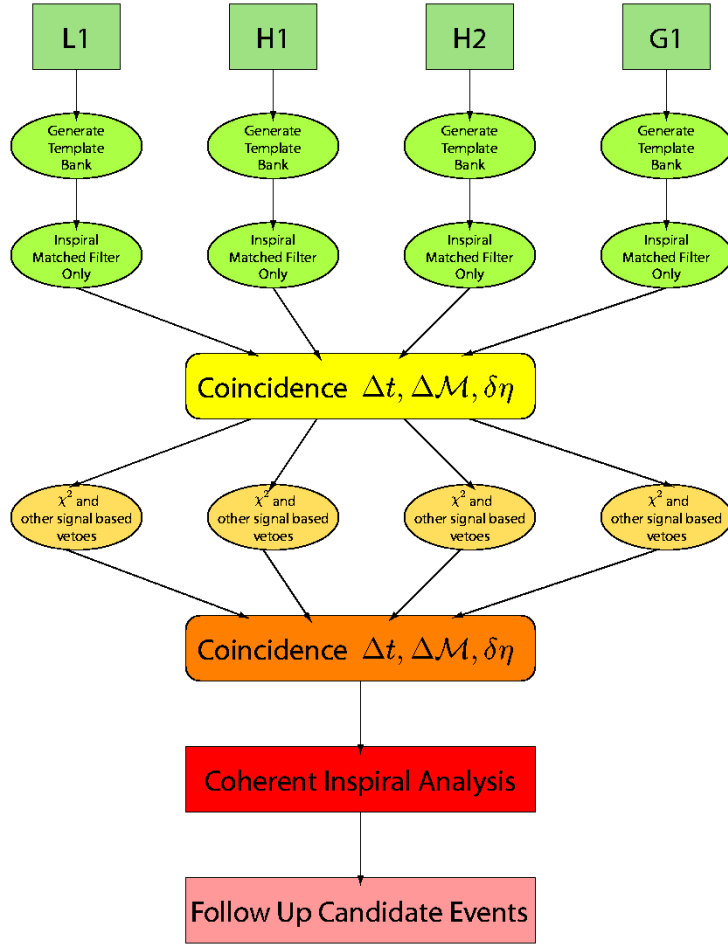


Figure 2.5: Schematic of the compact binary inspiral search pipeline

2.4 Matched Filtering

2.4.1 Introduction

Consider a detector output $s(t)$ which may or may not contain a weak signal of known form $h(t)$ superimposed on the noise $n(t)$

$$s(t) = \begin{cases} n(t) & \text{signal absent} \\ n(t) + h(t) & \text{signal present} \end{cases} \quad (2.4)$$

We assume, without loss of generality, that the signal, if present, occurs at $t = 0$. We also assume that the noise component of the detector output is a stationary random process with zero mean, Gaussian probability distribution and a one-sided

power spectral density $S_n(|f|)$ defined by

$$\overline{\tilde{n}(f)\tilde{n}^*(f')} = \frac{1}{2}S_n(|f|)\delta(f-f') \quad (2.5)$$

2.4.2 Wiener Optimal Filtering

Since we know the form of the signal we are looking for, the best way to determine whether or not it is present in the data is to pass the detector output through a filter $K(t)$. The output Z of the filter is meant to be a measure of how likely is for a given signal to be present in the data and is given by

$$Z \equiv \int_{-\infty}^{+\infty} K(t)s(t)dt \quad (2.6)$$

Our aim is to choose $K(t)$ such that Z will have a large value if the signal is present and a small value if it is not. We define

$$H \equiv \int_{-\infty}^{+\infty} K(t)h(t)dt \quad (2.7)$$

$$N \equiv \int_{-\infty}^{+\infty} K(t)n(t)dt \quad (2.8)$$

where H is the filtered signal, N is the filtered noise and

$$Z = H + N \quad (2.9)$$

if a signal is present. Note however that whereas $h(t)$ is a well-defined signal with finite duration, $n(t)$ is a random process

$$N(t) = \int_{-\infty}^{+\infty} K(t-t')n(t')dt' \quad (2.10)$$

and if we average N^2 over an ensemble of instantiations of the noise we get

$$\overline{N^2} = \int_0^{+\infty} |\tilde{K}(f)|^2 S_n(f)df \quad (2.11)$$

Using the convolution theorem and the fact that $K(t)$ and $h(t)$ are real (and so $\tilde{K}(-f) = \tilde{K}^*(f)$ and $\tilde{h}(-f) = \tilde{h}^*(f)$) we can write the filtered signal as

$$H = 2 \int_0^{+\infty} \tilde{K}^*(f)\tilde{h}(f)df \quad (2.12)$$

2. The Detection of Gravitational Waves

Next we define a statistic, the *signal-to-noise ratio* (SNR) ξ , and aim to find a filter $K(t)$ that maximizes this quantity

$$\xi \equiv \frac{H^2}{N^2} = \frac{4 \left| \int_0^{+\infty} \tilde{K}^*(f) \tilde{h}(f) df \right|^2}{\int_0^{+\infty} |\tilde{K}(f)|^2 S_n(f) df} = \frac{4 \left| \int_0^{+\infty} \left[\tilde{K}^*(f) \sqrt{S_n(f)} \right] \left[\tilde{h}(f) / \sqrt{S_n(f)} \right] df \right|^2}{\int_0^{+\infty} |\tilde{K}(f)|^2 S_n(f) df} \quad (2.13)$$

The Cauchy-Schwarz inequality tells us that for two arbitrary functions $A(f)$ and $B(f)$

$$\left| \int A(f) B(f) df \right| \leq \int |A(f)| df \int |B(f)| df \quad (2.14)$$

Identifying $\tilde{K}(f) \sqrt{S_n(f)}$ with $A(f)$ and $\tilde{h}(f) / \sqrt{S_n(f)}$ with $B(f)$ we can see that to attain the maximum value of ξ , we need the equality in equation (2.14) to hold, which only occurs when A and B are equal up to a constant C , thus

$$\tilde{K}(f) \sqrt{S_n(f)} = C \frac{\tilde{h}(f)}{\sqrt{S_n(f)}} \quad (2.15)$$

or

$$\tilde{K}(f) = C \frac{\tilde{h}(f)}{S_n(f)} \quad (2.16)$$

Thus the optimal filter for detecting signals of known form in coloured Gaussian noise is the Fourier transform of the signal $\tilde{h}(f)$ weighted by the inverse of the power spectrum.

2.4.3 Detection Statistic

Returning to our initial equation for the filter output equation (2.6) and allowing the signal to occur at some unknown time t , the filter output will be a function of t and it can be expressed as a convolution

$$Z(t) = C \int_{-\infty}^{+\infty} K(t-t') s(t') dt' \quad (2.17)$$

Using the convolution theorem this can be expressed as

$$Z(t) = C \int_{-\infty}^{+\infty} \tilde{s}(f) \tilde{K}^*(f) e^{2\pi i f t} df \quad (2.18)$$

and substituting in the expression for the optimal filter, equation (2.16), we get

$$Z(t) = C \int_{-\infty}^{+\infty} \frac{\tilde{s}(f) \tilde{h}^*(f) e^{2\pi i f t}}{S_n(|f|)} df \quad (2.19)$$

At this stage we could choose a threshold value of $|Z|$ above which a signal would be defined as being present and below which the signal is absent. However rather than thresholding directly on the filter output we first normalize by the variance of the optimal filter σ^2

$$\sigma^2 = 2 \int_{-\infty}^{+\infty} \frac{\tilde{h}(f)\tilde{h}^*(f)}{S_n(|f|)} df \quad (2.20)$$

for which $C = 2$. We define a statistic ρ , the SNR of the normalized output of the optimal filter, as

$$\rho(t) = \frac{|Z(t)|}{\sigma} \quad (2.21)$$

and choose a value ρ^* on which to threshold. Thus

$$\text{if } \rho \begin{cases} < \rho^* & \text{the signal is absent} \\ \geq \rho^* & \text{the signal is present} \end{cases} \quad (2.22)$$

With this comes the possibility of *false alarm* and *false dismissal*; the former occurs when $\rho \geq \rho^*$ and no signal is present and the latter occurs when $\rho < \rho^*$ and a signal is present. Thus ρ^* must be chosen carefully so as to minimize the rate of false alarms and false dismissals.

2.4.4 Inner Product

In the light of the above discussion, the filter we have chosen naturally defines an inner product between a real signal $s(t)$ and a real template $h(t)$, with Fourier transforms $\tilde{s}(f), \tilde{h}(f)$ as

$$\begin{aligned} \langle s, h \rangle &= 2 \int_{-\infty}^{+\infty} \frac{\tilde{s}(f)\tilde{h}^*(f)}{S_n(|f|)} df = 2 \int_0^{+\infty} \frac{\tilde{s}(f)\tilde{h}^*(f) + \tilde{s}(-f)\tilde{h}^*(-f)}{S_n(f)} df \\ &= 2 \int_0^{+\infty} \frac{\tilde{s}(f)\tilde{h}^*(f) + \tilde{s}^*(f)\tilde{h}(f)}{S_n(f)} df = 2 \int_0^{+\infty} \frac{\tilde{s}(f)\tilde{h}^*(f) + \left(\tilde{s}(f)\tilde{h}^*(f)\right)^*}{S_n(f)} df \\ &= 4 \Re \left[\int_0^{+\infty} \frac{\tilde{s}(f)\tilde{h}^*(f)}{S_n(f)} df \right] = 4 \Re \left[\int_0^{+\infty} \frac{\tilde{s}^*(f)\tilde{h}(f)}{S_n(f)} df \right] \end{aligned} \quad (2.23)$$

where in the third equality we used the fact that, for a real signal, $\tilde{s}^*(f) = \tilde{s}(-f)$.

For a waveform $h(t - t_e)$ with unknown *end time* t_e the value of the time-dependent inner product $\langle s, h \rangle$ is given by Eq.(2.19) with $C = 2$

$$\langle s, h(t_e) \rangle = 2 \int_{-\infty}^{+\infty} \frac{\tilde{s}(f)\tilde{h}^*(f)}{S_n(|f|)} e^{2\pi i f t_e} df = 4 \Re \left[\int_0^{\infty} \frac{\tilde{s}(f)\tilde{h}^*(f)}{S_n(f)} e^{2\pi i f t_e} df \right] \quad (2.24)$$

2.4.5 The Stationary-Phase Approximation

To calculate the inner products (2.23)(2.24), the Fourier transform $\tilde{h}(f)$ of the template is needed. Usually Fourier transforms are calculated using numerical packages like FFT, however, under certain assumptions, we can make use of the *stationary phase approximation* to express the template waveforms directly in the frequency domain and save a great deal of computational cost.

Given a function

$$B(t) = A(t) \cos(2\phi(t)) \quad (2.25)$$

where $A(t)$ and $\phi(t)$ satisfy the conditions

$$\frac{d \ln A}{dt} \ll \frac{d\phi}{dt} \quad (2.26a)$$

$$\frac{d^2 \ln A}{dt^2} \ll \frac{d^2 \phi}{dt^2} \quad (2.26b)$$

then the stationary approximation to the Fourier transform of $B(t)$ is given by

$$\begin{aligned} \tilde{B}(f) &= \frac{1}{2} A(t) \left(\frac{df}{dt} \right)^{-\frac{1}{2}} \exp \left[-i \left(2\pi f t' - 2\phi(f) - \frac{\pi}{4} \right) \right] \\ &= \frac{1}{2} A(t) \left(\frac{df}{dt} \right)^{-\frac{1}{2}} \exp [-i\Psi(f)] \end{aligned} \quad (2.27)$$

where we defined the phase $\Psi(f) \equiv 2\pi f t' - 2\phi(f) - \pi/4$ and t' is the time at which

$$\frac{d\phi(t)}{dt} = \pi f \quad (2.28)$$

2.5 Template Bank

Current searches for compact binary coalescence use the matched filtering techniques outlined in the previous section, which require the knowledge of template waveforms to characterize the expected signal from the source.

Waveform templates are described by a set of parameters λ^A that determine their “shape” and their duration; these parameters include masses, spins, orientation and direction angles and initial conditions like the orbital phase at a fiducial time t_0 . In order to detect a specific signal, the data must be filtered against a template that accurately models the signal itself, so that the SNR ρ will rise above the chosen threshold ρ^* ; however the signal is not known a-priori so we must find an algorithm that allows to find which template (i.e. which set of parameters) best describes it. Of course, filtering the data with *all possible templates* is not feasible

(and not even conceivable).

One could think about constructing a large set of templates, each with a different set of parameters and empirically find, through matched filtering, the template that yields the highest SNR; however the dimensionality of the parameter space to search over can be as high as 17 for generic binaries and matched filtering is a very computationally expensive operation. The challenge therefore is to find the *correct* template using the smallest possible amount of computational power.

2.5.1 Intrinsic and Extrinsic Parameters

The parameters a template depends on can be divided in two categories: *intrinsic* and *extrinsic* [20, 16, 33]. Extrinsic parameters can be disentangled from the dynamical variables of the system and they can generally be searched over analytically (or in the worst case numerically); conversely, intrinsic parameters influence the shape of the waveform in such a way that fast maximization is not possible.

Let us split our set of parameters in $\lambda^A = X^A + \Xi^A$, where X^A and Ξ^A represent, respectively, the intrinsic and extrinsic parameters. We can therefore implicitly find the set of extrinsic parameters that best matches the signal by analytically maximizing the expression for the SNR over the Ξ^A ; to find the best set of intrinsic parameters X^A we then need to construct a bank of templates so that any given signal can be recovered by at least one of the templates in the bank.

It is useful to define the *match* (or overlap) \mathcal{M} between two templates h and h' as the normalized versions of the inner products (2.23)-(2.24), maximized over the extrinsic parameters

$$\mathcal{M}[h, h'] \equiv \max_{\Xi^A} \frac{\langle h, h' \rangle}{\sqrt{\langle h, h \rangle} \sqrt{\langle h', h' \rangle}} = \max_{\Xi^A} \left\langle \frac{h}{\sqrt{\langle h, h \rangle}}, \frac{h'}{\sqrt{\langle h', h' \rangle}} \right\rangle \equiv \langle \hat{h}, \hat{h}' \rangle \quad (2.29)$$

where we introduced the notation \hat{h} to denote the normalized template $h/\sqrt{\langle h, h \rangle}$. In the next paragraphs we will see how to construct a template bank.

2.5.2 Parameter Space Metric

To quantify how well a template h matches a signal h' we can define a distance \mathcal{D} induced by the inner product (2.23), called the *mismatch* distance

$$\mathcal{D}[h, h'] = 1 - \frac{\langle h, h' \rangle}{\sqrt{\langle h, h \rangle} \sqrt{\langle h', h' \rangle}} \equiv 1 - \langle \hat{h}, \hat{h}' \rangle \quad (2.30)$$

with $0 < \mathcal{D} \leq 1$. A metric \mathbf{g} is associated with this distance, which describes up to quadratic order the degrading overlap between neighboring templates.

2. The Detection of Gravitational Waves

Let us consider a normalized template described by the set of parameters λ^A and a nearby template $\hat{h}(\lambda^A + \Delta\lambda^A)$; for small values of $\Delta\lambda^A$ we have $\langle \hat{h}(\lambda^A), \hat{h}(\lambda^A + \Delta\lambda^A) \rangle \simeq 1$ and the distance (2.30) can be expanded in powers of $\Delta\lambda^A$ to get

$$\begin{aligned}
\mathcal{D} \left[\hat{h}(\lambda^A), \hat{h}(\lambda^A + \Delta\lambda^A) \right] &= \left(1 - \langle \hat{h}(\lambda^A), \hat{h}(\lambda^A + \Delta\lambda^A) \rangle \right) \Big|_{\Delta\lambda^A=0} \\
&+ \frac{\partial \left(1 - \langle \hat{h}(\lambda^A), \hat{h}(\lambda^A + \Delta\lambda^A) \rangle \right)}{\partial(\Delta\lambda^B)} \Big|_{\Delta\lambda^A=0} (\Delta\lambda^B) \\
&+ \frac{1}{2} \frac{\partial^2 \left(1 - \langle \hat{h}(\lambda^A), \hat{h}(\lambda^A + \Delta\lambda^A) \rangle \right)}{\partial(\Delta\lambda^B)\partial(\Delta\lambda^C)} \Big|_{\Delta\lambda^A=0} (\Delta\lambda^B)(\Delta\lambda^C) \\
&+ \mathcal{O} \left((\Delta\lambda^B)(\Delta\lambda^C)(\Delta\lambda^D) \right) \\
&= - \frac{\partial \langle \hat{h}(\lambda^A), \hat{h}(\lambda^A + \Delta\lambda^A) \rangle}{\partial(\Delta\lambda^B)} \Big|_{\Delta\lambda^A=0} (\Delta\lambda^B) \\
&- \frac{1}{2} \frac{\partial^2 \langle \hat{h}(\lambda^A), \hat{h}(\lambda^A + \Delta\lambda^A) \rangle}{\partial(\Delta\lambda^B)\partial(\Delta\lambda^C)} \Big|_{\Delta\lambda^A=0} (\Delta\lambda^B)(\Delta\lambda^C) \\
&+ \mathcal{O} \left((\Delta\lambda^B)(\Delta\lambda^C)(\Delta\lambda^D) \right) \tag{2.31}
\end{aligned}$$

Now we know that the match $\langle \hat{h}(\lambda^A), \hat{h}(\lambda^A + \Delta\lambda^A) \rangle$ has a maximum of 1 for $\Delta\lambda^A = 0$, therefore the first derivative at this point will vanish and, ignoring terms of order $\mathcal{O} \left((\Delta\lambda^B)(\Delta\lambda^C)(\Delta\lambda^D) \right)$, we have

$$\begin{aligned}
\mathcal{D} \left[\hat{h}(\lambda^A), \hat{h}(\lambda^A + \Delta\lambda^A) \right] &= - \frac{1}{2} \frac{\partial^2 \langle \hat{h}(\lambda^A), \hat{h}(\lambda^A + \Delta\lambda^A) \rangle}{\partial(\Delta\lambda^B)\partial(\Delta\lambda^C)} \Big|_{\Delta\lambda^A=0} (\Delta\lambda^B)(\Delta\lambda^C) \\
&\equiv g_{BC}(\lambda^A) \Delta\lambda^B \Delta\lambda^C \\
&= ds^2 \tag{2.32}
\end{aligned}$$

and therefore the metric is given by

$$g_{BC}(\lambda^A) = - \frac{1}{2} \frac{\partial^2 \langle \hat{h}(\lambda^A), \hat{h}(\lambda^A + \Delta\lambda^A) \rangle}{\partial(\Delta\lambda^B)\partial(\Delta\lambda^C)} \Big|_{\Delta\lambda^A=0} = - \frac{1}{2} \left\langle \hat{h}(\lambda^A), \frac{\partial^2 \hat{h}(\lambda^A + \Delta\lambda^A)}{\partial(\Delta\lambda^B)\partial(\Delta\lambda^C)} \right\rangle \Big|_{\Delta\lambda^A=0} \tag{2.33}$$

It is also possible to rewrite the full metric (2.33) in terms of first-order derivatives of the overlap $\langle \hat{h}(\lambda^A), \hat{h}(\lambda^A + \Delta\lambda^A) \rangle$ around $\Delta\lambda^A = 0$ and get a more useful

expression.

We note that, since $\langle \hat{h}(\lambda^A), \hat{h}(\lambda^A) \rangle \equiv \langle \hat{h}, \hat{h} \rangle = 1$ for every λ^A , we have

$$\frac{\partial}{\partial \lambda^B} \langle \hat{h}, \hat{h} \rangle = 2 \left\langle \hat{h}, \frac{\partial \hat{h}}{\partial \lambda^B} \right\rangle = 0 \quad (2.34)$$

If we take the derivative of (2.34) with respect to λ^C we get

$$\left\langle \frac{\partial \hat{h}}{\partial \lambda^C}, \frac{\partial \hat{h}}{\partial \lambda^B} \right\rangle + \left\langle \hat{h}, \frac{\partial^2 \hat{h}}{\partial \lambda^B \partial \lambda^C} \right\rangle = 0 \quad (2.35)$$

and comparing with Eq.(2.33) we get

$$g_{BC} = \frac{1}{2} \left\langle \frac{\partial \hat{h}}{\partial \lambda^B}, \frac{\partial \hat{h}}{\partial \lambda^C} \right\rangle \quad (2.36)$$

which expresses the *Fisher information matrix* for the normalized waveforms $\hat{h}(\lambda^A)$ [51]. For non-normalized waveforms $h(\lambda^A)$ we can write

$$g_{BC} = \frac{1}{2 \langle h, h \rangle} \left\langle \frac{\partial h}{\partial \lambda^B}, \frac{\partial h}{\partial \lambda^C} \right\rangle - \frac{1}{2 \langle h, h \rangle^2} \left\langle \frac{\partial h}{\partial \lambda^B}, h \right\rangle \left\langle h, \frac{\partial h}{\partial \lambda^C} \right\rangle \quad (2.37)$$

Therefore, if we know the dependence of our templates on the parameters, we can construct the metrics (2.36)-(2.37) and calculate mismatch distances between nearby templates without actually computing the inner products (2.30) and save a great deal of computational cost.

2.5.3 Template Placement

In order to be able to detect any possible target signal s , we want to choose a discrete subset of the continuous family of template waveforms that belong to the parameter space, called *template bank*, such that s is matched “satisfactorily” by at least one of the N templates in the bank. We can quantify “satisfactorily” by requiring that, for any signal s there exists a template h_{n^*} in the bank such that $\mathcal{D}[\hat{s}, \hat{h}_{n^*}] < d^*$ or equivalently

$$\langle \hat{s}, \hat{h}_{n^*} \rangle > (1 - d^*) \equiv MM \quad (2.38)$$

where MM defines a chosen *minimal match*.

Of course our best model for a real signal is the template, so the prescription for

2. The Detection of Gravitational Waves

the construction of a bank is that, given a template corresponding to a generic set of parameters $\lambda^A = (X^A, \Xi^A)$, the maximum match over the bank must be greater than MM

$$\max_{\lambda^n} \langle \hat{h}(\lambda^A), \hat{h}(\lambda^n) \rangle > MM, \quad \forall A \quad (2.39)$$

with $1 < n < N$.

As stated in the previous section, the best configuration of extrinsic parameters Ξ_{best}^i can be determined implicitly by maximizing analytically the inner product $\langle \hat{h}(\lambda^A), \hat{h}(\lambda^n) \rangle$, so it is useful to rewrite the metric g_{BC} in such a way that intrinsic and extrinsic parameters are separated and the mismatch distance between two nearby templates is given by

$$\mathcal{D} \left[\hat{h}(X^i, \Xi^\alpha), \hat{h}(X^i + \Delta X^i, \Xi^\alpha + \Delta \Xi^\alpha) \right] = (\Delta X^i \quad \Delta \Xi^\alpha) \begin{pmatrix} G_{ij} & C_{i\beta} \\ C_{\alpha i} & \gamma_{\alpha\beta} \end{pmatrix} \begin{pmatrix} \Delta X^j \\ \Delta \Xi^\beta \end{pmatrix} \quad (2.40)$$

We have therefore split the full metric g_{BC} into four sections corresponding to intrinsic-intrinsic (G_{ij}), extrinsic-extrinsic ($\gamma_{\alpha\beta}$) and mixed ($C_{\alpha j} = C_{j\alpha}$) components. Maximizing the match over the extrinsic parameters is then equivalent to minimizing Eq.(2.40) over the $\Delta \Xi^\alpha$ given the ΔX^i , which is achieved when

$$\gamma_{\alpha\beta} \Delta \Xi^\beta + C_{\alpha j} \Delta X^j = 0 \quad (2.41)$$

while the resulting mismatch is

$$\begin{aligned} \min_{\Delta \Xi^\alpha} \mathcal{D} \left[\hat{h}(X^i, \Xi^\alpha), \hat{h}(X^i + \Delta X^i, \Xi^\alpha + \Delta \Xi^\alpha) \right] &= \left[G_{ij} - C_{i\alpha} (\gamma^{-1})^{\alpha\beta} C_{\beta j} \right] \Delta X^i \Delta X^j \\ &\equiv g_{ij}^{proj} \Delta X^i \Delta X^j \\ &= 1 - \mathcal{M} [h(X^i), h(X^i + \Delta X^i)] \end{aligned} \quad (2.42)$$

Here $(\gamma^{-1})^{\alpha\beta}$ is the matrix inverse of $\gamma_{\alpha\beta}$. For each point (X^i, Ξ^α) in the *full* parameter space, the projected metric g_{ij}^{proj} describes a set of concentric ellipsoids of constant ρ_{Ξ^α} in the intrinsic-parameter subspace. We emphasize that the projected metric has tensor indices corresponding to the intrinsic parameters, but it is a function of both the intrinsic and the extrinsic parameters, and so are the constant- ρ_{Ξ^α} ellipsoids. Therefore, to build a template bank that covers all the signals (for all X^i and Ξ^α) with a guaranteed MM, we must use the projected metric at each X^i to construct the constant-mismatch ellipsoids for all possible Ξ^α and then take the intersection of these ellipsoids to determine the size of the unit template-bank cell. This is a *minimax* prescription [37], because we are maximizing the overlap over the extrinsic parameters of the templates, and then setting the template-bank spacing according to the least favorable extrinsic parameters of the signal.

In general, the intersection of constant-mismatch ellipsoids is not an ellipsoid, even in the limit $\mathcal{D} \rightarrow 0$, so it is impossible to find a single intrinsic-parameter metric that can be used to enforce the minimax prescription. There is an exception: the projected metric is not a function of t_0 or Φ_0 so it can be used directly to lay down banks of nonspinning-binary templates [39, 58], for which t_0 and Φ_0 are the only extrinsic parameters.

Returning to the generic case, we can still use the projected metric to guide the placement of a template bank if we relax the minimax prescription and request that the minimum match be guaranteed on the average for a distribution of signal extrinsic parameters; this is called the *average-mismatch* prescription.

2.6 The χ^2 Veto

The chi-squared test is a time-frequency discriminator which can be thought of as a “goodness-of-fit” test between the data which generated the trigger and the template itself [15].

We start by dividing the frequency-domain normalized template $\tilde{h}(f)$ into p frequency bands $\Delta f_1, \Delta f_2, \dots, \Delta f_p$. In every frequency bin j the inner product (2.23) is redefined to be

$$\langle h, h \rangle_j \equiv 2 \int_{\Delta f_j} \frac{\tilde{h}^*(f)\tilde{h}(f)}{S_n(|f|)} df \quad (2.43)$$

where the range of integration is over both the positive and negative frequencies. Since $S_n(|f|)$ may be taken as infinite for $|f|$ greater than the Nyquist frequency f_N , the effective upper limit of the final frequency interval Δf_p is f_N rather than ∞ .

Every bin will contain a known amount of power q_j given by

$$\langle h, h \rangle_j = q_j \quad (2.44)$$

and since the frequency intervals don't overlap but cover all frequency values, the sum of the p inner products must yield the inner product (2.23)

$$\langle h, h \rangle = \sum_{j=1}^p \langle h, h \rangle_j = \sum_{j=1}^p q_j = 1 \quad (2.45)$$

In each band we then filter the data s with the template h to get

$$x_j = \langle s, h \rangle_j \quad (2.46)$$

and again we have

$$x = \langle s, h \rangle = \sum_{j=1}^p \langle s, h \rangle_j = \sum_{j=1}^p x_j \quad (2.47)$$

2. The Detection of Gravitational Waves

If we now define

$$\Delta x_j \equiv x_j - q_j x \quad (2.48)$$

we can construct the statistic

$$\chi^2 = \sum_{j=1}^p \frac{(\Delta x_j)^2}{q_j} \quad (2.49)$$

which is χ^2 distributed with $p - 1$ degrees of freedom.

In the special case of frequency bins with equal power content $\langle h, h \rangle_j = 1/p$, the quantities (2.48) become

$$\Delta x_j \equiv x_j - \frac{x}{p} \quad (2.50)$$

and the statistic (2.49) assumes a simpler form

$$\chi_{eq}^2 = p \sum_{j=1}^p (\Delta x_j)^2 \quad (2.51)$$

which is still χ^2 -distributed with $p - 1$ degrees of freedom.

If we now consider a template with N independent orthonormal components h^I , with $I = 1, 2, \dots, N$, such that $\langle h^I, h^J \rangle = \delta_{IJ}$, we can construct a χ^2 statistic by defining for every bin j

$$\langle h^I, h^{I'} \rangle_j = q_j^I, \quad I = I' = 1, 2, \dots, N \quad (2.52)$$

so that

$$\langle h^I, h^{I'} \rangle = \sum_{j=1}^p \langle h^I, h^{I'} \rangle_j = \sum_{j=1}^p q_j^I = 1, \quad I = I' = 1, 2, \dots, N \quad (2.53)$$

In each band j we then filter the data s with each component h^I to get

$$x_j^I = \langle s, h^I \rangle_j \quad (2.54)$$

and again we have

$$x^I = \langle s, h^I \rangle = \sum_{j=1}^p \langle s, h^I \rangle_j = \sum_{j=1}^p x_j^I \quad (2.55)$$

If we now define

$$\Delta x_j^I \equiv x_j^I - q_j^I x^I \quad (2.56)$$

we can construct a χ^2 distributed statistic

$$\chi_{(N)}^2 = \sum_{j=1}^p \left[\sum_{I=1}^N \frac{(\Delta x_j^I)^2}{q_j^I} \right] \quad (2.57)$$

which has $N(p - 1)$ degrees of freedom.

Again in the special case of equal-power bins we have

$$\begin{cases} \Delta x_j^I \equiv x_j^I - \frac{x^I}{p} \\ \chi_{eq(N)}^2 = p \sum_{j=1}^p \left[\sum_{I=1}^N (\Delta x_j^I)^2 \right] \end{cases} \quad (2.58)$$

which is still χ^2 -distributed with $N(p - 1)$ degrees of freedom.

It is clear that, for a perfectly matched signal and template, in the absence of noise, the value of χ^2 will be zero. In presence of stationary Gaussian noise only $x(t) = n(t)$, the statistic (2.49) will be χ^2 -distributed with $p - 1$ degrees of freedom. In fact, it can be shown that, even in the presence of a signal and noise, $s(t) = n(t) + h(t)$, the statistic still obeys a χ^2 -distribution with $p - 1$ degrees of freedom. However, if the data contains a spurious artifact which is picked up with a high SNR, but does not perfectly match the template, this will lead to a high value of χ^2 . Thus, this statistic is a useful discriminant for distinguishing between signals and noise glitches.

However usually the template and the signal will not match perfectly, mainly because to the discrete nature of the template banks used in the search but possibly also because the template lacks the ability of accurately describing the signal. To take into account these differences, in practice, we threshold on the value χ_*^2 , where

$$\chi^2 < \chi_*^2(p + \delta^2 \rho^2) \quad (2.59)$$

where δ^2 is a parameter used to take into account the mismatches between templates and potential signals. The values of δ^2 and χ_*^2 used for the search are tuned using Monte-Carlo simulations.

2.7 Searching for Gravitational Waves from Spinning Binaries

We will now describe the strain induced in the detector by GWs emitted by a generic binary and we will briefly overview the detection problem using different types of templates.

2.7.1 Detector Strain

Given a detector lying in the direction $\hat{\mathbf{N}}$ with respect to the source frame $\{\mathbf{e}_x^S, \mathbf{e}_y^S, \mathbf{e}_z^S\}$, we can introduce the *radiation frame* $\{\mathbf{e}_x^R, \mathbf{e}_y^R, \mathbf{e}_z^R\}$ where $\mathbf{e}_z^R \equiv \hat{\mathbf{N}}$ and $\mathbf{e}_{x,y}^R$ can be chosen arbitrarily in the plane orthogonal to $\hat{\mathbf{N}}$.

2. The Detection of Gravitational Waves

From the radiation frame basis vectors we can build the tensors $\mathbf{T}_{+, \times}$ given by

$$\mathbf{T}_+ \equiv \mathbf{e}_x^R \otimes \mathbf{e}_x^R - \mathbf{e}_y^R \otimes \mathbf{e}_y^R \quad (2.60)$$

$$\mathbf{T}_\times \equiv \mathbf{e}_x^R \otimes \mathbf{e}_y^R + \mathbf{e}_y^R \otimes \mathbf{e}_x^R \quad (2.61)$$

We then introduce an orthonormal reference frame attached to the detector $\{\bar{\mathbf{e}}_x, \bar{\mathbf{e}}_y, \bar{\mathbf{e}}_z\}$, where $\bar{\mathbf{e}}_{x,y}$ are unit vectors along the orthogonal interferometers arms. The *antenna patterns* $F_{+, \times}$ associated with this frame are given by

$$F_+ = \frac{1}{2} [\bar{\mathbf{e}}_x \otimes \bar{\mathbf{e}}_x - \bar{\mathbf{e}}_y \otimes \bar{\mathbf{e}}_y]^{ij} [\mathbf{T}_+]_{ij} \quad (2.62)$$

$$F_\times = \frac{1}{2} [\bar{\mathbf{e}}_x \otimes \bar{\mathbf{e}}_x - \bar{\mathbf{e}}_y \otimes \bar{\mathbf{e}}_y]^{ij} [\mathbf{T}_\times]_{ij} \quad (2.63)$$

If we define (ϕ, θ, ψ) to be the orientation angles of the detector frame with respect to the radiation frame (see figure 2.6), then we can rewrite (2.62)-(2.63) as

$$F_+ = \frac{1}{2} (1 + \cos^2 \theta) \cos 2\phi \cos 2\psi - \cos \theta \sin 2\phi \sin 2\psi \quad (2.64)$$

$$F_\times = \frac{1}{2} (1 + \cos^2 \theta) \cos 2\phi \sin 2\psi + \cos \theta \sin 2\phi \cos 2\psi$$

By projecting the radiative gravitational field h^{ij} onto the TT gauge we obtain the two transverse polarizations

$$\begin{cases} h_+ = \frac{1}{2} h^{ij} [\mathbf{T}_+]_{ij} \\ h_\times = \frac{1}{2} h^{ij} [\mathbf{T}_\times]_{ij} \end{cases} \quad (2.65)$$

and the strain induced in the detector is then given by

$$h = F_+ h_+ + F_\times h_\times \quad (2.66)$$

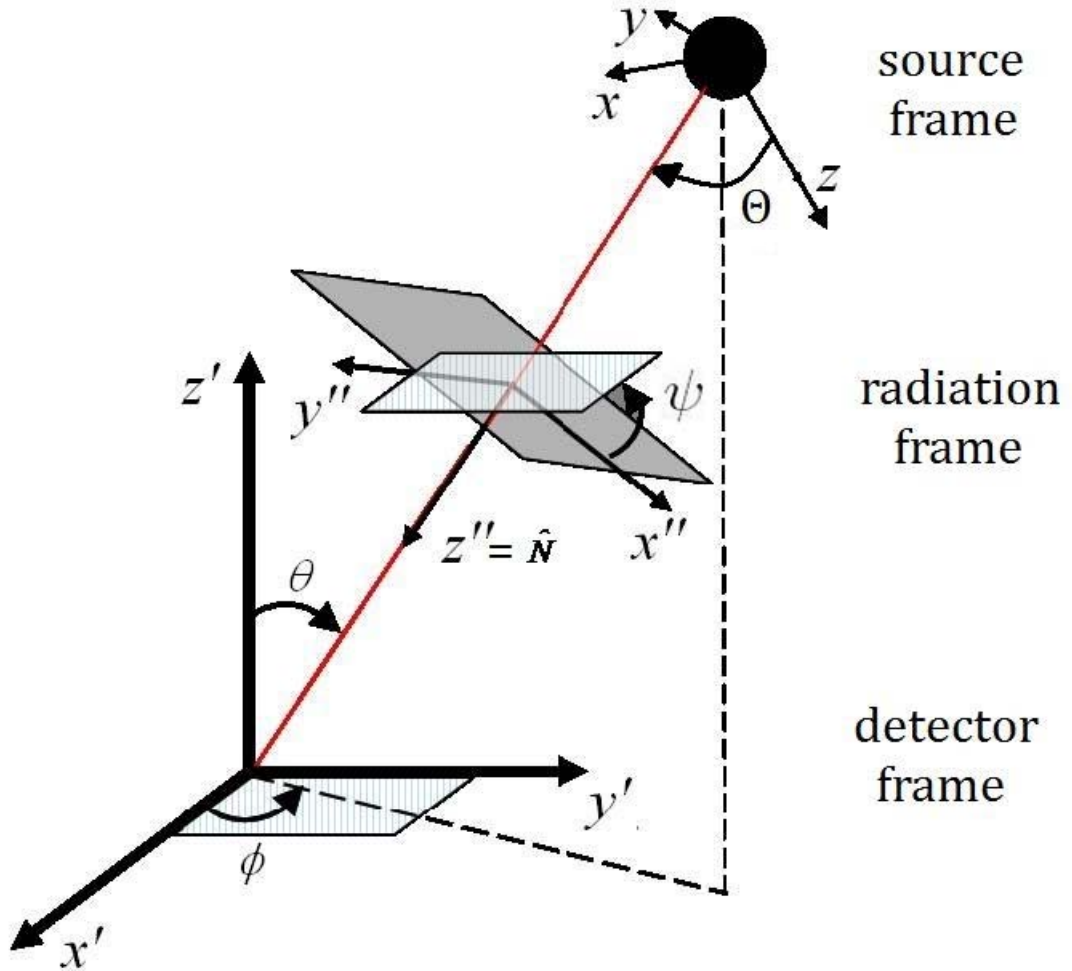


Figure 2.6: Illustration of source (x, y, z) , radiation (x'', y'', z'') and detector (x', y', z') frames.

2.7.2 Non-Spinning Templates

Gravitational waves from non-spinning compact-object binaries are the best modeled signals due to the simplicity of the dynamics and the absence of precession-induced effects.

For low-mass systems (with total mass $M \lesssim 35M_\odot$) the GWs emitted during the last stages of the adiabatic inspiral phase lie within the LIGO bandwidth and they can be modeled by Post-Newtonian waveforms in the circular orbit approximation. The equations of motion include terms up to 2PN order.

The radiative gravitational-wave field at a large distance R from the binary is described by the two transverse polarizations as

$$h_+(t) = -\frac{2\mu}{R} (\pi M f)^{2/3} (1 + \cos^2 \iota) \cos(2\pi f t - 2\Phi_0) \quad (2.67)$$

$$h_\times(t) = -\frac{2\mu}{R} (\pi M f)^{2/3} (\cos \iota) \sin(2\pi f t - 2\Phi_0) \quad (2.68)$$

where M and μ are the usual total and reduced masses, $f = \omega/\pi$ is the gravitational-wave frequency and ι is the inclination angle which defines the orientation of the orbital plane (i.e. of the (constant) orbital angular momentum $\hat{\mathbf{L}}_N$) with respect to the direction of propagation $\hat{\mathbf{N}}$

$$\hat{\mathbf{L}}_N \cdot \hat{\mathbf{N}} = \cos \iota \quad (2.69)$$

We define the *cosine chirp* h_c and *sine chirp* h_s as

$$h_c(t) = \frac{2\mu}{M_\odot} [\pi M f(t)]^{2/3} \cos[2\Phi(t) - 2\Phi_0] \quad (2.70)$$

$$h_s(t) = \frac{2\mu}{M_\odot} [\pi M f(t)]^{2/3} \sin[2\Phi(t) - 2\Phi_0] \quad (2.71)$$

where the orbital phase $\Phi(t)$ is given by

$$\Phi(t) = \frac{1}{2} \int f(t) dt \quad (2.72)$$

We can then rewrite the $+$ and \times polarizations as

$$h_+(t) = -\frac{M_\odot}{R} (1 + \cos^2 \iota) h_c(t) \quad (2.73)$$

$$h_\times(t) = -\frac{2M_\odot}{R} \cos(\iota) h_s(t) \quad (2.74)$$

The detector strain can be written in the usual form

$$h(t) = F_+ h_+(t) + F_\times h_\times(t) \quad (2.75)$$

where $F_{+,\times}(\theta, \phi, \psi)$ are the antenna patterns defined in Eq.(2.64).

Using eqs.(2.70)-(2.71) and (2.73)-(2.74) we can write $h(t)$ as

$$h(t) = \frac{A(t)}{D} \cos(2\Phi(t) - \Phi'_0) \quad (2.76)$$

where

$$A(t) = -2\mu [\pi M f(t)]^{2/3} \quad (2.77)$$

and D is the *effective distance*, given by

$$D = \frac{R}{\sqrt{F_+^2 (1 + \cos^2 \iota)^2 + F_\times^2 4 \cos^2(\iota)}} \quad (2.78)$$

and Φ'_0 is a new constant phase angle given by

$$\tan \Phi'_0 = \frac{F_\times 2 \cos(\iota)}{F_+ (1 + \cos^2 \iota)} \quad (2.79)$$

Looking at Eq.(2.76) we see that the waveform has been written in the form (2.25) and the stationary phase approximation can be used to write h directly in the frequency domain.

The expression of the cosine chirp in the stationary phase approximation is then given by

$$\tilde{h}_c(f) = \frac{2M_\odot^{5/6}}{R} \left(\frac{5\mu}{96M_\odot} \right)^{1/2} \left(\frac{M}{\pi^2 M_\odot} \right)^{1/3} f^{-7/6} e^{i\Psi(f; M, \eta)} \quad (2.80)$$

with $\eta = \mu/M$ the symmetric mass ratio. Since the sine chirp is the orthogonal waveform to the cosine chirp, in the stationary phase approximation we have

$$\tilde{h}_s(f) = i\tilde{h}_c(f) \quad (2.81)$$

therefore the SNR is simply given by

$$\rho = \frac{\sqrt{\langle s, h_c \rangle^2 + \langle s, h_s \rangle^2}}{\sigma} \quad (2.82)$$

where σ is a normalization factor defined by (2.20).

We note from Eq.(2.76) that for a non-spinning template all the extrinsic parameters, namely the angles $(\theta, \phi, \psi, \iota)$ are factorized out in the term D and they only contribute as an overall constant amplitude factor. This is very helpful when

constructing a template bank, since the match does not depend on the normalization of the template. The remaining extrinsic parameters are the end time t_e which is effectively searched over through the Fourier transform (2.24) and the initial phase Φ'_0 which is maximized over by summing the two orthogonal phases h_c and h_s in quadrature as in (2.82).

The only intrinsic parameters are M and μ (or m_1 and m_2), so the template bank space is 2-dimensional.

Non-spinning SPA templates are currently being used for all LIGO low-mass binary searches and they have shown a fairly good efficiency in recovering simulated waveforms from spinning binaries characterized by weak modulational effects; for example, in the case of NS-NS binaries, it appears that an unmodulated family of templates would be sufficient for the detection of inspiral events, even for maximally spinning NSs ($S_{NS}^2/m_{NS}^2 \simeq 0.6 - 0.7$) [21, 22, 23, 24].

However non-spinning templates are not able to reproduce the phase and amplitude modulations of spinning waveforms, therefore they show “holes” in efficiency for specific mass-spin configurations of the source. Specifically the loss of detection efficiency increases with the mass ratio between binary components, the spin magnitude of the more massive component and the spin misalignment from the orbital angular momentum axis; therefore in the case of asymmetric binary systems of type BH-NS the detection efficiency can decrease significantly if non-precessing waveforms are used in the search [10].

Furthermore, even when non-spinning templates can match spinning waveforms with high SNR, they are unable to accurately estimate the mass parameters of the source and they completely lack the ability to estimate spin parameters.

2.7.3 Phenomenological Spinning Templates - BCV

The dynamical evolution of spinning systems is complicated by spin-orbit and spin-spin interactions which cause precession of the orbital plane and therefore modulations in the phase and amplitude of the gravitational waves emitted; templates are in fact described by a large number of parameters (up to 17) and the high dimensionality of the parameter space implies very large template banks and therefore excessive computational costs.

To circumvent this problem, approximated phenomenological frequency-domain waveforms have been introduced which model GWs emitted by spinning binaries in terms of a smaller number of non-physical phenomenological parameters [9, 11, 12]. In particular Buonanno, Vallisneri and Chen (BCV) developed a family of phenomenological templates for spinning binaries (BVCSpin) in the precessing convention, described by as low as three intrinsic parameters [16].

The template is constructed directly in the frequency domain and the detector

strain is given by

$$h(\psi_{NM}, \mathcal{A}_k, t_0, \alpha_k; f) = \left[\sum_{k=1}^n (\alpha_k + i\alpha_{k+n}) \mathcal{A}_k(f) \right] e^{2\pi i f t_0} e^{i\psi_{NM}(f)}, \quad f > 0 \quad (2.83)$$

where $\mathcal{A}_k(f)$ are real *amplitude functions*, the α_k are their real coefficients and t_0 is the time of arrival of the GW signals. The function ψ_{NM} represents the phase of the unmodulated carrier signal; it is given as a series in the power of $f^{1/3}$

$$\psi_{NM}(f) = f^{-5/3} (\psi_0 + \psi_{1/2} f^{1/3} + \psi_1 f^{2/3} + \psi_{2/3} f + \dots) \quad (2.84)$$

In particular the family called $(\psi_0 \psi_{3/2} \mathcal{B})_6$ is given by

$$h = f^{-7/6} [(\alpha_1 + i\alpha_2) + (\alpha_3 + i\alpha_4) \cos(\mathcal{B} f^{-2/3}) + (\alpha_5 + i\alpha_6) \sin(\mathcal{B} f^{-2/3})] \times \theta(f_{\text{cut}} - f) e^{2\pi i f t_0} \exp i [\psi_0 f^{-5/3} + \psi_{3/2} f^{-2/3}] \quad (2.85)$$

where only ψ_i , f_{cut} and \mathcal{B} are phenomenological intrinsic parameters, while the α_k and t_0 are extrinsic parameters.

This family of templates can actually model remarkably well the dynamical and precessional effects on the GW signals from spinning BH-BH and BH-NS binaries, however it lacks the ability to estimate the physical parameters of the source, since the relation between actual mass and spin parameters and the phenomenological parameters that describe the templates are not well defined.

A comparison with the standard non-spinning SPA templates described in the previous section has recently shown that, while BCVSpin has a good efficiency in recovering simulated spinning GW signals injected in the data, it has also a high *false-alarm rate* (the rate of events caused by noise artifacts in the output of the detector). This is due to the fact that phenomenological templates effectively search over a much larger parameter space and therefore they tend to match a much higher number of non-physical signals.

In order to keep the false alarm rate below a chosen threshold, the SNR threshold must be set to a higher value, consequently lowering the overall efficiency; under this restriction, by requiring BCVSpin and non-spinning SPA templates to have the same false alarm rate, BCVSpin has shown slightly lower efficiencies than SPA in recovering injected signals [62].

2.7.4 Physical Spinning Templates

To reach the double objective of achieving lower false alarm rates and having more accurate estimation of physical parameter, a family of physical templates has been proposed by Pan, Buonanno, Chen and Vallisneri [33].

2. The Detection of Gravitational Waves

This family is aimed to model gravitational waves emitted by binaries with only one significantly spinning object and for which the GW signal is emitted in the band of sensitivity of the detector during the phase of adiabatic inspiral; for LIGO this corresponds to binaries with total mass $M \lesssim 15M_\odot$. In order for the single-spin assumption to be valid we consider only asymmetric binaries with mass ratio $m_1/m_2 > 2$, therefore we restrict the mass parameters in the regions $6 < m_1 < 14M_\odot$, $1 < m_2 < 3M_\odot$. The prototypical binary of this kind is the BH-NS binary, where the massive BH carries (possibly maximal) spin while the NS's spin is negligible.

To develop our search strategy using Physical Templates we will make a specific choice of the radiation frame and define the components of the basis vectors $\{\mathbf{e}_x^R, \mathbf{e}_y^R, \mathbf{e}_z^R\}$ in the source frame to be

$$\begin{aligned}\mathbf{e}_x^R &= -\mathbf{e}_x^S \sin \varphi + \mathbf{e}_y^S \cos \varphi \\ \mathbf{e}_y^R &= -\mathbf{e}_x^S \cos \Theta \cos \varphi - \mathbf{e}_y^S \cos \Theta \sin \varphi + \mathbf{e}_z^S \sin \Theta \\ \mathbf{e}_z^R &= +\mathbf{e}_x^S \sin \Theta \cos \varphi + \mathbf{e}_y^S \sin \Theta \sin \varphi + \mathbf{e}_z^S \cos \Theta \equiv \hat{\mathbf{N}}\end{aligned}\tag{2.86}$$

where $\hat{\mathbf{N}}$ is the direction of wave propagation and Θ, φ the corresponding angles in the *source frame*.

If we now restrict ourselves to the quasicircular motion approximation and consider the radiative gravitational field h_{ij} given by Eq.(1.43), the strain induced in the detector is once again given by Eq.(2.66) as

$$h(t) = F_+ h_+(t) + F_\times h_\times(t)\tag{2.87}$$

However we will find it more useful to rewrite $h(t)$ differently, by introducing two STF 3-tensors \mathbf{Q} and \mathbf{P} .

We then define the *wave-generation* tensor

$$Q^{ij} \equiv \frac{\mu}{R} \frac{M}{r} \mathcal{Q}_c^{ij}\tag{2.88}$$

where \mathcal{Q}_c^{ij} is given by (1.42), and the *detector projection* tensor

$$P_{ij} \equiv [\mathbf{T}_+]_{ij} F_+ + [\mathbf{T}_\times]_{ij} F_\times\tag{2.89}$$

The detector strain can then be re-written as

$$h = \underbrace{-\frac{2\mu}{R} \frac{M}{r} \left([\mathbf{e}_+]^{ij} \cos 2(\Phi + \Phi_0) + [\mathbf{e}_\times]^{ij} \sin 2(\Phi + \Phi_0) \right)}_{Q^{ij}} \underbrace{\left([\mathbf{T}_+]_{ij} F_+ + [\mathbf{T}_\times]_{ij} F_\times \right)}_{P_{ij}}\tag{2.90}$$

where sum over repeated indices i, j is implied.

In the precessing convention \mathbf{Q} depends on the time evolution of the dynamical variables and on parameters intrinsic to the binary only while \mathbf{P} depends on directional parameters only. As a matter of fact \mathbf{Q} expresses the components of the quadrupole moment, which depend only on the evolution of the binary inside the source frame, while \mathbf{P} expresses the projection of the quadrupole moment onto the radiation frame (TT gauge) and onto the antisymmetric mode of the detector, which depend only on the relative orientation between the source frame and the detector.

Chapter 3

The Physical Template Family of Spinning Waveforms - PTF

3.1 Symmetric Trace-Free Expansion of the GW-Induced Strain

The strain (2.90) of a ground-based interferometric detector to the GW signal can be rewritten in compact form as

$$h[\lambda^A; t] = h[M, \eta, \kappa_1, \chi_1, \Theta, \varphi, \phi, \theta, \psi, \Phi_0, t_0; t] \equiv Q^{ij} P_{ij}; \quad (3.1)$$

where λ_A is the set of all parameters h depends on; specifically $\eta \equiv (m_1 m_2)/M^2$ is the *symmetric mass ratio*, $\chi_1 \equiv |S_1|/m_1^2$ is the *spin magnitude* associated with the mass m_1 , $\kappa_1 \equiv \hat{\mathbf{S}}_1 \cdot \hat{\mathbf{L}}_N$ defines the angle between the spin vector and the orbital plane, t_0 is the *time of arrival* and t is the time.

In terms of matched-filtering, four of these parameters ($\Theta, \varphi, \Phi_0, t_0$) are *extrinsic parameters* and can be searched over algebraically while the remaining seven ($M, \eta, \kappa_1, \chi_1, \theta, \phi, \psi$) are *intrinsic parameters* and therefore we would need a different template for every point in this 7-dimensional space. A 7-dimensional template bank is extremely computationally expensive, therefore we need to reparametrize the waveform so as to reduce the total number of parameters and hopefully convert some intrinsic parameters to extrinsic ones.

The objects appearing on the right hand side of Eq.(3.1) are the STF tensors defined in eqs.(2.88)-(2.89) and here we rewrite explicitly their dependence on all the parameters

$$Q^{ij}[M, \eta, \chi_1, \kappa_1; \Phi_0, t_0; t] = -\frac{2\mu}{R} \frac{M}{r} \left[[\mathbf{e}_+]^{ij} \cos 2(\Phi + \Phi_0) + [\mathbf{e}_\times]^{ij} \sin 2(\Phi + \Phi_0) \right] \quad (3.2)$$

3.1. Symmetric Trace-Free Expansion of the GW-Induced Strain

$$P_{ij}[\Theta, \varphi; \theta, \phi, \psi] = [\mathbf{T}_+]_{ij} F_+ + [\mathbf{T}_\times]_{ij} F_\times \quad (3.3)$$

where in the quasi-circular orbit approximation we can set $M/r = (\pi M f)^{2/3}$. Now we make use of the fact that the *antenna patterns* (2.64) can be rewritten as

$$\begin{aligned} F_+ &= \frac{1}{2}(1 + \cos^2 \theta) \cos 2\phi \cos 2\psi - \cos \theta \sin 2\phi \sin 2\psi \equiv F \cos \alpha \\ F_\times &= \frac{1}{2}(1 + \cos^2 \theta) \cos 2\phi \sin 2\psi + \cos \theta \sin 2\phi \cos 2\psi \equiv F \sin \alpha \end{aligned} \quad (3.4)$$

where $F \equiv \sqrt{F_+^2 + F_\times^2}$ and $\alpha \equiv \alpha[\theta, \phi, \psi]$; this way we reduced the implicit dependence of h on three angles (θ, ϕ, ψ) to the explicit dependence on only one angle α which can now be considered an extrinsic parameter.

The factor F enters h as a multiplicative constant and, if we consider normalized templates and signals, we can set $F = 1$ to get

$$P_{ij} = [\mathbf{T}_+]_{ij} \cos \alpha + [\mathbf{T}_\times]_{ij} \sin \alpha \quad (3.5)$$

Both the Q_{ij} and the P_{ij} are *symmetric trace-free (STF)* rank-2 tensor and any such tensor can be expanded as follows [14]

$$A_{ij} = \sum_{m=-2}^{m=2} F^{2m} \mathcal{Y}_{ij}^{2m} \quad (3.6)$$

where $F^{2m} = \frac{8\pi}{15} A^{kl} \mathcal{Y}_{kl}^{2m}$ and \mathcal{Y}_{ij}^{2m} is the standard STF basis, given by

$$\mathcal{Y}_{ij}^{2m} q^i q^j = Y^{2m}(\hat{\mathbf{q}}) \quad (3.7)$$

where $Y^{2m}(\hat{\mathbf{q}})$ are the usual $l = 2$ spherical harmonics and $\hat{\mathbf{q}}$ is unit vector.

If we now introduce a new orthonormal STF basis $(M^I)_{ij}$, $I = 1, \dots, 5$ given by [33]

$$(M^1)_{ij} = \sqrt{\frac{4\pi}{15}} (\mathcal{Y}_{ij}^{22} + \mathcal{Y}_{ij}^{2-2}) \quad (3.8a)$$

$$(M^2)_{ij} = -i\sqrt{\frac{4\pi}{15}} (\mathcal{Y}_{ij}^{22} - \mathcal{Y}_{ij}^{2-2}) \quad (3.8b)$$

$$(M^3)_{ij} = -\sqrt{\frac{4\pi}{15}} (\mathcal{Y}_{ij}^{21} - \mathcal{Y}_{ij}^{2-1}) \quad (3.8c)$$

$$(M^4)_{ij} = i\sqrt{\frac{4\pi}{15}} (\mathcal{Y}_{ij}^{21} + \mathcal{Y}_{ij}^{2-1}) \quad (3.8d)$$

3. The Physical Template Family of Spinning Waveforms - PTF

$$(M^5)_{ij} = -\sqrt{\frac{8\pi}{15}} \mathcal{Y}_{ij}^{20} \quad (3.8e)$$

we can expand the STF tensors Q^{ij}, P^{ij} as follows

$$Q_{ij} = \sum_{I=1}^5 Q_I(M^I)_{ij} = \sum_{m=-2}^{m=2} F_{(Q)}^{2m} \mathcal{Y}_{ij}^{2m} \quad (3.9a)$$

$$P_{ij} = \sum_{I=1}^5 P_I(M^I)_{ij} = \sum_{m=-2}^{m=2} F_{(P)}^{2m} \mathcal{Y}_{ij}^{2m} \quad (3.9b)$$

Here we derive the explicit expression of the components Q_I and P_I obtained by comparing the two expansions above to obtain

$$\begin{aligned} Q_1 &= \sqrt{\frac{4\pi}{15}} Q^{kl} (\mathcal{Y}_{kl}^{22} + \mathcal{Y}_{kl}^{2-2})^* = Q^{kl} (M^1)_{kl}^* = \\ &= -\sqrt{2} \frac{\mu}{R} \frac{M}{r} [\cos 2(\Phi + \Phi_0) (e_{1x}^2 + e_{2y}^2 - e_{2x}^2 - e_{1y}^2) \\ &\quad + 2 \sin 2(\Phi + \Phi_0) (e_{1x}e_{2x} - e_{1y}e_{2y})] \end{aligned} \quad (3.10a)$$

$$\begin{aligned} Q_2 &= i\sqrt{\frac{4\pi}{15}} Q^{kl} (\mathcal{Y}_{kl}^{22} - \mathcal{Y}_{kl}^{2-2})^* = Q^{kl} (M^2)_{kl}^* = \\ &= -2\sqrt{2} \frac{\mu}{R} \frac{M}{r} [\cos 2(\Phi + \Phi_0) (e_{1x}e_{1y} - e_{2x}e_{2y}) + \sin 2(\Phi + \Phi_0) (e_{1x}e_{2y} + e_{1y}e_{2x})] \end{aligned} \quad (3.10b)$$

$$\begin{aligned} Q_3 &= -\sqrt{\frac{4\pi}{15}} Q^{kl} (\mathcal{Y}_{kl}^{21} - \mathcal{Y}_{kl}^{2-1})^* = Q^{kl} (M^3)_{kl}^* = \\ &= -2\sqrt{2} \frac{\mu}{R} \frac{M}{r} [\cos 2(\Phi + \Phi_0) (e_{1x}e_{1z} - e_{2x}e_{2z}) + \sin 2(\Phi + \Phi_0) (e_{1x}e_{2z} + e_{1z}e_{2x})] \end{aligned} \quad (3.10c)$$

$$\begin{aligned} Q_4 &= -i\sqrt{\frac{4\pi}{15}} Q^{kl} (\mathcal{Y}_{kl}^{21} + \mathcal{Y}_{kl}^{2-1})^* = Q^{kl} (M^4)_{kl}^* = \\ &= -2\sqrt{2} \frac{\mu}{R} \frac{M}{r} [\cos 2(\Phi + \Phi_0) (e_{1y}e_{1z} - e_{2y}e_{2z}) + \sin 2(\Phi + \Phi_0) (e_{1y}e_{2z} + e_{1z}e_{2y})] \end{aligned} \quad (3.10d)$$

$$\begin{aligned} Q_5 &= -\sqrt{\frac{8\pi}{15}} Q^{kl} (\mathcal{Y}_{kl}^{20})^* = Q^{kl} (M^5)_{kl}^* = \\ &= -\sqrt{\frac{2}{3}} \frac{\mu}{R} \frac{M}{r} [\cos 2(\Phi + \Phi_0) (2e_{2z}^2 - 2e_{1z}^2 + e_{1x}^2 + e_{1y}^2 - e_{2x}^2 - e_{2y}^2)] \end{aligned}$$

3.1. Symmetric Trace-Free Expansion of the GW-Induced Strain

$$+ 2 \sin 2(\Phi + \Phi_0) (e_{1x}e_{2x} + e_{1y}e_{2y} - 2e_{1z}e_{2z})] \quad (3.10e)$$

and similarly

$$P_1 = P^{kl} (M^1)_{kl}^* = \frac{F}{\sqrt{2}} \left[-\frac{1}{2} \cos \alpha \cos(2\varphi) (3 + \cos(2\Theta)) + \sin \alpha \cos \Theta \sin(2\varphi) \right] \quad (3.11a)$$

$$P_2 = P^{kl} (M^2)_{kl}^* = -\sqrt{2} F [\cos \alpha \cos \varphi \sin \varphi (1 + \cos^2 \Theta) + \sin \alpha \cos \Theta \cos(2\varphi)] \quad (3.11b)$$

$$P_3 = P^{kl} (M^3)_{kl}^* = \sqrt{2} F [\cos \alpha \cos \varphi \sin \Theta \cos \Theta - \sin \alpha \sin \Theta \sin \varphi] \quad (3.11c)$$

$$P_4 = P^{kl} (M^4)_{kl}^* = \sqrt{2} F [\cos \alpha \sin \varphi \sin \Theta \cos \Theta + \sin \alpha \sin \Theta \cos \varphi] \quad (3.11d)$$

$$P_5 = P^{kl} (M^5)_{kl}^* = \sqrt{\frac{3}{2}} F \cos \alpha \sin^2 \Theta \quad (3.11e)$$

Now we can factorize out the initial phase Φ_0 in Q^{ij} by defining [33]

$$Q_0^{ij} = Q^{ij}(\Phi_0 = 0) \quad (3.12a)$$

$$Q_{\pi/2}^{ij} = Q^{ij}(\Phi_0 = \pi/4) \quad (3.12b)$$

then we have

$$Q^{ij} = Q_0^{ij} \cos(2\Phi_0) + Q_{\pi/2}^{ij} \sin(2\Phi_0) = \sum_{I=1}^5 [Q_0^I \cos(2\Phi_0) + Q_{\pi/2}^I \sin(2\Phi_0)] (M_I)^{ij} \quad (3.13)$$

Upon defining $A(t) \equiv \frac{\mu M}{R r(t)} = \frac{\mu}{R} (\pi M f(t))^{2/3}$ we can write the components Q_0^I and $Q_{\pi/2}^I$ as

$$Q_0^1(t) = -\sqrt{2} A(t) \left\{ \cos(2\Phi(t)) [e_{1x}(t)^2 + e_{2y}(t)^2 - e_{2x}(t)^2 - e_{1y}(t)^2] + 2 \sin(2\Phi(t)) [e_{1x}(t)e_{2x}(t) - e_{1y}(t)e_{2y}(t)] \right\} \quad (3.14a)$$

$$Q_0^2(t) = -2\sqrt{2} A(t) \left\{ \cos(2\Phi(t)) [e_{1x}(t)e_{1y}(t) - e_{2x}(t)e_{2y}(t)] + \sin(2\Phi(t)) [e_{1x}(t)e_{2y}(t) + e_{1y}(t)e_{2x}(t)] \right\} \quad (3.14b)$$

$$Q_0^3(t) = -2\sqrt{2} A(t) \left\{ \cos(2\Phi(t)) [e_{1x}(t)e_{1z}(t) - e_{2x}(t)e_{2z}(t)] \right\}$$

$$+ \sin(2\Phi(t)) [e_{1x}(t)e_{2z}(t) + e_{1z}(t)e_{2x}(t)] \} \quad (3.14c)$$

$$Q_0^4(t) = -2\sqrt{2} A(t) \left\{ \begin{aligned} &\cos(2\Phi(t)) [e_{1y}(t)e_{1z}(t) - e_{2y}(t)e_{2z}(t)] \\ &+ \sin(2\Phi(t)) [e_{1y}(t)e_{2z}(t) + e_{1z}(t)e_{2y}(t)] \end{aligned} \right\} \quad (3.14d)$$

$$Q_0^5(t) = -\sqrt{\frac{2}{3}} A(t) \left\{ \begin{aligned} &\cos(2\Phi(t)) [2e_{2z}(t)^2 - 2e_{1z}(t)^2 + e_{1x}(t)^2 + e_{1y}(t)^2 - e_{2x}(t)^2 - e_{2y}(t)^2] \\ &+ 2\sin(2\Phi(t)) [e_{1x}(t)e_{2x}(t) + e_{1y}(t)e_{2y}(t) - 2e_{1z}(t)e_{2z}(t)] \end{aligned} \right\} \quad (3.14e)$$

and

$$Q_{\pi/2}^1(t) = -\sqrt{2} A(t) \left\{ \begin{aligned} &2\cos(2\Phi(t)) [e_{1x}(t)e_{2x}(t) - e_{1y}(t)e_{2y}(t)] \\ &- \sin(2\Phi(t)) [e_{1x}(t)^2 + e_{2y}(t)^2 - e_{2x}(t)^2 - e_{1y}(t)^2] \end{aligned} \right\} \quad (3.15a)$$

$$Q_{\pi/2}^2(t) = -2\sqrt{2} A(t) \left\{ \begin{aligned} &\cos(2\Phi(t)) [e_{1x}(t)e_{2y}(t) + e_{1y}(t)e_{2x}(t)] \\ &- \sin(2\Phi(t)) [e_{1x}(t)e_{1y}(t) - e_{2x}(t)e_{2y}(t)] \end{aligned} \right\} \quad (3.15b)$$

$$Q_{\pi/2}^3(t) = -2\sqrt{2} A(t) \left\{ \begin{aligned} &\cos(2\Phi(t)) [e_{1x}(t)e_{2z}(t) + e_{1z}(t)e_{2x}(t)] \\ &- \sin(2\Phi(t)) [e_{1x}(t)e_{1z}(t) - e_{2x}(t)e_{2z}(t)] \end{aligned} \right\} \quad (3.15c)$$

$$Q_{\pi/2}^4(t) = -2\sqrt{2} A(t) \left\{ \begin{aligned} &\cos(2\Phi(t)) [e_{1y}(t)e_{2z}(t) + e_{1z}(t)e_{2y}(t)] \\ &- \sin(2\Phi(t)) [e_{1y}(t)e_{1z}(t) - e_{2y}(t)e_{2z}(t)] \end{aligned} \right\} \quad (3.15d)$$

$$Q_{\pi/2}^5(t) = -\sqrt{\frac{2}{3}} A(t) \left\{ \begin{aligned} &2\cos(2\Phi(t)) [e_{1x}(t)e_{2x}(t) + e_{1y}(t)e_{2y}(t) - 2e_{1z}(t)e_{2z}(t)] \\ &- \sin(2\Phi(t)) [2e_{2z}(t)^2 - 2e_{1z}(t)^2 + e_{1x}(t)^2 + e_{1y}(t)^2 - e_{2x}(t)^2 - e_{2y}(t)^2] \end{aligned} \right\} \quad (3.15e)$$

where $M = m_1 + m_2$ is the total mass of the binary measured in solar masses, $\mu = m_1 m_2 / M$ is the reduced mass, D is the distance of the binary from the detector measured in units of Mpc, $\omega(t)$ is the orbital frequency, $\Phi(t)$ is the orbital phase and $\mathbf{e}_1(t), \mathbf{e}_2(t)$ are unit vectors which form a basis for the instantaneous orbital plane.

Finally we can rewrite the detector strain (2.90) as [33]

$$h[M, \eta, \kappa_1, \chi_1, \Theta, \varphi, \alpha] = P_I [Q_0^I \cos(2\Phi_0) + Q_{\pi/2}^I \sin(2\Phi_0)] \quad (3.16)$$

and it now depends only on 4 intrinsic parameters ($M, \eta, \kappa_1, \chi_1$) through the Q_I 's and on 5 extrinsic parameters ($t_0, \Phi_0, \alpha, \Theta, \varphi$), three of which through the P_I 's. The time evolution of $h(t)$ can be computed given the time evolution of $\mathbf{e}_1(t), \mathbf{e}_2(t)$ and of the orbital phase $\Phi(t)$.

Since we have been able to factorize out the initial phase, the strain given by (3.16) has now a particularly simple and convenient form; in fact, we note that we can rewrite h into a form that is reminiscent of that for non-spinning low-mass templates by setting

$$h_c^{PTF}(t) = P_I Q_0^I(t) \quad (3.17)$$

$$h_s^{PTF}(t) = P_I Q_{\pi/2}^I(t) \quad (3.18)$$

from which

$$h(t) = h_c^{PTF}(t) \cos(2\Phi_0) + h_s^{PTF}(t) \sin(2\Phi_0) \quad (3.19)$$

3.2 SNR Statistic

We recall that the strain of a ground-based interferometric detector to the GW signal emitted by a single spin binary can be written as

$$\begin{aligned} h[\lambda^A; t] &= h[\alpha, \Theta, \varphi, M, \eta, \chi_1, \kappa_1; \Phi_0, t_0; t] \\ &= P_I[\alpha, \Theta, \varphi] (Q_0^I[M, \eta, \chi_1, \kappa_1; t_0; t] \cos(2\Phi_0) + Q_{\pi/2}^I[M, \eta, \chi_1, \kappa_1; t_0; t] \sin(2\Phi_0)) \end{aligned} \quad (3.20)$$

where λ^A are all the parameters the strain depends on; $M = m_1 + m_2$ is the *total mass* of the binary measured in solar masses, $\eta \equiv (m_1 m_2) / M^2$ is the *symmetric mass ratio*, $\chi_1 \equiv |S_1| / m_1^2$ is the *spin magnitude* associated with the component of mass m_1 , $\kappa_1 \equiv \hat{\mathbf{S}}_1 \cdot \hat{\mathbf{L}}_N$ defines the angle between the spin vector and the orbital plane, t_0 is the *time of arrival*, (Θ, φ) are the angles which define the direction of wave propagation $\hat{\mathbf{N}}$ in the *source frame*, α is a function of the orientation

3. The Physical Template Family of Spinning Waveforms - PTF

angles (ϕ, θ, ψ) , Φ_0 is the initial orbital phase and the components $P_I, Q_{0,\pi/2}^I$ are given by equations (3.11), (3.14)-(3.15). Among the nine parameters λ^A , five are extrinsic parameters $(t_0, \Phi_0, \alpha, \Theta, \varphi) \equiv \Sigma^\alpha$ while four are intrinsic parameters $(M, \eta, \kappa_1, \chi_1) \equiv X^i$. We now wish to evaluate the normalized signal-to-noise ratio between the detector output $s(t)$ and a given template $h(t)$ defined as

$$\rho[s, h(\lambda^A)] = \frac{\langle s, h(\lambda^A) \rangle}{\sqrt{\langle h(\lambda^A), h(\lambda^A) \rangle}} \quad (3.21)$$

which must then be maximized over the extrinsic parameters to obtain the *maximized SNR*.

$$\rho_{\Sigma^\alpha} = \max_{\Sigma^\alpha} \frac{\langle s, h(X^i, \Sigma^\alpha) \rangle}{\sqrt{\langle h(X^i, \Sigma^\alpha), h(X^i, \Sigma^\alpha) \rangle}} \quad (3.22)$$

and substituting expression (3.16) for h we obtain

$$\rho_{\Sigma^\alpha} = \max_{t_0, \Phi_0, \Theta, \varphi, \alpha} \left[\frac{P_I \left(\langle s, Q_0^I \rangle_{t_0} \cos 2\Phi_0 + \langle s, Q_{\pi/2}^I \rangle_{t_0} \sin 2\Phi_0 \right)}{\sqrt{P_I P_J \langle Q_0^I \cos 2\Phi_0 + Q_{\pi/2}^I \sin 2\Phi_0, Q_0^J \cos 2\Phi_0 + Q_{\pi/2}^J \sin 2\Phi_0 \rangle}} \right] \quad (3.23)$$

where the subscript t_0 denotes the dependence of the signal-template inner product on the time of arrival parameter of the templates.

We can now make an approximation noting that the template components $P_I Q_0^I$ and $P_I Q_{\pi/2}^I$ are nearly orthogonal and have approximately the same signal power, therefore we can assume that [33]

$$\langle P_I Q_0^I, P_J Q_{\pi/2}^J \rangle \simeq 0 \quad (3.24)$$

$$\langle P_I Q_0^I, P_J Q_0^J \rangle \simeq \langle P_I Q_{\pi/2}^I, P_J Q_{\pi/2}^J \rangle \quad (3.25)$$

This approximation is accurate in the phase of adiabatic inspiral, i.e. when the time scales for the radiation-reaction-induced evolution of frequency and for the precession-induced evolution of phase and amplitude modulation are both much longer than the orbital period. More precisely the approximation above is valid up to leading-order stationary-phase approximation. Under this hypothesis the denominator of equation (3.23) becomes

$$\sqrt{P_I P_J \left[\langle Q_0^I, Q_0^J \rangle \cos^2(2\Phi_0) + \langle Q_{\pi/2}^I, Q_{\pi/2}^J \rangle \sin^2(2\Phi_0) \right]} = \quad (3.26a)$$

$$\sqrt{P_I P_J \langle Q_0^I, Q_0^J \rangle \left[\cos^2(2\Phi_0) + \sin^2(2\Phi_0) \right]} = \sqrt{P_I P_J \langle Q_0^I, Q_0^J \rangle} \quad (3.26b)$$

therefore the expression for the maximized SNR becomes

$$\rho_{\Sigma^\alpha} = \max_{t_0, \Phi_0, \Theta, \varphi, \alpha} \left[\frac{P_I \left(\langle s, Q_0^I \rangle_{t_0} \cos 2\Phi_0 + \langle s, Q_{\pi/2}^I \rangle_{t_0} \sin 2\Phi_0 \right)}{\sqrt{P_I P_J \langle Q_0^I, Q_0^J \rangle}} \right] \quad (3.27)$$

Now we can easily find the maximum over the initial phase Φ_0 by summing in quadrature the matched filter output for two orthogonal phases $2\Phi_0 = 0$ and $2\Phi_0 = \pi/2$. As a matter of fact we need to maximize the function

$$f(\Phi_0) = P_I \left(\langle s, Q_0^I \rangle_{t_0} \cos 2\Phi_0 + \langle s, Q_{\pi/2}^I \rangle_{t_0} \sin 2\Phi_0 \right) \equiv C_c \cos 2\Phi_0 + C_s \sin 2\Phi_0 \quad (3.28)$$

with

$$\begin{cases} C_c \equiv P_I \langle s, Q_0^I \rangle_{t_0} \\ C_s \equiv P_I \langle s, Q_{\pi/2}^I \rangle_{t_0} \end{cases} \quad (3.29)$$

by setting

$$\frac{df}{d\Phi_0} = -2C_c \sin 2\Phi_0 + 2C_s \cos 2\Phi_0 = 0 \quad \implies \quad (3.30a)$$

$$\sin(2\Phi_0^{max}) = \frac{C_s}{C_c} \cos(2\Phi_0^{max}) = \frac{C_s}{C_c} \sqrt{1 - \sin^2(2\Phi_0^{max})} \quad \implies \quad (3.30b)$$

$$\sin(2\Phi_0^{max}) = \frac{C_s}{\sqrt{C_c^2 + C_s^2}}, \quad \cos(2\Phi_0^{max}) = \frac{C_c}{\sqrt{C_c^2 + C_s^2}} \quad \implies \quad (3.30c)$$

$$f(2\Phi_0^{max}) = \frac{C_c^2}{\sqrt{C_c^2 + C_s^2}} + \frac{C_s^2}{\sqrt{C_c^2 + C_s^2}} = \sqrt{C_c^2 + C_s^2} \quad (3.30d)$$

and we obtain for the SNR

$$\rho_{\Sigma^\alpha} = \max_{t_0, \Theta, \varphi, \alpha} \frac{\sqrt{[P_I \langle s, Q_0^I \rangle_{t_0}]^2 + [P_I \langle s, Q_{\pi/2}^I \rangle_{t_0}]^2}}{\sqrt{P_I P_J \langle Q_0^I, Q_0^J \rangle}} \quad (3.31a)$$

$$= \max_{t_0, \Theta, \varphi, \alpha} \sqrt{\frac{P_I P_J \left[\langle s, Q_0^I \rangle_{t_0} \langle s, Q_0^J \rangle_{t_0} + \langle s, Q_{\pi/2}^I \rangle_{t_0} \langle s, Q_{\pi/2}^J \rangle_{t_0} \right]}{P_I P_J \langle Q_0^I, Q_0^J \rangle}} \quad (3.31b)$$

$$\equiv \max_{t_0, \Theta, \varphi, \alpha} \sqrt{\frac{P_I P_J A^{IJ}}{P_I P_J B^{IJ}}} \equiv \max_{t_0, \Theta, \varphi, \alpha} \rho_{\Phi_0} \quad (3.31c)$$

where symmetric the matrices A^{IJ} and B^{IJ} are defined as

$$A^{IJ}(t_0) = \langle s, Q_0^I \rangle_{t_0} \langle s, Q_0^J \rangle_{t_0} + \langle s, Q_{\pi/2}^I \rangle_{t_0} \langle s, Q_{\pi/2}^J \rangle_{t_0} \quad (3.32)$$

3. The Physical Template Family of Spinning Waveforms - PTF

$$B^{IJ} = \langle Q_0^I, Q_0^J \rangle \quad (3.33)$$

Writing out explicitly the inner products in these expressions above we get

$$\begin{aligned} A^{IJ}(t_0) &= 4 \int_{-\infty}^{+\infty} \frac{\tilde{n}(f) \tilde{Q}_0^{I*}(f)}{S_n(|f|)} e^{2\pi i f t_0} df \times \int_{-\infty}^{+\infty} \frac{\tilde{n}(f') \tilde{Q}_0^{J*}(f')}{S_n(|f'|)} e^{2\pi i f' t_0} df' \\ &\quad + 4 \int_{-\infty}^{+\infty} \frac{\tilde{s}(f) \tilde{Q}_{\pi/2}^{I*}(f)}{S_n(|f|)} e^{2\pi i f t_0} df \times \int_{-\infty}^{+\infty} \frac{\tilde{s}(f') \tilde{Q}_{\pi/2}^{J*}(f')}{S_n(|f'|)} e^{2\pi i f' t_0} df' \\ &= 4 \int_{-\infty}^{+\infty} \int_{-\infty}^{+\infty} \frac{\tilde{s}(f) \tilde{s}^*(f') \tilde{Q}_0^{I*}(f) \tilde{Q}_0^J(f')}{S_n(|f|) S_n(|f'|)} e^{2\pi i (f-f') t_0} df df' \\ &\quad + 4 \int_{-\infty}^{+\infty} \int_{-\infty}^{+\infty} \frac{\tilde{s}(f) \tilde{s}^*(f') \tilde{Q}_{\pi/2}^{I*}(f) \tilde{Q}_{\pi/2}^J(f')}{S_n(|f|) S_n(|f'|)} e^{2\pi i (f-f') t_0} df df' \quad (3.34) \end{aligned}$$

$$\begin{aligned} B^{IJ} &= 2 \int_{-\infty}^{\infty} \frac{\tilde{Q}_0^I(f) \tilde{Q}_0^{J*}(f)}{S_n(|f|)} df = 4 \Re \int_0^{\infty} \frac{\tilde{Q}_0^I(f) \tilde{Q}_0^{J*}(f)}{S_n(f)} df \\ &= 4 \Re \int_0^{\infty} \frac{\tilde{Q}_0^{I*}(f) \tilde{Q}_0^J(f)}{S_n(f)} df \quad (3.35) \end{aligned}$$

Now the signal-to-noise ratio depends on the remaining extrinsic parameters $(\Theta, \varphi, \alpha)$ through the P_I 's in a simple way; evidently however the five components of P_I are not all independent since they are functions of three parameters only and must therefore satisfy two constraints [33]. We start by noting that, given the expression of Eq.(3.31c), we can rescale the components P_I 's without affecting the value of $\rho_{\Sigma\alpha}$, in particular we can impose the constraint

$$P_I P_J B^{IJ} = 1 \quad (3.36)$$

The second constraint can be derived by recalling that P_{ij} , given by Eq.(3.5), is the polarization tensor for a plane gravitational-wave propagating along the direction vector

$$\hat{N}^i = (\sin \Theta \cos \varphi, \sin \Theta \sin \varphi, \cos \Theta) \quad (3.37)$$

and, because gravitational-waves are transverse, P_{ij} must admit \hat{N}^i as an eigenvector with null eigenvalue; it then follows that the second constraint is given by

$$\det P_{ij} = 0 \quad (3.38)$$

Therefore the maximization of ρ_{Φ_0} over $(\Theta, \varphi, \alpha)$ can be thought of as the maximization with respect to the five-dimensional vector P_I , constrained to the three dimensional submanifold $P_I(\Theta, \varphi, \alpha)$.

However, as a first step, we can choose to perform an *unconstrained* maximization by considering the P_I 's as free parameters and then discard the times t_0 for

which the unconstrained match $\rho'_{\Sigma\alpha}$ is below a certain threshold; doing so we can save a great deal of computational power and speed up the search.

For the purpose of developing a fast search using PTF templates, the unconstrained maximization can be the only stage actually performed if we are then able to discard triggers which correspond to unphysical values of the parameters a posteriori, by checking whether the constraint (3.38) is satisfied or not up to a chosen accuracy. In the following of this thesis we will only develop and test the unconstrained detection statistic, leaving the (possible) development of a constrained search to future studies.

3.2.1 Unconstrained Detection Statistic

The unconstrained SNR is therefore given by

$$\rho'_{\Sigma\alpha} = \max_{P_I} \rho_{\Phi_0} = \max_{P_I} \sqrt{\frac{P_I P_J A^{IJ}}{P_I P_J B^{IJ}}} = \max_{P_I} \sqrt{\frac{A^{IJ} P_I P_J}{B^{IJ} P_I P_J}} \quad (3.39)$$

Since the constraint (3.36) does not affect the value of the $\rho'_{\Sigma\alpha}$ but simply enforces the normalization of the templates, we can rewrite the partially constrained maximization problem as

$$\begin{cases} (\rho'_{\Sigma\alpha})^2 = \max_{P_I} (\rho_{\Phi_0})^2 = \max_{P_I} (A^{IJ} P_I P_J) \\ B^{IJ} P_I P_J - 1 = 0 \end{cases} \quad (3.40)$$

and find the maximum over the P_I 's using the method of Lagrangian multipliers to find the stationary points of the function [33]

$$g(\mathbf{P}) = A^{IJ} P_I P_J - \lambda (B^{IJ} P_I P_J - 1) \quad (3.41)$$

to get

$$\frac{\partial g(\mathbf{P})}{\partial P_I} = (A^{IJ} - \lambda B^{IJ}) P_J = 0 \quad (3.42)$$

and multiplying from the left by \mathbf{B}^{-1} we get

$$(\mathbf{B}^{-1} \mathbf{A} - \lambda \mathbf{I}) \mathbf{P} = 0 \quad (3.43)$$

which is the eigenvalue problem for the matrix $\mathbf{B}^{-1} \mathbf{A}$; this has solutions only for λ corresponding to an eigenvalue and the vector \mathbf{P} being the corresponding eigenvector $\mathbf{P} \equiv \mathbf{v}_\lambda$. For those solutions we can multiply Eq.(3.42) by P_J to get

$$A^{IJ} P_I P_J = \lambda (B^{IJ} P_I P_J) = \lambda \quad (3.44)$$

3. The Physical Template Family of Spinning Waveforms - PTF

and using Eq.(3.40) we can see that the values of λ which are solutions to the eigenvalue problem (3.43), correspond to the extremal values of $(\rho_{\Phi_0})^2$, so $(\rho'_{\Sigma\alpha})^2$ should be chosen as the largest eigenvalue of $\mathbf{B}^{-1}\mathbf{A}$

$$\rho'_{\Sigma\alpha} = \max_{P_I} \sqrt{\frac{P_I P_J A^{IJ}}{P_I P_J B^{IJ}}} = \sqrt{\max \text{eigv} [\mathbf{B}^{-1}\mathbf{A}]} \quad (3.45)$$

Now, if we look at the structure of the matrix $\mathbf{B}^{-1}\mathbf{A}$, we can actually derive an analytic expression for its maximum eigenvalue. We start by introducing four five-dimensional vectors $\mathbf{v}_{1,2}$ and $\mathbf{u}_{1,2}$ defined as

$$v_1^I \equiv \langle s, Q_0^I \rangle, \quad v_2^I \equiv \langle s, Q_{\pi/2}^I \rangle \quad I = 1, \dots, 5 \quad (3.46)$$

$$\mathbf{u}_{1,2} \equiv \mathbf{B}^{-1} \mathbf{v}_{1,2} \quad (3.47)$$

and we then express $\mathbf{B}^{-1}\mathbf{A}$ as the tensorial product

$$\mathbf{B}^{-1}\mathbf{A} = \mathbf{u}_1 \otimes \mathbf{v}_1 + \mathbf{u}_2 \otimes \mathbf{v}_2 \quad (3.48)$$

This implies that the Kernel of the above 5-dimensional matrix $\text{Ker}(\mathbf{B}^{-1}\mathbf{A})$ is at least 3-dimensional, since any vector \mathbf{v} lying in the 3-dimensional sub-space orthogonal to the sub-space spanned by the vectors $\mathbf{v}_{1,2}$ will be an eigenvector with null eigenvalue; as a matter of fact we have

$$(\mathbf{B}^{-1}\mathbf{A}) \mathbf{v} = (u_1^I v_1^J) v_J + (u_2^I v_2^J) v_J = \mathbf{u}_1 (\mathbf{v}_1 \cdot \mathbf{v}) + \mathbf{u}_2 (\mathbf{v}_2 \cdot \mathbf{v}) = \mathbf{0} \quad (3.49)$$

where $\mathbf{0}$ is the null vector and we used the fact that $v_{1,2}^J v_J \equiv \mathbf{v}_{1,2} \cdot \mathbf{v} = 0$. At the same time we see that any eigenvector corresponding to a non-null eigenvalue must be a linear combination of the vectors $\mathbf{u}_{1,2}$ and must satisfy

$$\mathbf{u}_1 (\mathbf{v}_1 \cdot \mathbf{v}_\lambda) + \mathbf{u}_2 (\mathbf{v}_2 \cdot \mathbf{v}_\lambda) = \lambda \mathbf{v}_\lambda \quad (3.50)$$

If we write \mathbf{v}_λ in terms of its component on $\mathbf{u}_{1,2}$ as $\mathbf{v}_\lambda = \alpha \mathbf{u}_1 + \beta \mathbf{u}_2$ we have

$$\begin{cases} \mathbf{v}_1 \cdot \mathbf{v}_\lambda = \alpha (\mathbf{v}_1 \cdot \mathbf{u}_1) + \beta (\mathbf{v}_1 \cdot \mathbf{u}_2) \\ \mathbf{v}_2 \cdot \mathbf{v}_\lambda = \alpha (\mathbf{v}_2 \cdot \mathbf{u}_1) + \beta (\mathbf{v}_2 \cdot \mathbf{u}_2) \end{cases} \quad (3.51)$$

which yields a new 2-dimensional eigenvalue problem

$$\begin{pmatrix} \mathbf{v}_1 \cdot \mathbf{u}_1 & \mathbf{v}_1 \cdot \mathbf{u}_2 \\ \mathbf{v}_2 \cdot \mathbf{u}_1 & \mathbf{v}_2 \cdot \mathbf{u}_2 \end{pmatrix} \begin{pmatrix} \alpha \\ \beta \end{pmatrix} = \lambda \begin{pmatrix} \alpha \\ \beta \end{pmatrix} \quad (3.52)$$

It is now easy to evaluate the two non-null eigenvalues of $\mathbf{B}^{-1}\mathbf{A}$ by finding the roots of the *characteristic polynomial*

$$\begin{aligned} \begin{vmatrix} \mathbf{v}_1 \cdot \mathbf{u}_1 - \lambda & \mathbf{v}_1 \cdot \mathbf{u}_2 \\ \mathbf{v}_2 \cdot \mathbf{u}_1 & \mathbf{v}_2 \cdot \mathbf{u}_2 - \lambda \end{vmatrix} &= (\mathbf{v}_1 \cdot \mathbf{u}_1 - \lambda)(\mathbf{v}_2 \cdot \mathbf{u}_2 - \lambda) - (\mathbf{v}_1 \cdot \mathbf{u}_2)(\mathbf{v}_2 \cdot \mathbf{u}_1) = \\ &= \lambda^2 - \lambda(\mathbf{v}_1 \cdot \mathbf{u}_1 + \mathbf{v}_2 \cdot \mathbf{u}_2) + (\mathbf{v}_1 \cdot \mathbf{u}_1)(\mathbf{v}_2 \cdot \mathbf{u}_2) - \\ &\quad (\mathbf{v}_1 \cdot \mathbf{u}_2)(\mathbf{v}_2 \cdot \mathbf{u}_1) = 0 \end{aligned} \quad (3.53)$$

which has solutions for

$$\lambda_{\pm} = \frac{1}{2} \left[\mathbf{v}_1 \cdot \mathbf{u}_1 + \mathbf{v}_2 \cdot \mathbf{u}_2 \pm \sqrt{(\mathbf{v}_1 \cdot \mathbf{u}_1 - \mathbf{v}_2 \cdot \mathbf{u}_2)^2 + 4(\mathbf{v}_2 \cdot \mathbf{u}_1)(\mathbf{v}_1 \cdot \mathbf{u}_2)} \right] \quad (3.54)$$

and the signal-to-noise ratio is therefore

$$\begin{aligned} \rho &\equiv \rho'_{\Sigma\alpha} = \sqrt{\lambda_+} \\ &= \sqrt{\frac{1}{2} \left[\mathbf{v}_1 \cdot \mathbf{u}_1 + \mathbf{v}_2 \cdot \mathbf{u}_2 + \sqrt{(\mathbf{v}_1 \cdot \mathbf{u}_1 - \mathbf{v}_2 \cdot \mathbf{u}_2)^2 + 4(\mathbf{v}_2 \cdot \mathbf{u}_1)(\mathbf{v}_1 \cdot \mathbf{u}_2)} \right]} \end{aligned} \quad (3.55)$$

Once we have obtained the maximum eigenvalue of $\mathbf{B}^{-1}\mathbf{A}$ we can also calculate an algebraic expression for its associated eigenvector whose 5-dimensional components correspond to the values P_{max}^I which yield the maximized overlap Eq.(3.55), i.e. $\mathbf{P}_{max} = \mathbf{v}_{\lambda_+}$.

This vector must satisfy the eigensystem (3.52) with $\lambda = \lambda_+$, therefore we have two equations

$$\begin{pmatrix} \mathbf{v}_1 \cdot \mathbf{u}_1 - \lambda_+ & \mathbf{v}_1 \cdot \mathbf{u}_2 \\ \mathbf{v}_2 \cdot \mathbf{u}_1 & \mathbf{v}_2 \cdot \mathbf{u}_2 - \lambda_+ \end{pmatrix} \begin{pmatrix} \alpha \\ \beta \end{pmatrix} = \begin{pmatrix} 0 \\ 0 \end{pmatrix} \quad (3.56)$$

The first equation admits solution for

$$\begin{aligned} (\mathbf{v}_1 \cdot \mathbf{u}_1 - \lambda_+) \alpha + (\mathbf{v}_1 \cdot \mathbf{u}_2) \beta &= 0 \implies \\ \beta &= \frac{\lambda_+ - \mathbf{v}_1 \cdot \mathbf{u}_1}{\mathbf{v}_1 \cdot \mathbf{u}_2} \alpha \equiv c \alpha \end{aligned} \quad (3.57)$$

where we defined $c \equiv (\lambda_+ - \mathbf{v}_1 \cdot \mathbf{u}_1) / (\mathbf{v}_1 \cdot \mathbf{u}_2)$. It is then easy to show that, substituting expression (3.57) into the second equation (3.56), this is identically satisfied.

We now must impose the constraint (3.36) to obtain the value of α

$$\begin{aligned} B_{IJ} P_{max}^I P_{max}^J &= B_{IJ} (\alpha u_1^I + \beta u_2^I) (\alpha u_1^J + \beta u_2^J) = B_{IJ} (\alpha u_1^I + c \alpha u_2^I) (\alpha u_1^J + c \alpha u_2^J) \\ &= \alpha^2 B_{IJ} (u_1^I + c u_2^I) (u_1^J + c u_2^J) = 1 \end{aligned} \quad (3.58)$$

3. The Physical Template Family of Spinning Waveforms - PTF

We recall from (3.47) that $u_{1,2}^I = B_{IK}^{-1} v_{1,2}^K$ therefore we have

$$B_{IJ} (u_1^I + c u_2^I) = B_{IJ} (B_{IK}^{-1} v_1^K + c B_{IK}^{-1} v_2^K) = \delta^J_K (v_1^K + c v_2^K) = v_1^J + c v_2^J \quad (3.59)$$

and substituting into (3.58) we get

$$\begin{aligned} B_{IJ} P_{max}^I P_{max}^J &= \alpha^2 (v_1^J + c v_2^J) (u_1^J + c u_2^J) \\ &= \alpha^2 [\mathbf{v}_1 \cdot \mathbf{u}_1 + c (\mathbf{v}_2 \cdot \mathbf{u}_1 + \mathbf{v}_1 \cdot \mathbf{u}_2) + c^2 (\mathbf{v}_2 \cdot \mathbf{u}_2)] = 1 \end{aligned} \quad (3.60)$$

which yields

$$\alpha = \sqrt{\frac{1}{\mathbf{v}_1 \cdot \mathbf{u}_1 + c (\mathbf{v}_2 \cdot \mathbf{u}_1 + \mathbf{v}_1 \cdot \mathbf{u}_2) + c^2 (\mathbf{v}_2 \cdot \mathbf{u}_2)}} \quad (3.61)$$

It's then easy to verify that, with the calculated values of α and β , the vector

$$\mathbf{P}_{max} \equiv \alpha \mathbf{u}_1 + \beta \mathbf{u}_2 \quad (3.62)$$

satisfies Eq.(3.44) as expected

$$\begin{aligned} A_{IJ} P_{max}^I P_{max}^J &= (v_1^I v_1^J + v_2^I v_2^J) (\alpha u_1^I + \beta u_2^I) (\alpha u_1^J + \beta u_2^J) \\ &= \alpha^2 [\mathbf{v}_1 \cdot \mathbf{u}_1 + c (\mathbf{v}_1 \cdot \mathbf{u}_2)]^2 + \alpha^2 [\mathbf{v}_2 \cdot \mathbf{u}_1 + c (\mathbf{v}_2 \cdot \mathbf{u}_2)]^2 \\ &= \frac{[\mathbf{v}_1 \cdot \mathbf{u}_1 + c (\mathbf{v}_1 \cdot \mathbf{u}_2)]^2 + [\mathbf{v}_2 \cdot \mathbf{u}_1 + c (\mathbf{v}_2 \cdot \mathbf{u}_2)]^2}{\mathbf{v}_1 \cdot \mathbf{u}_1 + c (\mathbf{v}_2 \cdot \mathbf{u}_1 + \mathbf{v}_1 \cdot \mathbf{u}_2) + c^2 (\mathbf{v}_2 \cdot \mathbf{u}_2)} \\ &= \lambda_+ = \rho^2 \end{aligned} \quad (3.63)$$

Once we have calculated the components of the vector P_{max}^I for every value of the arrival time t_0 , we can construct the templates (3.17)-(3.18) and, from Eq. (3.31a), the unconstrained SNR statistic can be expressed in a form analogous to that of non-spinning binaries

$$(\rho'_{\Sigma\alpha})^2 = \frac{1}{\sigma^2} [\langle s, h_c^{PTF} \rangle^2 + \langle s, h_s^{PTF} \rangle^2] \quad (3.64)$$

with

$$\begin{cases} \sigma^2 = B_{IJ} P_{max}^I P_{max}^J = 1 \\ h_c^{PTF}(t; t_0) = P_I^{max}(t_0) Q_0^I(t) \\ h_s^{PTF}(t; t_0) = P_I^{max}(t_0) Q_{\pi/2}^I(t) \end{cases} \quad (3.65)$$

3.2.2 Normalization and False-Alarm Statistic

The constrained maximized SNR for the PTF statistic is given by equation (3.23), which we rewrite explicitly as

$$\rho_{\Sigma\alpha} = \max_{t_0, \Phi_0, \Theta, \varphi, \alpha} \left[\frac{P_I[\alpha; \Theta, \varphi] \left(\langle s, Q_0^I \rangle_{t_0} \cos 2\Phi_0 + \langle s, Q_{\pi/2}^I \rangle_{t_0} \sin 2\Phi_0 \right)}{\sqrt{P_I[\alpha; \Theta, \varphi] P_J[\alpha; \Theta, \varphi] \mathcal{B}^{IJ}}} \right] \quad (3.66)$$

with $\mathcal{B}^{IJ} = \langle Q_0^I \cos 2\Phi_0 + Q_{\pi/2}^I \sin 2\Phi_0, Q_0^J \cos 2\Phi_0 + Q_{\pi/2}^J \sin 2\Phi_0 \rangle$. The range of maximization for t_0 is $[0, T]$, with T the length of the data segment being analyzed, $\Phi_0 \in [0, 2\pi[$, $\alpha \in [0, 2\pi[$, (Θ, φ) are the usual polar coordinates on a sphere and the constraints (3.36), (3.38) must hold. The corresponding unconstrained maximum is obtained maximizing the same quantity over the P_I 's considered as free variables, that is over the entire five-dimensional Euclidean space, to get

$$\rho'_{\Sigma\alpha} = \max_{t_0, \Phi_0, P_I} \left[\frac{P_I \left(\langle s, Q_0^I \rangle_{t_0} \cos 2\Phi_0 + \langle s, Q_{\pi/2}^I \rangle_{t_0} \sin 2\Phi_0 \right)}{\sqrt{P_I P_J \langle Q_0^I \cos 2\Phi_0 + Q_{\pi/2}^I \sin 2\Phi_0, Q_0^J \cos 2\Phi_0 + Q_{\pi/2}^J \sin 2\Phi_0 \rangle}} \right] \quad (3.67)$$

We can now combine the five Q_0^I 's and the five $Q_{\pi/2}^I$'s in one ten-dimensional vector $Q^{\mathcal{I}}$ with $\mathcal{I} = 1, \dots, 10$ [33]. Let us now assume that the noise is stationary and Gaussian with zero mean $s = n$, i.e. for every time t_i $n(t_i)$ has a probability density function of the form

$$p(x) = \frac{1}{\sqrt{2\pi\sigma}} e^{-\frac{(x-\mu)^2}{2\sigma^2}} = \frac{1}{\sqrt{2\pi\sigma}} e^{-\frac{x^2}{2\sigma^2}} \quad (3.68)$$

where $\mu = 0$ and σ^2 are respectively the expectation value and the variance of the variable x , defined by

$$\begin{aligned} \mu \equiv E(x) &\equiv \bar{x} = \int_{-\infty}^{+\infty} x p(x) dx = 0 \\ \sigma^2 \equiv E((x - \mu)^2) &= E(x^2) = \int_{-\infty}^{+\infty} x^2 p(x) dx \end{aligned} \quad (3.69)$$

If $\sigma = 1$ then x is called a *normal Gaussian random variable*.

Now if x is a random Gaussian variable with mean μ and variance σ^2 then any linear transformation on x will result in a Gaussian random variable; if we define

$y = y(x) = a \cdot x$ where a is a complex number then we have

$$\begin{aligned}
 \bar{y} &= \int_{-\infty}^{+\infty} y(x) \cdot p_x(x) dx = \int_{-\infty}^{+\infty} y(x) \frac{1}{\sqrt{2\pi}\sigma} e^{-\frac{(x-\mu)^2}{2\sigma^2}} dx = \int_{-\infty}^{+\infty} y \frac{1}{\sqrt{2\pi}\sigma} e^{-\frac{(\frac{y}{a}-\mu)^2}{2\sigma^2}} \frac{dy}{a} \\
 &= \int_{-\infty}^{+\infty} y \frac{1}{\sqrt{2\pi}(a\sigma)} e^{-\frac{1}{a^2} \frac{(y-a\mu)^2}{2\sigma^2}} dy = \int_{-\infty}^{+\infty} y \frac{1}{\sqrt{2\pi}(a\sigma)} e^{-\frac{(y-a\mu)^2}{2(a\sigma)^2}} dy \\
 &= \int_{-\infty}^{+\infty} y \frac{1}{\sqrt{2\pi}(\sigma')} e^{-\frac{(y-\mu')^2}{2\sigma'^2}} dy \equiv \int_{-\infty}^{+\infty} y p_y(y) dy
 \end{aligned} \tag{3.70}$$

which shows that y is Gaussian distributed with mean $\mu' = a\mu$ and variance $\sigma'^2 = (a\sigma)^2$. Analogously if we have a Gaussian random process $x(t)$ then any linear transformation

$$y = \int_a^b x(t)a(t)dt \tag{3.71}$$

where $a(t)$ is a real (complex) continuous function, yields a real (complex) Gaussian random variable. As a matter of fact we can discretize the interval (a, b) in N sub-intervals and approximate the integral with a sum

$$y_N = \sum_{n=1}^N x(t_n)a(t_n)\delta t_n \tag{3.72}$$

It is then clear that y_N is a sum of linear transformations of a set of Gaussian random variables and it is therefore a linear transformation itself. It can then be shown that, if the integral (3.71) exists, then both the mean and the variance associated with the variable (3.72) will converge to the true values in the limit $N \rightarrow \infty$ and $\delta t_n \rightarrow 0$; analogously the sum (3.72) itself will converge in mean (and therefore in probability and in distribution) to the integral (3.71) in the same limit [64], that is

$$\lim_{N \rightarrow \infty} \overline{(y - y_N)^2} = 0 \tag{3.73}$$

In particular the Fourier transform \tilde{x} is a linear transformation, therefore the frequency domain function $\tilde{n}(f)$ will be a Gaussian random process with zero mean.

Now the variable $g(t) = \langle n(t)Q(t) \rangle$ is the Fourier transform of the function $\tilde{n}^*(f)\tilde{Q}(f)/S_n(|f|)$, where both $\tilde{Q}(f)$ and $S_n(|f|)$ are continuous functions of f , so $g(t)$ is a Gaussian random process with zero mean; it then follows that each object $\langle n, Q^{\mathcal{I}} \rangle$ for a fixed \mathcal{I} will itself be a Gaussian process with zero mean. We can therefore define the ten-dimensional random vector [33] $Y^{\mathcal{I}} \equiv \langle n, Q^{\mathcal{I}} \rangle$. The components $Y^{\mathcal{I}}$ are dependent and correlated to each other so the covariance

matrix is non-null and is given by

$$\begin{aligned}
 \text{Cov}(Y^{\mathcal{I}}, Y^{\mathcal{J}}) &\equiv \overline{(Y^{\mathcal{I}} - \overline{Y^{\mathcal{I}}})(Y^{\mathcal{J}} - \overline{Y^{\mathcal{J}}})} = \overline{Y^{\mathcal{I}}Y^{\mathcal{J}}} = \overline{\langle n, Q^{\mathcal{I}} \rangle \langle n, Q^{\mathcal{J}} \rangle} \\
 &= \left[4 \int_{-\infty}^{+\infty} \frac{\tilde{n}^*(f) \tilde{Q}^{\mathcal{I}}(f)}{S_n(|f|)} e^{2\pi i f t_0} df \times \int_{-\infty}^{+\infty} \frac{\tilde{n}^*(f') \tilde{Q}^{\mathcal{J}}(f')}{S_n(|f'|)} e^{2\pi i f' t_0} df' \right] \\
 &= 4 \int_{-\infty}^{+\infty} \int_{-\infty}^{+\infty} \frac{\tilde{n}^*(f) \tilde{n}(f')}{S_n(|f|) S_n(|f'|)} \frac{\tilde{Q}^{\mathcal{I}}(f) \tilde{Q}^{\mathcal{J}*}(f')}{S_n(|f|) S_n(|f'|)} e^{2\pi i (f-f') t_0} df df' \\
 &= 4 \int_{-\infty}^{+\infty} \int_{-\infty}^{+\infty} \frac{1}{2} S_n(|f|) \delta(f-f') \frac{\tilde{Q}^{\mathcal{I}}(f) \tilde{Q}^{\mathcal{J}*}(f')}{S_n(|f|) S_n(|f'|)} e^{2\pi i (f-f') t_0} df df' \\
 &= 2 \int_{-\infty}^{+\infty} \frac{\tilde{Q}^{\mathcal{I}}(f) \tilde{Q}^{\mathcal{J}*}(f)}{S_n(|f|)} df = \langle Q^{\mathcal{I}} Q^{\mathcal{J}} \rangle \equiv C^{\mathcal{I}\mathcal{J}}
 \end{aligned} \tag{3.74}$$

where we made use of the fact that $\tilde{n}^*(f) = \tilde{n}(-f)$ and $\tilde{Q}^{\mathcal{I}*}(f) = \tilde{Q}^{\mathcal{I}}(-f)$ and we used the definition of the power spectral density (2.5).

We can also combine the components $P_I \cos 2\Phi_0$ and $P_I \sin 2\Phi_0$ in another ten-dimensional vector $P_{\mathcal{I}}(\Phi_0, \alpha; \Theta, \varphi)$ and write the maximized match as

$$\rho = \max_{P_{\mathcal{I}}} \frac{P_{\mathcal{I}} \langle n, Q^{\mathcal{I}} \rangle}{\sqrt{P_{\mathcal{I}} P_{\mathcal{J}} \langle Q^{\mathcal{I}}, Q^{\mathcal{J}} \rangle}} = \max_{P_{\mathcal{I}}} \frac{P_{\mathcal{I}} Y^{\mathcal{I}}}{\sqrt{P_{\mathcal{I}} P_{\mathcal{J}} C^{\mathcal{I}\mathcal{J}}}} \tag{3.75}$$

the range of $P_{\mathcal{I}}$ depending on whether we wish to evaluate the unconstrained or the constrained maximum.

We can now introduce ten independent standard normal random variables with zero mean and unit variance $Z^{\mathcal{I}}$ and rewrite the $Y^{\mathcal{I}}$ as [33]

$$Y^{\mathcal{I}} = Z_{\mathcal{J}} [\sqrt{C}]^{\mathcal{I}\mathcal{J}} \tag{3.76}$$

where the matrix \sqrt{C} can be defined as $[\sqrt{C}]^{\mathcal{I}\mathcal{K}} [\sqrt{C}]^{\mathcal{K}\mathcal{J}} = C^{\mathcal{I}\mathcal{J}}$.

We can verify that the $Y^{\mathcal{I}}$ still satisfy the correct statistics

$$\begin{aligned}
 \text{Cov}(Y^{\mathcal{I}}, Y^{\mathcal{J}}) &= \overline{(Y^{\mathcal{I}} - \overline{Y^{\mathcal{I}}})(Y^{\mathcal{J}} - \overline{Y^{\mathcal{J}}})} = \overline{Y^{\mathcal{I}}Y^{\mathcal{J}}} = \left[Z_{\mathcal{K}} [\sqrt{C}]^{\mathcal{I}\mathcal{K}} Z_{\mathcal{L}} [\sqrt{C}]^{\mathcal{J}\mathcal{L}} \right] \\
 &= \overline{Z_{\mathcal{K}} Z_{\mathcal{L}} [\sqrt{C}]^{\mathcal{I}\mathcal{K}} [\sqrt{C}]^{\mathcal{J}\mathcal{L}}} = \delta_{\mathcal{K}\mathcal{L}} [\sqrt{C}]^{\mathcal{I}\mathcal{K}} [\sqrt{C}]^{\mathcal{J}\mathcal{L}} = C^{\mathcal{I}\mathcal{J}}
 \end{aligned} \tag{3.77}$$

Now the matched filter statistics becomes a function of the new variables

$$\rho = \rho[Y^{\mathcal{I}}(Z^{\mathcal{I}})] = \max_{P_{\mathcal{I}}} \frac{P_{\mathcal{I}} Z_{\mathcal{J}} [\sqrt{C}]^{\mathcal{I}\mathcal{J}}}{\sqrt{P_{\mathcal{I}} P_{\mathcal{J}} C^{\mathcal{I}\mathcal{J}}}} \tag{3.78}$$

3. The Physical Template Family of Spinning Waveforms - PTF

Since the statistics ρ is homogeneous with respect to the vector $Z^{\mathcal{I}}$ we can introduce a unit ten-vector $\hat{Z}^{\mathcal{I}}$ defined as $Z^{\mathcal{I}} = r\hat{Z}^{\mathcal{I}}$, with $r \equiv \sqrt{Z^{\mathcal{I}}Z_{\mathcal{I}}}$ and $\hat{Z}^{\mathcal{I}}\hat{Z}_{\mathcal{I}} = 1$ so that the statistics can be written as

$$\rho[Y^{\mathcal{I}}(Z^{\mathcal{I}})] = r\rho[Y^{\mathcal{I}}(\hat{Z}^{\mathcal{I}})] = r \left[\max_{P^{\mathcal{I}}} \frac{P_{\mathcal{I}}\hat{Z}_{\mathcal{J}}[\sqrt{C}]^{\mathcal{I}\mathcal{J}}}{\sqrt{P_{\mathcal{I}}P_{\mathcal{J}}C^{\mathcal{I}\mathcal{J}}}} \right] \equiv r\rho'(\Omega) \quad (3.79)$$

where Ω is the direction of $\hat{Z}^{\mathcal{I}}$ in its ten-dimensional Euclidean space.

If we have n independent random variables x_n , then their joint probability density function is simply given by the product of their individual density functions $F(x_1, x_2, \dots, x_n) = f(x_1) \cdot f(x_2) \cdot \dots \cdot f(x_n)$; if the variables are standard normal Gaussian distributed random variables, their joint probability density function is given by

$$F(x_1, x_2, \dots, x_n) = \frac{1}{(2\pi)^{n/2}} e^{-\frac{x_1^2 + x_2^2 + \dots + x_n^2}{2}} \equiv F(x) \quad (3.80)$$

If we now wish to evaluate the expectation values of a function $g(x_1, x_2, \dots, x_n) \equiv g(x)$ this will simply be given by

$$E(g(x)) \equiv \overline{g(x)} = \int_{-\infty}^{+\infty} g(x) F(x) dx \quad (3.81)$$

In particular the expectation value of the sum of the squares of the variables x_1, x_2, \dots, x_n will be

$$\int_{-\infty}^{+\infty} \int_{-\infty}^{+\infty} \dots \int_{-\infty}^{+\infty} \frac{1}{(2\pi)^{n/2}} (x_1^2 + x_2^2 + \dots + x_n^2) e^{-\frac{x_1^2 + x_2^2 + \dots + x_n^2}{2}} dx_1 dx_2 \dots dx_n \quad (3.82)$$

Now the integrand is spherically symmetric so it is useful to introduce n-dimensional polar coordinates and rewrite the integral in terms of the radius $r^2 = x_1^2 + x_2^2 + \dots + x_n^2$ and the n-dimensional solid angle $d^n\Omega$ as

$$\frac{1}{(2\pi)^{n/2}} \int_0^{+\infty} \int_{n\text{-sphere}} r^2 e^{-\frac{r^2}{2}} dr d^n\Omega \quad (3.83)$$

The surface area of a n-sphere is given by $\frac{n\pi^{n/2}}{(n/2)!} r^{n-1}$ so the integral becomes

$$\int_0^{+\infty} r^2 \frac{n}{(2)^{n/2} (n/2) (n/2 - 1)!} r^{n-1} e^{-\frac{r^2}{2}} dr = \int_0^{+\infty} r^2 \frac{1}{(2)^{n/2-1} \Gamma(n/2)} r^{n-1} e^{-\frac{r^2}{2}} dr \quad (3.84)$$

and introducing the variable $x = r^2$ we have

$$\int_0^{+\infty} x \frac{1}{(2)^{n/2-1} \Gamma(n/2)} x^{(n-1)/2} e^{-\frac{x}{2}} \frac{dx}{2x^{1/2}} = \int_0^{+\infty} x \frac{1}{(2)^{n/2} \Gamma(n/2)} x^{n/2-1} e^{-\frac{x}{2}} dx \quad (3.85)$$

which shows that the variable $x = r^2$ is χ^2 distributed with n degrees of freedom

$$F(x) = \frac{1}{(2)^{n/2}\Gamma(n/2)} x^{n/2-1} e^{-\frac{x}{2}} \quad (3.86)$$

In our case the variable r represents the ten-norm of the vector $\hat{Z}^{\mathcal{I}}$ whose components are independent normal standard Gaussian variables, so if we take r^2 this variable will be χ^2 distributed with ten degrees of freedom, that is its probability density function is given by

$$\begin{cases} p_{r^2}(x) = \frac{x^4 e^{-x/2}}{2^5 \cdot \Gamma(5)} & x \geq 0; \\ p_{r^2}(x) = 0 & x < 0; \end{cases} \quad (3.87)$$

The statistics $\rho'(\Omega)$ depends on the actual range of maximization of the $P_{\mathcal{I}}$'s however, if we consider it to be the whole ten-dimensional space, then $\rho'(\Omega) = 1$ uniformly for every Ω

$$\rho'(\Omega) = \max_{P^{\mathcal{I}}} \frac{P_{\mathcal{I}}[\sqrt{C}]^{\mathcal{I}\mathcal{J}}}{\sqrt{P_{\mathcal{I}}P_{\mathcal{J}}C^{\mathcal{I}\mathcal{J}}}} \hat{Z}_{\mathcal{J}} \equiv \max_{P^{\mathcal{I}}} \frac{R^{\mathcal{J}}}{\sqrt{R_{\mathcal{I}}R_{\mathcal{J}}\delta^{\mathcal{I}\mathcal{J}}}} \hat{Z}_{\mathcal{J}} = 1 \quad (3.88)$$

where $R_{\mathcal{I}} = [\sqrt{C}]_{\mathcal{I}\mathcal{J}} P^{\mathcal{J}}$; as a matter of fact the above statistics can be seen as the scalar product of two unit ten-vectors and the maximum value will be reached when they are parallel.

In this case the combined statistics $\rho[Y^{\mathcal{I}}(Z^{\mathcal{I}})] = r$, so $\rho^2 = r^2$ is χ^2 -distributed with ten degrees of freedom and its expectation value is therefore

$$\begin{aligned} \overline{\rho^2} &= \int_0^{+\infty} x p_x(x) dx = \int_0^{+\infty} \frac{x^5 e^{-x/2}}{2^5 \cdot \Gamma(5)} dx = \frac{2}{\Gamma(5)} \int_0^{+\infty} x^5 e^{-x} dx = \frac{2 \cdot \Gamma(6)}{\Gamma(5)} \\ &= \frac{2 \cdot 120}{24} = 10 \end{aligned} \quad (3.89)$$

In general however the range of maximization of the $P_{\mathcal{I}}$ will not be the entire space, so the statistics $\rho'(\Omega)$ will not be uniform for all Ω and in particular its value will be less than one so the effective degrees of freedom associated to the joint statistics ρ will be less than 10.

Numerical simulations performed with stretches of simulated white and colored Gaussian noise show that the number of degrees of freedom of the statistic ρ distribution is actually 6 [33], as one might guess by counting the five extrinsic parameters $P_{\mathcal{I}}$ plus the initial phase Φ_0 over which the overlap is maximized.

3.2.3 A Posteriori SNR Statistics

In presence of pure Gaussian noise $\tilde{s}(f) = \tilde{n}(f)$ we can calculate the expectation value of the maximum SNR in Eq.(3.64). Let's start by evaluating

$$\begin{aligned}
 \overline{\langle n, h_c \rangle^2} &= \overline{\langle n, P_I^{max} Q_0^I \rangle_{t_0} \langle n, P_J^{max} Q_0^J \rangle_{t_0}} = \\
 &= \overline{4 P_I^{max} P_J^{max} \int_{-\infty}^{+\infty} \frac{\tilde{n}(f) \tilde{Q}_0^{I*}(f)}{S_n(|f|)} e^{2\pi i f t_0} df \times \int_{-\infty}^{+\infty} \frac{\tilde{n}(f') \tilde{Q}_0^{J*}(f')}{S_n(|f'|)} e^{2\pi i f' t_0} df'} \\
 &= 4 P_I^{max} P_J^{max} \int_{-\infty}^{+\infty} \int_{-\infty}^{+\infty} \frac{\tilde{n}(f) \tilde{n}^*(f') \tilde{Q}_0^{I*}(f) \tilde{Q}_0^J(f')}{S_n(|f|) S_n(|f'|)} e^{2\pi i (f-f') t_0} df df' \\
 &= 4 P_I^{max} P_J^{max} \int_{-\infty}^{+\infty} \int_{-\infty}^{+\infty} \frac{\tilde{n}(f) \tilde{n}^*(f') \tilde{Q}_0^{I*}(f) \tilde{Q}_0^J(f')}{S_n(|f|) S_n(|f'|)} e^{2\pi i (f-f') t_0} df df' \\
 &= 4 P_I^{max} P_J^{max} \int_{-\infty}^{+\infty} \int_{-\infty}^{+\infty} \frac{1}{2} S_n(|f|) \delta(f-f') \frac{\tilde{Q}_0^{I*}(f) \tilde{Q}_0^J(f')}{S_n(|f|) S_n(|f'|)} e^{2\pi i (f-f') t_0} df df' \\
 &= 2 P_I^{max} P_J^{max} \int_{-\infty}^{+\infty} \frac{\tilde{Q}_0^{I*}(f) \tilde{Q}_0^J(f)}{S_n(|f|)} df = P_I^{max} P_J^{max} \langle Q_0^I, Q_0^J \rangle = P_I^{max} P_J^{max} B^{IJ} \\
 &= 1
 \end{aligned} \tag{3.90}$$

where we used the definition of the one-sided power spectral density (2.5). Analogously we have

$$\begin{aligned}
 \overline{\langle n, h_s \rangle^2} &= \overline{\langle n, P_I^{max} Q_{\pi/2}^I \rangle_{t_0} \langle n, P_J^{max} Q_{\pi/2}^J \rangle_{t_0}} = P_I^{max} P_J^{max} \langle Q_{\pi/2}^I, Q_{\pi/2}^J \rangle \\
 &= \langle P_I^{max} Q_{\pi/2}^I, P_J^{max} Q_{\pi/2}^J \rangle \simeq \langle P_I^{max} Q_0^I, P_J^{max} Q_0^J \rangle = P_I^{max} P_J^{max} B^{IJ} \tag{3.91} \\
 &= 1
 \end{aligned}$$

where we made use of approximation (3.25).

Therefore for the expectation value of the SNR squared we simply have

$$\begin{aligned}
 \overline{(\rho'_{\Sigma^\alpha})^2} &= \frac{1}{\sigma^2} [\overline{\langle n, h_c \rangle^2} + \overline{\langle n, h_s \rangle^2}] = [\overline{\langle n, h_c \rangle^2} + \overline{\langle n, h_s \rangle^2}] \\
 &= \overline{\langle n, P_I^{max} Q_0^I \rangle \langle n, P_J^{max} Q_0^J \rangle} + \overline{\langle n, P_I^{max} Q_{\pi/2}^I \rangle \langle n, P_J^{max} Q_{\pi/2}^J \rangle} \tag{3.92} \\
 &= 2
 \end{aligned}$$

3.2.4 Digital Matched Filtering

Given a discretely sampled time domain quantity $x_j \equiv x(t_j) \equiv x(j\Delta t)$ with sampling interval Δt and N total sample points, the discrete approximation to the continuous forward and inverse Fourier transform are given by

$$\begin{aligned}\tilde{x}(f_k) &= \sum_{j=0}^{N-1} x_j e^{-2\pi i f_k t_j} \Delta t = \Delta t \sum_{j=0}^{N-1} x_j e^{-2\pi i j k/N} \equiv \Delta t \tilde{x}_k \\ x(t_j) &= \frac{1}{N\Delta t} \sum_{k=0}^{N-1} \tilde{x}(f_k) e^{2\pi i f_k t_j} = \Delta f \sum_{k=0}^{N-1} \tilde{x}(f_k) e^{2\pi i j k/N} \equiv \frac{1}{N} \sum_{k=0}^{N-1} \tilde{x}_k e^{2\pi i j k/N}\end{aligned}\quad (3.93)$$

where $f_k = k/(N\Delta t) \equiv k\Delta f$ is the discretized frequency, Δf is the corresponding sampling interval and we have introduced the notation $\tilde{v}_k \equiv \tilde{v}(f_k)/\Delta t$.

Note that the positive frequencies $0 < f < f_{N_y}$ correspond to values of k in the range $0 < k < N/2$ while negative frequencies $-f_{N_y} < f < 0$ correspond to $N/2 < k < N$, where $f_{N_y} \equiv 1/2\Delta t$ is the *Nyquist critical frequency*.

Going now to the discretized version of the above equations we get

$$\begin{aligned}\langle s, h \rangle &= 2 \sum_{k=0}^{N-1} \frac{\tilde{s}(f_k) \tilde{h}^*(f_k)}{S_n(|f_k|)} \Delta f = (\Delta t)^2 \left[4 \Re \sum_{k=1}^{N/2-1} \frac{\tilde{s}_k \tilde{h}_k^*}{S_n(f_k)} \Delta f \right] \\ \langle s, h(t_j) \rangle &= 2 \frac{1}{N\Delta t} \sum_{k=0}^{N-1} \frac{\tilde{s}(f_k) \tilde{h}^*(f_k)}{S_n(|f_k|)} e^{2\pi i j k/N} = 2 \frac{\Delta t}{N} \sum_{k=0}^{N-1} \frac{\tilde{s}_k \tilde{h}_k^*}{S_n(|f_k|)} e^{2\pi i j k/N}\end{aligned}\quad (3.94)$$

where for simplicity we take N to be even (generally a power of 2).

What numerical packages actually compute when performing a Fourier Transform is \tilde{x}_k rather than $\tilde{x}(f_k)$, so this means that we have to carry around normalization factors of $1/N\Delta t$ and Δt to make the result of our matched filtering routine agree with the analytical expression (3.45). Let us evaluate explicitly the discretized expressions of the components of the vectors $\mathbf{v}_{1,2}$, $\mathbf{u}_{1,2}$ in Eq.(3.46) and of the matrix \mathbf{B} in Eq. (3.33)

$$\begin{aligned}v_1^I(t_j) &= \langle s, Q_0^I \rangle(t_j) = \frac{2}{N\Delta t} \sum_{k=0}^{N-1} \frac{\tilde{s}(f_k) \tilde{Q}_0^{I*}(f_k)}{S_n(|f_k|)} e^{2\pi i j k/N} = \frac{2\Delta t}{N} \sum_{k=0}^{N-1} \frac{\tilde{s}_k \tilde{Q}_{0k}^{I*}}{S_n(|f_k|)} e^{2\pi i j k/N} \\ &\equiv \frac{2\Delta t}{N} \tilde{v}_1^I(t_j)\end{aligned}\quad (3.95)$$

$$\begin{aligned}
 v_2^I(t_j) &= \langle s, Q_{\pi/2}^I \rangle(t_j) = \frac{2}{N\Delta t} \sum_{k=0}^{N-1} \frac{\tilde{s}(f_k) \tilde{Q}_{\pi/2}^{I*}(f_k)}{S_n(|f_k|)} e^{2\pi i j k/N} = \frac{2\Delta t}{N} \sum_{k=0}^{N-1} \frac{\tilde{s}_k \tilde{Q}_{(\pi/2)k}^{I*}}{S_n(|f_k|)} e^{2\pi i j k/N} \\
 &\equiv \frac{2\Delta t}{N} \bar{v}_2^I(t_j)
 \end{aligned} \tag{3.96}$$

$$\begin{aligned}
 B^{IJ} &= 4 \operatorname{Re} \left[\sum_{k=1}^{N/2-1} \frac{\tilde{Q}_0^I(f_k) \tilde{Q}_0^{J*}(f_k)}{S_n(|f_k|)} \Delta f \right] = (\Delta t)^2 \left[4 \operatorname{Re} \sum_{k=1}^{N/2-1} \frac{\tilde{Q}_{0k}^I \tilde{Q}_{0k}^{J*}}{S_n(|f_k|)} \Delta f \right] \\
 &\equiv (\Delta t)^2 \bar{B}^{IJ}
 \end{aligned} \tag{3.97}$$

where the barred quantities are those calculated by the numerical routines. We can then rewrite the vectors $\mathbf{u}_{1,2}$ as

$$\begin{cases} \mathbf{u}_1(t_j) = \frac{2}{N\Delta t} \bar{\mathbf{B}}^{-1} \bar{\mathbf{v}}_1(t_j) \equiv \frac{2}{N\Delta t} \bar{\mathbf{u}}_1(t_j) \\ \mathbf{u}_2(t_j) = \frac{2}{N\Delta t} \bar{\mathbf{B}}^{-1} \bar{\mathbf{v}}_2(t_j) \equiv \frac{2}{N\Delta t} \bar{\mathbf{u}}_2(t_j) \end{cases} \tag{3.98}$$

Now inserting expressions (3.98) into Eq.(3.55) for the SNR we get

$$\begin{aligned}
 \rho'_{\Sigma\alpha} &= \sqrt{\frac{1}{2} \frac{4}{N^2} \left[\bar{\mathbf{u}}_1 \cdot \bar{\mathbf{v}}_1 + \bar{\mathbf{u}}_2 \cdot \bar{\mathbf{v}}_2 + \sqrt{(\bar{\mathbf{u}}_1 \cdot \bar{\mathbf{v}}_1 - \bar{\mathbf{u}}_2 \cdot \bar{\mathbf{v}}_2)^2 + 4(\bar{\mathbf{u}}_1 \cdot \bar{\mathbf{v}}_2)(\bar{\mathbf{u}}_2 \cdot \bar{\mathbf{v}}_1)} \right]} \\
 &\equiv \frac{2}{N} \bar{\rho}'_{\Sigma\alpha}
 \end{aligned} \tag{3.99}$$

3.3 χ^2 Veto

In order to construct an exact χ^2 veto for PTF templates as given in equation (3.16), we need to identify the six orthonormal components of the template, so that the SNR statistic can be written as the sum of the square of six independent Gaussian normal distributed variables

$$\rho^2 = \sum_{i=1}^6 \langle s, \hat{h}_i \rangle^2 \tag{3.100}$$

Unfortunately this is an extremely complicated task that might not be completed analytically.

However, we can resort to the a posteriori statistic we described in secs. 3.2.1-3.2.3 and construct the χ^2 veto given the knowledge of the extrinsic parameters P_I^{MAX} that yield the maximum SNR at every time t_0 . It is clear that different values

of P_I effectively define different templates and, if we wish to construct a χ^2 veto with equal-power frequency bins, we find ourselves in need of re-computing the binning for every t_0 . This is clearly not feasible as it is extremely computationally expensive, therefore we are forced to construct bins with unequal power content, as outlined in Sec. 2.6.

The implementation of the χ^2 veto actually consists in dividing the frequency band in p bins of equal power for the template component \tilde{Q}_0^1 , and then calculating the amount of power all other components \tilde{Q}_0^I , $I = 2, 3, 4, 5$ have in the same bins. Following the calculations in Sec. 2.6 we construct the quantities (2.52) where in our case $h^I = Q_0^I$, so we have

$$\langle Q_0^1, Q_0^1 \rangle_j = \frac{B_{11}}{p} \quad (3.101)$$

$$\langle Q_0^I, Q_0^{I'} \rangle_j = (B_{II'})_j, \quad I = I' = 2, 3, 4, 5 \quad (3.102)$$

where B_{IJ} are the components of the matrix (3.35) and $(B_{IJ})_j$ are the components of the normalization matrix corresponding to the frequency bin Δf_j

$$(B_{IJ})_j = 4\Re \left[\int_{\Delta f_j} \frac{\tilde{Q}_0^I(f) \tilde{Q}_0^{J*}(f)}{S_n(f)} df \right] \quad (3.103)$$

so that

$$\langle Q_0^I, Q_0^{I'} \rangle = \sum_{j=1}^p \langle Q_0^I, Q_0^{I'} \rangle_j = B_{II'}, \quad I = I' = 1, 2, \dots, 5 \quad (3.104)$$

In each band j we then filter the data s with each component Q_0^I to get

$$\langle s, Q_0^I \rangle_j = (v_1^I)_j \quad (3.105)$$

where $(v_1^I)_j$ is the j^{th} -band I^{th} component of the vector \mathbf{v}_1 defined by Eq. (3.46). Again we have

$$\langle s, Q_0^I \rangle = \sum_{j=1}^p \langle s, Q_0^I \rangle_j = \sum_{j=1}^p (v_1^I)_j = v_1^I \quad (3.106)$$

However now our orthonormal components are not the five Q_0^I 's (the matrix B_{IJ} is not diagonal), but the two components h_c^{PTF} and h_s^{PTF} , given by eqs. (3.17)-(3.18)

$$h_c^{PTF}(t; t_0) = P_I^{\text{max}}(t_0) Q_0^I(t) \quad (3.107)$$

$$h_s^{PTF}(t; t_0) = P_I^{\text{max}}(t_0) Q_{\pi/2}^I(t) \quad (3.108)$$

3. The Physical Template Family of Spinning Waveforms - PTF

which satisfy $\langle h_c^{PTF}, h_s^{PTF} \rangle \simeq 0$ by virtue of the stationary phase approximation (3.24) and $\langle h_s^{PTF}, h_s^{PTF} \rangle \simeq \langle h_c^{PTF}, h_c^{PTF} \rangle = 1$ by virute of (3.25) and (3.36).

If we now drop the superscript PTF and define at every time t_0

$$\langle h_c(t_0), h_c(t_0) \rangle_j = \langle P_I^{max}(t_0)Q_0^I, P_J^{max}(t_0)Q_0^J \rangle_j = P_I^{max}(t_0)P_J^{max}(t_0) (B_{IJ})_j \equiv q_j \quad (3.109)$$

$$\langle h_s(t_0), h_s(t_0) \rangle_j \simeq \langle P_I^{max}(t_0)Q_0^I, P_J^{max}(t_0)Q_0^J \rangle_j = P_I^{max}(t_0)P_J^{max}(t_0) (B_{IJ})_j \equiv q_j \quad (3.110)$$

and

$$x_j^c \equiv \langle s, h_c(t_0) \rangle_j = P_I^{max}(t_0) \langle s, Q_0^I \rangle_j = P_I^{max}(t_0) (v_1^I)_j \quad (3.111)$$

$$x_j^s \equiv \langle s, h_s(t_0) \rangle_j = P_I^{max}(t_0) \langle s, Q_{\pi/2}^I \rangle_j = P_I^{max}(t_0) (v_2^I)_j \quad (3.112)$$

where $(v_2^I)_j$ is the j^{th} -band I^{th} component of the vector \mathbf{v}_2 defined by Eq. (3.46), and

$$x^c \equiv \langle s, h_c(t_0) \rangle = P_I^{max}(t_0) \langle s, Q_0^I \rangle = P_I^{max}(t_0) v_1^I \quad (3.113)$$

$$x^s \equiv \langle s, h_s(t_0) \rangle = P_I^{max}(t_0) \langle s, Q_{\pi/2}^I \rangle = P_I^{max}(t_0) v_2^I \quad (3.114)$$

we can construct the quantity

$$\chi_{PTF}^2(t_0) = \sum_{j=1}^p \frac{[x_j^c - q_j x^c]^2 + [x_j^s - q_j x^s]^2}{q_j} \quad (3.115)$$

which is χ^2 -distributed with $2(p-1)$ degrees of freedom.

In reality, since the statistic (3.115) is calculated a posteriori, by effectively constructing a different template for every t_0 using information from the knowledge of $\rho(t_0)$, the two components h_c^{PTF} and h_s^{PTF} are correlated and the actual distribution of χ_{PTF}^2 , while being a χ^2 , shows a lower number of degrees of freedom than expected (see Sec. 4.5).

3.3.1 Numerical Implementation

To construct the χ^2 veto we need to calculate p equal-power frequency bins for $\tilde{Q}_0^1(f)$ so that

$$(B_{11})_j = (\Delta t)^2 4\Re \left[\sum_{k=(k_j)_{min}}^{(k_j)_{max}} \frac{\tilde{Q}_{0k}^1 \tilde{Q}_{0k}^{1*}}{S_n(|f_k|)} \Delta f \right] \equiv (\Delta t)^2 (\bar{B}_{11})_j = (\Delta t)^2 \frac{\bar{B}_{11}}{p} \quad (3.116)$$

$$(B_{II'})_j = (\Delta t)^2 4\Re \left[\sum_{k=(k_j)_{min}}^{(k_j)_{max}} \frac{\tilde{Q}_{0k}^I \tilde{Q}_{0k}^{I'*}}{S_n(|f_k|)} \Delta f \right] \equiv (\Delta t)^2 (\bar{B}_{II'})_j \quad (3.117)$$

where $(k_j)_{min}$ and $(k_j)_{max}$ are the integration boundaries for the bin j and the barred objects, defined in eqs. (3.97), are the quantities calculated by numerical routines; in practice the values of q_j^I are calculated from the integration of the matrix B_{IJ} , whose values are stored for every iteration k .

We then need to calculate

$$x^c = \frac{2}{N} \bar{P}_I^{max} \bar{v}_1^I \equiv \frac{2}{N} \bar{x}^c \quad (3.118)$$

$$x^s = \frac{2}{N} \bar{P}_I^{max} \bar{v}_2^I \equiv \frac{2}{N} \bar{x}^s \quad (3.119)$$

where $\bar{v}_{1,2}^I$ are defined in eqs. (3.95)-(3.96) and

$$\bar{P}_{max}^I = \bar{\alpha} \bar{u}_1^I + \bar{\beta} \bar{u}_2^I \quad (3.120)$$

where the objects $\bar{\mathbf{u}}_{1,2}$ are defined in eqs. (3.98) and $\bar{\alpha}, \bar{\beta}$ are given by eqs. (3.61)-(3.57) with the substitutions $\mathbf{v}_{1,2} \rightarrow \bar{\mathbf{v}}_{1,2}$, $\mathbf{u}_{1,2} \rightarrow \bar{\mathbf{u}}_{1,2}$.

The same expressions are valid for the objects x_j^c and x_j^s with the difference that the summations in eqs. (3.95)-(3.96) are performed within the frequency range of each bin j

$$x_j^c = \frac{2}{N} \bar{P}_I^{max} (\bar{v}_1^I)_j \equiv \frac{2}{N} \bar{x}_j^c \quad (3.121)$$

$$x_j^s = \frac{2}{N} \bar{P}_I^{max} (\bar{v}_2^I)_j \equiv \frac{2}{N} \bar{x}_j^s \quad (3.122)$$

And finally we have the normalization factors

$$q_j = P_I^{max} P_J^{max} (B_{IJ})_j = \bar{P}_I^{max} \bar{P}_J^{max} (\bar{B}_{IJ})_j \quad (3.123)$$

The χ^2 statistic therefore is given by

$$\chi_{PTF}^2(t_0) = \frac{4}{N^2} \sum_{j=1}^p \frac{[\bar{x}_j^c - q_j \bar{x}^c]^2 + [\bar{x}_j^s - q_j \bar{x}^s]^2}{q_j} \equiv \frac{4}{N^2} \bar{\chi}_{PTF}^2(t_0) \quad (3.124)$$

3.4 Detection Pipeline

Here we review details and issues related to the implementation of the various stages of the pipeline for a PTF search.

3.4.1 Integration of the Equations of Motion

The set of coupled differential equation (1.33)-(1.47) is solved numerically using a Runge-Kutta-Fehlberg integrator (`gsl_odeiv_step_rkf45`) with adaptive time step. The dynamical variables are evolved and their value is calculated every $1/N$ seconds, with N the number of sample points per seconds. Even though LIGO data are sampled at 16384 Hz, for most data analysis applications it is sufficient to downsample to 4096 Hz, so the sampling interval is $\delta t = 1/4096 = 0.000244140625s$.

This set of equations is valid only in the regime of validity of the Post-Newtonian adiabatic approximation, so we should stop the integration when the system approaches merger and evolves in the strong-field regime. To ensure that at each time step we are still in the adiabatic regime we need a physically motivated check on our dynamical variables and/or their time derivatives, together with the MECO condition (1.32).

We notice that, since the binary system is losing energy, the orbital frequency $\omega(t)$ must be an increasing function of time during the inspiral phase; at every time step we then check whether the time-derivative of the orbital frequency $\dot{\omega}$ has become negative and if it has we stop the integration.

As a further check we ensure that at every time all the dynamical variables in eqs.(3.40)-(1.47) have not become NaN, otherwise we abort the code; in general, the physical conditions $d\epsilon/d\omega \geq 0$ or $\dot{\omega} \leq 0$ stop the integration before such a problem can arise, but some systems might evolve in such a way that the integrator fails before any of the above conditions happens.

In fact, evolving the dynamical equations for a large number of templates we ran into a few failures of the Runge-Kutta integrator, due to the fact that the value of the orbital frequency generated within one of the internal sub-steps of the integrator was negative, causing all dynamical variables to become NaN at the next time step. This always happened for system with mass-ratio $m_1/m_2 \sim 2$ and high values of the spin $\chi_1 \gtrsim 0.8$, with the spin vector \mathbf{S}_1 almost aligned with the orbital angular momentum \mathbf{L}_N , i.e. $\kappa_1 \gtrsim 0.8$; this configuration corresponds to systems which evolve very quickly toward merger and have an inspiral phase of $\lesssim 4s$.

The problem disappears if the sample rate is doubled to 8192 Hz, suggesting that the reason for these failures is indeed the very rapid evolution of the system which makes the transition from the adiabatic regime to the strong-field regime happen in a time significantly smaller than the sampling interval δt ; the numerical integrator therefore is not able to adjust the internal time stepping and it fails to evolve the orbital frequency correctly from a time t to a time $t + \delta t$ since the adiabatic Post-Newtonian approximation breaks down at t' with $t < t' < t + \delta t$.

This can be verified by looking at the time evolution of $d\epsilon/d\omega$ for one of these

templates (see figure 3.1); we see that, at the last time step before the integrator fails, this quantity is very close to 0, i.e. to the MECO condition, and its time-derivative (the slope of the curve) is rapidly increasing. Since the integration would be stopped at the MECO condition anyway, we can avoid getting a failure if we are able to identify this situation before the code actually aborts.

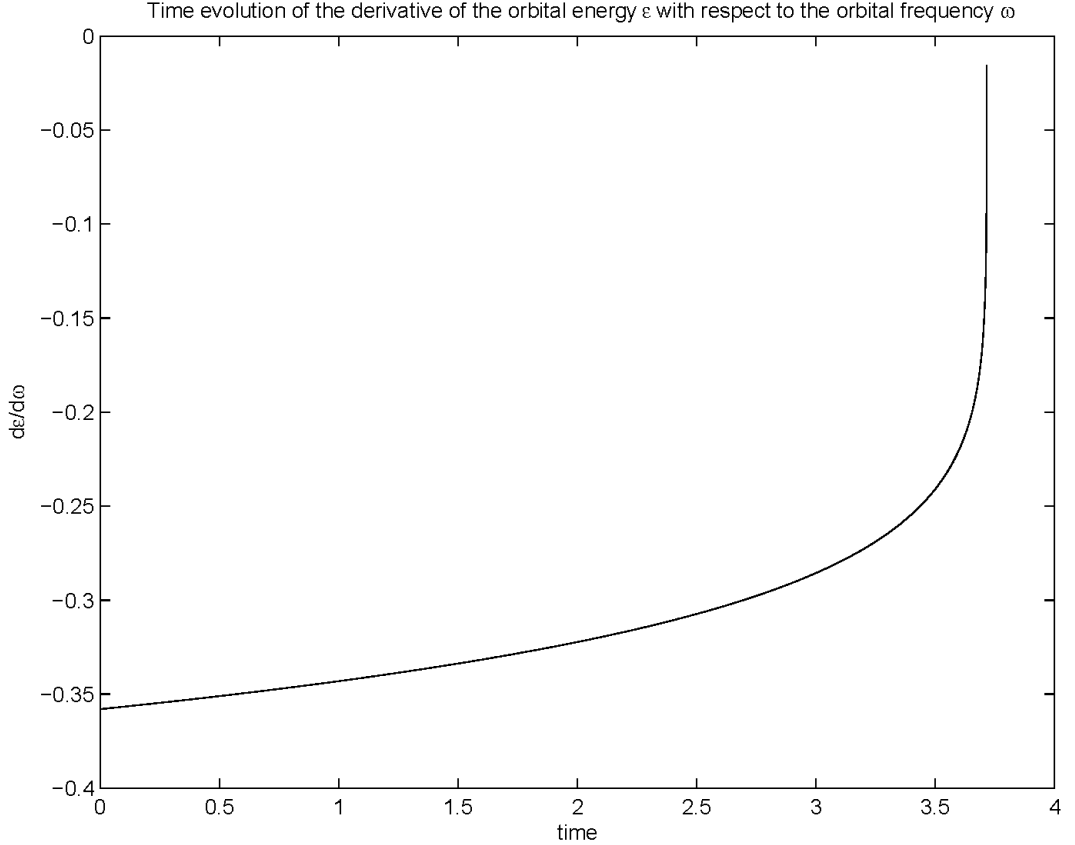


Figure 3.1: Time evolution of the derivative of the orbital energy ϵ with respect to the orbital frequency ω for a template with parameters $m_1 = 7.16M_\odot$, $m_2 = 2.93M_\odot$, $\chi_1 = 0.9$, $\kappa_1 = 0.9$. Vertical axis units are arbitrary, horizontal axis in units of seconds.

For every time t_{n-1} we can calculate the average value of the time derivative of $d\epsilon/d\omega$ between times t_{n-1} and t_{n-2} and approximate the time evolution for times t_m with $m > n - 1$ with a straight line as

$$\begin{aligned} \epsilon'(t_m) &\equiv \frac{d\epsilon}{d\omega}(t_m) \simeq \frac{d\epsilon}{d\omega}(t_{n-1}) + (m - n + 1) \left[\frac{d\epsilon}{d\omega}(t_{n-1}) - \frac{d\epsilon}{d\omega}(t_{n-2}) \right] \\ &= \epsilon'(t_{n-1}) + N_{steps} [\epsilon'(t_{n-1}) - \epsilon'(t_{n-2})] \end{aligned} \quad (3.125)$$

3. The Physical Template Family of Spinning Waveforms - PTF

with $N_{steps} \equiv m - n + 1$.

In case one or more of the dynamical variables assume a NaN value at time t_n , we calculate how many time steps are needed for the projection of $d\epsilon/d\omega$ given by (3.125) to cross the 0-axis

$$N_{steps} = \frac{\epsilon'(t_{n-1})}{\epsilon'(t_{n-2}) - \epsilon'(t_{n-1})} \quad (3.126)$$

If this happens within a few steps from time t_{n-1} (we will take 5) we can assume that the code is failing because the MECO condition is approaching and the adiabatic approximation is about to break down, so we can stop the integration without aborting the code.

Note that the estimate of $d\epsilon'/dt$ at step $n - 1$ is a very rough one and we expect $(d\epsilon'/dt)_{real}(t_n) \gg d\epsilon'/dt(t_{n-1})$, in fact we are claiming that the MECO condition is reached at some time $t_{n-1} < t < t_n$; however the number of steps needed to reach the condition $d\epsilon/d\omega = 0$, even if calculated assuming that the slope of ϵ' remains constant after step $n - 1$, give us a measure of how close the MECO condition is.

We performed a large simulation generating 10000 templates in the range $6 < m_1 < 9.5$, $1.6 < m_2 < 3$, $0.6 < \chi_1 < 1$, $0.6 < \kappa_1 < 1$, of which only 61 failed (see figs.3.2-3.3).

For each failing templates we calculated the number of projected time-steps needed to reach the MECO condition and we found that this number is never greater than 5, thus indicating that all the failures are due to the breakdown of the adiabatic approximation.

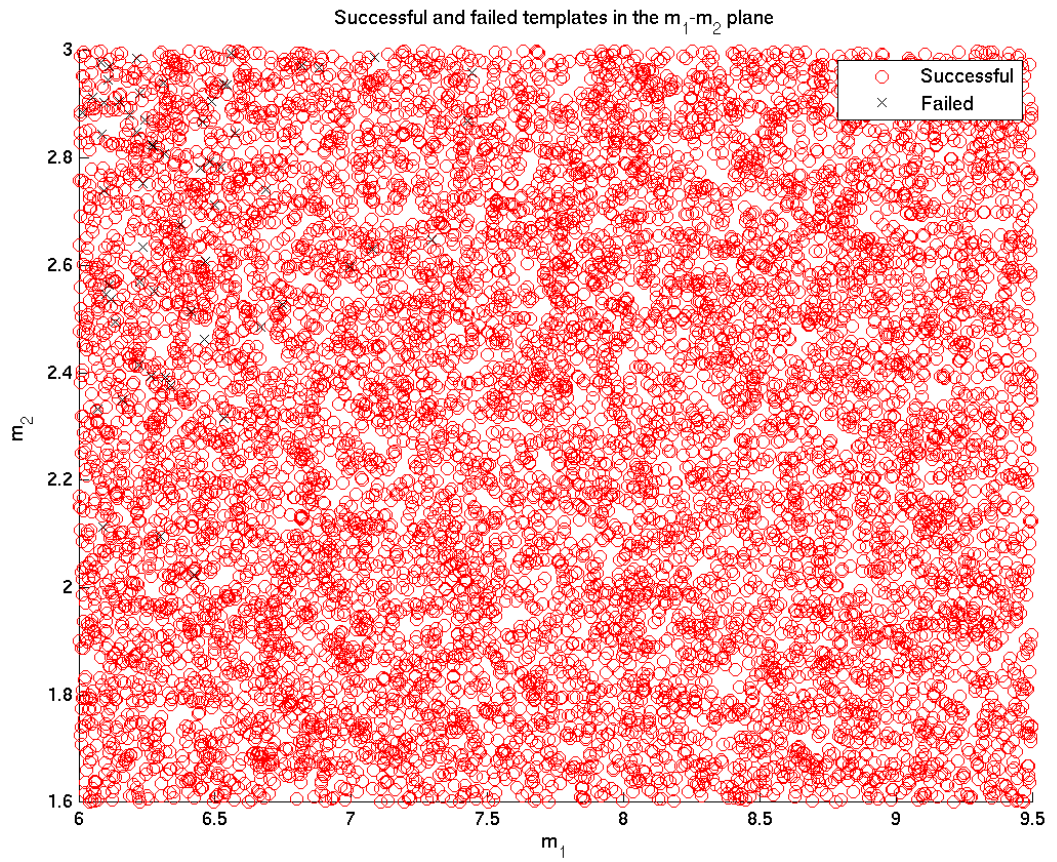


Figure 3.2: Scatterplot of successful and failed templates in the m_1 - m_2 plane.

3. The Physical Template Family of Spinning Waveforms - PTF

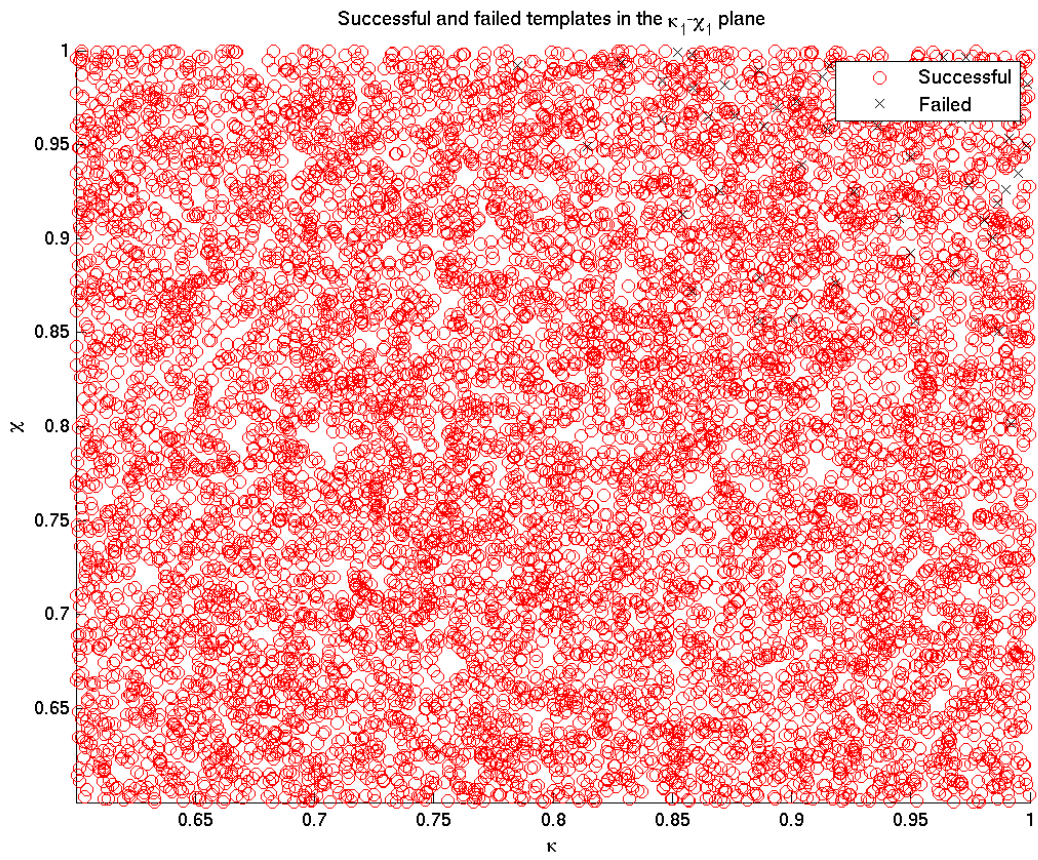


Figure 3.3: Scatterplot of successful and failed templates in the χ_1 - κ_1 plane.

Failed templates in the m_1 - m_2 space. On the vertical axis: number of projected time steps required to reach the MECO condition

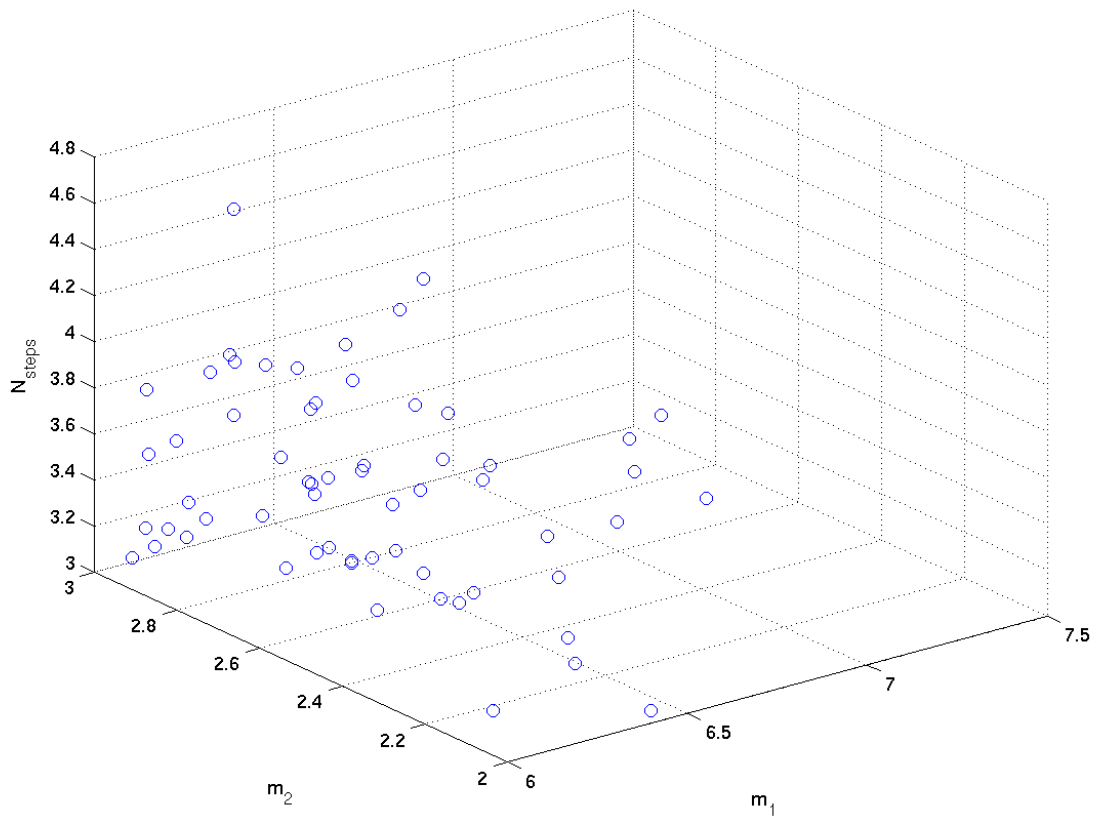


Figure 3.4: Number of projected time steps needed to reach the MECO condition vs the m_1 - m_2 plane.

3. The Physical Template Family of Spinning Waveforms - PTF

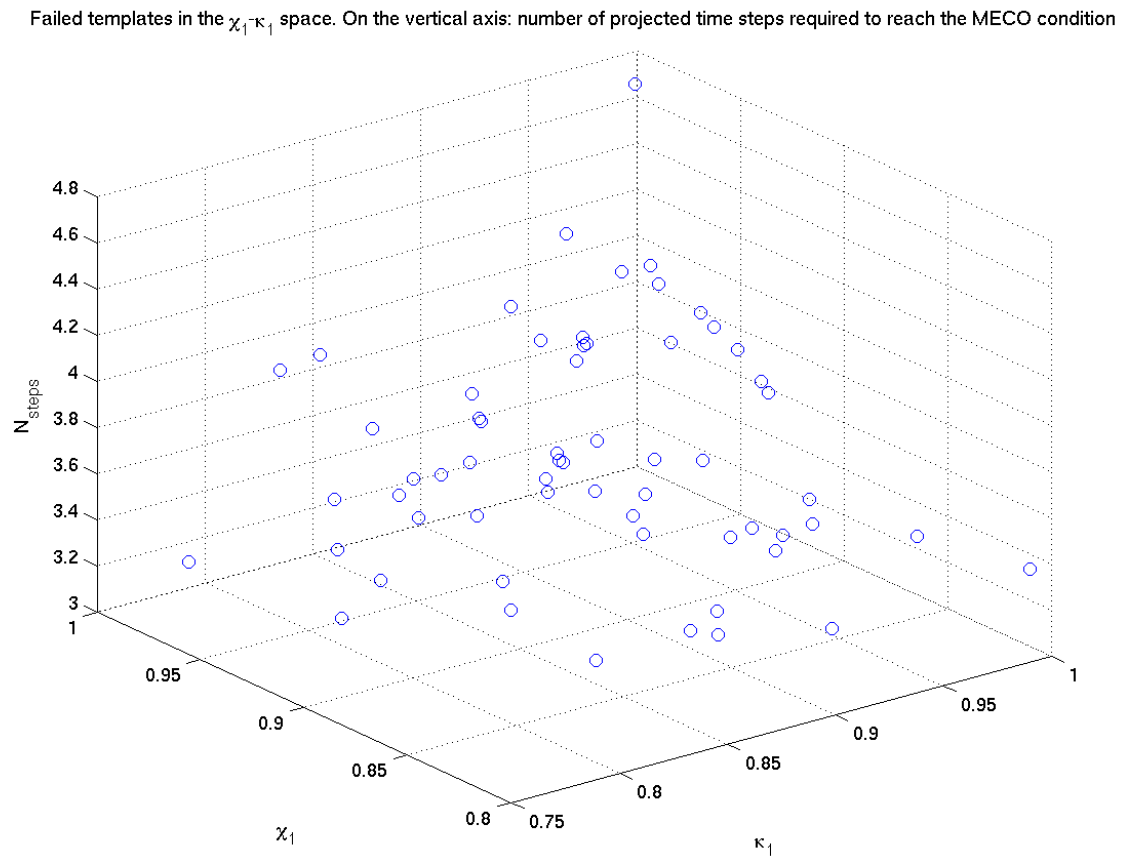


Figure 3.5: Number of projected time steps needed to reach the MECO condition vs the χ_1 - κ_1 plane.

We then tested the wave-generation code with the new “safety” check on the MECO condition, setting to five the maximum number of allowed projected time steps; with this precaution all 10000 templates were generated successfully.

3.4.2 Template Implementation

The construction of the template (3.16) requires the calculation of the 10 quantities $Q_0^I(t)$, $Q_{\pi/2}^I(t)$ with $I = 1, \dots, 5$. From these time-domain functions we construct the Fourier-transformed frequency-domain quantities $\tilde{Q}_0^1(f)$ and $\tilde{Q}_{\pi/2}^1(f)$, which are then required for the calculation of the SNR, described in the previous section. Fourier transforms, even if calculated using fast numerical algorithms (FFT), are very computationally expensive operations and the speed of the matched filtering is dominated by the number of such operations performed.

In the case of non-spinning templates, for binaries with total mass $M \lesssim 35M_\odot$, the SNR can be calculated out of the inner product between the signal s and the orthogonal components of the templates h_c and h_s (given by (2.70)-(2.71)), as

$$\rho = \frac{1}{\sigma} \sqrt{\langle s, h_c(t) \rangle^2 + \langle s, h_s(t) \rangle^2} \quad (3.127)$$

where $\sigma^2 = \langle h_c, h_c \rangle + \langle h_s, h_s \rangle$ is the template normalization factor.

To implement the digital matched filtering the discretized versions of $\langle s, h_c \rangle$ and $\langle s, h_s \rangle$ need to be evaluated; we see that these are analogous to the quantities (3.95)-(3.96) with the substitutions $\tilde{Q}_0^I \rightarrow h_c$ and $\tilde{Q}_{\pi/2}^I \rightarrow h_s$, therefore we have

$$\begin{aligned} \langle s, h_c \rangle(t_j) &= \frac{2\Delta t}{N} \sum_{k=0}^{N-1} \frac{\tilde{s}_k \tilde{h}_{ck}^*}{S_n(|f_k|)} e^{2\pi i j k/N} \\ &= \frac{2\Delta t}{N} \left[\sum_{k=N/2+1}^{N-1} \frac{\tilde{s}_k \tilde{h}_{ck}^*}{S_n(|f_k|)} e^{2\pi i j k/N} + \sum_{k=1}^{N/2-1} \frac{\tilde{s}_k \tilde{h}_{ck}^*}{S_n(|f_k|)} e^{2\pi i j k/N} \right] \\ &= \frac{2\Delta t}{N} \left[\sum_{k=1}^{N/2-1} \frac{\tilde{s}_k^* \tilde{h}_{ck}}{S_n(|f_k|)} e^{-2\pi i j k/N} + \sum_{k=1}^{N/2-1} \frac{\tilde{s}_k \tilde{h}_{ck}^*}{S_n(|f_k|)} e^{2\pi i j k/N} \right] \end{aligned} \quad (3.128)$$

$$\begin{aligned} \langle s, h_s \rangle(t_j) &= \frac{2\Delta t}{N} \sum_{k=0}^{N-1} \frac{\tilde{s}_k \tilde{h}_{sk}^*}{S_n(|f_k|)} e^{2\pi i j k/N} \\ &= \frac{2\Delta t}{N} \left[\sum_{k=N/2+1}^{N-1} \frac{\tilde{s}_k \tilde{h}_{sk}^*}{S_n(|f_k|)} e^{2\pi i j k/N} + \sum_{k=1}^{N/2-1} \frac{\tilde{s}_k \tilde{h}_{sk}^*}{S_n(|f_k|)} e^{2\pi i j k/N} \right] \end{aligned}$$

3. The Physical Template Family of Spinning Waveforms - PTF

$$= \frac{2\Delta t}{N} \left[\sum_{k=1}^{N/2-1} \frac{\tilde{s}_k^* \tilde{h}_{sk}}{S_n(|f_k|)} e^{-2\pi i j k/N} + \sum_{k=1}^{N/2-1} \frac{\tilde{s}_k \tilde{h}_{sk}^*}{S_n(|f_k|)} e^{2\pi i j k/N} \right] \quad (3.129)$$

where we set the DC ($k = 0$) terms to zero, since earth based gravitational wave detectors have no useful low-frequency response. Furthermore we assumed that there is no power at the Nyquist frequency ($k = N/2$), as the low pass filter that band limits the interferometer data to frequencies below f_{Ny} falls off rapidly as the Nyquist frequency is approached.

The validity of the Stationary Phase Approximation (see Sec. 2.4.5) for low-mass non-spinning templates allows to set $\tilde{h}_s(f) = i\tilde{h}_c(f)$ for $f > 0$, so Eq. (3.129) can be rewritten as

$$\begin{aligned} \langle s, h_s \rangle(t_j) &= \frac{2\Delta t}{N} \left[\sum_{k=1}^{N/2-1} \frac{\tilde{s}_k^* i\tilde{h}_{ck}}{S_n(|f_k|)} e^{-2\pi i j k/N} + \sum_{k=1}^{N/2-1} \frac{\tilde{s}_k (-i)\tilde{h}_{ck}^*}{S_n(|f_k|)} e^{2\pi i j k/N} \right] \\ &= 2i \frac{2\Delta t}{N} \left[\sum_{k=1}^{N/2-1} \frac{\tilde{s}_k^* \tilde{h}_{ck}}{S_n(|f_k|)} e^{-2\pi i j k/N} - \sum_{k=1}^{N/2-1} \frac{\tilde{s}_k \tilde{h}_{ck}^*}{S_n(|f_k|)} e^{2\pi i j k/N} \right] \end{aligned} \quad (3.130)$$

If we now introduce the complex object

$$T_j \equiv \sum_{k=1}^{N/2-1} \frac{\tilde{s}_k \tilde{h}_{ck}^*}{S_n(|f_k|)} e^{2\pi i j k/N} \quad (3.131)$$

we have

$$\langle s, h_c \rangle(t_j) = \frac{2\Delta t}{N} (T_j^* + T_j) = \frac{4\Delta t}{N} \Re(T_j) \quad (3.132)$$

$$\langle s, h_s \rangle(t_j) = \frac{2\Delta t}{N} (T_j^* - T_j) = \frac{4\Delta t}{N} \Im(T_j) \quad (3.133)$$

This allows to calculate the quantities $\langle s, h_c \rangle$ and $\langle s, h_s \rangle$ by a single complex inverse Fourier transform instead of two complex-to-real transforms, by defining

$$z_j \equiv \frac{4\Delta t}{N} T_j = \frac{4\Delta t}{N} \sum_{k=1}^{N/2-1} \frac{\tilde{s}_k \tilde{h}_{ck}^*}{S_n(|f_k|)} e^{2\pi i j k/N} = \frac{\Delta t}{N} \sum_{k=1}^{N/2-1} \tilde{z}_k e^{2\pi i j k/N} \quad (3.134)$$

where

$$\tilde{z}_k = \begin{cases} 4 \frac{\tilde{s}_k \tilde{h}_{ck}^*}{S_n(|f_k|)} & 0 < k < \frac{N}{2}, \\ 0 & \text{otherwise} \end{cases} \quad (3.135)$$

We then have

$$\Re(z_j) = \langle s, h_c \rangle(t_j) \quad (3.136)$$

$$\Im(z_j) = \langle s, h_s \rangle(t_j) \quad (3.137)$$

and the SNR can be written as

$$\rho(t_j) = \frac{|z_j|}{\sigma} \quad (3.138)$$

If we could do something similar for PTF templates we would be able to reduce the computation time significantly. We have seen in Sec. 3.2 that during the phase of adiabatic inspiral, both the time scale for the radiation-reaction induced evolution of frequency and the typical time of evolution of precession-induced amplitude and phase modulations are much bigger than the orbital period so that we can assume the validity of eqs.(3.24)-(3.25); however, to reduce computational costs, we would like to make an even stronger assumption, i.e. $\tilde{Q}_{\pi/2}^I(f) \simeq i\tilde{Q}_0^I(f)$ for $f > 0$.

This has indeed been investigated numerically for 1000 different random templates by evolving the dynamical variables, calculating $\tilde{Q}_{\pi/2}^I(f)$ and $i\tilde{Q}_0^I(f)$ for the same set of parameters and calculating the match between the two quantities; as a matter of fact, in terms of matched filtering, it is important that the two quantities are *close* with respect to the distance (2.30), i.e. $\mathcal{D} [Q_{\pi/2}^I, iQ_0^I] \simeq 0$.

Results show that these five quantities agree up to 2% for all the templates generated (see fig 3.6); this is acceptable since the MM usually required for a template bank is 0.97.

With the above assumptions the numerical implementation of the vectors $\mathbf{v}_{1,2}$ given by eqs. (3.95)-(3.96) can be obtained with the algorithm outlined above, by defining

$$\tilde{z}_k^I \equiv \begin{cases} 4 \frac{\tilde{s}_k \tilde{Q}_{0k}^{I*}}{S_n(|f_k|)} & 0 < k < \frac{N}{2}, \\ 0 & \text{otherwise} \end{cases} \quad (3.139)$$

and therefore

$$v_1^I(t_j) = \Re(\tilde{z}_j^I) \quad (3.140)$$

$$v_2^I(t_j) = \Im(\tilde{z}_j^I) \quad (3.141)$$

Using this approximation we are able to reduce the number of real-to-complex forward FFTs performed by a factor of 2; as a matter of fact for every template we only need to calculate the components \tilde{Q}_0^I and not the $\tilde{Q}_{\pi/2}^I$. Furthermore,

3. The Physical Template Family of Spinning Waveforms - PTF

for every template, we traded two complex-to-real inverse FFTs for one complex-to-complex FFT, therefore reducing the overall computation time of the matched filtering algorithm of more than a factor 2.

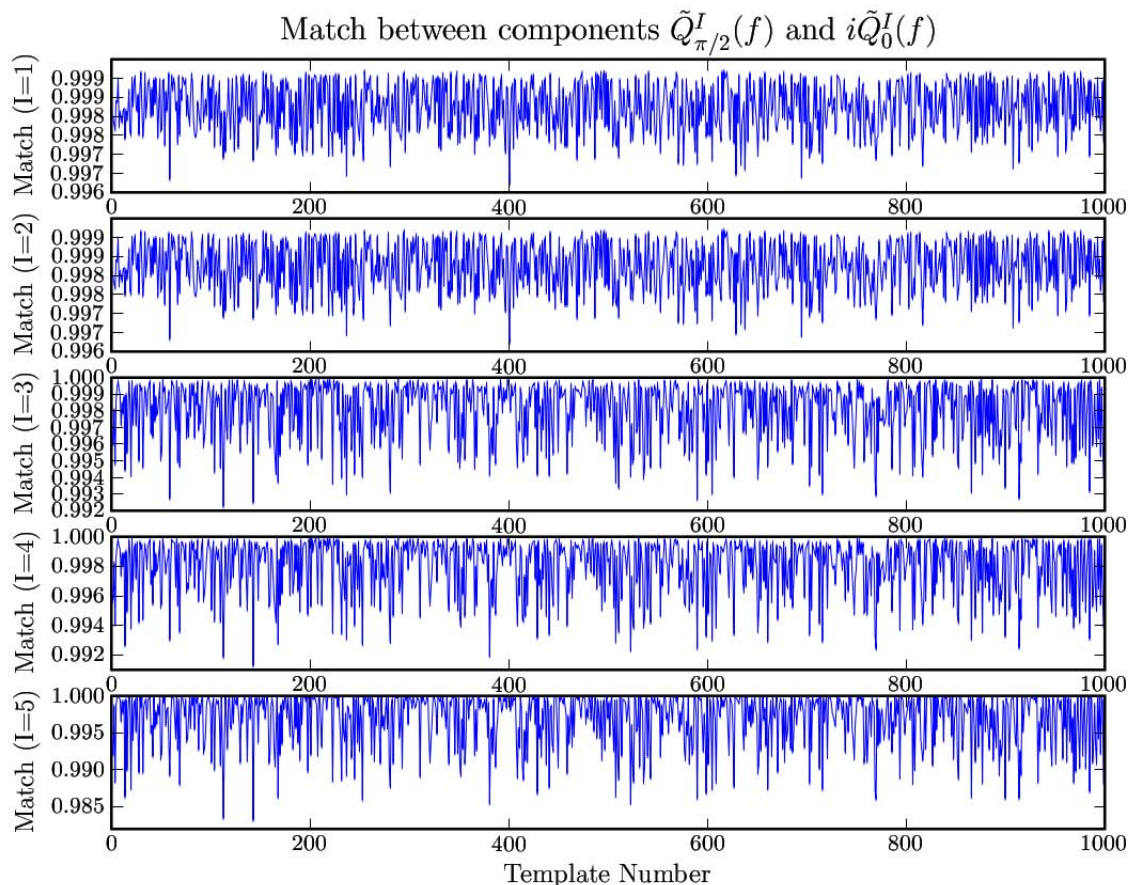


Figure 3.6: Match between the components $\tilde{Q}_{\pi/2}^I(f)$ and $i\tilde{Q}_0^I(f)$ for 1000 randomly generated single-spin templates.

3.4.3 Template Bank Generation

As we explained in Sec. 2.5 the algorithm for constructing a template bank requires the knowledge of the parameters space metric \mathbf{g} (this is not the only method; a few different random template-placement algorithms have been used for higher-dimension parameter spaces [62, 63]).

We have seen in Sec. 2.7.2 that for low-mass non-spinning templates the only intrinsic parameters are the two masses m_1 and m_2 and therefore the template-bank

space is 2-dimensional. The metric in the intrinsic parameter space is uniquely defined since the dependence of the templates on the extrinsic parameters is just through the effective distance factor which does not influence the value of the match (2.29) (see Sec. 2.5); we have indeed seen in Sec. 2.5.3 that the projected metric (2.42) does not depend on the extrinsic parameters.

The templates are then placed on a hexagonal lattice using the metric defined on the parameter space.

For the spinning case on the other hand the dependence of the templates on the extrinsic parameters is more complicated and this influences the value of the match differently in each point of the intrinsic parameter space; therefore the projected metric needs to be calculated for every point in the intrinsic parameter space using one of the prescriptions outlined in Sec. 2.5.3.

We have seen from Sec. 3.1 that PTF templates can be re-parametrized so that they depend on four intrinsic parameters only, therefore the template-bank space is 4-dimensional and we need to construct the projected metric $g_{BC}^{proj}[m_1, m_2, \chi_1, \kappa_1]$ by maximizing over all the remaining extrinsic parameters.

Unfortunately such a metric has not been fully implemented yet, therefore we had to resort to alternative methods to place templates. Since the goal of this work is to investigate the feasibility of a full search with PTF templates by testing all the stages of the pipeline, we decided to leave the implementation of a metric-based template placement code to future projects and develop a temporary algorithm, based on the existing code.

Since non-spinning binaries have a good efficiency in recovering spinning injections, we expect that a straightforward extension of the non-spinning template placement code should yield an effective kludge template bank. We therefore implemented an algorithm that first calls the template-placement code for non-spinning binaries to populate the mass space; for each point in the mass space we then construct $N_{\chi_1} \times N_{\kappa_1}$ templates, where N_{χ_1} and N_{κ_1} are the number of desired points respectively in the χ_1 and κ_1 directions of the template bank.

The non-spinning template-placement code has been modified so that the covered range of masses is restricted to the region of validity of the adiabatic approximation for single-spin binaries, i.e. $7 < M < 15M_\odot$ with $6 < m_1 < 14M_\odot$ and $1 < m_2 < 3M_\odot$, while a regular template-bank for low-mass non-spinning binaries spans the mass-space $M < 35M_\odot$, with $1 < m_1, m_2 < 34M_\odot$.

Obviously a Minimal Match MM cannot be defined a priori for this kludge template-bank but it can be calculated a posteriori through *bank simulations*, where a large number of random signals are filtered through the template bank yielding the highest match for each signal; the minimum value of the match in the limit of infinitely dense sets of injected signals is called the *fitting factor* (FF). The density of points in the spin directions χ_1 and κ_1 can then be increased until the FF reaches a maximum, above which the template-bank over-covers the parameter space without

further improvements.

In the perspective of developing a reasonably fast pipeline (until a metric-based or a random template-placement code is available) we decided to construct template banks with discrete values of χ_1 and κ_1 on square grids so that the total number of templates generated is $\lesssim 3$ -5 times bigger than the corresponding non-spinning low-mass full template bank (~ 4000 -7000 templates); this is obtained by constructing ~ 15 templates for every point in the m_1 - m_2 mass space. Bank simulations (see Sec. 4.2) show that this template bank has an average match of 0.94 in recovering random single-spin signals.

The reason why the PTF template bank does not contain 15 times more templates than the non-spinning one is that the latter covers a much wider mass region; in particular the region for which $1 < m_{1,2} < 3 M_\odot$ has a very high density.

The figures below show sections of a typical PTF template bank (14744 templates) in the mass plane and in the spin plane, compared to a typical non-spinning low-mass full template bank (4302 templates).

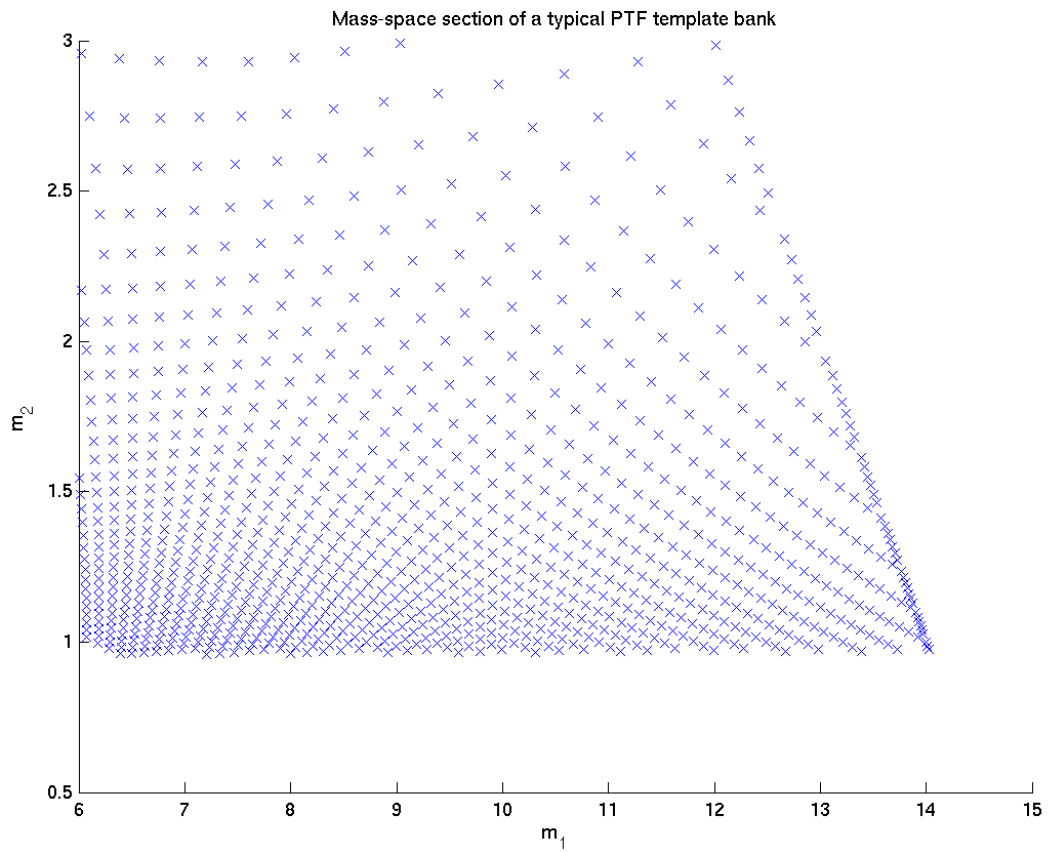


Figure 3.7: Typical PTF template bank projected in the m_1 - m_2 plane. Masses are in units of M_\odot

3. The Physical Template Family of Spinning Waveforms - PTF

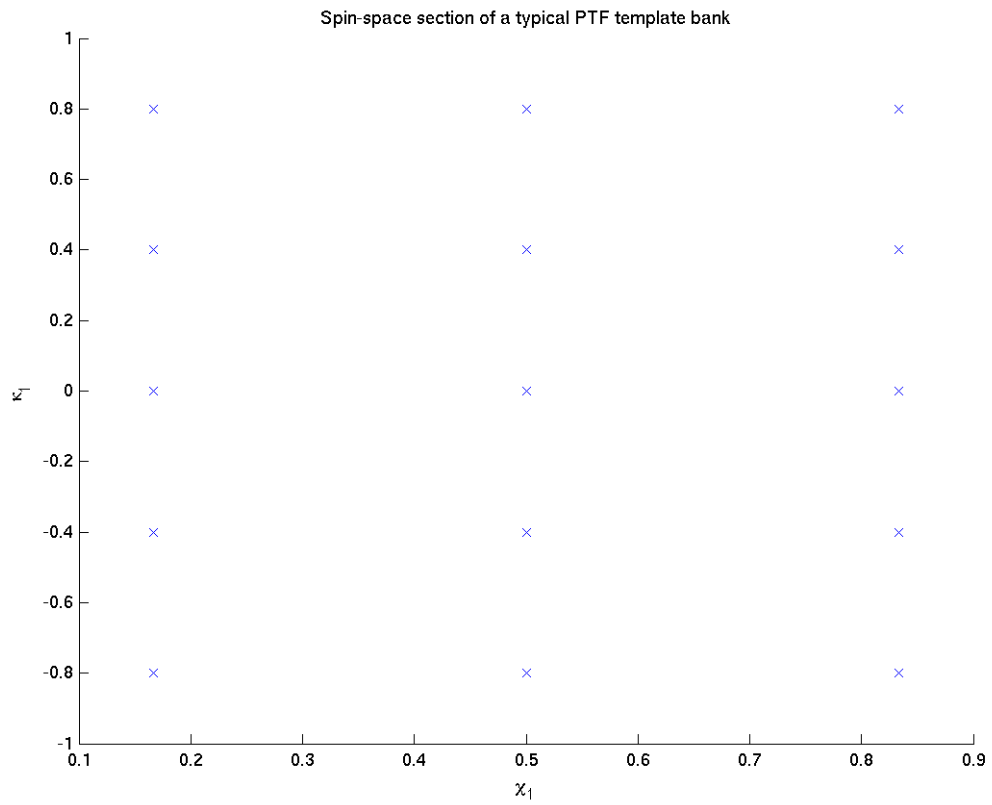


Figure 3.8: Typical PTF template bank projected in the χ_1 - κ_1 plane.

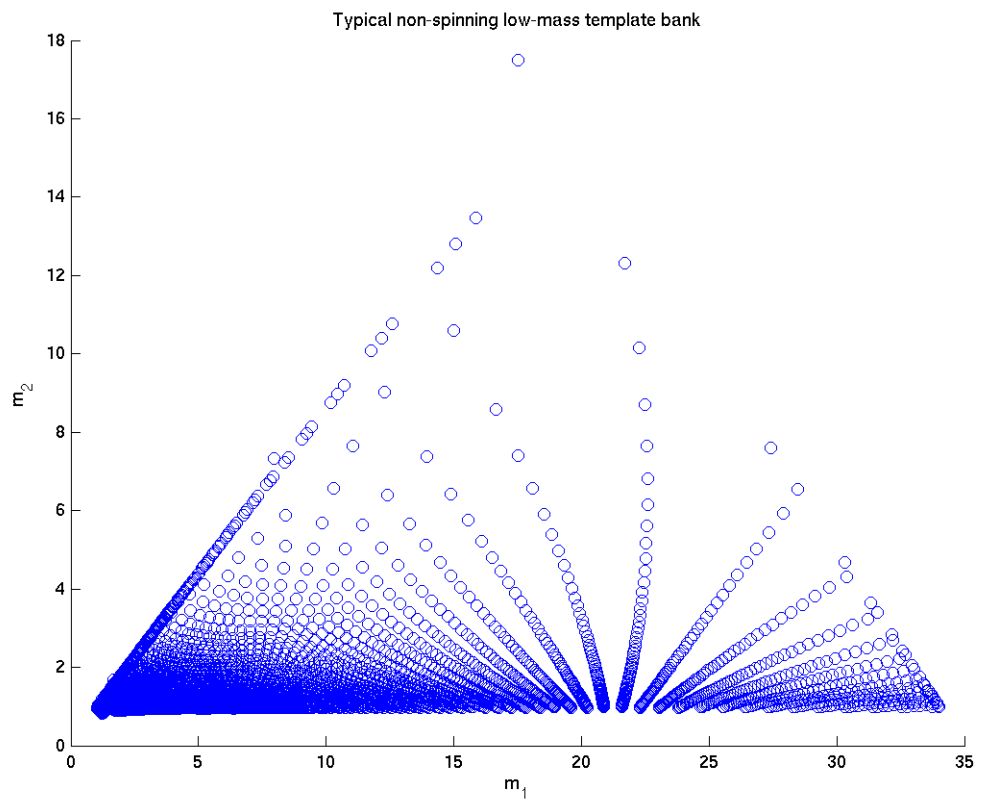


Figure 3.9: Typical non-spinning low-mass full template bank.

3.4.4 Coincidence Stage

Long baseline interferometric gravitational wave detectors, such as (LIGO) [41], Virgo [42] and GEO 600 [43], are currently acquiring the best data ever. However, despite the great achievements in noise isolation, controls and electronic feedbacks, the detector noise is neither Gaussian nor stationary, so the output of matched filtering of data segments from single interferometers is still dominated by noise triggers, called glitches. To prevent such noise artifacts from being mistakenly considered GW signals, the first step is to compare outputs of different interferometers to look for *coincident triggers*; if a trigger corresponds to a real GW signal from the distant universe, then it must be detected by all 3 LIGO interferometers (possibly by VIRGO and GEO as well), if they are operating at the time of the detection. Triggers from two different detectors must be recorded within the light travel time $\tau = dist_{1-2}/c$ between the two sites.

In coincidence analysis data sets from each detector will be analyzed separately and the triggers from the end of the pipeline from different detectors compared with one another to identify triggers that might be in coincidence with one another. More precisely, the goal is to find if the parameters (e.g., in the case of a coalescing binary the time of merger, the component masses and spins) of a trigger from one detector are identical to those from another. Since the background noise corrupts any inherent signal it is highly improbable that the same gravitational wave in different detectors can be associated with exactly the same set of parameters. However, it should be possible to detect signals in coincidence by demanding that the measured parameters lie in a sufficiently small range [44, 45, 46, 47, 48, 49]. Thus, we can revise the coincidence criteria as follows: triggers from different detectors are said to be in coincidence if their parameters all lie within a certain range.

From the above discussion it is clear that an important aspect of coincidence analysis is the determination of the range of parameter values to be associated with each trigger. To this end, until recently, the LIGO Scientific Collaboration (LSC) has deployed a phenomenological method for assigning the ranges [44, 45, 46, 47, 48, 49]. More precisely, one performs a large number of simulations in which a signal with a known set of parameters is added in software to the data which is then passed through the analysis pipeline. The pipeline identifies the most probable parameters with each injected signal and the ensemble of injected and measured parameters gives the distribution of the errors incurred in the measurement process. Given the distribution of the errors, one can choose a range for each parameter such that more than, say, 95% of the injected signals are detected in coincidence. Choosing wider windows will enable greater detection probability but also increases the rate of accidental triggers. On the contrary, smaller windows decrease the false alarm rate but also reduce the detection probability.

However, because this method uses rectangular windows, it ignores the correlations between different parameters. For instance, in the case of a chirping signal from a BH binary the shape of the signal depends, among others, on the component masses. However, not all combinations of the two masses lead to signals that are easily distinguishable from one another. Indeed, at the lowest post-Newtonian order the waveform depends only on a certain combination of the masses called the chirp mass; binaries of different values for the two masses but the same chirp mass produce essentially the same signal. This degeneracy is broken when post-Newtonian corrections are included. Nevertheless, the two mass parameters continue to be highly correlated.

Another drawback is that the method employs windows of the same size throughout the parameter space while we know that errors in the measurement of the parameters depends, in some cases quite sensitively, on the parameters. Drawing again from our example of a binary, the error in the estimation of the chirp mass can vary by more than two orders of magnitude across the parameter space of interest in the case of systems that LIGO is expected to observe (see, e.g., [52, 35, 53, 54, 55, 56, 58, 59, 60]). Clearly, it is not optimal to deploy windows of the same size all over the parameter space.

Furthermore, by not taking into account parameter covariances, the method entails independent tuning of several parameters at the same time. This could be a horrendous problem when dealing with signals characterized by many parameters. For instance, continuous radiation from a pulsar is characterized by the location of the pulsar, its spin frequency, the derivative of the frequency and so on. These physical parameters are all not independent; the existence of covariances among them means that not all variations of the parameters leads to distinct signals. This further implies that it may not be necessary to tune each parameter separately, rather it should be enough to tune only a subset of the parameters or, more precisely, only the principal components. Finally, by using windows of the same size irrespective of the signal-to-noise ratio of the trigger, the method suffers from an undesirably high false alarm rate, particularly in the tail of the SNR distribution. Needless to say, a successful detection of gravitational waves necessitates as clean a distribution of the SNRs as possible, with little contamination of the tails. One way of reducing the false alarm rate is by using tighter windows at higher SNRs. This is well-motivated since true high-SNR events will be associated with smaller errors.

A much more efficient algorithm, now used for low-mass non-spinning templates, takes into account the correlations amongst the various parameters and deploys parameter- and SNR-dependent ellipsoidal windows defined by the Fisher information matrix using a single parameter. For each interferometer an ellipsoid centered around the trigger is considered; if two or more ellipsoids from different interferometers have a non-null intersection, then we have a coincidence (which

3. The Physical Template Family of Spinning Waveforms - PTF

can be double, triple, quadrupole etc.).

This method however requires the knowledge of the metric (2.36) of the intrinsic parameter space which is not available yet for PTF, we therefore decided to use the rectangular window method, leaving the implementation of a metric-based coincidence stage to future works. Also, since the template bank is very coarse in the intrinsic parameter space (see Fig.(3.8)), we decided to test for coincidences only on the mass parameters (and on time of arrival).

Chapter 4

Results

Here we present tests and results obtained at the different stages of the pipeline.

4.1 Testing the Filtering Code

4.1.1 Gaussian Noise

In order to validate the matched filtering engine we initially perform a series of tests to check that the normalization and the statistic in presence of Gaussian noise are correct. We therefore generate stretches of simulated colored Gaussian noise (colored with the theoretical LIGO power spectral density curve $S_n(f)$) with different numbers of sample points N_{points} and for different sampling intervals Δt , and then we filter them with many templates in different corners of the parameter space. We recall that the SNR statistic (3.45) for PTF templates is χ -distributed with six degrees of freedom, therefore ρ^2 is χ^2 -distributed with six degrees of freedom.

We plot the output $\rho(t)$ time series from the matched filtering algorithm, we histogram it and we fit it with a (non-normalized) χ probability density function

$$\chi(x; k) = \begin{cases} A \frac{x^{k-1} e^{-x^2/2}}{2^{k/2-1} \Gamma(\frac{k}{2})} & \text{for } x > 0, \\ 0 & \text{for } x \leq 0 \end{cases} \quad (4.1)$$

where k is the number of degrees of freedom of the distribution and A is a constant multiplicative factor to be fitted with the actual data distribution. In our case $k = 6$ so $\Gamma(3) = 2! = 2$ and Eq. (4.1) becomes

$$\chi(x) = A \frac{x^5 e^{-x^2/2}}{8} \quad (4.2)$$

4. Results

The corresponding probability distribution for ρ^2 is a χ^2 (given by Eq. (3.86) with $n \rightarrow k$) with mean corresponding to the number of degrees of freedom, $\overline{\rho^2} = 6$. In the figures below the mean is denoted as $\bar{x} = \langle x \rangle$ and it is calculated over the entire stretch of data.

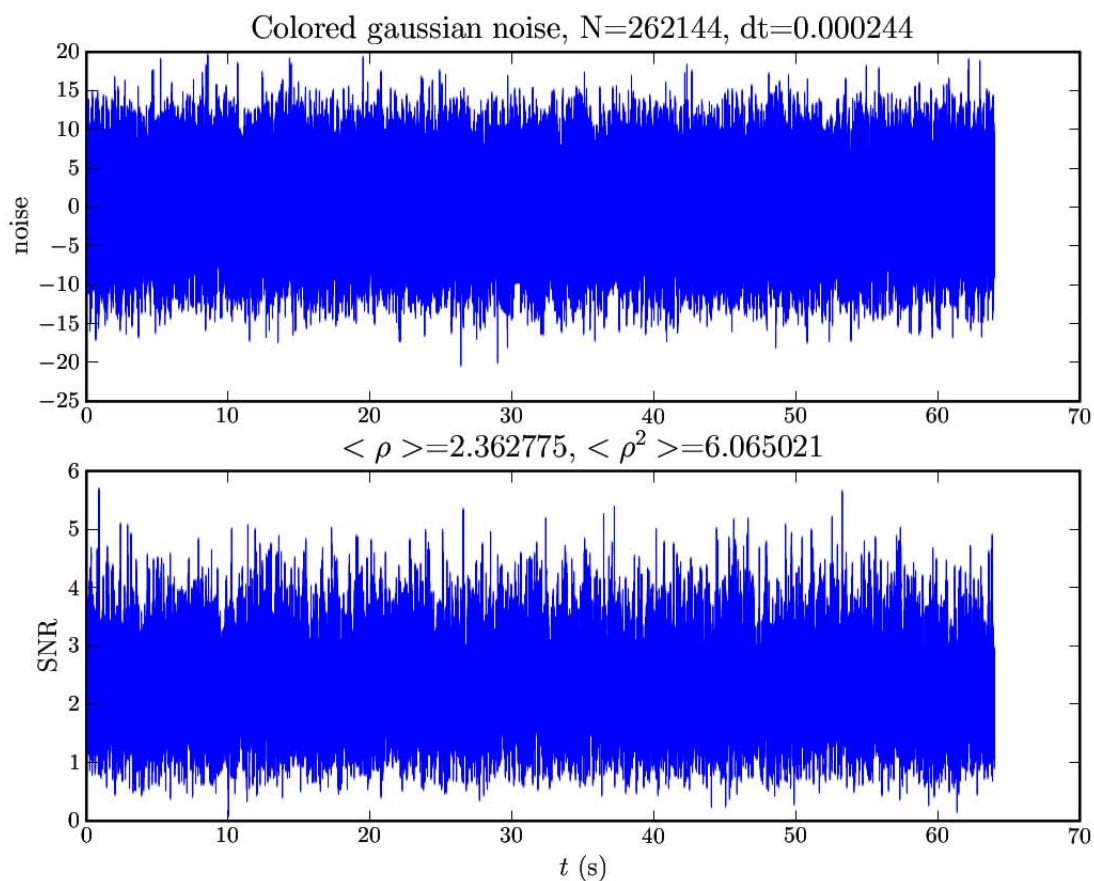


Figure 4.1: Plot of 64 seconds of simulated colored Gaussian noise (top figure) and corresponding $\rho(t)$ time series (bottom figure) for a PTF template with intrinsic parameters $m_1 = 9M_\odot$, $m_2 = 2.0M_\odot$, $\chi_1 = 0.5$, $\kappa_1 = 0.5$; $N_{points} = 262144$ sampled at $4096Hz$ ($\Delta t = 0.000244s$) and noise generation seed 130772. $\langle \rho \rangle = 2.362775$ and $\langle \rho^2 \rangle = 6.065021$.

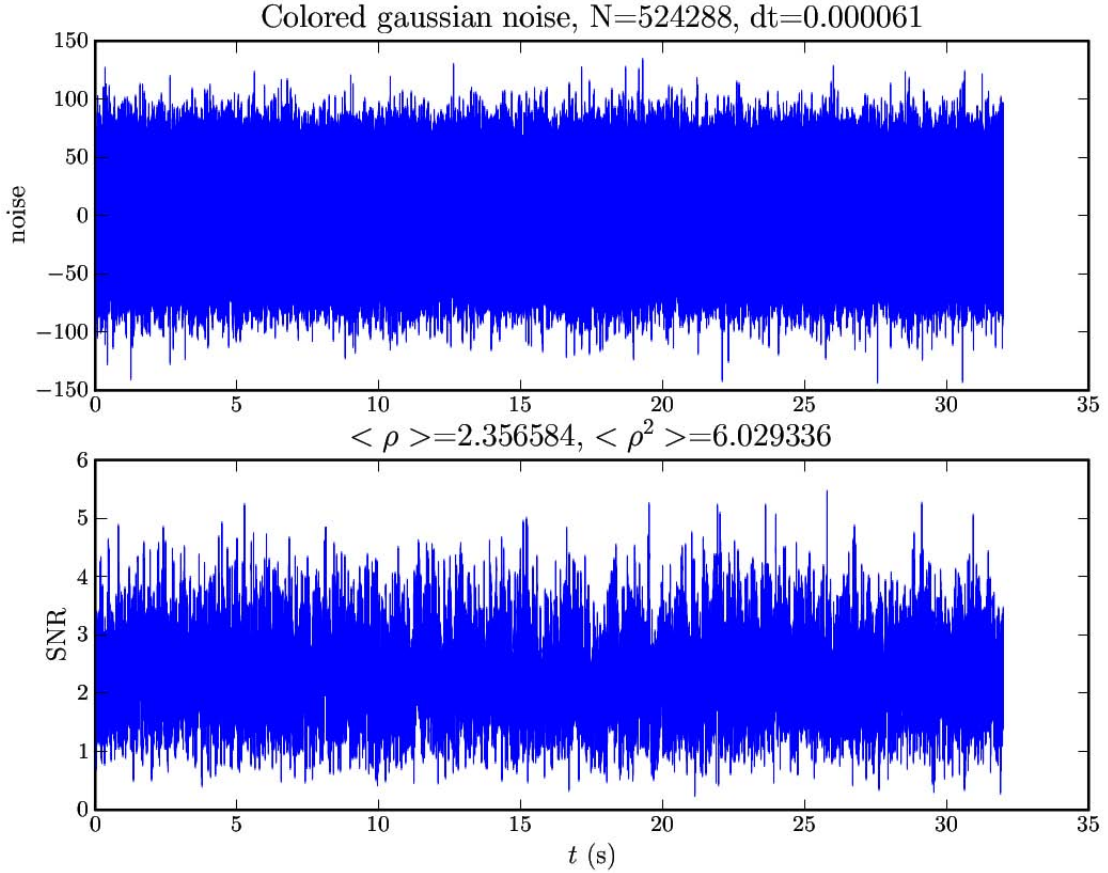


Figure 4.2: Plot of 32 seconds simulated colored Gaussian noise (top figure) and corresponding $\rho(t)$ time series (bottom figure), for a PTF template with intrinsic parameters $m_1 = 9M_\odot$, $m_2 = 2.0M_\odot$, $\chi_1 = 0.5$, $\kappa_1 = 0.5$; $N_{points} = 524288$ sampled at $16384Hz$ ($\Delta t = 0.000061s$) and noise generation seed 130772. $\langle \rho \rangle = 2.356584$ and $\langle \rho^2 \rangle = 6.029336$.

4. Results

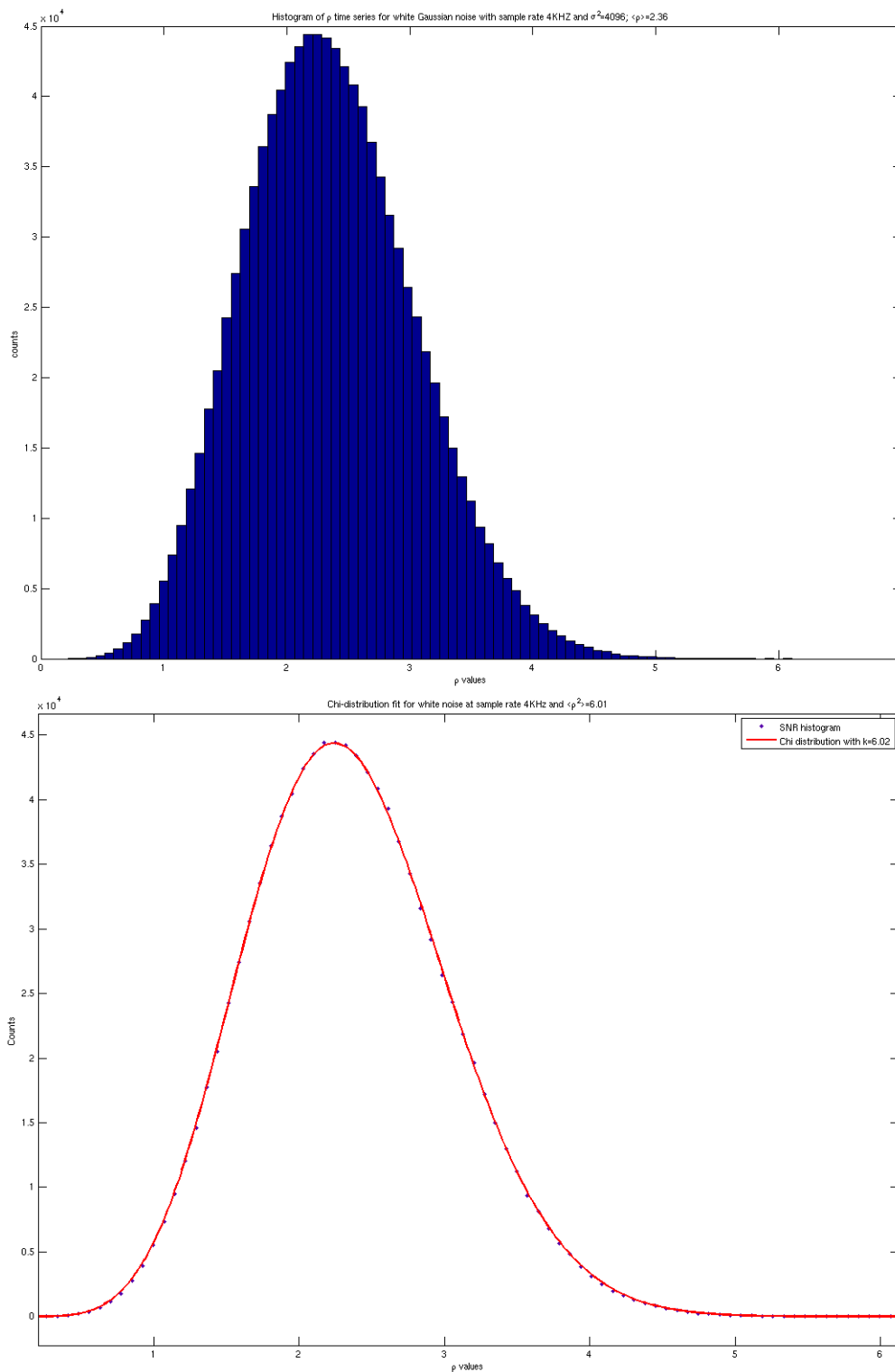


Figure 4.3: Histogram of ρ values for a PTF template with intrinsic parameters $m_1 = 8M_\odot$, $m_2 = 1.4M_\odot$, $\chi_1 = 0.7$, $\kappa_1 = 0.6$, obtained filtering a stretch of simulated white Gaussian noise sampled at 4096Hz ($\Delta t = 0.000244\text{s}$) (top figure) and fit with a χ distribution probability function with $k = 6.02$ (bottom figure). $\langle \rho^2 \rangle = 6.01$

4.1.2 Gaussian Noise with Injected Software Signals

After testing the normalization and the statistics of the matched filtering output in presence of Gaussian noise, we proceed to injecting many different simulated software signals on top of the noise and check whether the filter is able to recover them by using exactly matching templates. Fig. 4.4 shows a typical signal injected with intrinsic parameters $m_1 = 9.0 M_\odot$, $m_2 = 2.0 M_\odot$, $\chi_1 = 0.8$, $\kappa_1 = 0.7$.

We inject signals at the beginning of the data segment so that the arrival time corresponds to the length of the signal; Fig. 4.5 shows the time series of Gaussian noise plus injection and the output of the matched filtering process for a signal (and a template) with intrinsic parameters $m_1 = 7 M_\odot$, $m_2 = 1.4 M_\odot$, $\chi_1 = 0.5$, $\kappa_1 = 0.99$, at a distance of 1 Mpc directly above the detector (*optimally located*) and with orbital plane initially perpendicular to the line of sight (*optimally oriented*). In practice, when we search for signals, we don't store the whole time series but only the times at which the SNR rises above a chosen threshold.

All simulations performed showed that the PTF filter is able to recover signals injected at close distance (1 Mpc) with the expected SNR and with accurate arrival time.

4. Results

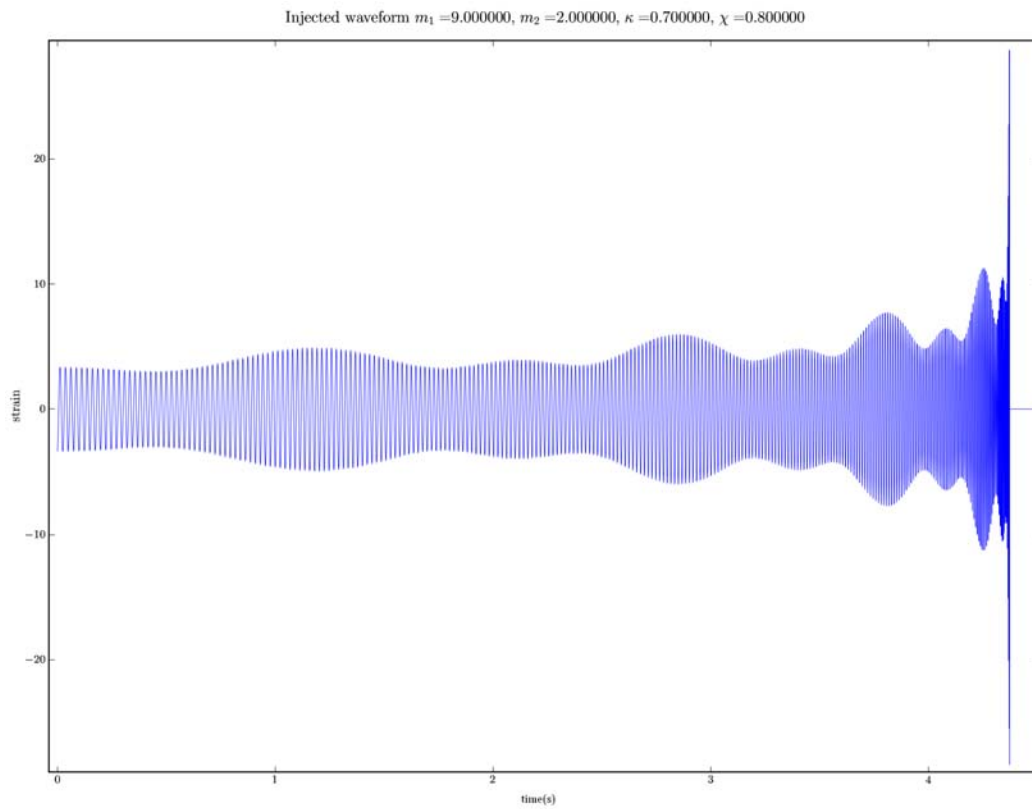


Figure 4.4: Simulated gravitational wave signal emitted by a single-spin binary with parameters $m_1 = 9.0 M_\odot$, $m_2 = 2.0 M_\odot$, $\chi_1 = 0.8$, $\kappa_1 = 0.7$.

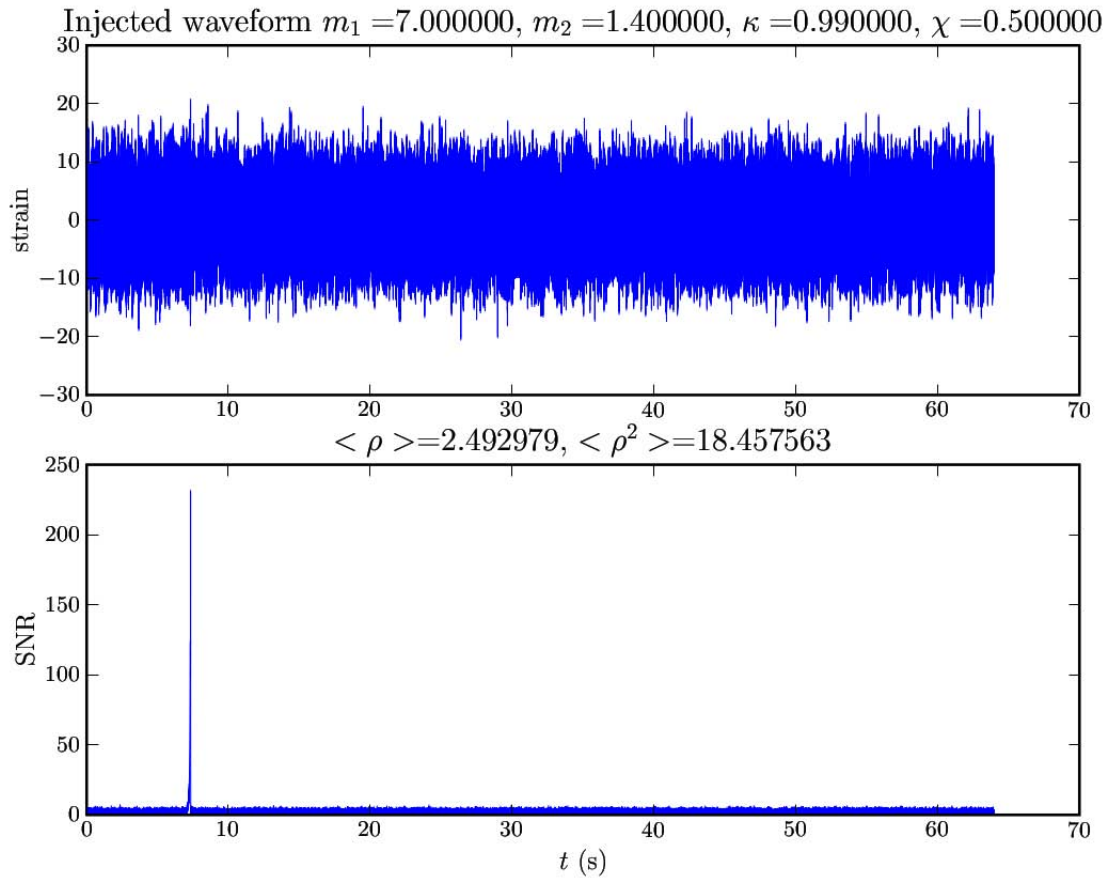


Figure 4.5: Plot of the SNR time series (bottom figure) for a segment of simulated Gaussian noise with an injected signal (top figure) at a distance of 1 Mpc, with parameters $m_1 = 7 M_\odot$, $m_2 = 1.4 M_\odot$, $\chi_1 = 0.5$, $\kappa_1 = 0.99$.

4.2 Bank Simulations

We test the efficiency of the template bank by injecting a large number of single-spin signals (injections) with masses and spins randomly chosen in the PTF ranges ($6 \leq m_1 \leq 14 M_\odot$, $1 \leq m_2 \leq 3 M_\odot$, $0 \leq \chi_1 \leq 1$, $-1 \leq \kappa_1 \leq 1$), random distance and random sky location and orientation, and calculating the maximum match over the entire bank for every injection. Matches are calculated in the absence of noise, only the power spectral density $S_n(f)$ of simulated Gaussian noise is used to compute inner products.

The plots below show results from a bank simulation containing 4096 random signals; we compare results with a parallel simulation done using a low-mass non-spinning template bank. Results show that PTF templates have higher average matches (~ 0.94) than non-spinning SPA templates (~ 0.87) over the whole parameter space.

In particular plots (4.6)-(4.7) show that PTF templates have higher efficiency in matching signals corresponding to binaries with low value of the m_2 component mass, while plots (4.8) show that they have higher efficiencies in recovering signals from binaries with high values of the spin magnitude parameter χ_1 and misalignment between $\hat{\mathbf{L}}_N$ and \mathbf{S}_1 , corresponding to values of $-0.8 < \kappa_1 < 0.8$; these results confirm what was expected from previous studies, i.e. that detection efficiency for non-modulated templates decreases with increasing mass-ratio, increasing spin magnitude and increasing misalignment of the spin with the orbital angular momentum [7, 10, 33].

Figures (4.9)-(4.10) show that only 139 signals ($\sim 3.4\%$) have a match lower than 0.8 using the PTF template bank, while for the SPA template bank the number is 977 ($\sim 23.85\%$). If we look at signals with match lower than 0.7 (figs. (4.11)-(4.12)), the above numbers drop to 6 injections ($\lesssim 0.15\%$) for PTF, and 382 injections ($\sim 9.33\%$) for SPA.

We note that the trigger with the lowest match ($\mathcal{M}_{PTF} = 0.1917$, $\mathcal{M}_{SPA} = 0.2980$), corresponding to parameters $m_1 = 11.43 M_\odot$, $m_2 = 1.07 M_\odot$, $\chi_1 = 0.87$, $\kappa_1 = -0.19$, is actually caused by a failure of the injection code which generated a truncated waveform; if we remove this trigger, the minimum match for the PTF template bank is $MM_{PTF} = 0.6714$ while for the non-spinning SPA template bank $MM_{SPA} = 0.4629$.

We expect that, once a template-placement code is available, an optimal PTF template bank will allow for much better minimal matches, especially in the regions where non-spinning SPA templates perform worse.

In the figures below we plot match both in the m_1 - m_2 plane and in the M_{chirp} - η space, where M_{chirp} is the *chirp mass* given by

$$M_{chirp} = M\eta^{3/5} \quad (4.3)$$

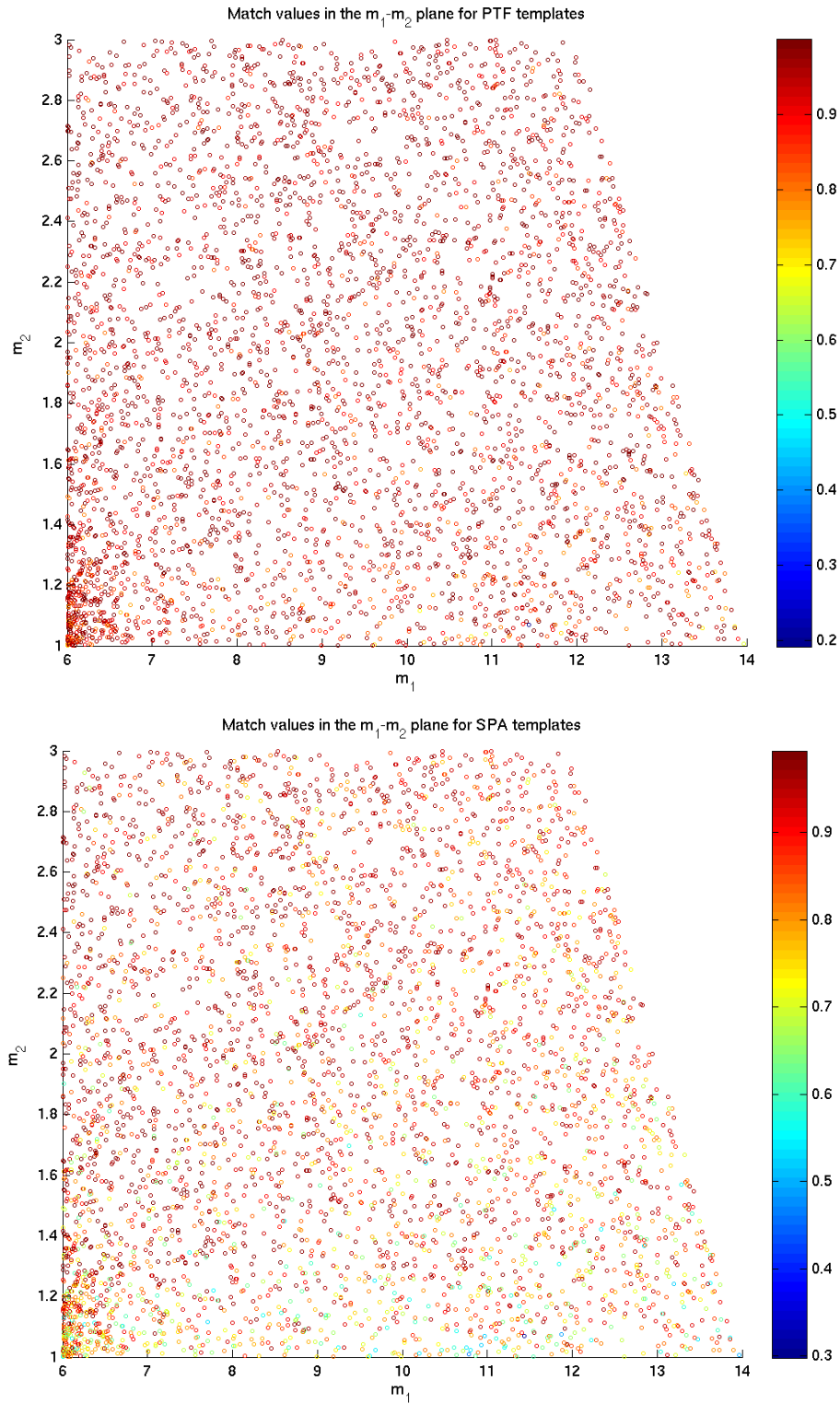


Figure 4.6: Comparison of bank-simulation results between PTF templates (top figure) and non-spinning SPA templates (bottom figure) in the m_1 - m_2 plane.

4. Results

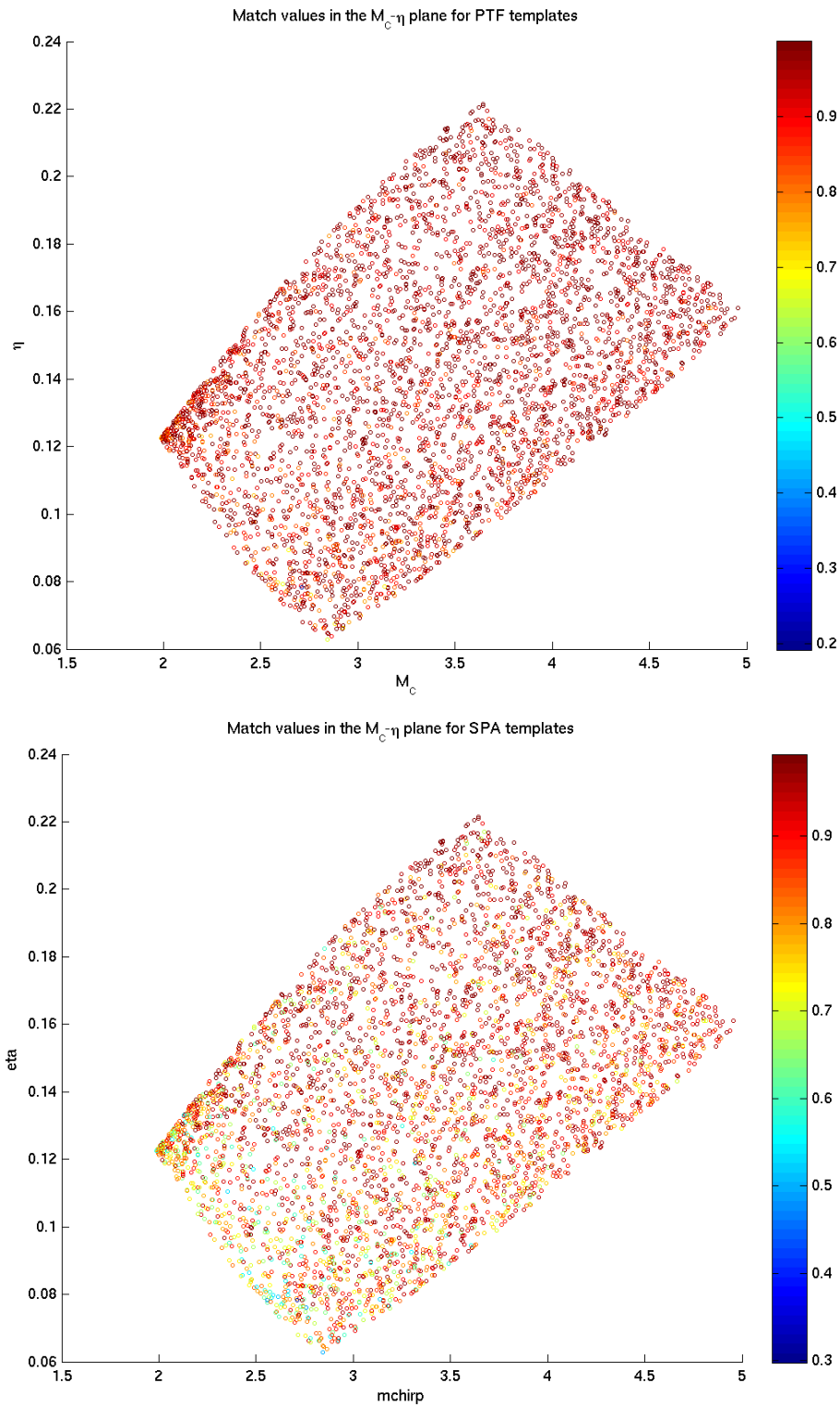


Figure 4.7: Comparison of bank-simulation results between PTF templates (top figure) and non-spinning SPA templates (bottom figure) in the M_C - η plane.

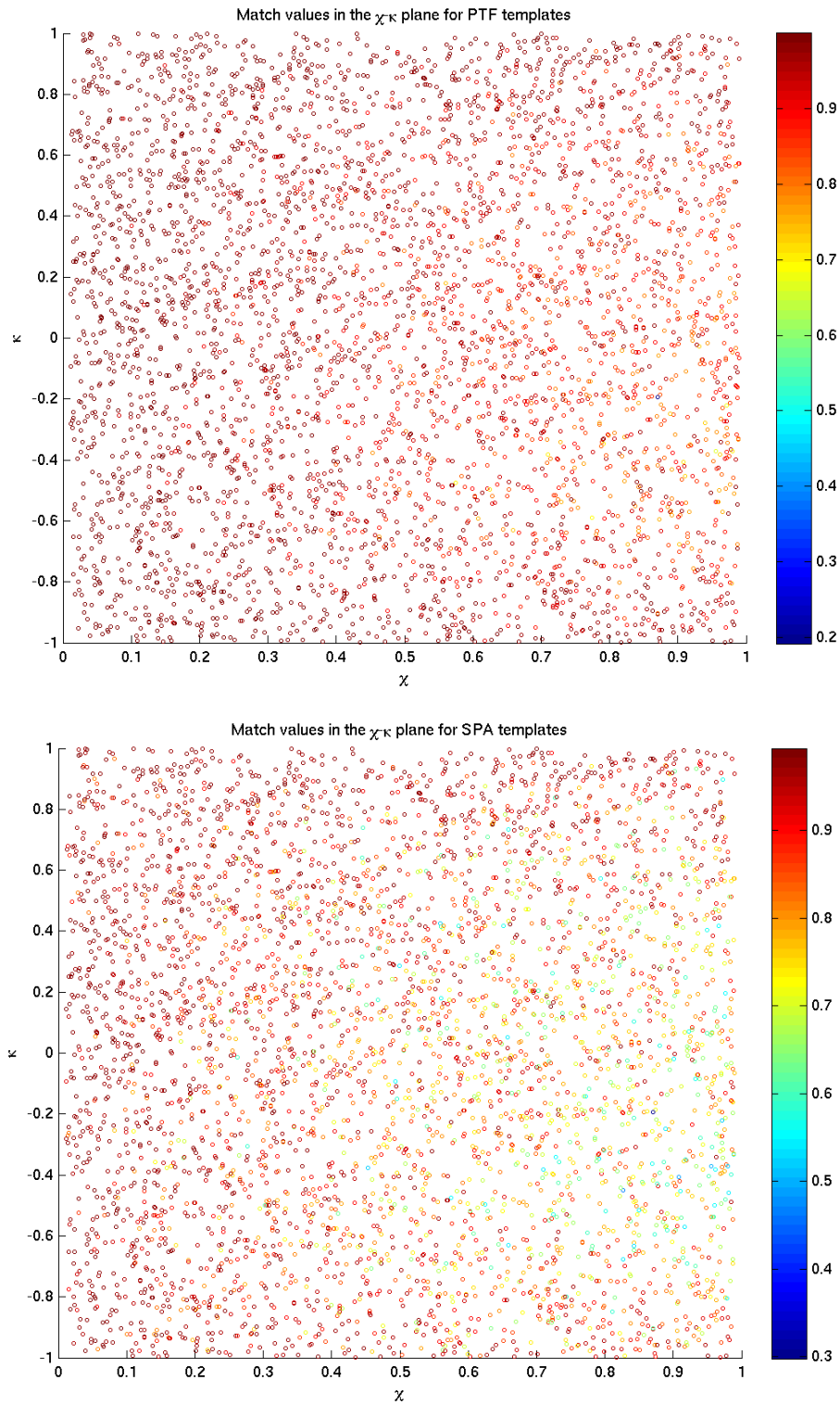


Figure 4.8: Comparison of bank-simulation results between PTF templates (top figure) and non-spinning SPA templates (bottom figure) in the κ_1 - χ_1 plane.

4. Results

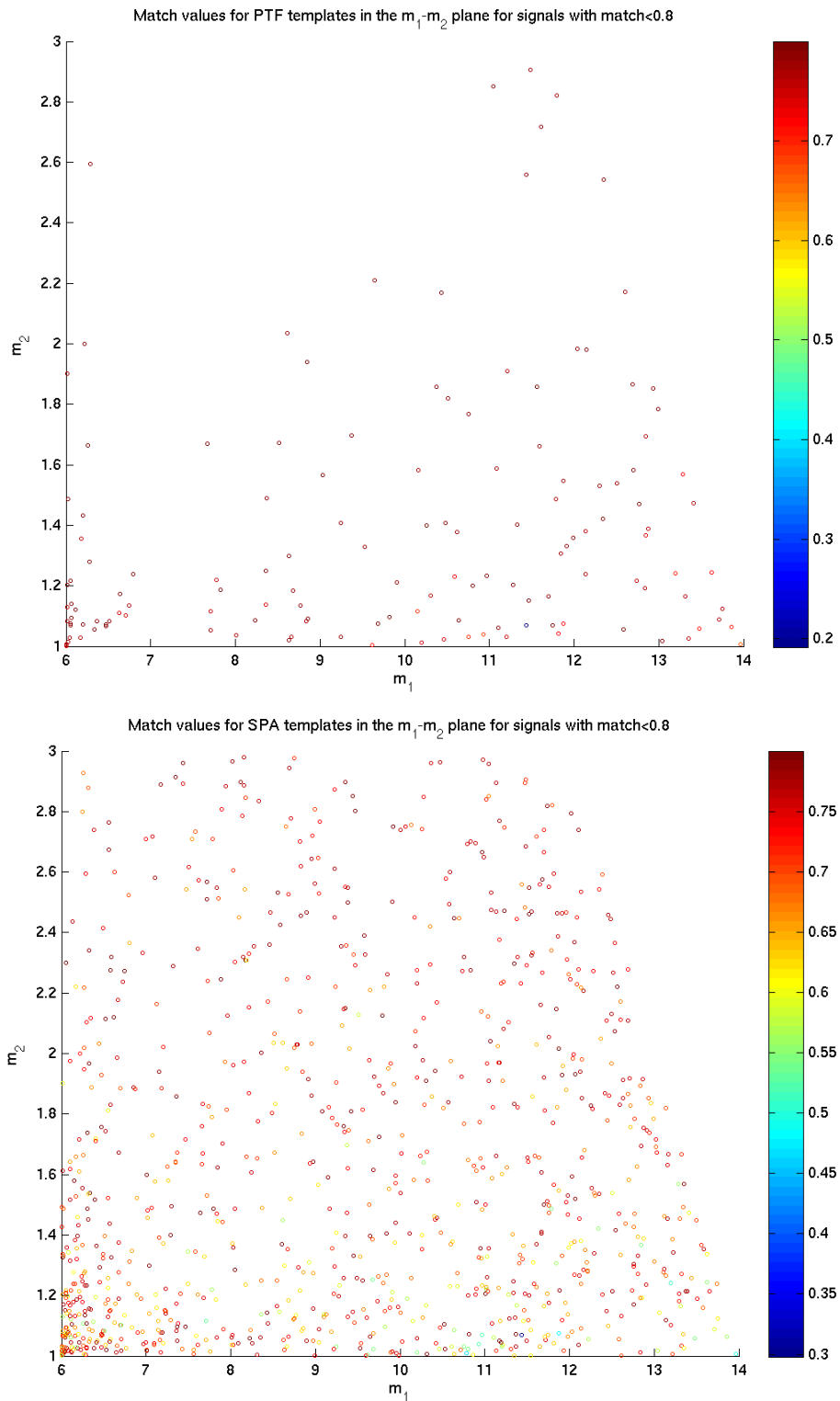


Figure 4.9: Signals with match lower than 0.8 for PTF templates (top figure - 139 points) and non-spinning SPA templates (bottom figure - 977 points) in the m_1 - m_2 plane.

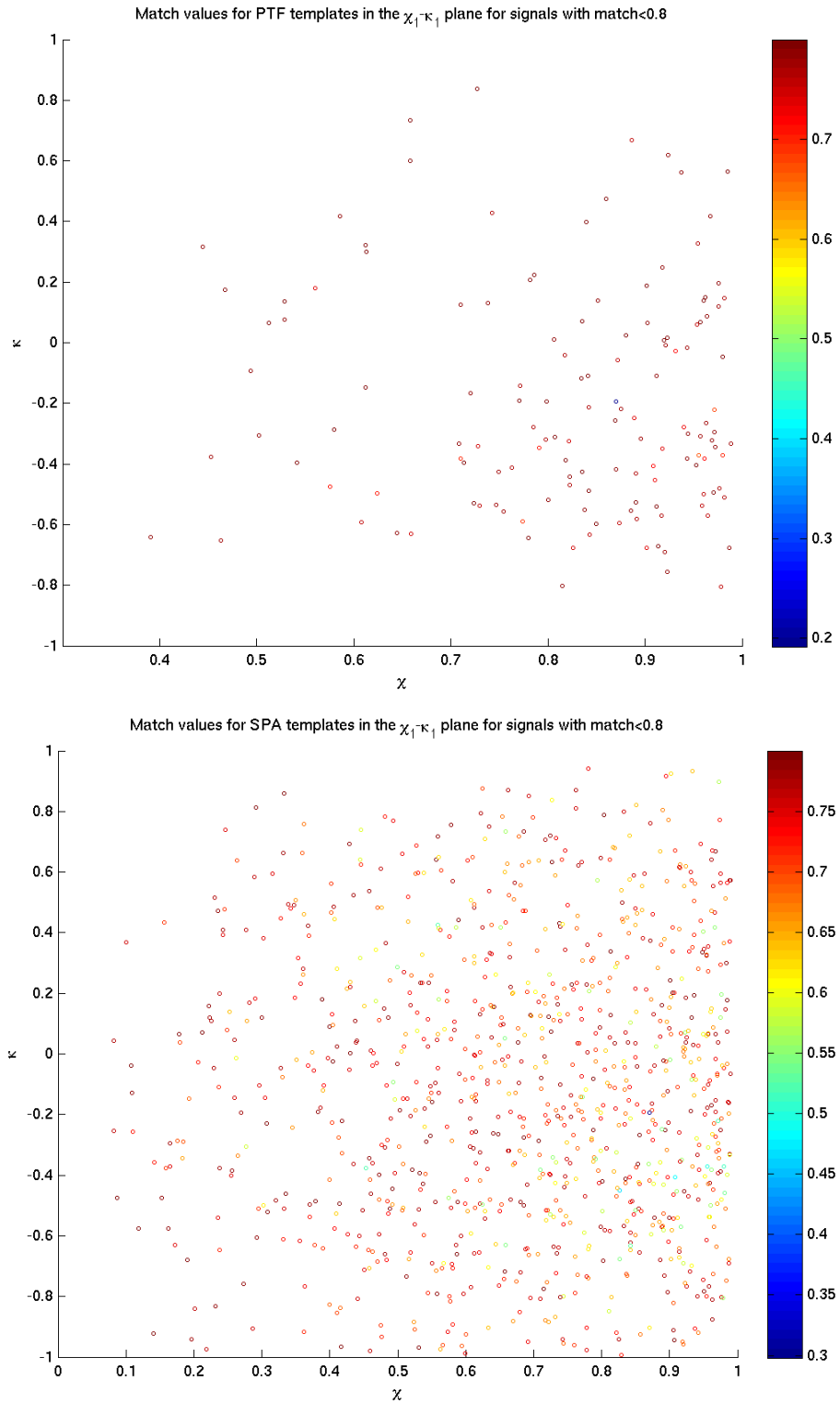


Figure 4.10: Signals with match lower than 0.8 for PTF templates (top figure - 139 points) and non-spinning SPA templates (bottom figure - 977 points) in the χ_1 - κ_1 plane.

4. Results

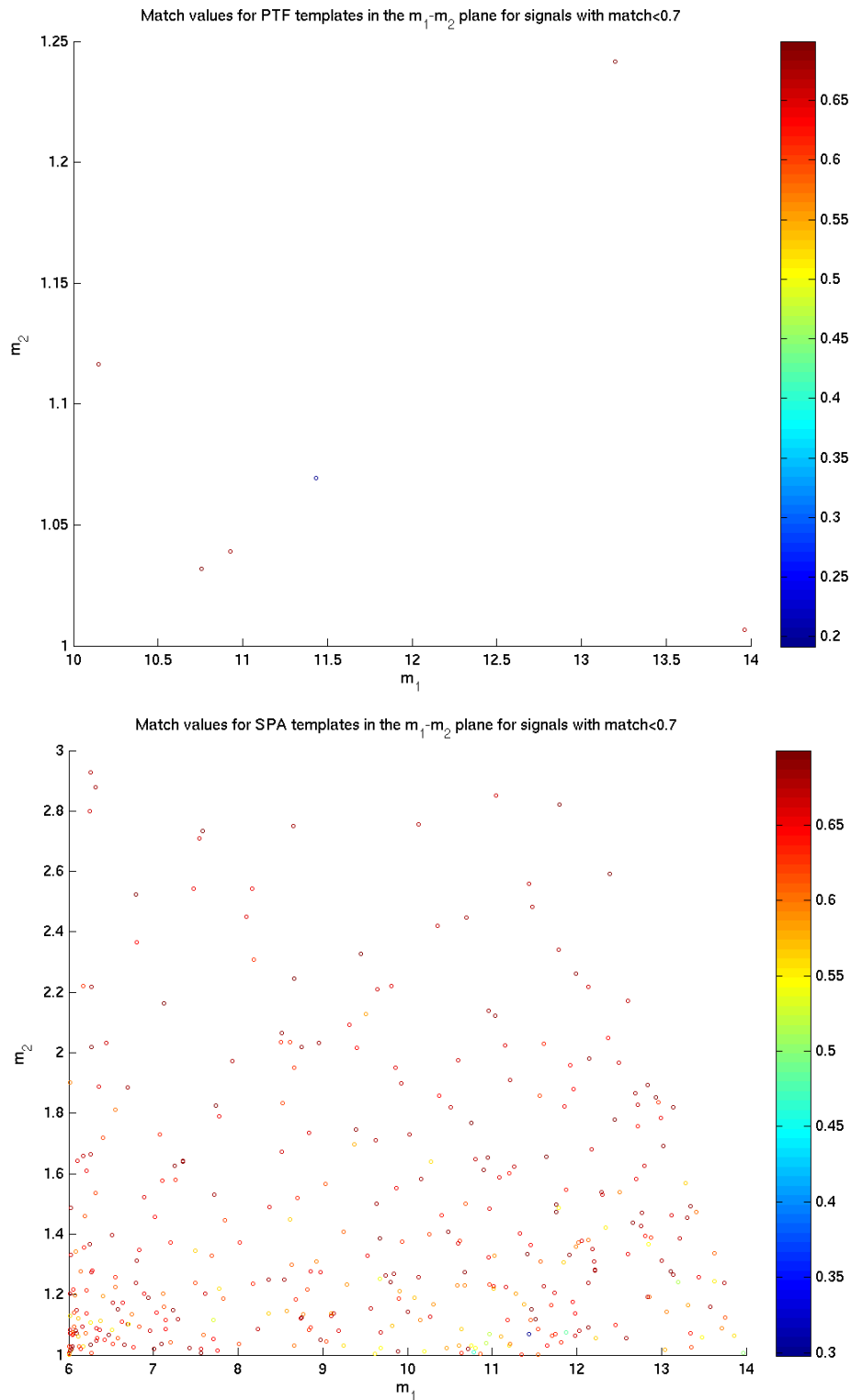


Figure 4.11: Signals with match lower than 0.7 for PTF templates (top figure - 6 points) and non-spinning SPA templates (bottom figure - 382 points) in the m_1 - m_2 plane.

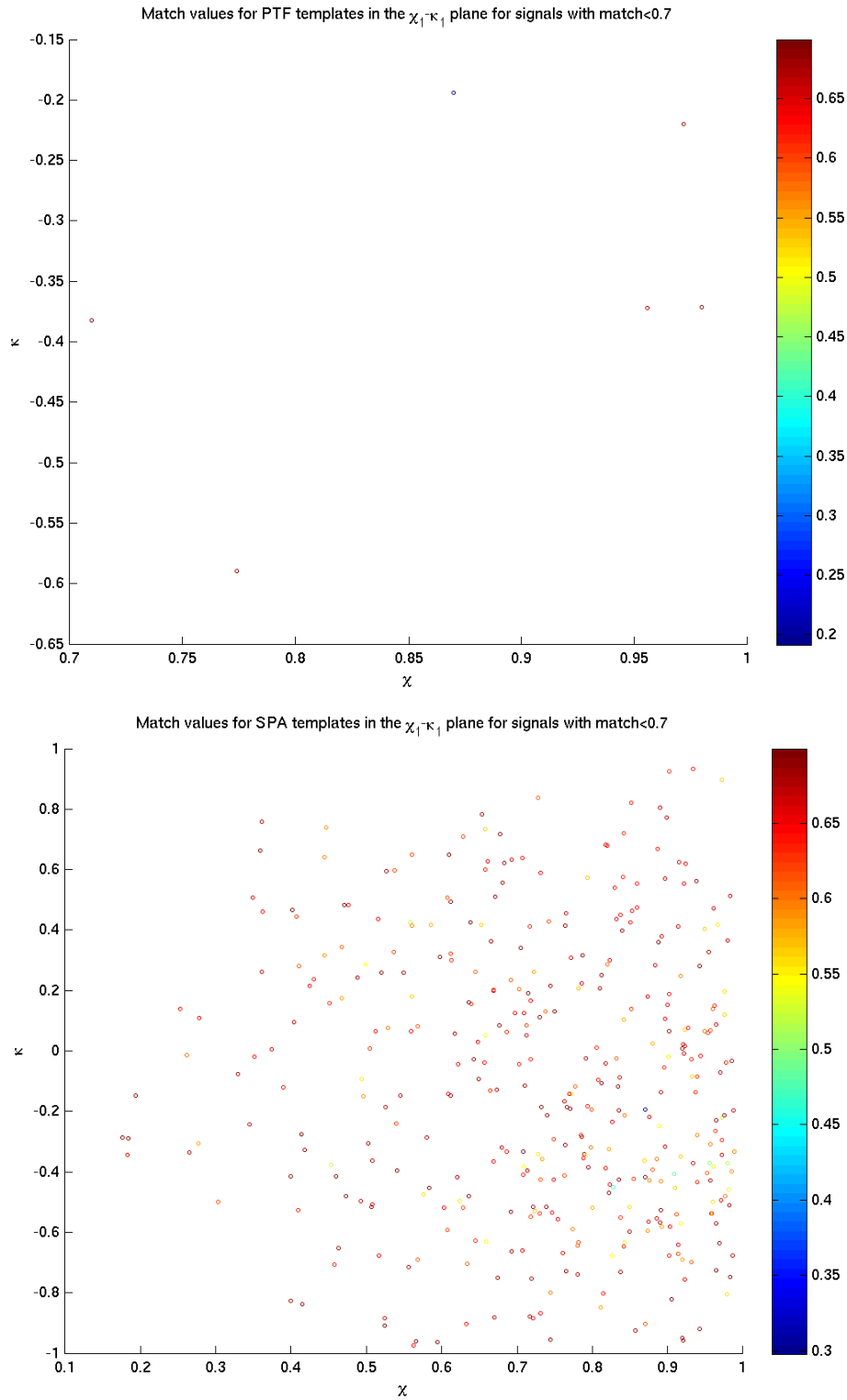


Figure 4.12: Signals with match lower than 0.7 for PTF templates (top figure - 6 points) and non-spinning SPA templates (bottom figure - 382 points) in the χ - κ plane.

4.3 First Inspiral Stage

We test the efficiency of the template bank by injecting a large amount of simulated GW signals in real LIGO S5 data and we check how many injections are found and how many are missed. Efficiency depends mainly on the distance of the source from the earth and on the instantaneous orientation of the orbital plane with respect to the detector frame, which can be combined at every instant of time to calculate the *effective distance* factor given by Eq. (2.78); as seen in the previous section different values of the intrinsic parameters of the source affect the detection probability.

First template banks are generated for each segment of 2048s of data, then the data is filtered against all the templates in the bank. The process of filtering each template will produce an SNR time-series $\rho(t)$; if this exceeds the chosen threshold, ρ^* at any time, we store its value as a *trigger*.

Performing such filtering across the entire template bank will produce a prohibitively large number of triggers, which will mostly be due to noise transients contained in the data. Therefore, it is necessary to perform data reduction on this set of triggers. This is done in two ways: firstly, for the SNR time-series of each individual template, clustering is performed over a sliding window of duration $\delta t = 10s$. The clustering works as follows: if we have a trigger at time t such that $\rho > \rho^*$, if this trigger is within δt of an earlier trigger at t' from the same template, which had a larger value of ρ , we discard the current trigger; however, if the earlier trigger has a smaller value of ρ , we discard the earlier trigger.

Once this clustering has been performed, the surviving triggers are then clustered across the parameters (t_c, m_1, m_2) , where t_c is the coalescence time, and τ_0 and τ_3 are the *chirp times*, which are a parametrization of the masses of the system. The clustering works by making use of the metric on the space and assigning triggers which are “near” to each other in this space as being part of a cluster. The trigger with the highest SNR in each cluster is then kept, while the rest are thrown away.

We injected 4096 simulated software single-spin GW signal into the first month of S5 data and compared detection efficiencies in each interferometer with the low-mass non-spinning SPA template banks. Results in Figures 4.14, 4.15, 4.18, 4.19, 4.22, 4.23 show that, at this stage, the PTF template bank is more consistent in recovering injections at low effective distance, therefore increasing the probability of detecting a closeby source. Furthermore the PTF template bank yields a better estimation of the masses of the source and an estimation of the spin parameters as well, as shown in Figures 4.16, 4.20, 4.24.

As a matter of fact, we see that an injection at very close effective distance (3.84 Mpc for H1 and 4.40 Mpc for L1) is missed by the non-spinning filtering code but it is found by the PTF filter in both H1 and L1; the parameters of the source are $m_1 = 12.52M_\odot$, $m_2 = 2.14M_\odot$, $\chi_1 = 0.90$, $\kappa_1 = 0.12$ and they lie in the

region where non-modulated templates are expected to have lower efficiency, i.e. high mass-ratio, high spin magnitude and high misalignment between \mathbf{S}_1 and $\hat{\mathbf{L}}_N$ [7, 10, 33].

Two injections were missed by the PTF filter at effective distance $< 10Mpc$ in H1 and L1 and we followed them up to see why this is happening (see section 4.3.4 below); looking at the raw SNR time series it is clear that all these injections happen within clustering distance to a nearby noise glitch with higher SNR, therefore the clustering code only records the time of the highest SNR, causing the injection to be missed. Three of these injections at GPS times 816099067 and 817300523 in H1 and 816747858 in L1 were missed by the non-spinning SPA filter as well, while the injection at GPS time 817201405 in L1 was found; this happened because the two spikes in the SNR time series we see in figure 4.29, corresponding to the injection and to a glitch, lie just within the clustering distance for PTF, but they are clustered as different events by the SPA filter.

These kind of features are usually eliminated at the coincidence stage, since the signal will be present in other interferometers but the glitch will not, hence the lower SNR trigger corresponding to the signal will be recovered.

For PTF template the SNR threshold ρ^* is set to a value of 6.4. If we were to perform an actual search we would need to tune this value a posteriori, based on the number of triggers we get at the first inspiral stage; the maximum number of triggers that can be stored N_t is limited by the maximum amount of memory available and the threshold is set so that the number of triggers is close but lower than N_t .

We skipped this tuning and estimated the threshold for PTF templates from the threshold used for SPA templates (5.5), which has been tuned; we imposed that the theoretical cumulative distribution function in Gaussian noise at ρ^* for PTF equals the value of the cumulative distribution function at 5.5 for SPA, and this is obtained for $\rho^* \simeq 6.4$. We recall that the detection statistic for SPA templates is a χ distribution with two degrees of freedom while the detection statistic for PTF templates is a χ distribution with six degrees of freedom (Figure 4.13 illustrates this computation).

4. Results

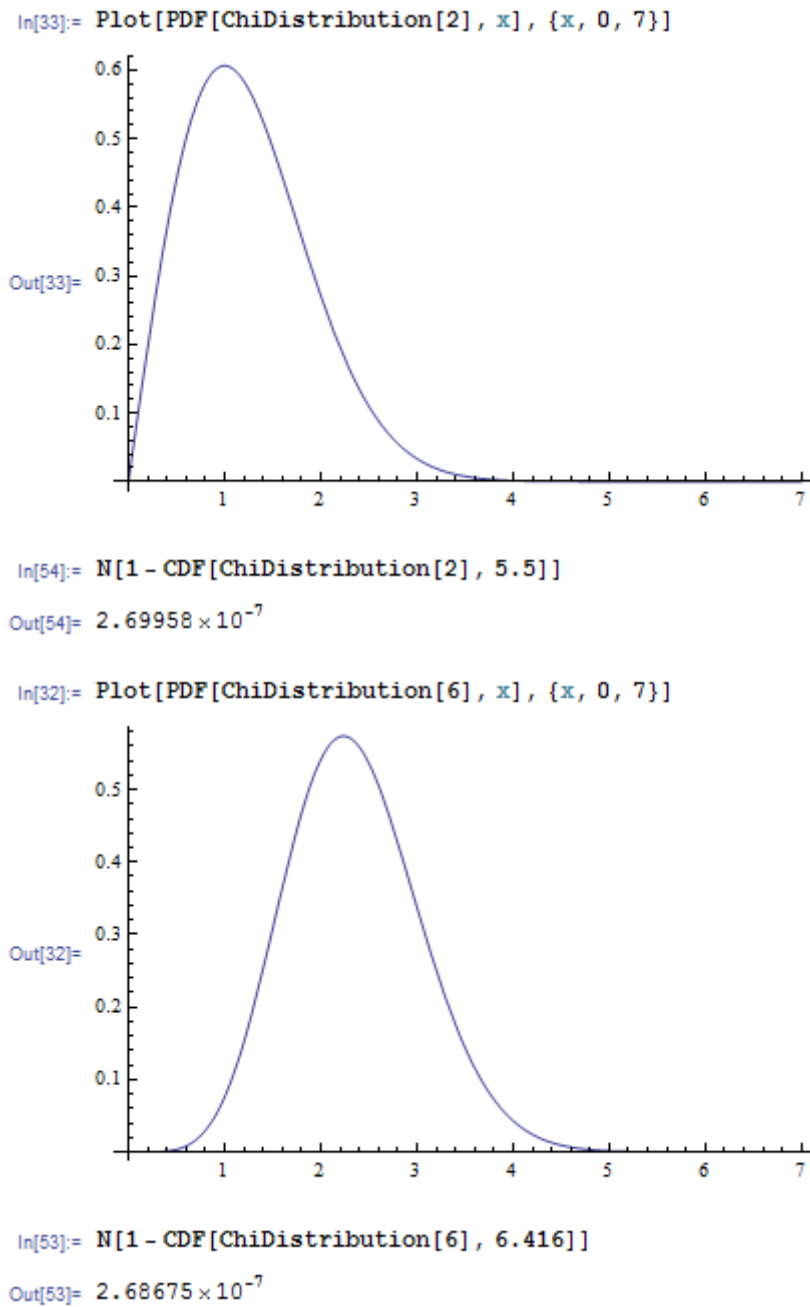


Figure 4.13: Theoretical probability density functions for SPA (top figure) and PTF (bottom figure) and comparison of the cumulative distribution functions at ρ^* .

4.3.1 H1 Results

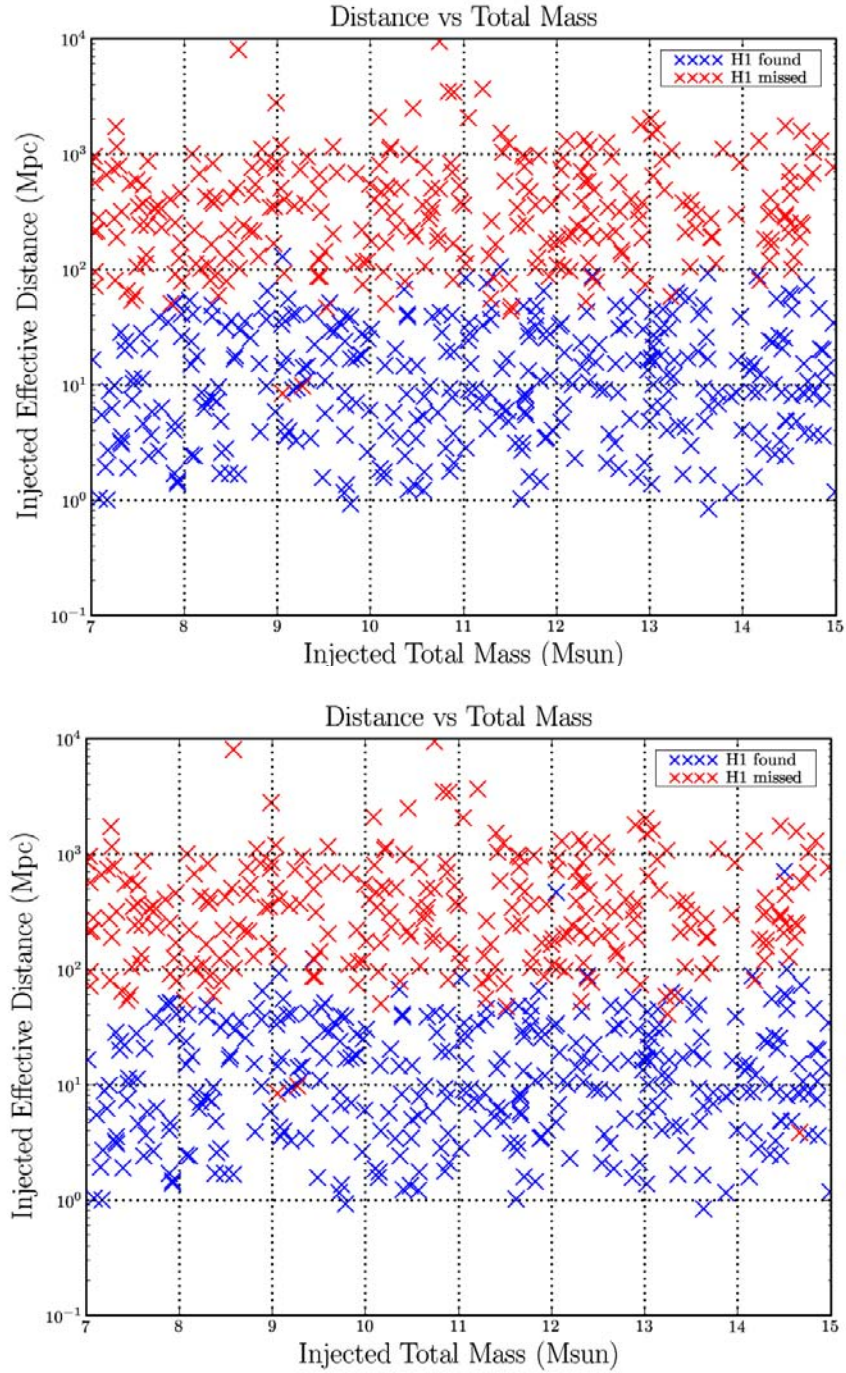


Figure 4.14: Plots of missed and found injections in the $M - D_{eff}$ plane for the interferometer H1. Top figure PTF, bottom figure SPA.

4. Results

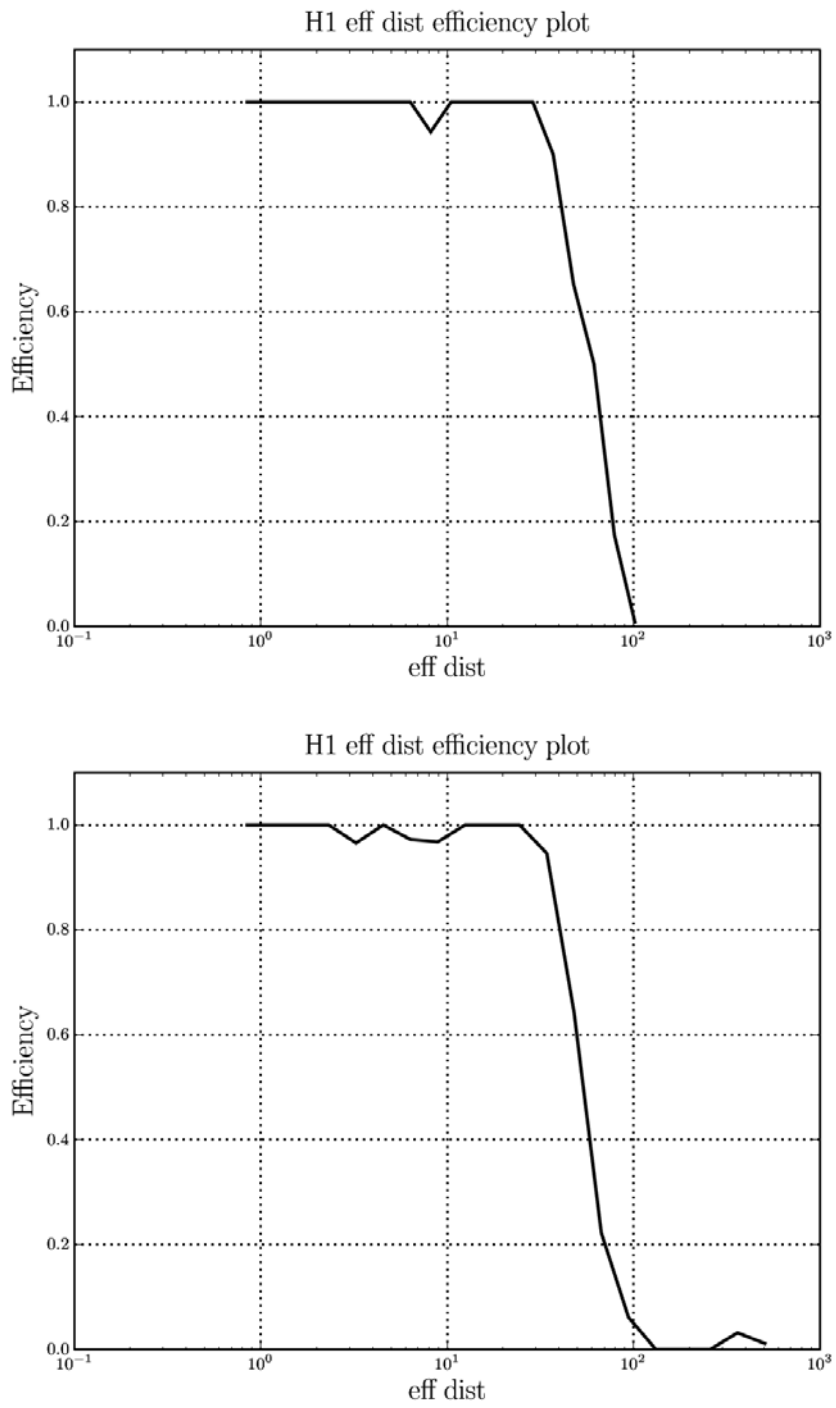


Figure 4.15: Plot of efficiency vs D_{eff} for the interferometer H1. Top figure PTF, bottom figure SPA.

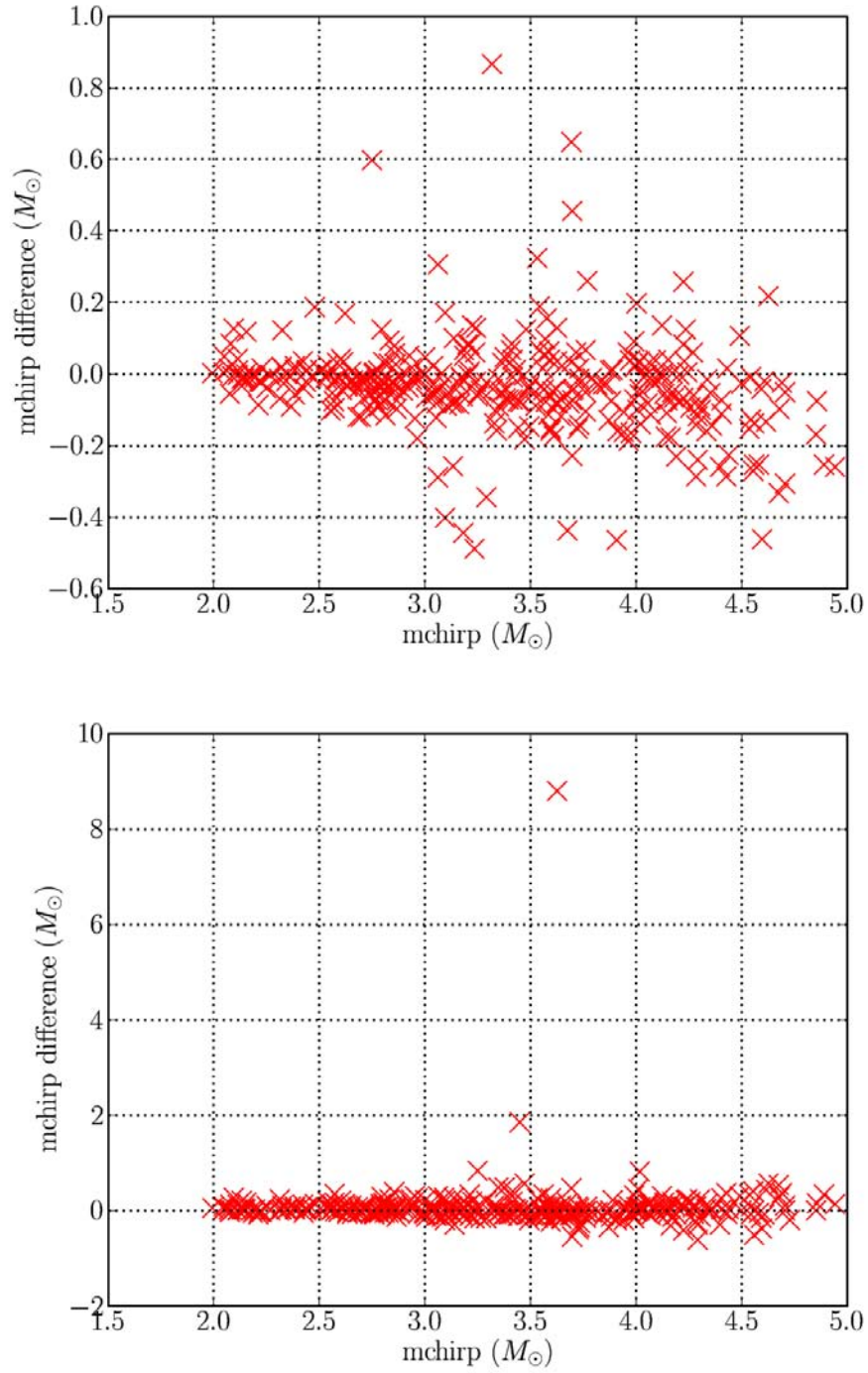


Figure 4.16: Plot of accuracy ΔM_c vs M_c for the interferometer H1. Top figure PTF, bottom figure SPA.

4. Results

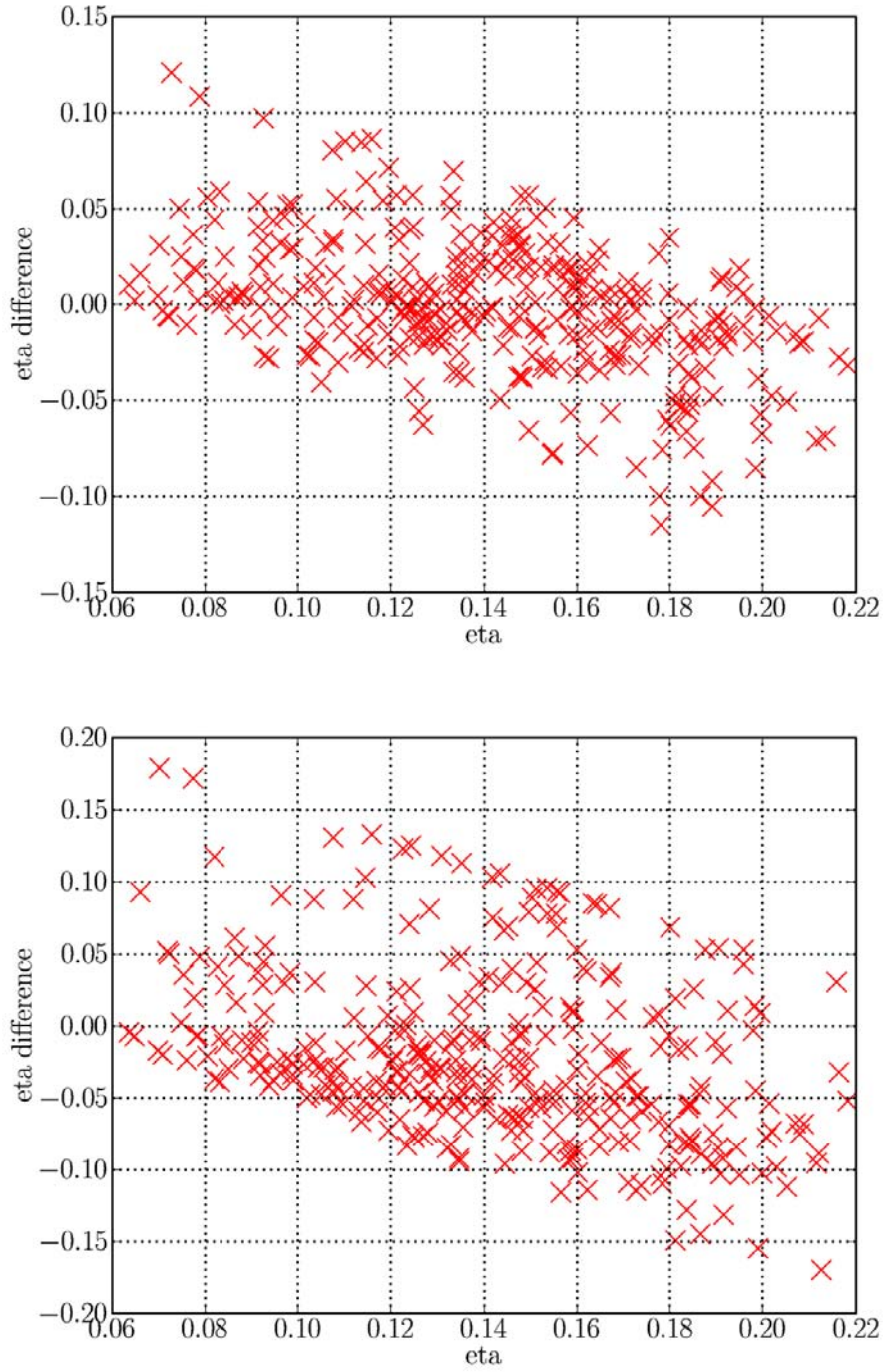


Figure 4.17: Plot of accuracy $\Delta\eta$ vs η for the interferometer H1. Top figure PTF, bottom figure SPA.

4.3.2 H2 Results

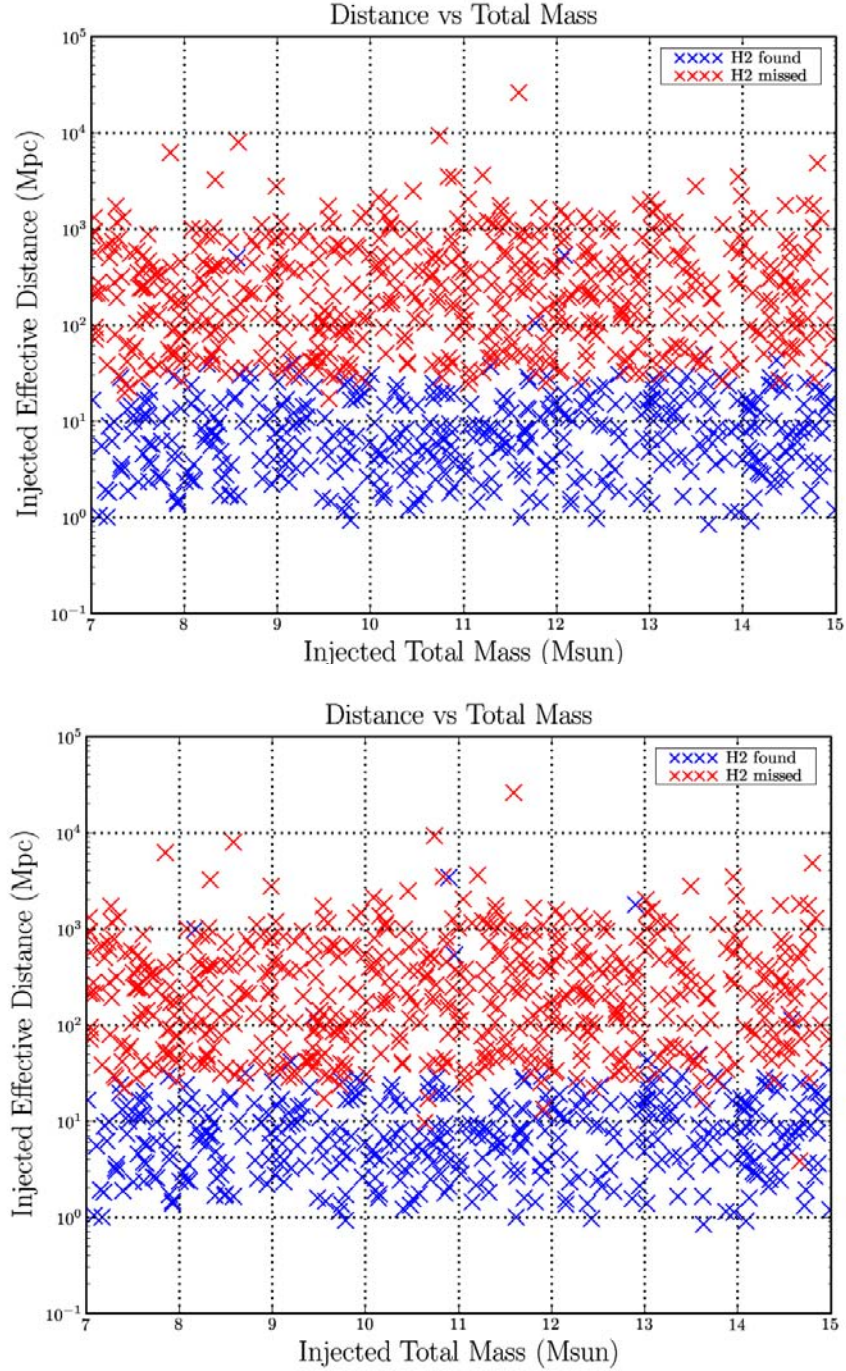


Figure 4.18: Plots of missed and found injections in the $M - D_{eff}$ plane for the interferometer H2. Top figure PTF, bottom figure SPA.

4. Results

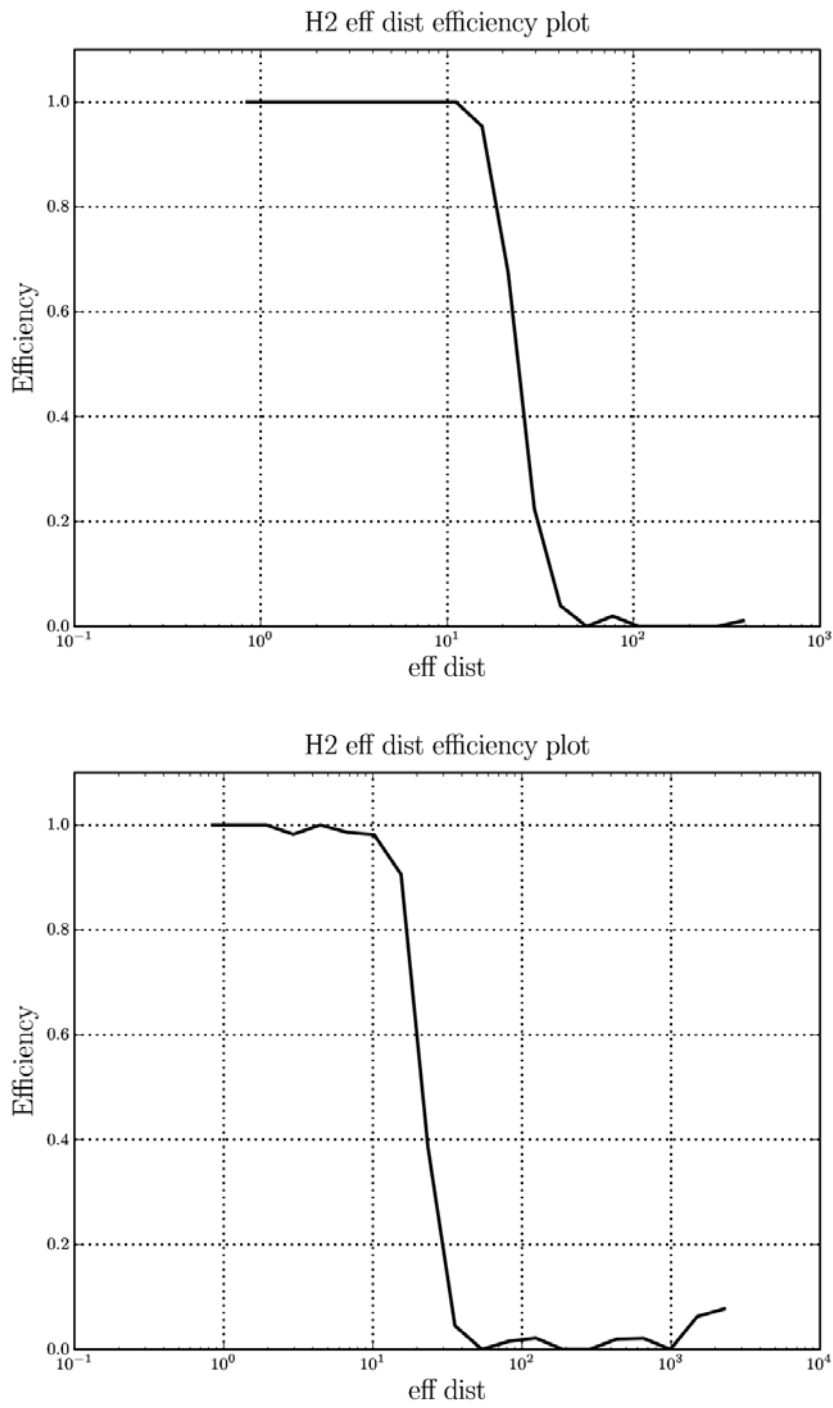


Figure 4.19: Plot of efficiency vs D_{eff} for the interferometer H2. Top figure PTF, bottom figure SPA.

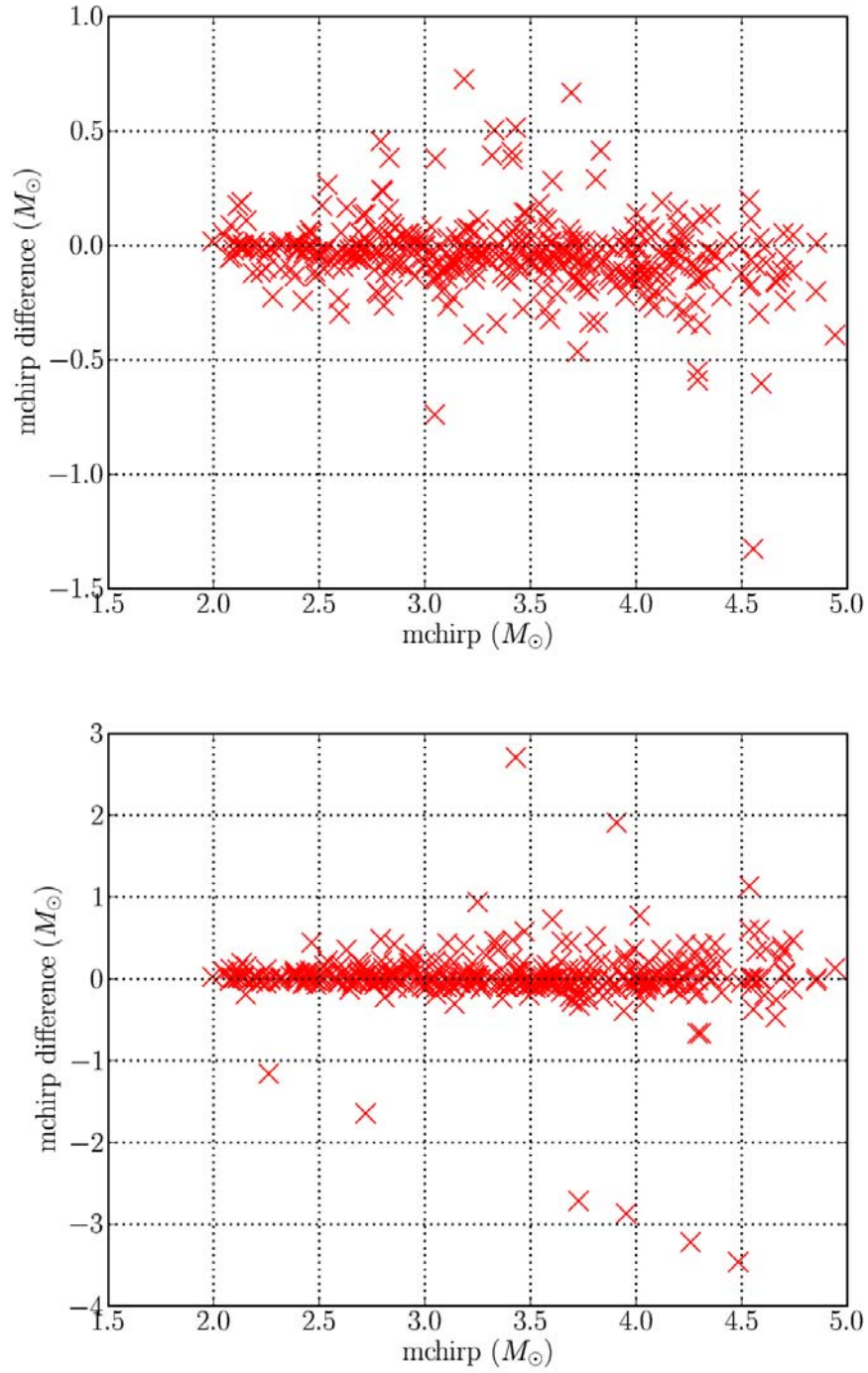


Figure 4.20: Plot of accuracy ΔM_c vs M_c for the interferometer H2. Top figure PTF, bottom figure SPA.

4. Results

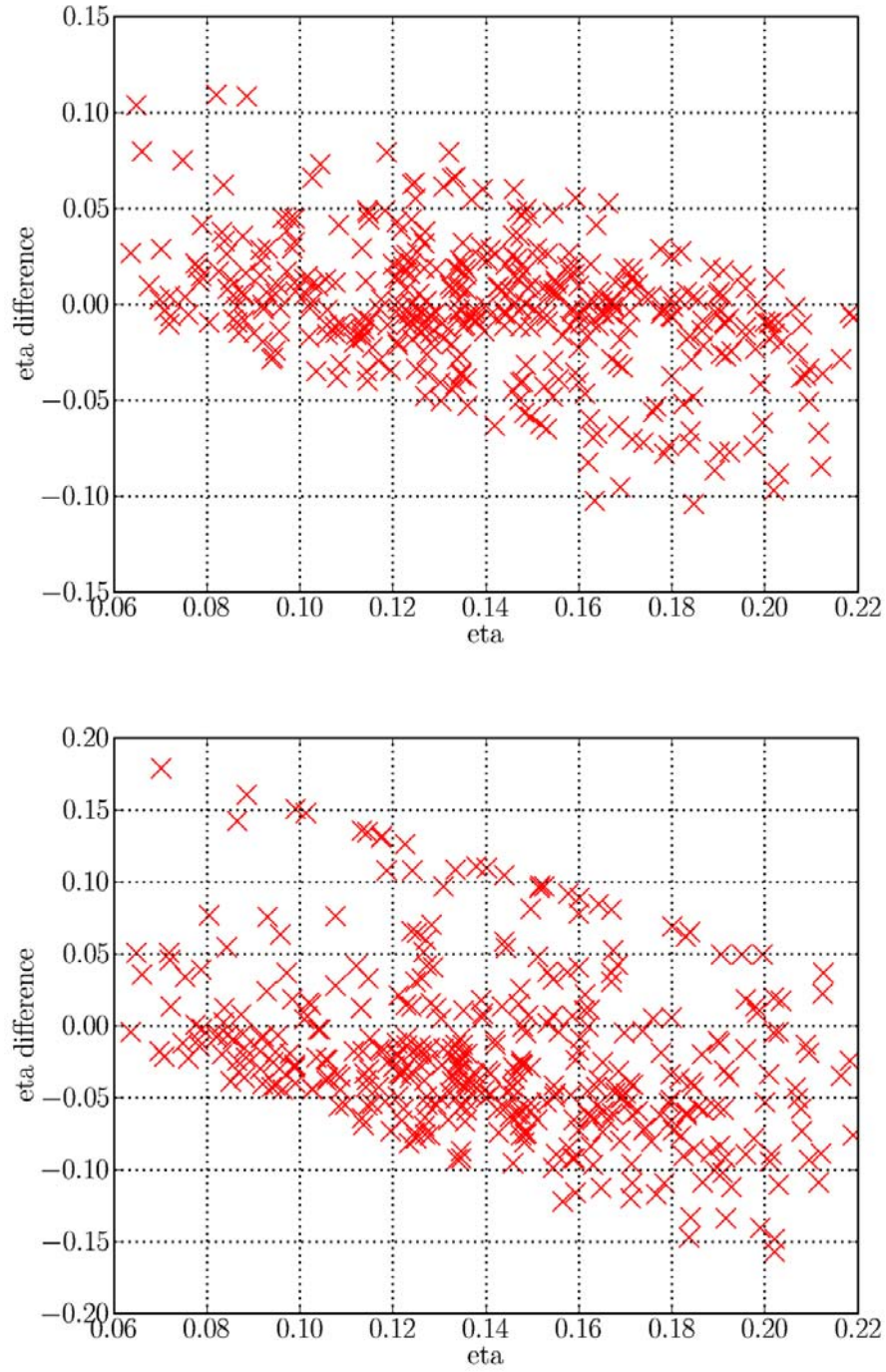


Figure 4.21: Plot of accuracy $\Delta\eta$ vs η for the interferometer H2. Top figure PTF, bottom figure SPA.

4.3.3 L1 Results

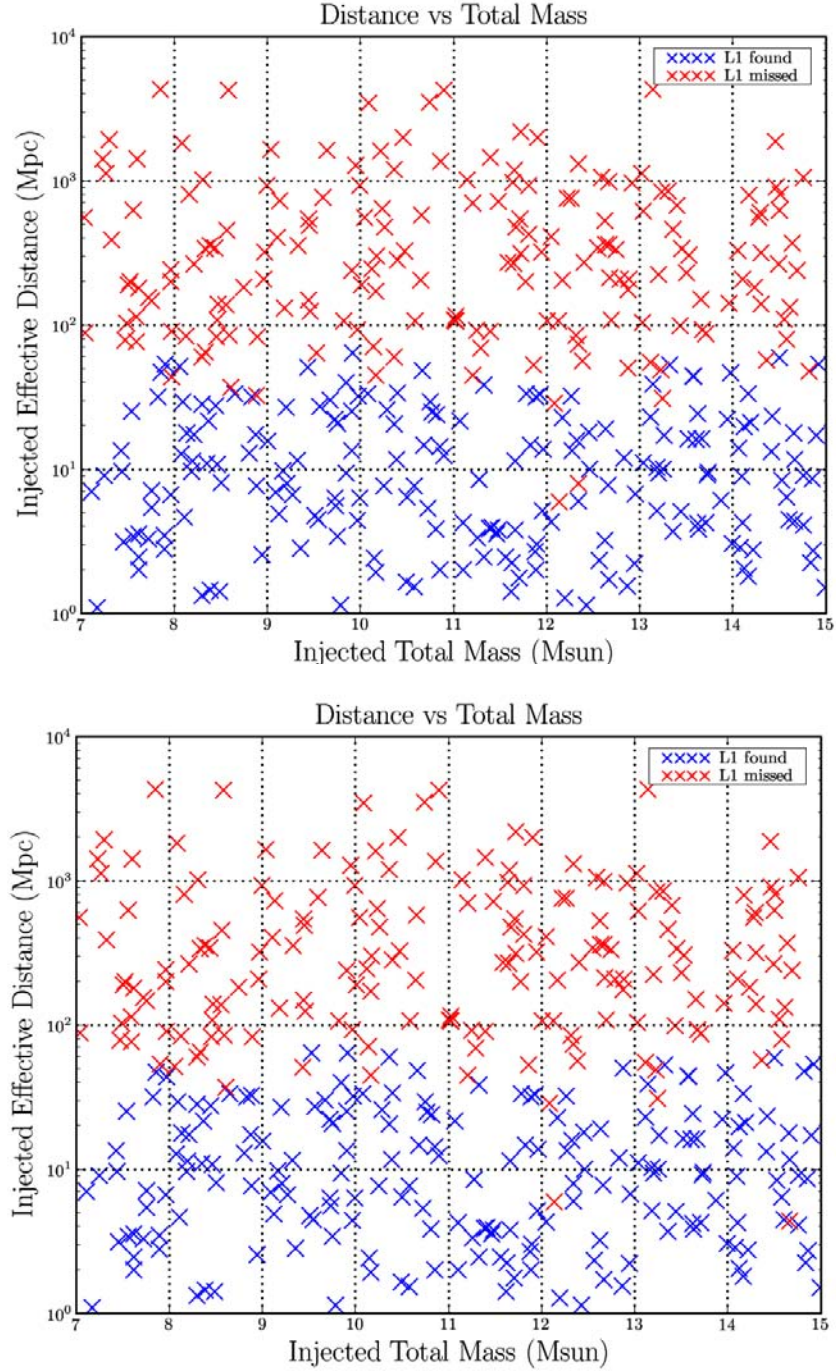


Figure 4.22: Plots of missed and found injections in the $M - D_{eff}$ plane for the interferometer L1. Top figure PTF, bottom figure SPA.

4. Results

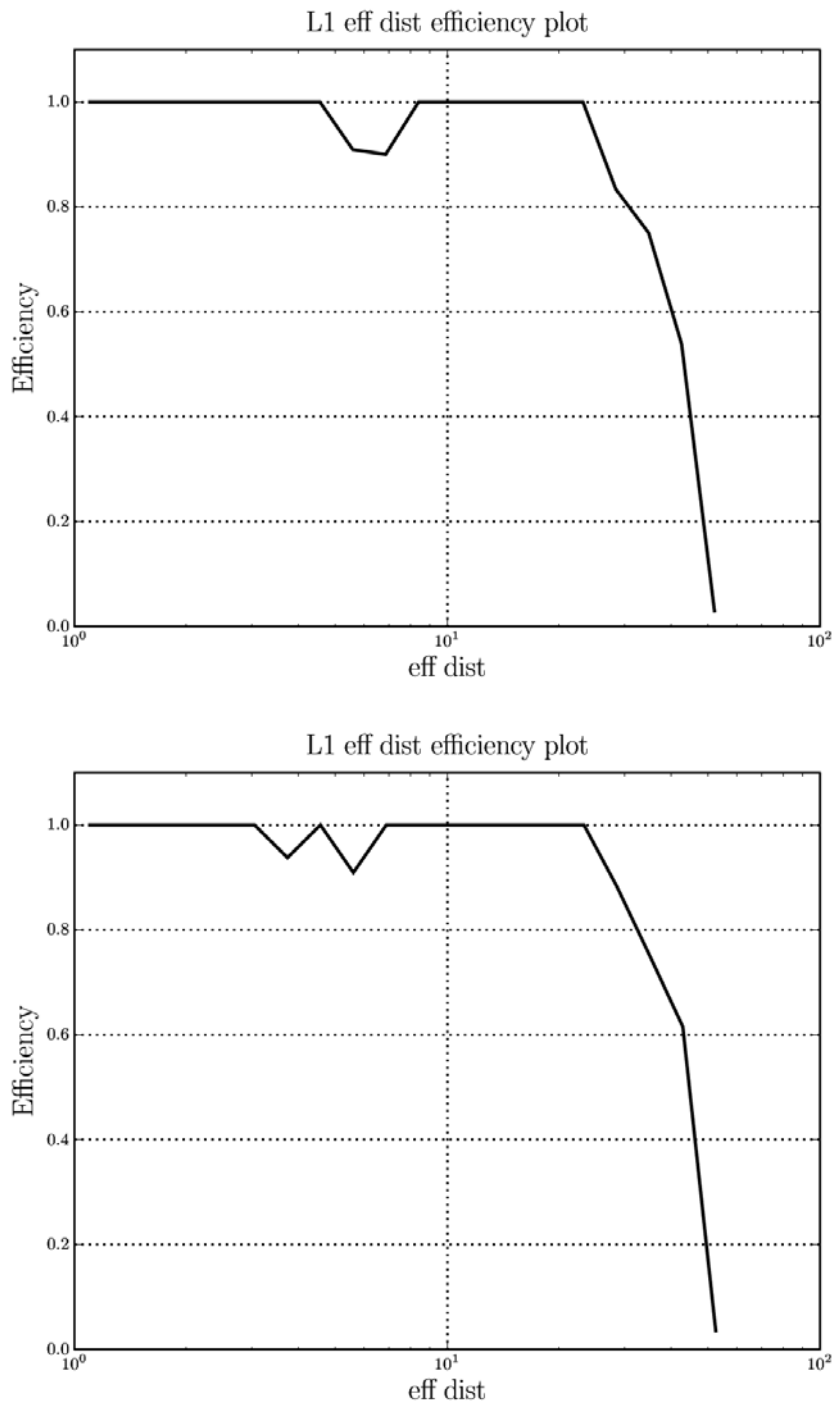


Figure 4.23: Plot of efficiency vs D_{eff} for the interferometer L1. Top figure PTF, bottom figure SPA.

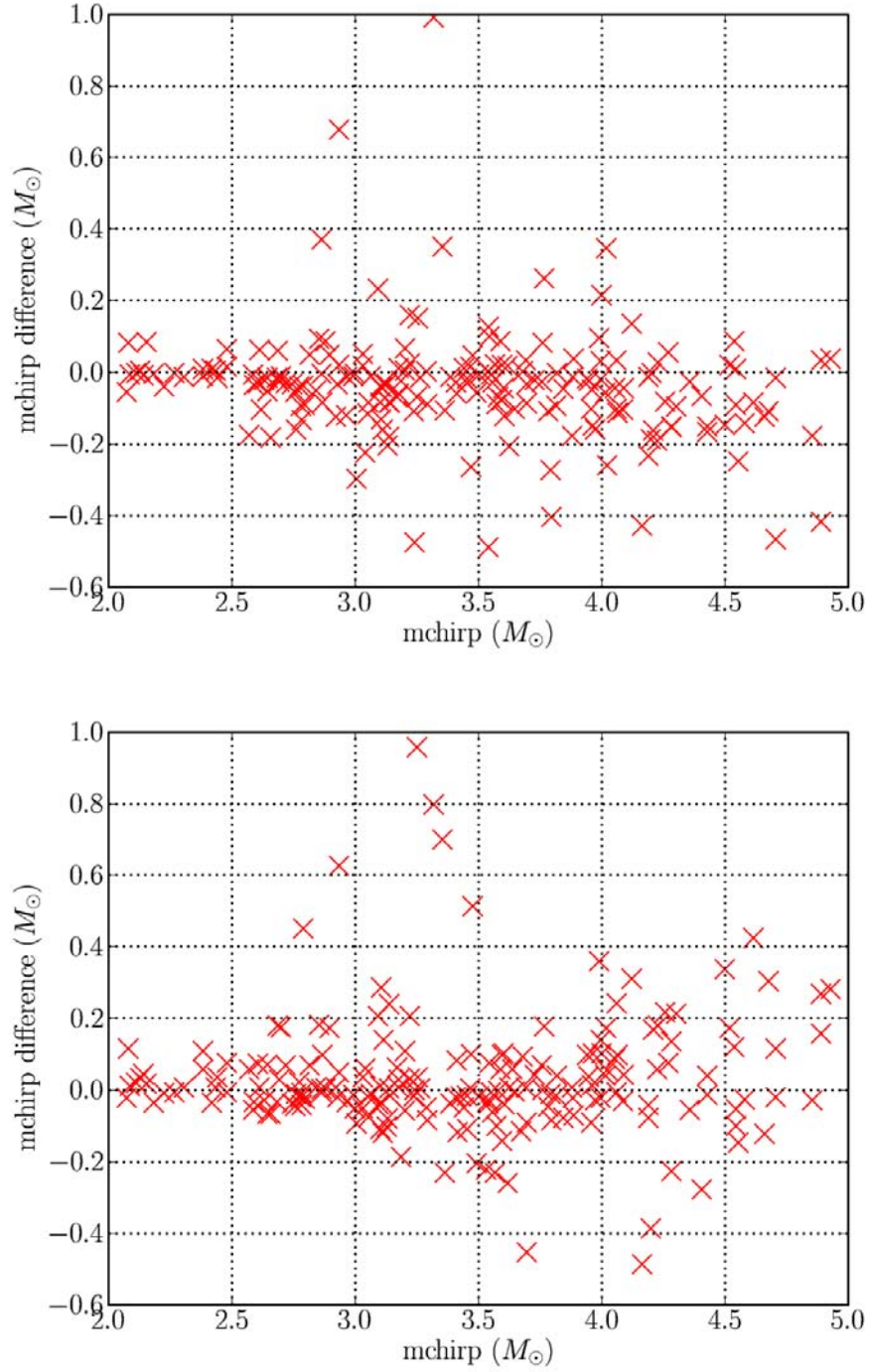


Figure 4.24: Plot of accuracy ΔM_c vs M_c for the interferometer L1. Top figure PTF, bottom figure SPA.

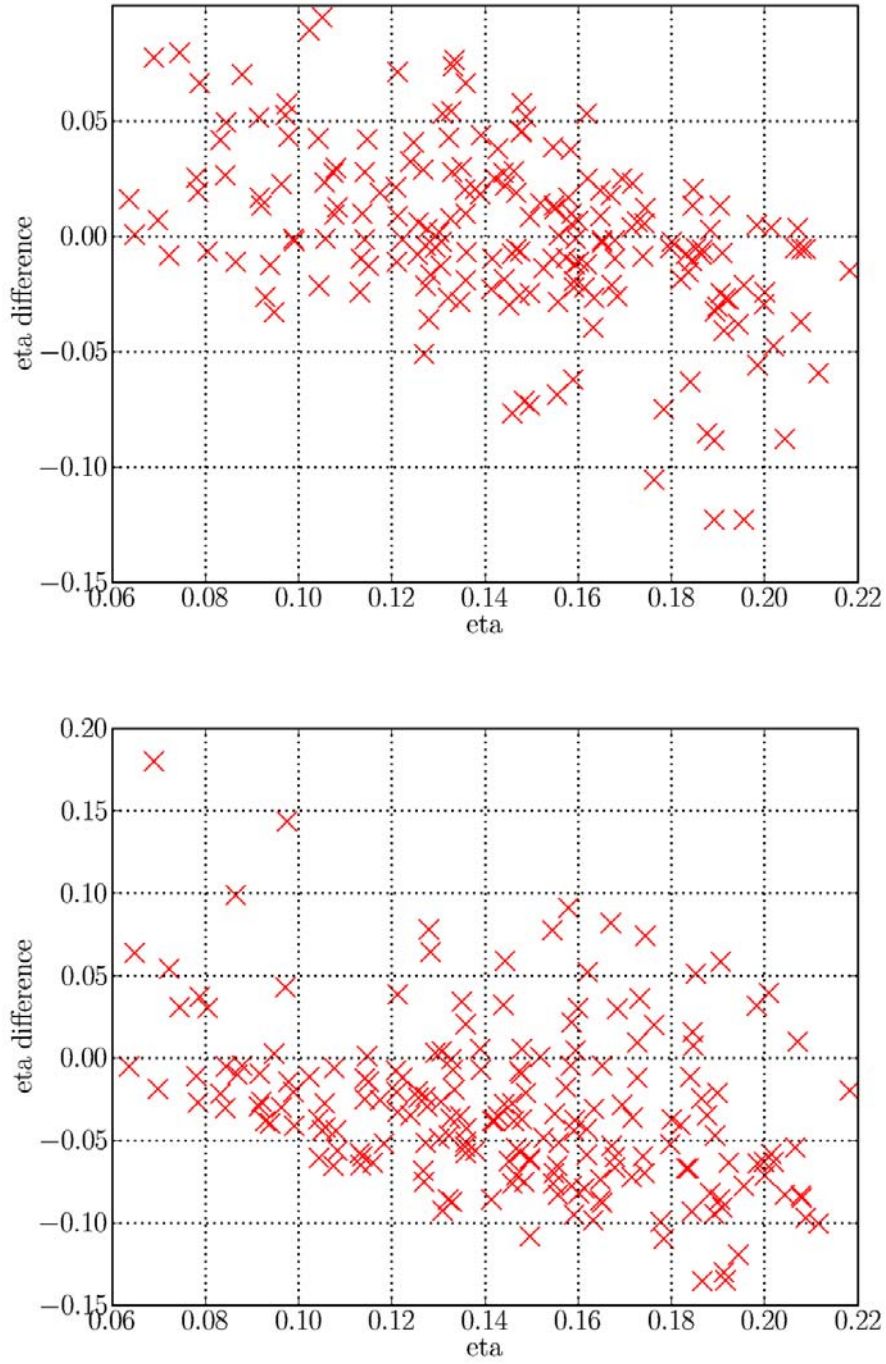


Figure 4.25: Plot of accuracy $\Delta\eta$ vs η for the interferometer L1. Top figure PTF, bottom figure SPA.

4.3.4 Follow-up of Nearby Missed Injections

Two injections were missed in H1 at GPS times:

- **816099067:** $m_1 = 7.7093878 M_\odot$, $m_2 = 1.553704 M_\odot$, $\chi_1 = 0.829323$, $\kappa_1 = -0.682579$, $D_{eff} = 9.701283$ Mpc
- **817300523:** $m_1 = 7.0665259 M_\odot$, $m_2 = 1.98138 M_\odot$, $\chi_1 = 0.801927$, $\kappa_1 = 0.402034$, $D_{eff} = 8.423931$ Mpc

and two in L1 at GPS times:

- **816747858:** $m_1 = 10.57036 M_\odot$, $m_2 = 1.5598741 M_\odot$, $\chi_1 = 0.131946$, $\kappa_1 = 0.892554$, $D_{eff} = 5.921156$ Mpc
- **817201405:** $m_1 = 10.64566 M_\odot$, $m_2 = 1.690677 M_\odot$, $\chi_1 = 0.272925$, $\kappa_1 = -0.712562$, $D_{eff} = 7.954970$ Mpc

The plots below show the raw $\rho(t)$ time series and the corresponding clustered triggers around the time of the injections.

4. Results

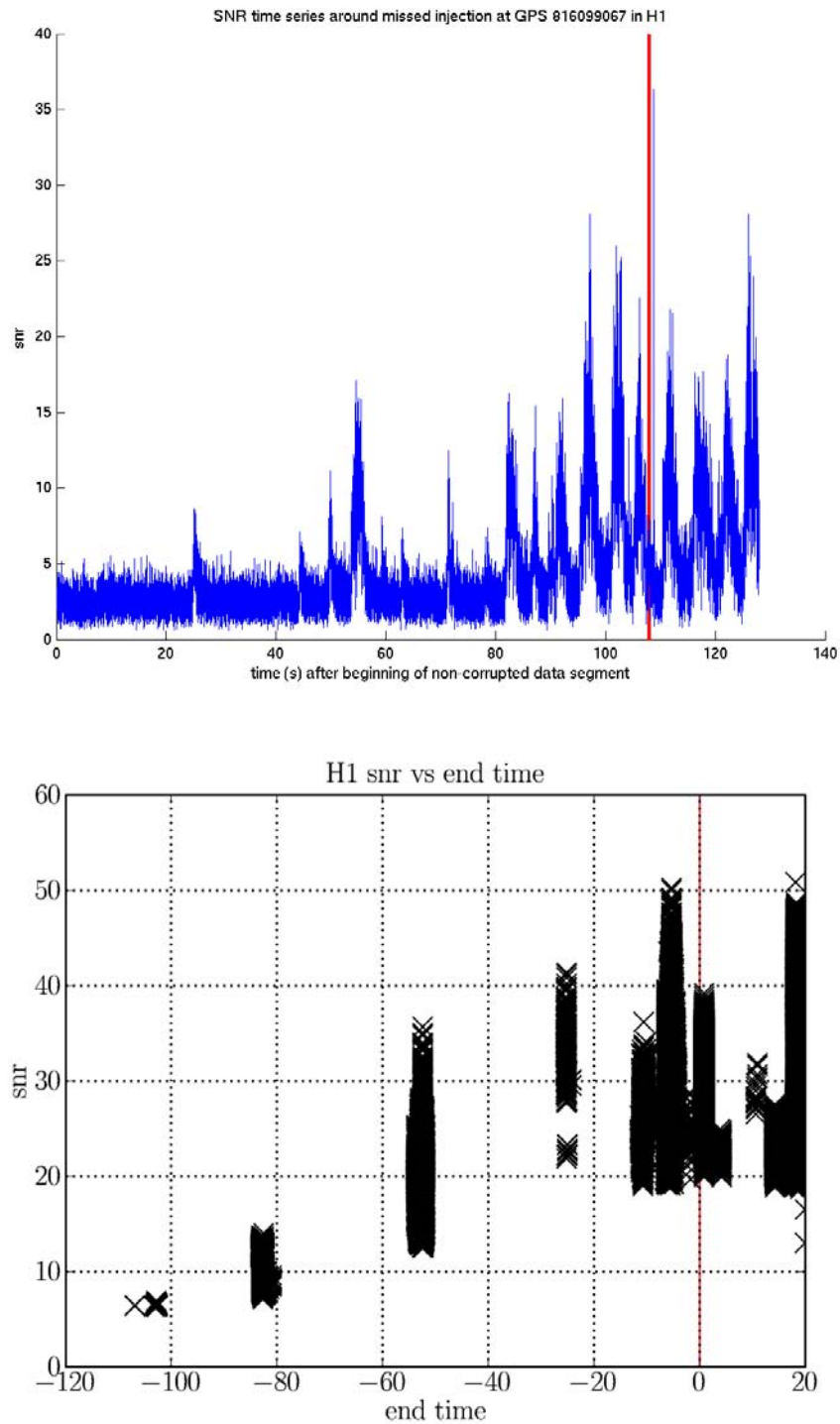


Figure 4.26: Plots of raw $\rho(t)$ time series (top figure) and corresponding clustered triggers (bottom figure) around the time of the injection (red vertical line)

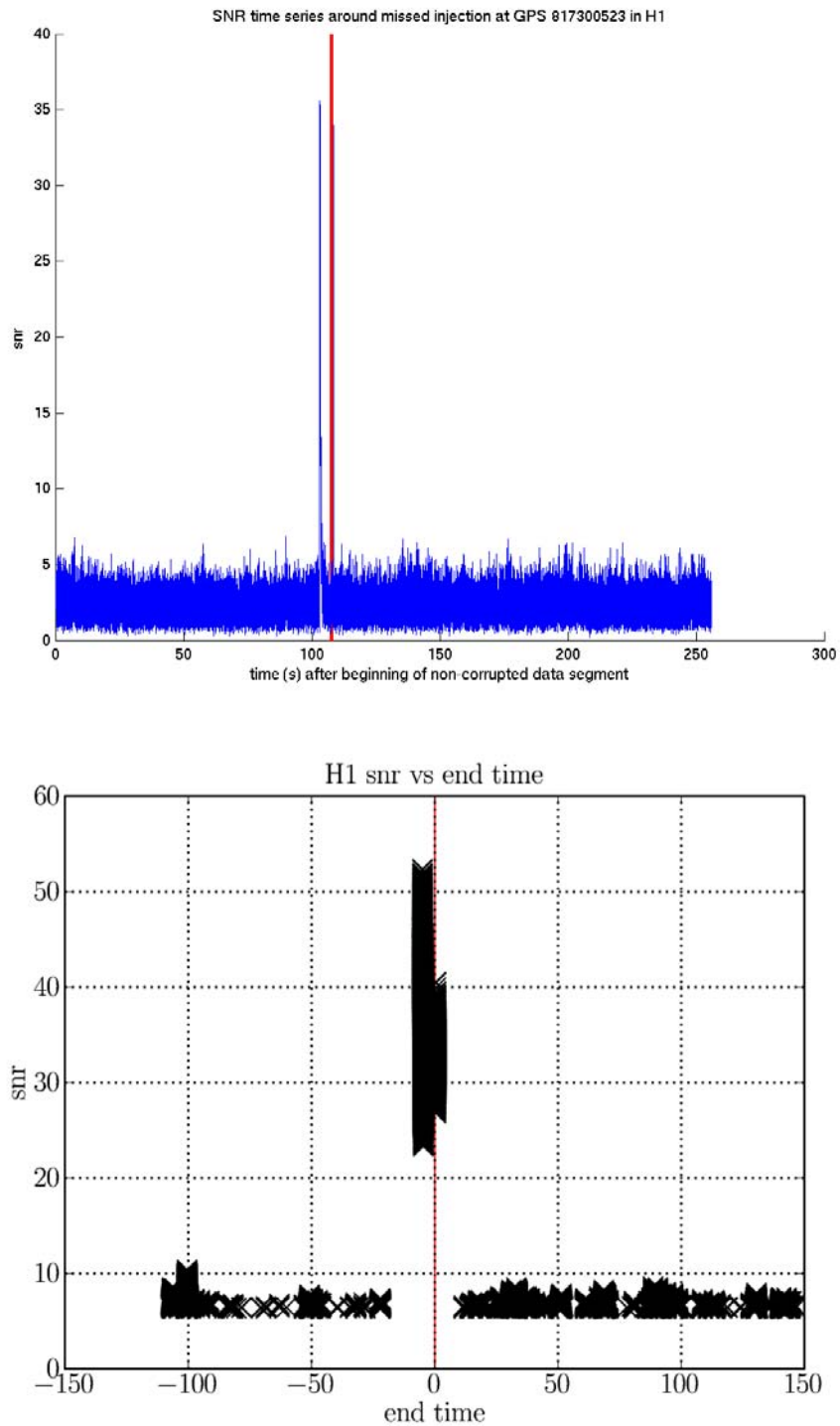


Figure 4.27: Plots of raw $\rho(t)$ time series (top figure) and corresponding clustered triggers (bottom figure) around the time of the injection (red vertical line)

4. Results

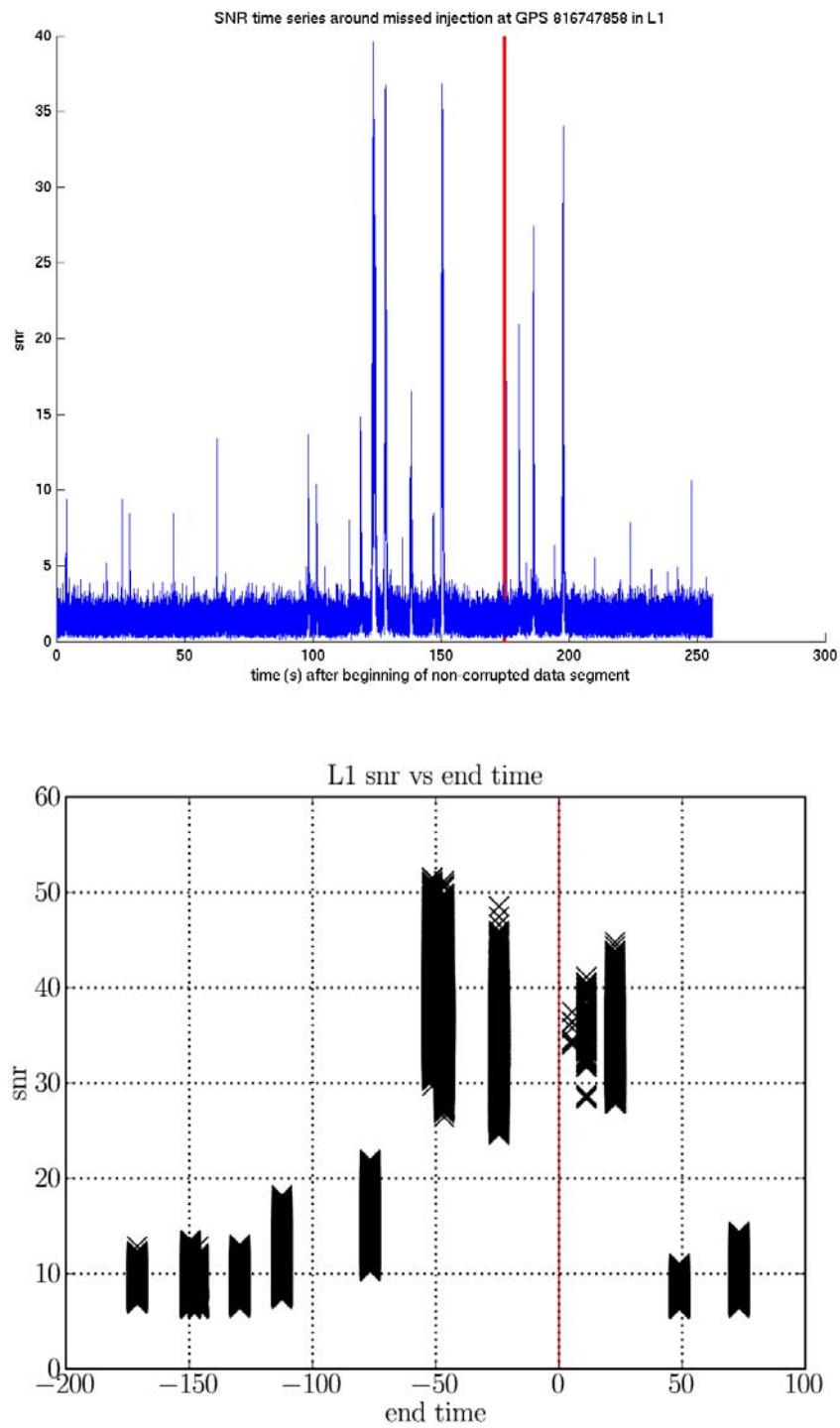


Figure 4.28: Plots of raw $\rho(t)$ time series (top figure) and corresponding clustered triggers (bottom figure) around the time of the injection (red vertical line)

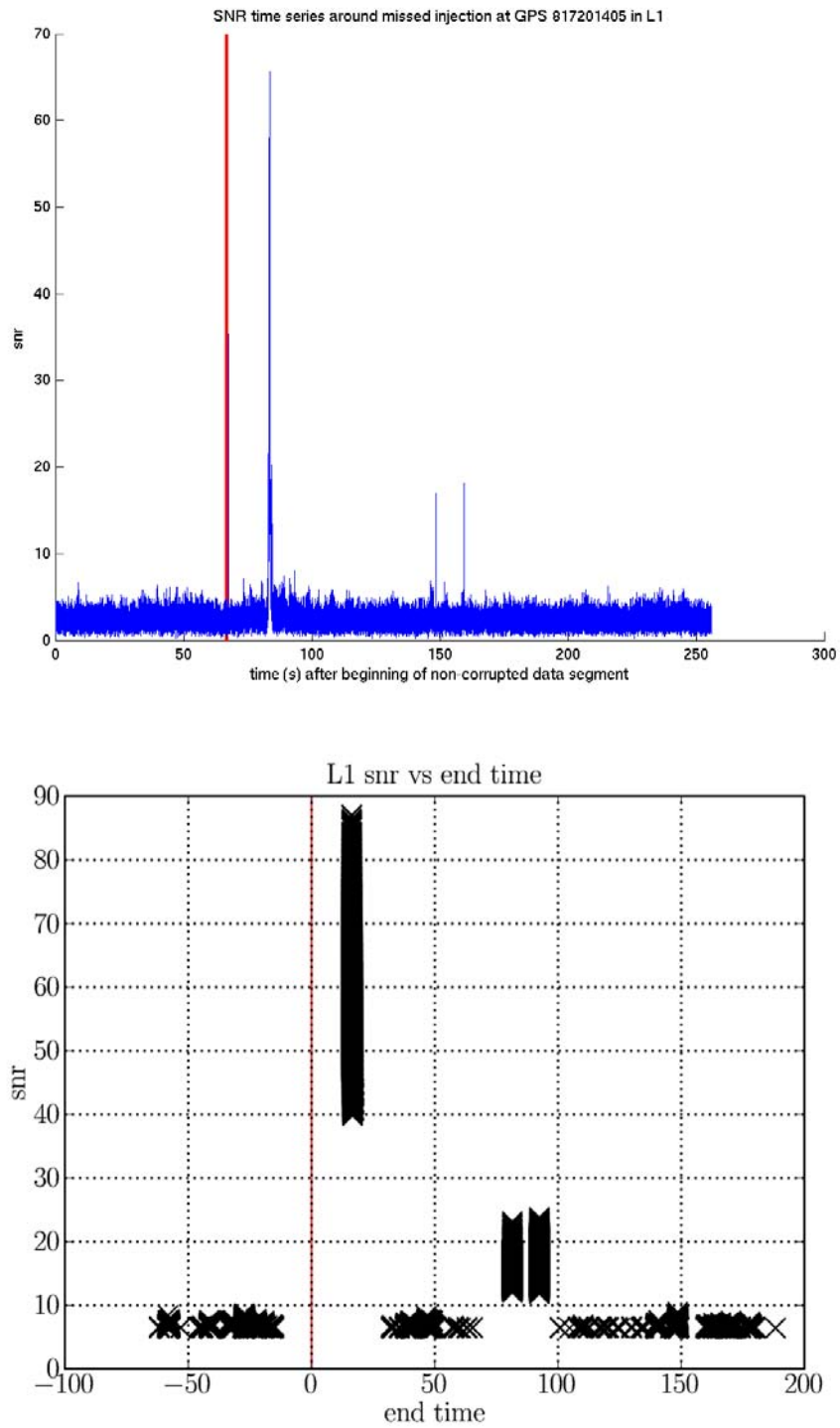


Figure 4.29: Plots of raw $\rho(t)$ time series (top figure) and corresponding clustered triggers (bottom figure) around the time of the injection (red vertical line)

4.4 The Coincidence Stage

The coincidence stage needs to be tuned in order to be able to recover injected simulated signals with high efficiency and minimize the number of spurious triggers. We start by looking at the accuracy plots in the previous section and set coincidence windows on the mass parameters so that (most) injection triggers from different interferometers are found in coincidence. In order to find the “best” windows we then need to run the pipeline on a sample of real noise that does not contain any real (or simulated) signal, so as to estimate the rate of accidental triggers. Since we cannot be sure whether signals are present or not in the data, we time slide first-inspiral triggers from different detectors by a time much longer than the expected length of the signal (and light travel time for separated detectors) and look for coincidences; these coincidences must necessarily be accidental since they cannot be causally related with each other, therefore giving an estimation of the number of *background* noise triggers. We adjust the coincidence windows together with the SNR threshold and the χ^2 threshold so as to get the desired efficiency and the desired false alarm rate.

Unfortunately, to perform this kind of tuning, the whole pipeline must be in place, while we are still developing one for PTF. In particular, since we don’t have a metric for the intrinsic parameter space, both the template bank stage and the coincidence stage are not optimized and the tuning would not be particularly significant.

We instead decided to set the size of coincidence windows based on the parameter accuracy results from the previous section and just ran the coincidence stage to test the efficiency of the algorithm in recovering injections. We used coincidence windows of $\Delta M_{chirp} = 1$ and $\Delta \eta = 0.15$. Even at this stage we see that PTF is more consistent in recovering injections at low effective distance, as a matter of fact many triggers that appear as double coincidences for the SPA pipeline, are found in triple coincidence by the PTF pipeline, as can be seen from Figure 4.30 below.

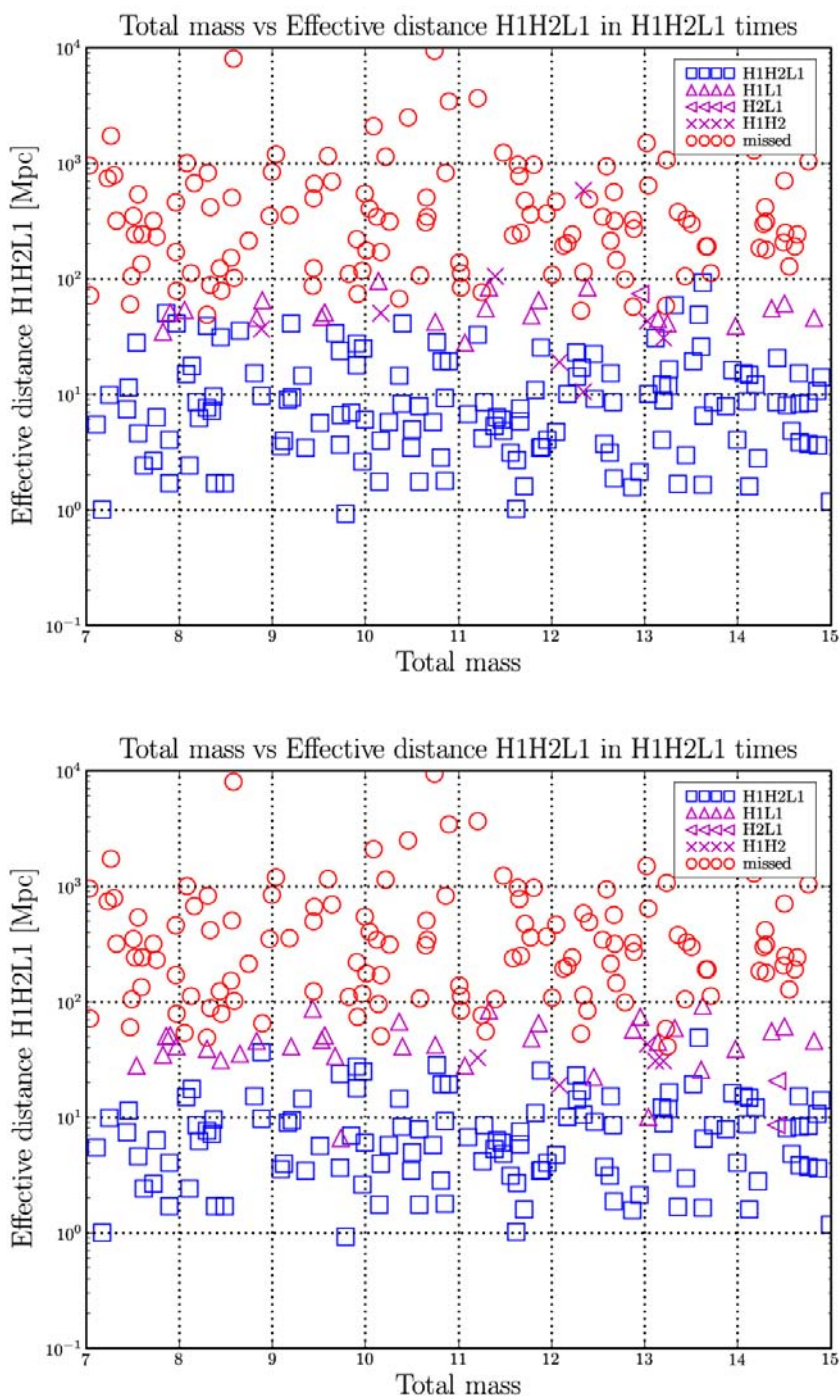


Figure 4.30: Plots of missed and found injections in the M - D_{eff} plane after the first coincidence stage for times during which all three interferometers were operating. Both double-coincident and triple-coincident triggers are shown; the effective distance refers to the H1-H2 location. Top figure PTF, bottom figure SPA.

4.5 χ^2 Veto

The χ^2 veto is still in a testing stage so we report here preliminary results. This so called *signal-based* veto is designed to discriminate real signals from noise artifacts by comparing the energy content in different frequency bins and making sure that this agrees, up to a certain accuracy, with the expected value for a real signal. The idea is that, while real signals have a very specific energy content in every bin, due to the dynamical evolution of the frequency and amplitude, noise glitches usually have not.

Here we test the statistic of the quantity (3.115) by fitting the distribution of $\chi_{PTF}^2(t)$ in simulated Gaussian noise with a χ^2 -distributed (non-normalized) probability density function for two different number of bins, 8 and 16 (see Figures 4.32, 4.33). We see that, as discussed in Sec. 3.115, while $\chi_{PTF}^2(t)$ is χ^2 distributed in presence of Gaussian noise, the actual number of degrees of freedom of the distribution is lower than the expected value, due to correlations between the two template components h_c^{PTF} and h_s^{PTF} at different times t_0 .

We then show a comparison of the values of χ_{PTF}^2 vs ρ for noise triggers and for injection triggers from single interferometers in real S5 LIGO data, using 8 frequency bins. Even if the statistic is low, results in Figures 4.34, 4.35, 4.36 suggest that there is a separation between noise triggers and injection triggers; larger simulations will allow to tune the threshold on χ_*^2 given by Eq. (2.59) and efficiently veto spurious noise triggers.

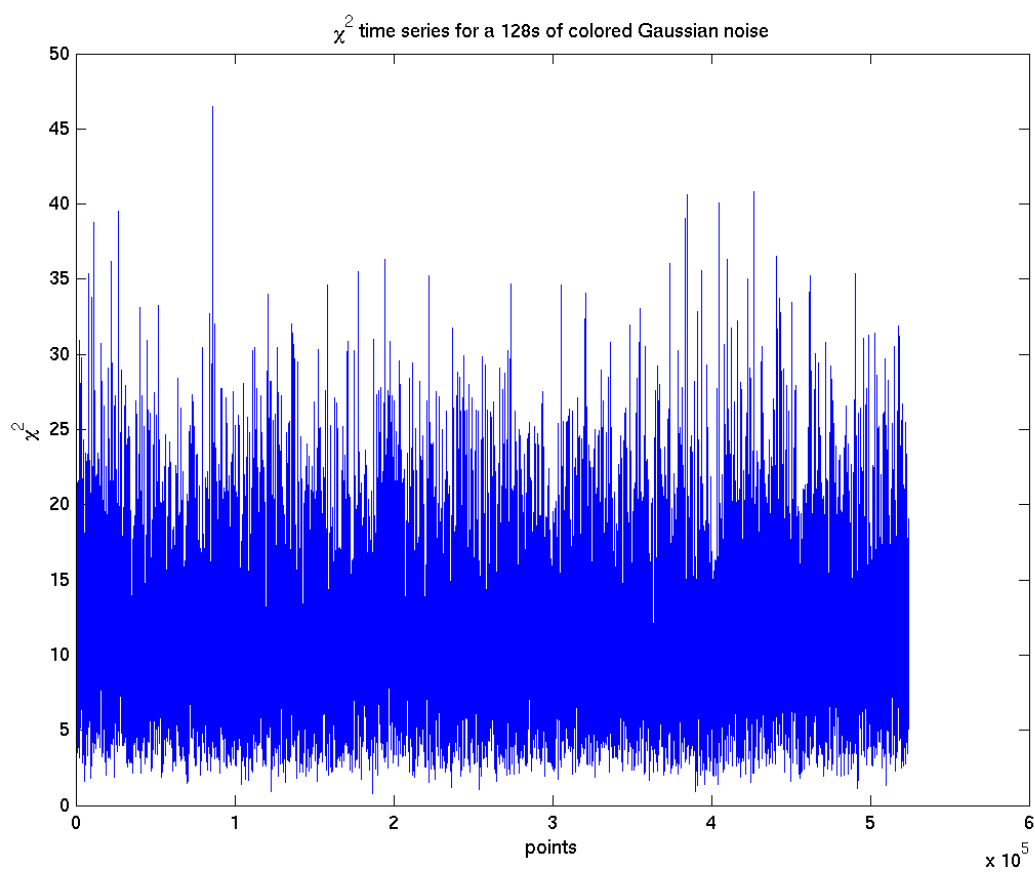


Figure 4.31: Plot of $\chi_{PTF}^2(t)$ time series from H1 in 128s of simulated Gaussian noise.

4. Results

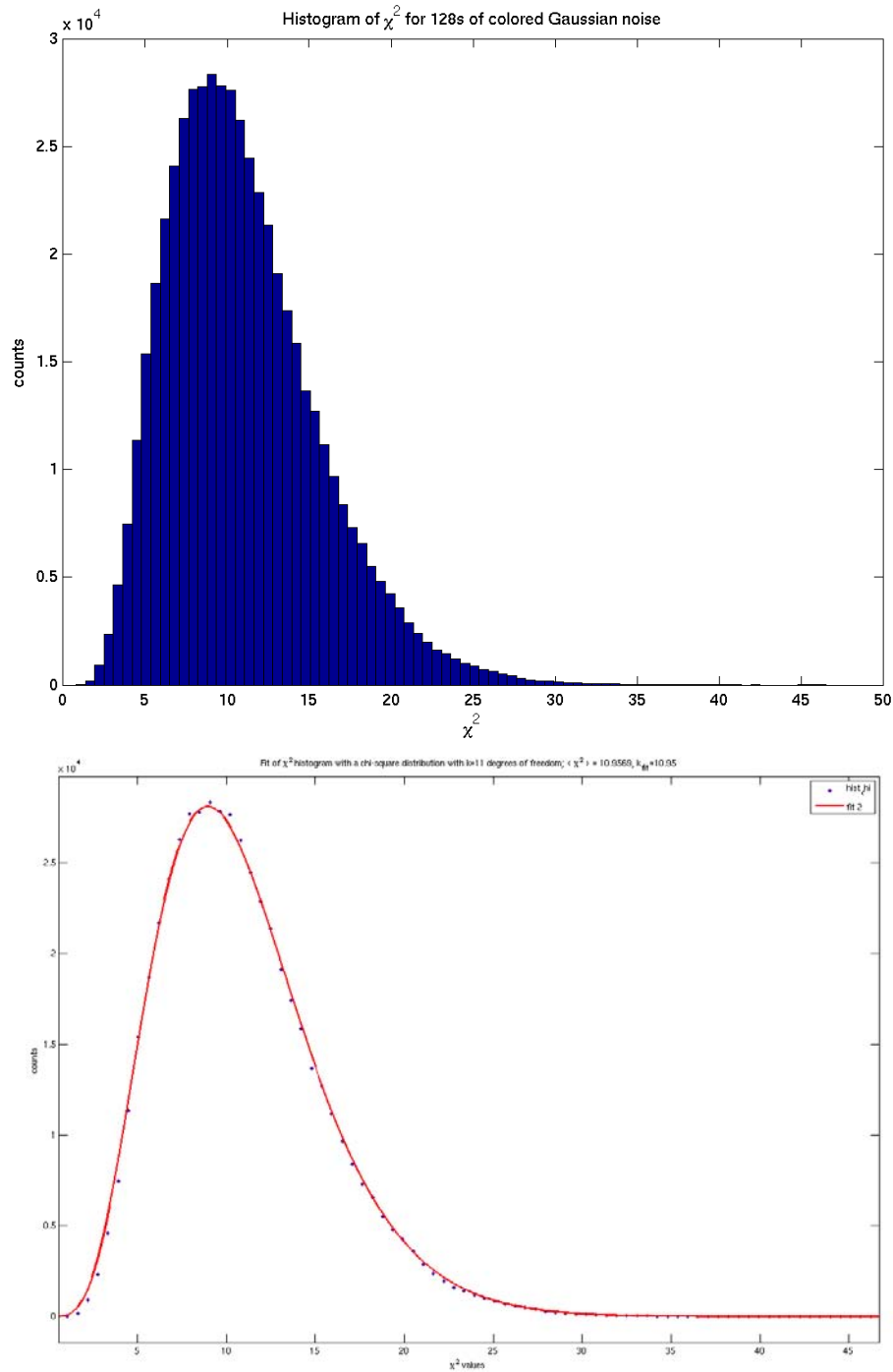


Figure 4.32: Histogram of $\chi_{PTF}^2(t)$ time series from H1 in 128s of simulated Gaussian noise (top figure) and fit with a χ^2 distribution (bottom figure); the frequency band is divided in 8 bins. The fit factor $k = 10.95$ is lower than the expected value of $2 \times (8 - 1) = 14$.

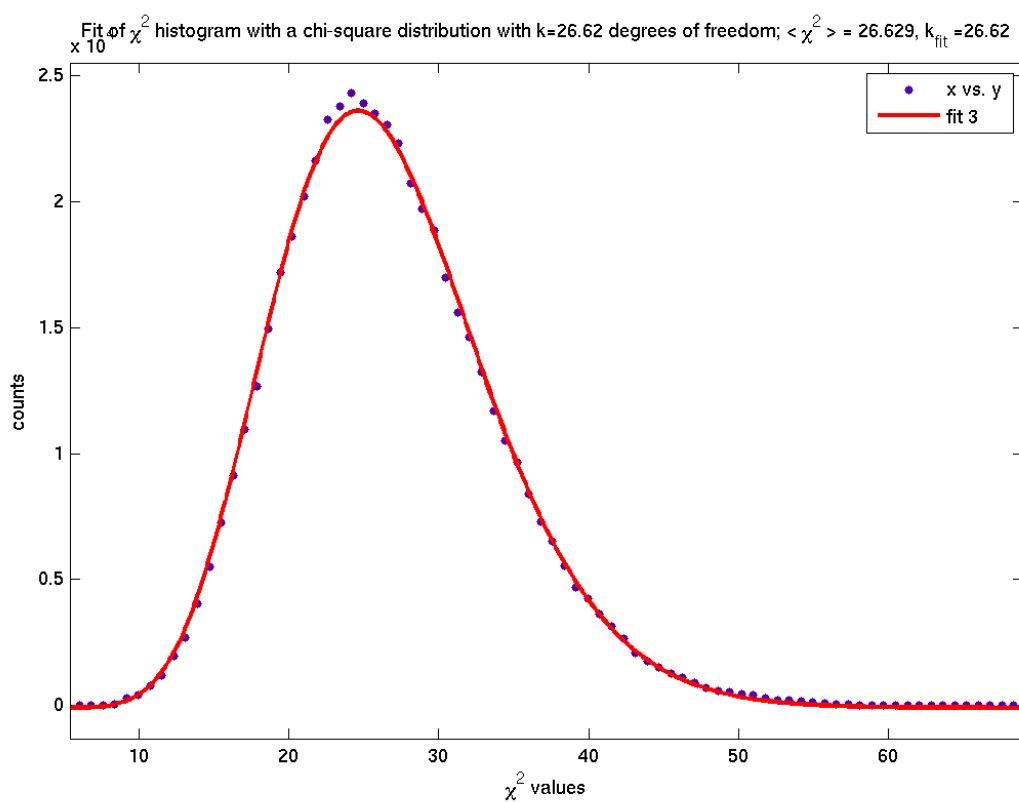


Figure 4.33: Fit of $\chi^2_{PTF}(t)$ time series with a χ^2 distribution; the frequency band is divided in 16 bins. The fit factor $k = 26.5$ is lower than the expected value of $2 \times (16 - 1) = 30$.

4. Results

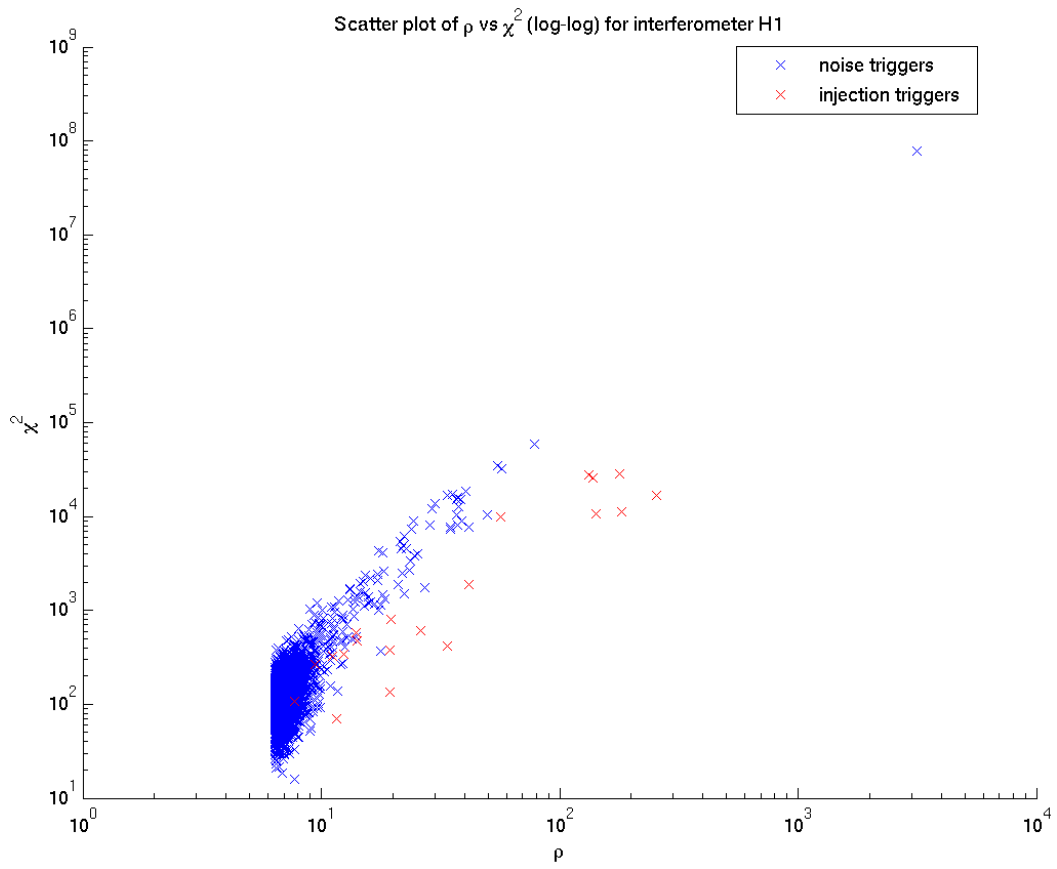


Figure 4.34: Scatter plot of χ^2 vs ρ values on a log-log scale for noise triggers (blue crosses) and injections (red crosses) in H1 real S5 data.

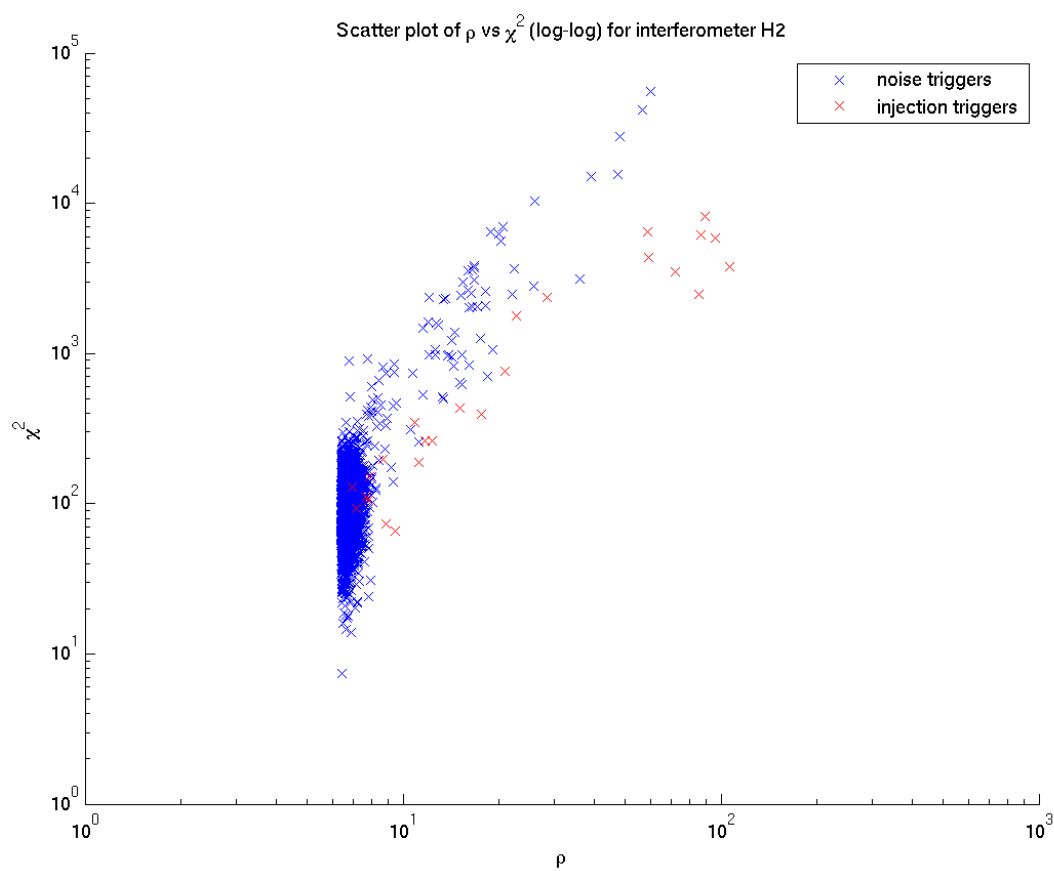


Figure 4.35: Scatter plot of χ^2 vs ρ values on a log-log scale for noise triggers (blue crosses) and injections (red crosses) in H2 real S5 data.

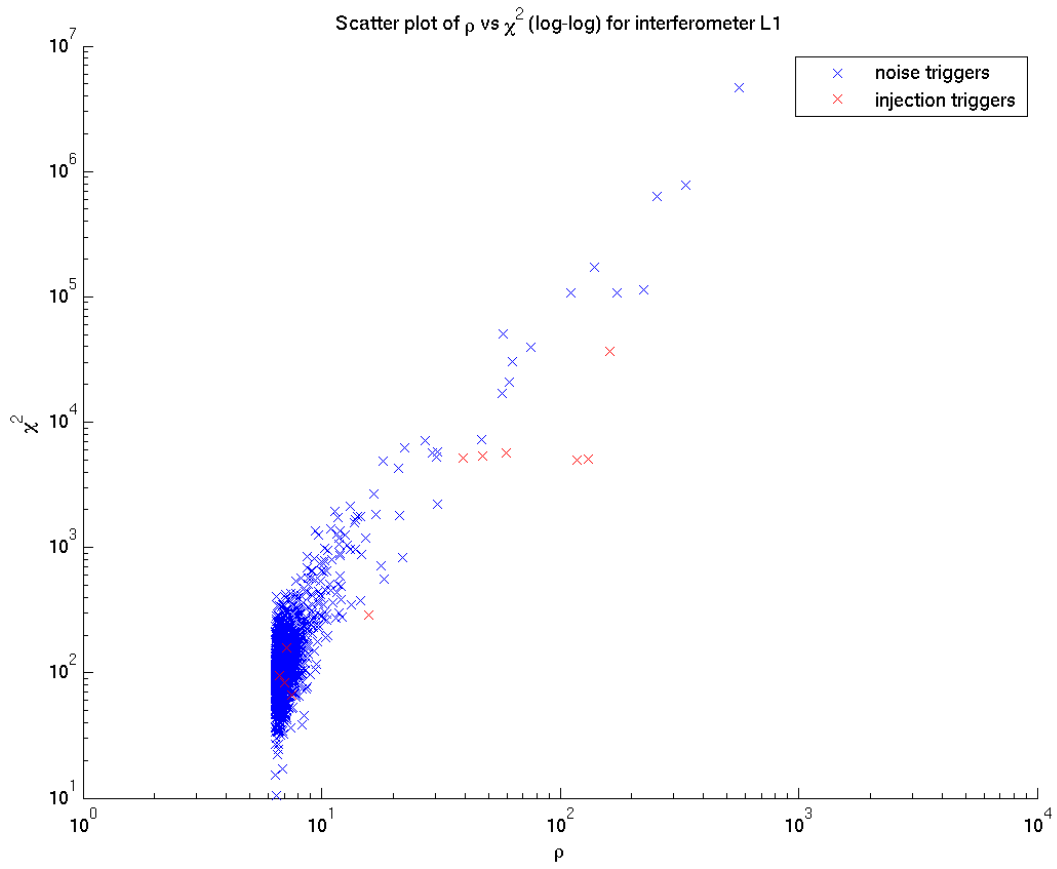


Figure 4.36: Scatter plot of χ^2 vs ρ values on a log-log scale for noise triggers (blue crosses) and injections (red crosses) in L1 real S5 data.

Conclusions

We have implemented and tested the theoretical and numerical tools necessary to analyze LIGO data using a new family of Physical Templates for gravitational waves emitted by low mass asymmetric compact object binaries with only one significantly spinning component; these systems emit modulated GW signals which, for particular configurations of the source, cannot be recovered with high efficiency using non-spinning templates.

We implemented numerical algorithms written in C language and integrated them in the LIGO Algorithm Library (LAL) as part of the Compact Coalescence Group (CBC) inspiral search pipeline.

We wrote code that numerically solves the Post-Newtonian equations of motion for the source and generates the time evolution of the dynamical variables needed to construct the templates and we solved numerical issues that lead to failures for a small fraction of parameter configurations (Sections 3.4.1, 3.4.2).

We have been able to develop a reasonably fast matched filtering engine which shows high efficiency in recovering simulated gravitational-wave signals, both in simulated Gaussian noise and in real LIGO S5 data (Sec. 4.1).

We constructed a kludge template bank that covers the region of interest of the intrinsic parameter space (Sec. 3.4.3) and we performed bank simulations by filtering a large number of random simulated signals with the whole template bank and calculating the maximum match for every signal (Sec. 4.2); results show that the PTF template bank has an average match of ~ 0.94 while the corresponding low-mass non-spinning template bank has an average match of 0.87 . The match has a dependence on both the mass and the spin parameters of the signal being filtered, decreasing in regions of the parameter space characterized by larger magnitude of the spin, larger misalignment of the spin with respect to the orbital angular momentum and larger mass-ratio; PTF shows a substantially better efficiency with respect to SPA in recovering GWs from systems that lie in this region of the parameter space and, in general, from systems with a low mass component $m_2 \lesssim 1.4M_\odot$.

We tested the matched filtering algorithm with the chosen SNR threshold of 6.4 by injecting a large number of random simulated spinning signals in a set of real

noisy data and filtering it with the PTF template bank (Sec. 4.3); we performed a parallel simulation using the SPA template bank and we compared the number of injections found. The PTF template bank is able to recover injections more consistently at low effective distance, while the SPA template bank shows “holes” in efficiency corresponding to the high-spin high-mass-ratio region of the parameter space; furthermore PTF shows a better accuracy in estimating the mass parameters of the source.

We tested the coincidence stage using rectangular windows on the estimated parameters from different interferometers to identify coincident triggers (Sec. 4.4); we passed the injection triggers from the first inspiral stage through the coincidence test and compared the number of injections found by the PTF and the SPA pipelines. A better parameter estimation allows PTF templates to recover more injections in triple coincidence.

Finally we made preliminary tests on the χ^2 veto for physical templates and results suggest that this veto is able to discriminate between noise triggers and injection triggers with fairly good efficiency (Sec. 4.5).

Concluding, the Physical Template Family is a promising data-analysis strategy candidate to address the problem of detection of gravitational waves emitted by asymmetric compact-object binaries of type BH-NS, both in terms of detection efficiency and in terms of parameter estimation.

Future Prospects

Depending on the level of development of each stage of the PTF pipeline, different types of searches on LIGO data are viable.

The availability of a metric for the intrinsic parameter space in the future would allow for the implementation of an optimal template-placement code (see Sec. 2.5) and for the construction of a more effective “ellipsoidal” coincidence stage which takes into account correlations between different intrinsic parameters (see Sec. 3.4.4). In this case each stage of the pipeline could be tuned so as to obtain the desired false alarm rate, and the efficiency of the whole pipeline in recovering injected signals could be determined. If this efficiency turns out to be higher than that of the corresponding non-spinning pipeline, a full search with PTF will be the optimal choice.

If a random template-placement code is implemented but no metric is available, the coincidence stage cannot be optimized and rectangular windows must be used instead of ellipsoids; the pipeline can still be tuned to obtain the desired false alarm rate but the detection efficiency would be lower. In this case a phenomenological ellipsoidal coincidence stage could be implemented performing large Monte Carlo simulations to determine the shape of the ellipsoid empirically.

If no metric and no template-placement algorithm are available, a targeted search can still be performed by restricting the region of the intrinsic parameter space to search over; simulations (see Sections 4.2, 4.3) show that PTF is mostly needed in specific regions where precession-induced modulatory effects are stronger and non-spinning templates fail to match spinning GW signals with high SNR; in these restricted regions, kludge template banks with a desired minimal match can be constructed and an empirical ellipsoidal coincidence test can be implemented.

Finally PTF templates can be used in a triggered search to accurately estimate parameters corresponding to triggers from the non-spinning search; since non-spinning SPA templates have some efficiency in detecting GW signals from spinning binaries but they lack the capability of estimating spin parameters, very fine PTF template banks can be constructed around specific values of the mass parameters to obtain an estimate of the spin parameters.

Bibliography

- [1] L.D. Landau and E.M. Lifshitz. *The classical theory of fields*. Pergamon, Oxford, 1971.
- [2] K. S. Thorne, *300 Years of Gravitation*, edited by S.W. Hawking and W. Israel, Cambridge University Press, Cambridge, England (1987).
- [3] K. D. Kokkotas and B. G. Schmidt, *Living Rev. Relativity*, **2**, 2 (1999).
- [4] L. M. Goggin, *A Search For Gravitational Waves from Perturbed Black Hole Ringdowns in LIGO Data*, PhD Thesis, (2008)
- [5] H. A. Bethe and G. E. Brown, “Evolution of Binary Compact Objects Which Merge,” *Astrophys. J.* **506**, 780 (1998)
- [6] S. F. Portegies Zwart and L. R. Yungelson, “Formation and evolution of binary neutron stars”, *Astronomy and Astrophysics*, **332**, 173 (1998).
- [7] V. Kalogera, “Spin-Orbit Misalignment in Close Binaries with Two Compact Objects”, *Astrophys. J.* **541**, 319 (2000)
- [8] C. L. Fryer and V. Kalogera, “Theoretical Black Hole Mass Distributions,” *Astrophys. J.* **554**, 548 (2001)
- [9] T. A. Apostolatos, C. Cutler, G. J. Sussman and K.S.Thorne, *Phys. Rev. D* **49**, 49 (1994).
- [10] T.A. Apostolatos, *Phys. Rev. D*, **52**, 605 (1995)
- [11] T. A. Apostolatos, *Phys. Rev. D* **54**, 2438 (1996).
- [12] P. Grandclément, V. Kalogera and A. Vecchio, *Phys. Rev. D* **67**, 042003 (2003).
- [13] B.F. Schutz, *The Detection of Gravitational Waves*, ed. D.G. Blair (Cambridge: Cambridge University Press), 406 (1991).

-
- [14] K. S. Thorne, “Multipole Expansions Of Gravitational Radiation”, *Rev. Mod. Phys.* **52**, 299 (1980).
- [15] B. Allen, “A χ^2 time-frequency discriminator for gravitational wave detection,” *Phys. Rev. D* **71**, 062001 (2005) [arXiv:gr-qc/0405045].
- [16] A. Buonanno, Y. b. Chen and M. Vallisneri, “Detecting gravitational waves from precessing binaries of spinning compact objects: Adiabatic limit”, *Phys. Rev. D* **67**, 104025 (2003) [Erratum-*ibid.* *D* **74**, 029904 (2006)] [arXiv:gr-qc/0211087].
- [17] L. E. Kidder, “Coalescing binary systems of compact objects to postNewtonian $5/2$ order. 5. Spin effects”, *Phys. Rev. D* **52**, 821 (1995) [arXiv:gr-qc/9506022].
- [18] L. E. Kidder, C.M. Will and A.G. Wiseman, *Phys. Rev. D* **47**, 4183 (R) (1993).
- [19] T. Damour, B. R. Iyer and B. S. Sathyaprakash, *Phys. Rev. D* **63**, 044023 (2001); **66**, 027502 (2002).
- [20] BCV1: A. Buonanno, Y. Chen and M. Vallisneri, *Phys. Rev. D* **67**, 024016 (2003).
- [21] M. Salgado, S. Bonazzola, E. Gourgoulhon and P. Haensel, *Astrophys. J.* **291**, 155 (1994).
- [22] G.B. Cook, S.L. Shapiro and S.A. Teukolsky, *Astrophys. J.* **424**, 823 (1994).
- [23] P. Haensel, M. Salgado, and S. Bonazzola, *Astronomy and Astrophysics* **296**, 745 (1995).
- [24] W.G. Laarakkers and E. Poisson, *Astrophys. J.* **512**, 282L (1999).
- [25] C. S. Kochanek, *Astrophys. J.* **398**, 234 (1992);
- [26] L. Bildsten and C. Cutler, *Astrophys. J.* **400**, 175 (1992).
- [27] P. Jaranowski and G. Schäfer, *Phys. Rev. D* **57**, 7274(1998); **60**, 124003 (1999); T. Damour, P. Jaranowski and G. Schäfer, *ibid.* **62**, 044024 (2000); 021501(R) (2000); **63**, 044021 (2001).
- [28] L. Blanchet, G. Faye, B. R. Iyer, B. Joguet, *Phys. Rev. D* **65**, 061501 (2002)
- [29] L. Blanchet, B. R. Iyer and B. Joguet, *Phys. Rev. D* **65**, 064005 (2002).

BIBLIOGRAPHY

- [30] L. Blanchet, T. Damour, B. R. Iyer, C. M. Will and A. G. Wiseman, *Phys. Rev. Lett.* **74**, 3515 (1995)
- [31] L. Blanchet, T. Damour and B. R. Iyer, *Phys. Rev. D* **51**, 536 (1995)
- [32] C. M. Will and A. G. Wiseman, *Phys. Rev. D* **54**, 4813 (1996).
- [33] Y. Pan, A. Buonanno, Y. b. Chen and M. Vallisneri, “A physical template family for gravitational waves from precessing binaries of spinning compact objects: Application to single-spin binaries”, *Phys. Rev. D* **69**, 104017 (2004) [Erratum-ibid. *D* **74**, 029905 (2006)] [arXiv:gr-qc/0310034]
- [34] R. A. Hulse and J. H. Taylor, *Ap. J.*, **195**, L51 (1975).
- [35] C Cutler and K.S. Thorne. “An overview of gravitational-wave sources.” In N.T Bishop and S.D Maharaj, editors, *Proceedings of GR-17*. World Scientific, 2002.
- [36] S. Mitra, S. Dhurandhar, T. Souradeep, A. Lazzarini, V. Mandic, S. Bose and S. Ballmer, “Gravitational wave radiometry: Mapping a stochastic gravitational wave background”, *Phys. Rev. D* **77**, 042002 (2008) [arXiv:0708.2728 [gr-qc]].
- [37] T. Damour, B. R. Iyer and B. S. Sathyaprakash, *Phys. Rev. D* **57**, 885 (1998).
- [38] T. Damour, P. Jaranowski and G. Schäfer, *Phys. Lett. B* **513**, 147 (2001).
- [39] B. J. Owen, *Phys. Rev. D* **53**, 6749 (1996)
- [40] R. Balasubramanian, B. S. Sathyaprakash and S. V. Dhurandhar, *Phys. Rev. D* **53**, 3033 (1996).
- [41] B. Abbott et al., “Detector description and performance for the first coincidence observations between ligo and geo.” *Nucl. Instrum. Meth.*, **A517**:154-179, 2004.
- [42] F. Acernese et al., “The virgo status.” *Class. Quant. Grav.*, **23**:S635-S642, 2006.
- [43] H. Luck et al., “Status of the geo600 detector.” *Class. Quant. Grav.*, **23**:S71-S78, 2006.
- [44] B. Abbott et al. Analysis of ligo data for gravitational waves from binary neutron stars., *Phys. Rev. D* **69**:122001, 2004.

- [45] B. Abbott et al., “Search for gravitational waves from galactic and extragalactic binary neutron stars.” *Phys. Rev. D* **72**:082001, 2005.
- [46] B. Abbott et al., “Search for gravitational waves from primordial black hole binary coalescences in the galactic halo.” *Phys. Rev. D* **72**:082002, 2005.
- [47] B. Abbott et al. “Search for gravitational waves from binary black hole inspirals in ligo data.” *Phys. Rev. D* **73**:062001, 2006.
- [48] B. Abbott et al., “Upper limits on gravitational wave bursts in ligo’s second science run.” *Phys. Rev. D* **72**:062001, 2005.
- [49] B. Abbott et al., “Search for gravitational wave bursts in ligo’s third science run.” *Class. Quant. Grav.* **23**:S29-S39, 2006.
- [50] C. Cutler and E.E. Flanagan. “Gravitational waves from merging compact binaries: How accurately can one extract the binary’s parameters from the inspiral waveform?” *Phys. Rev. D* **49**:2658-2697, 1994
- [51] L.S. Finn. “Detection, measurement, and gravitational radiation.” *Phys. Rev. D* **46**:5236,
- [52] Eanna E. Flanagan and Scott A. Hughes. “Measuring gravitational waves from binary black hole coalescences. ii: The waves’ information and its extraction, with and without templates.” *Phys. Rev. D* **57**:4566-4587, 1998.
- [53] L.S. Finn and D.F. Chernoff. “Observing binary inspiral in gravitational radiation: One interferometer.”, *Phys. Rev. D* **47**:2198-2219, 1993.
- [54] David F. Chernoff and Lee Samuel Finn. “Gravitational radiation, inspiraling binaries, and cosmology.”, *Astrophys. J.*, **411**:L5-L8, 1993.
- [55] K.D. Kokkotas, A. Królak, and G. Tsegas. “Statistical analysis of the estimators of the parameters of the gravitational-wave signal from a coalescing binary.”, *Class. Quantum. Grav*, **11**:1901, 1994.
- [56] A. Królak, K.D. Kokkotas, and G. Schäfer. “Estimation of the post-newtonian parameters in the gravitational-wave emission of a coalescing binary.”, *Phys. Rev. D*, **52**:2089-2111, 1995.
- [57] E. Poisson and C.M. Will. “Gravitational waves from inspiralling compact binaries parameter-estimation using second-post-newtonian wave-forms.”, *Phys. Rev. D*, **52**:848-855, 1995.

BIBLIOGRAPHY

- [58] R. Balasubramanian, B. S. Sathyaprakash, and S. V. Dhurandhar. “Estimation of parameters of gravitational waves from coalescing binaries.”, *Pramana*, **45**:L463, 1995.
- [59] R Balasubramanian, B S Sathyaprakash, and S V Dhurandhar. “Gravitational waves from coalescing binaries: detection strategies and monte carlo estimation of parameters.”, *Phys. Rev. D*, **53**:3033, 1996. Erratum-ibid. D **54**, 1860 (1996).
- [60] K G Arun, B R Iyer, B S Sathyaprakash, and P A Sundararajan. “Parameter estimation of inspiralling compact binaries using 3.5 post-newtonian gravitational wave phasing: The non-spinning case.”, *Phys. Rev. D* **71**:084008, 2005. Erratum-ibid. D **72**, 069903 (2005).
- [61] C W Misner, K S Thorne, and J A Wheeler. *Gravitation*. W.H. Freeman, New York, NY, 1973.
- [62] C. V. D. Broeck *et al.*, “Template banks to search for compact binaries with spinning components in gravitational wave data”, arXiv:0904.1715 [gr-qc].
- [63] C. Messenger, R. Prix and M. A. Papa, “Random template banks and relaxed lattice coverings”, arXiv:0809.5223 [gr-qc].
- [64] W.B. Davenport, Jr. and W.L. Root, *An Introduction to the Theory of Random Signals and Noise*, IEEE Computer Society Press, 1975.